Thermal Conductivity of the Spin-Ice Compound $Dy_2Ti_2O_7$ and the Spin-Chain System $BaCo_2V_2O_8$

I n a u g u r a l - D i s s e r t a t i o n

zur

Erlangung des Doktorgrades
der Mathematisch-Naturwissenschaftlichen Fakultät
der Universität zu Köln

vorgelegt von

Gerhard Kolland

aus Hamburg

Köln, 2013

Berichterstatter:	Priv. Doz. Dr. T. Lorenz Prof. Dr. A. Rosch
Vorsitzender der Prüfungskommission:	Prof. Dr. L. Bohatý
Tag der mündlichen Prüfung:	21.01.2013

Für Tina, Henri & Bruno

Contents

1 Introduction

Competing magnetic interaction cause frustration and may prevent conventional magnetic order. As a consequence, complex ground states with unusual excitations can be realized, leading to a variety of interesting physical properties. One example is the so-called spin-ice material $Dy_2Ti_2O_7$. In $Dy_2Ti_2O_7$, the magnetic Dy ions form a pyrochlore sublattice, consisting of corner-sharing tetrahedra. Due to a strong crystal field, the Dy momenta are aligned along their local easy axes pointing either into or out of the tetrahedra. The magnetic Dy ions interact via nearest-neighbor exchange and long-range dipole-dipole interaction. This highly frustrated spin-spin interaction is analogous to the proton displacement in water ice and leads to a residual entropy given by the Pauling's entropy [1]. The macroscopically degenerate spin-ice ground state is realized by the ice rule 2in-2out which is fulfilled when two Dy spins per tetrahedra point into and the other two out of the tetrahedra. Elementary dipole excitations can be created by flipping one spin resulting in two neighboring tetrahedra with configurations 3in-1out and 1in-3out, respectively. These dipole excitations can fractionalize into two individual monopole excitations which can move independently within the pyrochlore lattice and are realizations of Dirac monopoles which are connected via Dirac strings [2].

Less is known about the interaction of these monopole excitations with each other or with other quasi particles. The aim of this thesis is to investigate the dynamics of these monopole excitations. In Refs. [3, 4], the observation of a monopole current due to a small magnetic field was reported. This point, however, is currently under strong debate [5] and remains an open question up to now. Suitable probes to study the dynamics of such elementary excitations are measurements of the thermal conductivity which are the main subject of this thesis. Up to now, only one experimental study about the thermal conductivity of $Dy_2Ti_2O_7$ is published [6]. This work focuses on the relaxation times of the magnetic system in $Dy_2Ti_2O_7$ which are anomalously enhanced at lowest temperatures. In Ref. [6], the thermal conductivity has been measured along the [110] direction for magnetic fields up to 1.5 T parallel to the heat current $\vec{j}$. Within this thesis, the thermal conductivity of $Dy_2Ti_2O_7$ has been measured in great detail for different heat-current directions and various magnetic-field directions.

To study the different transport mechanisms contributing to the heat transport, three reference compounds are investigated in this thesis, the non-magnetic $Y_2Ti_2O_7$ and two doped magnetic reference compounds $(Dy_{0.5}Y_{0.5})_2Ti_2O_7$

and $Dy_2(Ti_{0.9}Zr_{0.1})_2O_7$. In case of $(Dy_{0.5}Y_{0.5})_2Ti_2O_7$, the idea is to suppress the spin-ice features by essentially conserving the phononic properties. In $Dy_2(Ti_{0.9}Zr_{0.1})_2O_7$, the substitution with much larger Zr ions is supposed to affect the phononic properties by basically conserving the spin-ice properties.

Unconventional magnetic ordering can also be observed when reducing the dimensionality of the magnetic system, *i.e.* in low-dimensional spin systems. The second part of this thesis concerns the quasi one-dimensional antiferromagnetic spin-chain compound $BaCo_2V_2O_8$, which is a realization of an effective spin-1/2 Ising-like spin chain. For magnetic fields parallel to the c axis, the magnetization saturates at $B_{s||} \simeq 23\,\mathrm{T}$ and perpendicular to the c axis at $B_{s\perp} \simeq 41\,\mathrm{T}$. In zero field, the system orders due to inter-chain coupling at $T_N = 5.4\,\mathrm{K}$ [7].

In low-dimensional spin systems, magnetic excitations can lead to large and unusual magnetic heat transport [8]. In integrable spin models, the heat transport is ballistic, *i.e.* dissipationless, and the magnetic thermal conductivity diverges. Enhanced heat transport was found mainly for low-dimensional $S = 1/2$ Heisenberg spin systems, like spin chains, spin ladders, and 2D square lattices. In this context, the question arises whether a magnetic heat transport can be observed for the Ising-like spin chain $BaCo_2V_2O_8$. To resolve this issue, the thermal conductivity of $BaCo_2V_2O_8$ has been measured for different heat-current directions parallel and perpendicular to the spin chains and for various magnetic-field directions. To study the transport mechanisms in $BaCo_2V_2O_8$, additional thermal-conductivity measurements have been performed on two doped compounds, $(Ba_{0.9}Sr_{0.1})Co_2V_2O_8$ and $Ba(Co_{0.95}Mg_{0.05})_2V_2O_8$, and on the iso-structural $BaMn_2V_2O_8$. The idea of Sr doping in $(Ba_{0.9}Sr_{0.1})Co_2V_2O_8$ is to increase defect scattering in order to suppress the phononic thermal conductivity by essentially conserving the magnetic properties. In $Ba(Co_{0.95}Mg_{0.05})_2V_2O_8$, doping with the non-magnetic Mg splits the Co chains into finite chain segments. This is assumed to have a strong influence on the magnetic system. The Heisenberg $S = 5/2$ spin chain $BaMn_2V_2O_8$ is an iso-structural reference compound with isotropic magnetic properties.

This thesis is structured as follows. First, a brief introduction into the theoretical and experimental framework of the thermal conductivity is given. In Sec. 4, the thermal-transport properties of the spin-ice compound $Dy_2Ti_2O_7$ is studied. Sec. 5 deals with the study of the thermal conductivity of the spin-chain compound $BaCo_2V_2O_8$. In the appendix, additional measurements which were performed during this thesis are presented.

2 Theory

2.1 Thermal Conductivity

In this chapter, basics of transport theory are briefly summarized. A more detailed introduction can be found in Refs. [9–21]. The thermal conductivity κ of a solid is defined as

$$\vec{j} = -\underline{\underline{\kappa}}\,\vec{\nabla}T\,, \tag{2.1}$$

where $\vec{j}$ is the heat current and $\vec{\nabla}T$ is the temperature gradient over the sample. The negative sign reflects the fact that the heat flows from the hot to the cold end of the sample. Generally, $\underline{\underline{\kappa}}$ is a 2nd-order tensor. For an isotropic crystal, $\underline{\underline{\kappa}}$ is reduced to a scalar κ. By means of the kinetic gas theory, the thermal conductivity κ can be written as

$$\kappa = \frac{1}{d} c v \ell\,, \tag{2.2}$$

where d is the dimensionality (usually $d = 3$) and c is the specific heat of the considered (quasi-) particles with mean velocity v and mean free path ℓ. In the case of phonons, the thermal conductivity is described by the Debye model, presented in the following chapters.

2.1.1 Phononic Contribution (Debye Model)

The phononic specific heat (lattice contribution) can be calculated via the Debye formula

$$c_{\mathrm{ph}} = 9 N_{\mathrm{A}} k_{\mathrm{B}} \left(\frac{T}{\Theta_{\mathrm{D}}}\right)^3 \int_0^{\Theta_{\mathrm{D}}/T} \frac{x^4 \mathrm{e}^x}{(\mathrm{e}^x - 1)^2}\,\mathrm{d}x\,, \tag{2.3}$$

where Θ_{D} denotes the Debye temperature. The integral in Eq. (2.3) can only be numerically calculated. In the limit $T \to \infty$, the integral converges to $\frac{1}{3}(\Theta_{\mathrm{D}}/T)^3$ and, thus, one obtains the high-temperature limit $c = 3 N_{\mathrm{A}} k_{\mathrm{B}}$ (Dulong-Petit). For $T \to 0$, the integral in Eq. (2.3) converges to $\int_0^\infty = 4\pi^4/15 \approx 25.9758$. This yields the low-temperature T^3 dependence for the phononic specific heat

$$c_{\mathrm{ph}} = \frac{12\pi^4}{5} \frac{N_{\mathrm{A}} k_{\mathrm{B}}}{{\Theta_{\mathrm{D}}}^3}\, T^3\,. \tag{2.4}$$

Within the Debye model, the phononic thermal conductivity is given by

$$\kappa_{\mathrm{ph}} = \frac{k_{\mathrm{B}}}{2\pi^2 v} \left(\frac{k_{\mathrm{B}}}{\hbar}\right)^3 \int_0^{\Theta_{\mathrm{D}}/T} \frac{x^4 \mathrm{e}^x \tau(\omega, T)}{(\mathrm{e}^x - 1)^2}\,\mathrm{d}x\,, \tag{2.5}$$

where v is the mean sound velocity, ω is the phononic angular frequency, $x = (\hbar\omega)/(k_\mathrm{B}T)$, and $\tau^{-1}(\omega, T) = v/\ell$ is the total scattering rate, where ℓ is the mean free path. The mean sound velocity can be estimated via

$$v = \Theta_\mathrm{D} \left(\frac{k_\mathrm{B}}{\hbar} \right) (6\pi^2 n)^{-1/3} , \tag{2.6}$$

where $n = N/V$ is the atomic density per volume.

The integrals in Eqs. (2.3) and (2.5) can only be numerically calculated. In this thesis, the calculations and the fitting of experimental data is performed by the numerical computation software Scilab [22]. Assuming the different scattering processes to act independently, the total scattering rate is given by the sum of the scattering rates of each process (Matthiessen's rule), *i.e.*

$$\tau_\mathrm{tot}^{-1} = \sum_i \tau_i^{-1} . \tag{2.7}$$

A variety of different scattering rates can be found in literature. The scattering rates used for the analysis in this thesis are the following:[1]

Boundary Scattering

$$\tau_\mathrm{bd}^{-1} = v/L \tag{2.8}$$

This term describes reflection of phonons by the crystal surface, where L is the characteristic sample length. At very low temperatures ($T \to 0$), the phononic thermal conductivity is essentially dominated by boundary scattering, *i.e.* the mean free path is only limited by the effective sample length ($\ell \sim L$).

The phononic specific heat c_ph and the sound velocity can be estimated by Eqs. (2.4) and (2.6), respectively. By inserting these quantities into Eq. (2.2), one can estimate the phononic thermal conductivity at low temperatures ($T \to 0$). In Refs. [26, 27], this estimation of the phononic thermal conductivity at lowest temperatures is used to investigate the presence of phonon scattering on magnetic excitations in the low-temperature limit. The authors calculate the mean free path ℓ via Eqs. (2.2), (2.4), and (2.6) and compare the (temperature-dependent) mean free path ℓ with the effective sample width $W = 2\bar{w}/\sqrt{\pi}$, where $\bar{w}$ is the geometric mean width of a rectangular sample [28–30]. For a ratio $W/\ell \simeq 1$, one can assume the phononic thermal conductivity to be affected only by boundary scattering. $W/\ell < 1$ indicates an additional scattering process, *e.g.* on magnetic excitations.

[1] A detailed discussion of different scattering rates can be found in Refs. [12, 17, 23–25].

Point-Defect Scattering

$$\tau_{\mathrm{pd}}^{-1} = P\omega^4 \tag{2.9}$$

This term describes scattering of phonons on point defects, where P is an adjustable parameter. Short-wave phonons are more scattered than long-wave phonons, which dominate at low temperatures. Thus, this term is most effective in the temperature range of the phononic maximum of $\kappa(T)$. At higher temperatures, the Umklapp scattering dominates.

Umklapp Scattering

$$\tau_{\mathrm{um}}^{-1} = U\omega^2 T \exp\left(-\frac{\Theta_{\mathrm{D}}}{uT}\right) \tag{2.10}$$

This term describes Umklapp scattering, where U and u are adjustable parameters. The parameter u reflects the temperature range where Umklapp scattering sets in.

Resonant Phonon Scattering

$$\tau_{\mathrm{res}}^{-1} = R\,\frac{4\omega^4\Delta^4}{(\Delta^2-\omega^2)^2}\,(N_0+N_1) \tag{2.11}$$

This term describes resonant scattering on a two- (or multi-) level system [31, 32]. R is an adjustable parameter, Δ is the energy splitting, and N_0 and N_1 are the population factors of the two considered levels. In the special case of a two-level system, N_0 and N_1 sum up to 1. This scattering process affects phonons with an energy (frequency) close to the energy splitting Δ, which can depend on temperature as well as on the external magnetic field.

Scattering on magnetic Excitations at a magnetic Transition

$$\tau_{\mathrm{mag}}^{-1} = M\omega^4 T^2 C_{\mathrm{mag}}(T) \tag{2.12}$$

This term describes scattering on magnetic excitations around a magnetic transition [24, 25] and results in a suppression of $\kappa(T)$ around the transition temperature. M is an adjustable parameter and $C_{\mathrm{mag}}(T)$ is the temperature-dependent magnetic specific heat, which exhibits a peak around the magnetic transition.

2.1.2 Minimum Thermal Conductivity

In the high-temperature regime, the phononic thermal conductivity is proportional to $1/T$ (due to Umklapp scattering). To avoid the mean free path ℓ to become smaller than the inter-atomic distance, one can introduce a minimum mean free path ℓ_{min} [33, 34] and, thus, a lower limit for the relaxation times

$$\tau(\omega, T) = \max\left\{\tau_{\Sigma}(\omega, T), \frac{\ell_{\mathrm{min}}}{v}\right\}, \tag{2.13}$$

where $\tau_{\Sigma}(\omega, T)$ is the relaxation time obtained from the scattering rates discussed above. The minimum mean free path results in a minimum thermal conductivity κ_{min} at high temperatures (typically at room temperature).

2.1.3 Electronic Contribution

The transport properties of electrons are described in detail in Ref. [35]. Here, a brief introduction is given. The electronic contribution κ_{el} of the thermal conductivity can be obtained by Eq. (2.2). The specific heat of the Fermi gas is given by [10]

$$c_{\mathrm{el}} = \frac{1}{2}\pi^2 n k_{\mathrm{B}} \frac{T}{T_{\mathrm{F}}} \tag{2.14}$$

with the Fermi temperature $T_{\mathrm{F}} = \epsilon_{\mathrm{F}}/k_{\mathrm{B}}$ and the electron density n. The Fermi energy can be expressed in terms of the Fermi velocity

$$\epsilon_{\mathrm{F}} = \frac{1}{2} m v_{\mathrm{F}}^2 . \tag{2.15}$$

By inserting Eq. (2.14) into Eq. (2.2) one obtains

$$\kappa_{\mathrm{el}} = \frac{1}{3} c_{\mathrm{el}} v_{\mathrm{F}} \ell = \frac{\pi^2 n k_{\mathrm{B}}^2 T \tau}{3m}, \tag{2.16}$$

where the dimensionality is $d = 3$ and the mean free path $\ell = v_{\mathrm{F}}\tau$ can be written in terms of the scattering time τ. The electron mass is $m = 9.1094 \cdot 10^{-31}\,\mathrm{kg}$ [36]. Analogues to Eq. (2.2), the total scattering rate is the sum of the different scattering rates of each involved process,

$$\tau_{\mathrm{el}}^{-1} = \tau_{\mathrm{defect}}^{-1} + \tau_{\text{el-ph}}^{-1} . \tag{2.17}$$

At very low temperatures, the defect scattering dominates. As the defects are essentially temperature independent, the scattering rate is basically constant and results in a linear increase of the electronic thermal conductivity at very low temperatures. At higher temperatures, the scattering of electrons on phonons is the dominant process. This leads to a reduction of κ at higher temperatures and, thus, to a characteristic low-temperature maximum of $\kappa(T)$ [37].

2.1.4 Wiedemann-Franz Law

Good electrical conductors (metals) also are good thermal conductors. This results from the fact that the electrons which carry the electric charge can also transport heat. Within the Drude model, the electrical conductivity is given by [11]

$$\sigma = \frac{ne^2\tau}{m}\,, \tag{2.18}$$

where n is the electron density, $e = 1.602 \cdot 10^{-19}\,\mathrm{C}$ is the elementary charge [36], τ is the scattering time, and m is the electron mass. Assuming only elastic scattering of the electrons, one obtains the Wiedemann-Franz law by combining Eqs. (2.16) and (2.18),

$$\frac{\kappa_{\mathrm{el}}}{\sigma} = \frac{\pi^2}{3}\left(\frac{k_{\mathrm{B}}}{e}\right)^2 T \equiv L_0\,T\,, \tag{2.19}$$

where $L_0 = 2.45 \cdot 10^{-8}\mathrm{W}\Omega/\mathrm{K}^2$ is the Lorenz number. In good metals, the electronic contribution κ_{el} is much larger than the phononic contribution κ_{ph}, which can basically be neglected.

2.1.5 Magnetic Contribution

The preceding sections dealt with the heat transport by phonons and electrons. In principle, every (quasi) particle with a specific heat and a non-vanishing group velocity can carry heat. A detailed introduction to the heat transport by magnetic excitations can be found in Refs. [8, 9, 38]. Here, the essential points of Ref. [8] are briefly summarized.

Magnetic heat transport has been observed for a wide range of different materials [39–45]. Here, we focus on a special class of magnetic systems with reduced dimensionality, *i.e.* one- or two-dimensional spin systems, and antiferromagnetic Heisenberg exchange between nearest-neighbor spins. The most prominent compounds realizing a magnetic heat transport are copper-oxide systems (cuprates) which will be introduced in the following.

Fig. 2.1 illustrates three different spin structures which are realized by various cuprate systems. $S = 1/2$ Heisenberg AF spin chains (Fig. 2.1(a)) are realized by, *e.g.*, $CaCu_2O_3$, $SrCuO_2$, and Sr_2CuO_3. The $S = 1/2$ Heisenberg AF two-leg spin ladder (Fig. 2.1(b)) can be realized by different compounds of the type $(Sr,Ca,La)_{14}Cu_{24}O_{41}$. The 2D square lattice (Fig. 2.1(c)) can be regarded as a spin ladder with an infinite number of legs and can be realized by La_2CuO_4. These compounds have rather large coupling constants of $J \approx 1500\,\mathrm{K} - 2000\,\mathrm{K}$ [8].

The different spin structures shown in Fig. 2.1 have different ground-state properties and elementary excitations. Within the spin chain, the correlation of the spins is quasi-long range and decays algebraically with increasing distance

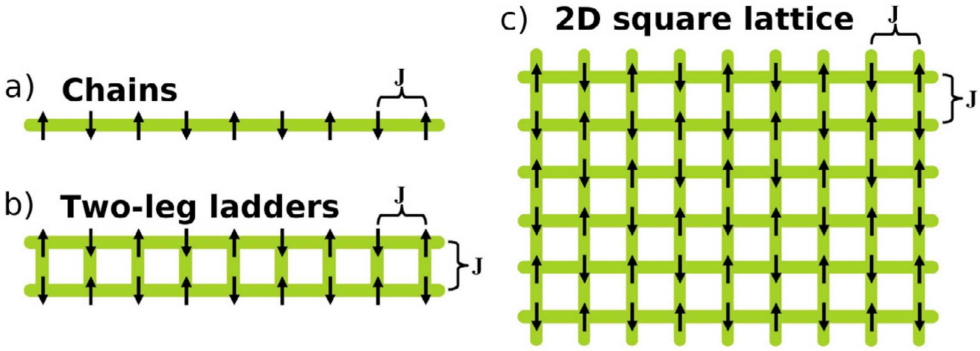

Figure 2.1: Different spin structures of antiferromagnetically coupled $S = 1/2$ Heisenberg spins. a) spin chain, b) two-leg spin ladder, c) two-dimensional square lattice (taken from [8]).

between the spins [46]. The elementary excitations are called spinons. They are gapless and carry a spin of $S = 1/2$ [47]. The ground state of the two-leg $S = 1/2$ Heisenberg spin ladder is a spin liquid. The short-range spin-spin correlations decay exponentially with increasing distances. The elementary excitations are magnons (triplons) with spin $S = 1$ and a spin gap Δ [48]. The ground state of the antiferromagnetic Heisenberg $S = 1/2$ 2D square lattice is a Néel state [49]. The elementary excitations are spin waves.

The magnetic heat transport in one-dimensional antiferromagnetic $S = 1/2$ Heisenberg chains is predicted to be dissipationless, *i.e.* to have no thermal resistivity [50, 51]. This so-called ballistic heat transport originates from the fact that the thermal-current operator and the Hamiltonian commute, *i.e.* the thermal-current operator is a conserved quantity. The question whether the heat transport is conserved also in spin-ladder compounds is currently under debate [52–55]. In real crystals, the thermal conductivity is affected by external scattering processes and, hence, remains finite. In the following, experimental results of thermal-conductivity measurements are shown for different types of low-dimensional spin systems.

The upper panels of Fig. 2.2 illustrate experimental thermal-conductivity data for the compounds realizing the different spin structures shown in Fig. 2.1, *i.e.* (a) spin chain, (b) spin ladder, and (c) 2D square lattice [8, 56–59]. The extracted magnetic contributions κ_{mag} are shown in the lower panels.[2] The magnetic thermal conductivity κ_{mag} of the gapless spin-chain compound $CaCu_2O_3$ (Fig. 2.2(a)) almost linearly increases with increasing temperature. The magnetic contributions κ_{mag} of the gapped spin-ladder compounds $Sr_{14}Cu_{24}O_{41}$ and $Ca_9La_5Cu_{24}O_{41}$ (Fig. 2.2(b)) show an activated behavior at low temperatures. At $\sim 150\,\mathrm{K}$, depending on the actual compound, κ_{mag} exhibits a broad maximum and decreases

[2]Details of how to extract the magnetic contribution of the respect data can be found in [8].

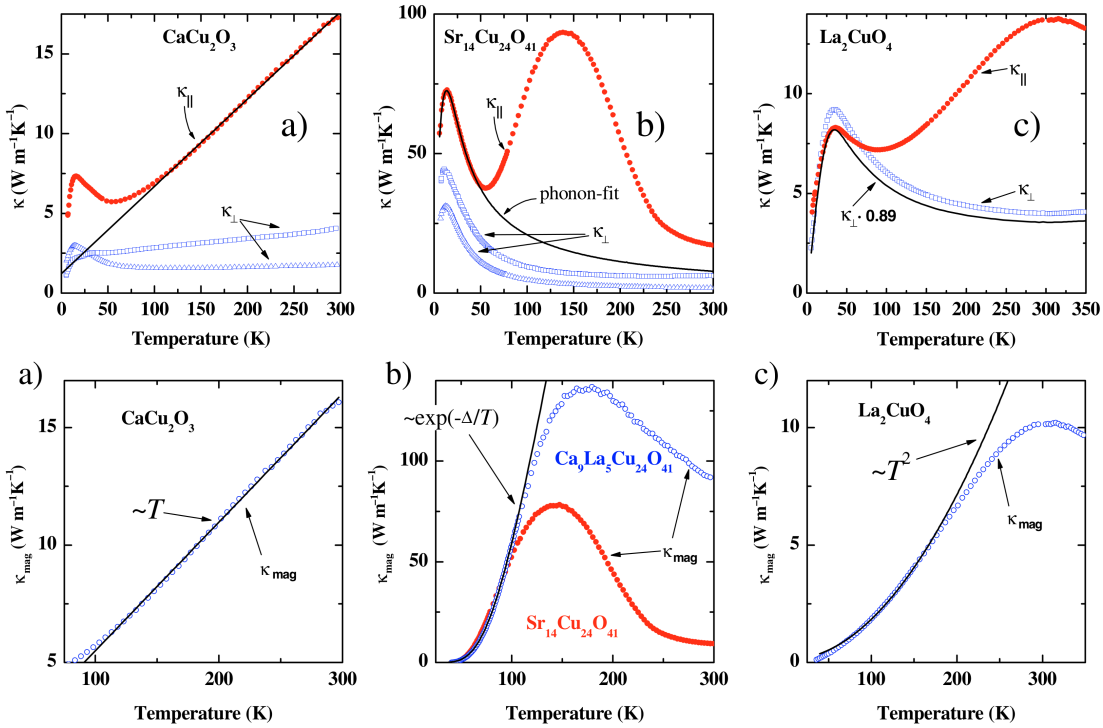

Figure 2.2: Upper panels: Thermal conductivity of $S = 1/2$ Heisenberg antiferromagnets. (a) spin chain, (b) spin ladder, (c) 2D square lattice. Lower panels: Extracted magnetic thermal conductivity κ_{mag} for the respective spin systems (taken from [8, 56–59]).

at higher temperatures. Fig. 2.2(c) shows κ_{mag} for the 2D square lattice La_2CuO_4. At low temperatures, κ_{mag} increases quadratically with increasing temperature and shows a maximum around $\sim 300\,\mathrm{K}$.

The spin systems presented up to here have rather large exchange couplings J. In the following, a class of low-dimensional spin systems with much lower exchange energies is presented. Due to the lower J, one can strongly influence the spin gap by magnetic fields which can be realized by typical laboratory magnets. A disadvantage of the lower J, however, is that one needs to measure the thermal conductivity at far lower temperatures well below 1 K to observe κ_{mag}. A magnetic heat transport was observed for the Haldane spin-chain compound $Ni(C_2H_8N_2)_2NO_2(ClO_4)$ (NENP) [60] and for the $S = 1/2$ Heisenberg spin-chain compound $Cu(C_4H_4N_2)(NO_3)_2$ (CuPzN) [61, 62]. The latter will be briefly discussed in the following.

CuPzN is a Heisenberg $S = 1/2$ spin chain with intra-chain exchange coupling $J = 10.3\,\mathrm{K}$ and a rather small inter-chain coupling $|J'/J| \approx 4 \cdot 10^{-3}$ [63–65]. At a critical field $B_{\mathrm{c}} = 15.0\,\mathrm{T}$, the spin system enters a gapped phase. The reduction of $\kappa(B)$ parallel to the spin chains due to the magnetic field is illustrated in

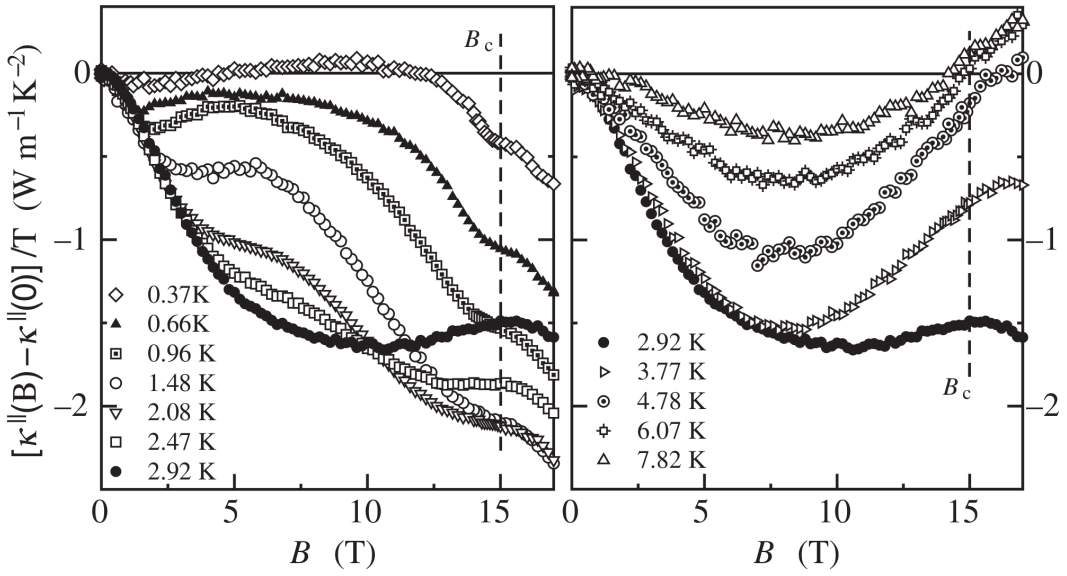

Figure 2.3: Magnetic-field dependent reduction of $\kappa(B)$ for CuPzN at various constant temperatures between 0.37 K and 7.82 K (taken from [61]).

Fig. 2.3. At lowest temperatures, $\kappa(B)$ stays almost constant up to $\sim 13\,\mathrm{T}$. At higher fields, $\kappa(B)$ decreases with increasing field and forms a plateau around the critical field B_c. For fields above B_c, $\kappa(B)$ further decreases. The plateau feature is observable up to $\sim 2.5\,\mathrm{K}$, although broadened. Above $\sim 3.5\,\mathrm{K}$, the plateau feature vanishes. At low temperatures and small magnetic fields, $\kappa(B)$ exhibits a small local minimum which can probably be attributed to phonon scattering on magnetic excitations (*cf.* discussions in Ref. [66]).

The thermal-conductivity data in Fig. 2.3 very clearly show the presence of a magnetic heat transport within the gapless phase below B_c. Above B_c where the spin gap opens, $\kappa(B)$ drastically decreases with increasing field. The magnetic thermal conductivity κ_mag can be calculated via mean-field theory including the Jordan-Wigner transformation [67–69] by assuming a momentum-independent mean free path ℓ. Comparison with experimental data provide an essentially field-independent mean free path which increases linearly with increasing temperature [61]. This is in accordance to theoretical predictions for Luttinger liquids [61, 70, 71].

Heisenberg Spin-ladder compounds with rather small exchange couplings can be realized by $(C_5H_{12}N)_2CuBr_4$ (HPIP) and $(C_7H_{10}N)_2CuBr_4$ (DIMPY). The main difference between HPIP and DIMPY is the ratio of the exchange couplings along the legs and the rungs, $J_{||}$ and $J_\perp$, respectively. In the case of HPIP, the coupling $J_{||} \simeq 3.6$ K is smaller than $J_\perp \simeq 13$ K [66, 72–78]. Between the critical fields $B_{c_1} \simeq 6.6\,\mathrm{T}$ and $B_{c_2} \simeq 14.6\,\mathrm{T}$ [72], the zero-field spin gap $\Delta \simeq 9.5\,\mathrm{K}$ vanishes and the spin system is in a Luttinger-liquid state. In the case of DIMPY,

the leg coupling $J_{||} \simeq 8.4$ K is larger than the rung coupling $J_{\perp} \simeq 4.3$ K. The spin system has a zero-field spin gap of $\Delta \simeq 3.7\,\mathrm{K}$ and two critical fields $B_{c_1} \simeq 3\,\mathrm{T}$ and $B_{c_2} \simeq 30\,\mathrm{T}$ [79, 80].

The thermal conductivity of HPIP has been measured in magnetic fields up to 17 T at temperatures down to 0.37 K [66]. In this temperature range, no magnetic heat transport is observed, *i.e.* κ is purely phononic. The field dependence of κ can be attributed to scattering on magnetic excitations in the gapless phase [66]. Up to now, no literature data of the thermal conductivity of DIMPY has been published.

Within the framework of this thesis, efforts were made to measure the thermal conductivity of HPIP and DIMPY in a dilution refrigerator, to test if a magnetic contribution κ_{mag} is observable at lower temperatures. Due to weak thermal couplings of the HPIP crystals to the sample holder, the κ measurements were only possible above 0.2 K. The results are shown in Appendix A (Fig. A.1). The features observed in $\kappa(B)$ above 0.4 K [66] can be reproduced up to 10 T. When lowering the temperature, the observed features indeed become sharper. However, no magnetic heat transport can be observed down to 0.2 K.

The thermal conductivity of DIMPY has been measured down to 0.35 K. Due to sample instability and incompatibility with the adhesives, the thermal conductivity could not be measured reproducibly. Two datasets of κ of DIMPY are shown in Appendix A (Figs. A.4 and A.5). Unfortunately, both datasets show a different behavior and do not allow a conclusive interpretation. Hence, the question whether the spin-ladder compound DIMPY shows magnetic heat transport remains an open question.

2.2 Demagnetization

The demagnetization field (stray field) is a magnetic field which is generated by the magnetization M of a magnetic sample. In case of a paramagnet, the demagnetization field counteracts an external magnetic field H_{ext} and, thus, leads to a reduction of H_{ext}. As the magnetization $M(H)$ itself is a response to an external magnetic field, magnetization and demagnetization influence each other. In case of a paramagnet, an increase of the external field leads to an increase of the magnetization and, thus, to a reduction of the causative field.

The demagnetization effect is strongly anisotropic with respect to the sample geometry and to the sample orientation within the external magnetic field (shape anisotropy). For the simplified case of an ellipsoidal sample, the demagnetization field H_{D} is homogeneous within the sample and proportional to the magnetization M, *i.e.*

$$H_{\mathrm{D}} = -DM\,, \tag{2.20}$$

where D is the demagnetization factor which depends on the actual shape of the

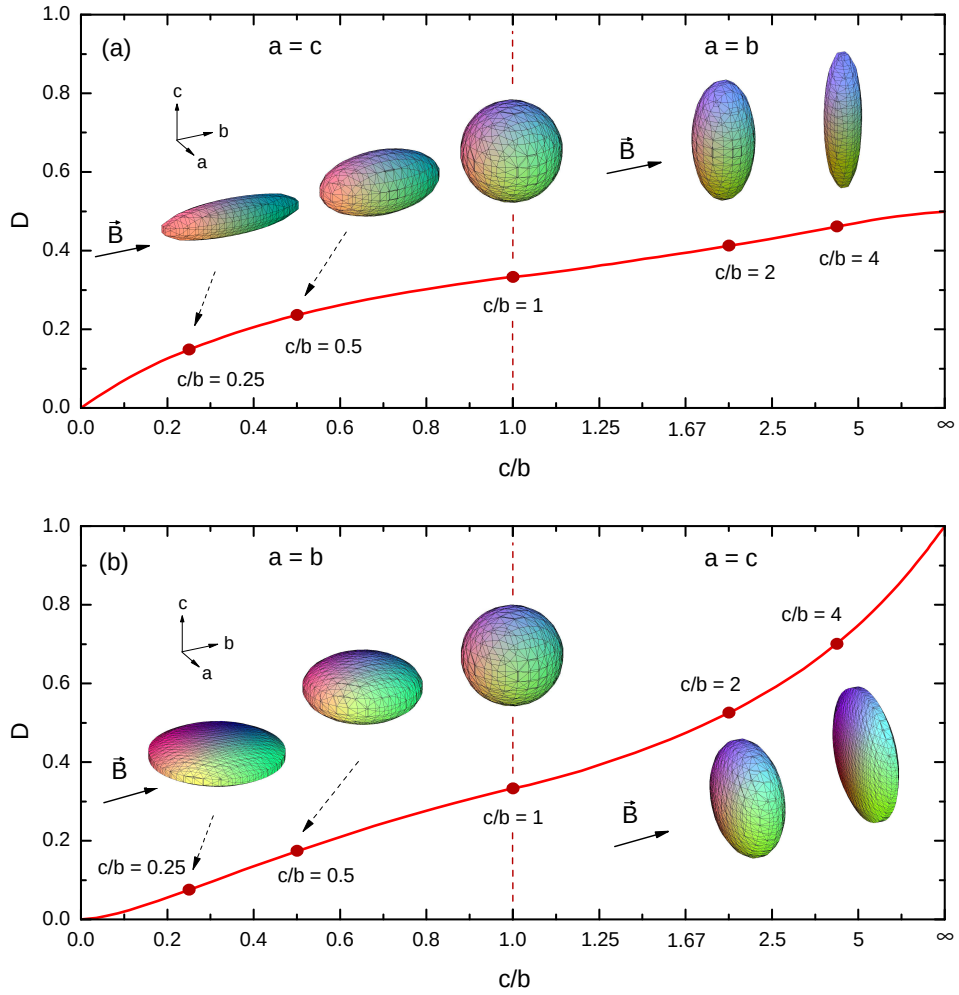

Figure 2.4: Demagnetization factor of a (a) cigar and (b) planar-shaped ellipsoidal sample as a function of the ratios of the semi-major axes a, b, and c. The external magnetic field is directed parallel to b. [81]

ellipsoid. Hence, the reduced magnetic field is given by

$$H = H_{\text{ext}} - DM\,. \tag{2.21}$$

Obviously, the demagnetization field H_{D} becomes constant when the magnetization reaches its saturation value. For larger fields, the demagnetization correction simply is a constant offset.

The demagnetization factor D of an ellipsoid can be calculated numerically depending on the ratio of the three semi-major axes a, b, and c [81]. Fig. 2.4 shows the demagnetization factor D for a cigar- and a planar-shaped ellipsoidal sample (panel (a) and (b), respectively). In both cases, the special case of a circle ($a = b = c$) leads to a demagnetization factor of $D = 1/3$. On the left

hand side of Fig. 2.4(a), the magnetic field is parallel to the long semi-major axis b. For an infinitesimally thin sample, the demagnetization factor vanishes. On the right hand side, the magnetic field is directed along one of the short axes. Here, D converges to 1/2 for an infinitesimally thin sample. Fig. 2.4(b) shows the demagnetization factor of a planar-shaped sample. When applying the magnetic field parallel to one of the longer semi-major axes, D vanishes in the limit of an infinitesimally thin plane. For $\vec{B}$ parallel to the short axis, the demagnetization factor converges to 1 in the limit of an infinitesimally thin plane.

Demagnetization effects can be minimized by choosing a suitable sample geometry, *i.e.* a thin planar- or cigar-shaped sample with the long edge parallel to the external magnetic field. In some cases, the measurement setup inhibits a convenient orientation of the sample with respect to the magnetic field. In this case, the demagnetization can have a strong influence on the applied external field. Therefore, the demagnetization field has to be subtracted from the external field to obtain the correct internal field. This requires the knowledge of the actual magnetization $M(H)$, which has to be measured separately on a sample of suitable shape.

One possibility to calculate H_{D} is to approximate the sample by an ellipsoid with a known demagnetization factor. Alternatively, one can calculate the demagnetization field numerically by means of a MATHEMATICA script (written by O. Breunig), which makes use of the RADIA package [82, 83]. The script works as follows. The spatial distribution of the magnetic field inside the sample is calculated on the basis of experimental magnetization data. Generally, one can choose an arbitrary sample geometry within the calculation software. The demagnetization corrections for the measurements within the framework of this thesis were done by approximating the samples as rectangular-shaped samples. In a last step, the average internal magnetic field is obtained by integrating the field over the whole sample.

The thermal-conductivity measurements are treated in a slightly different way. As one can make an assertion about the measured κ only between the different temperature contacts (Fig. 3.1 on page 24), which are attached on the sample at approximately 1/3 and 2/3 of the sample height, the average magnetic field is obtained by integrating over the sample volume between these two temperature contacts.

All measurements within this thesis, including a magnetic field, were corrected by means of this script. The corresponding magnetization data were measured by M. Hiertz during his diploma thesis [84].

3 Experimental

This chapter concerns the experimental environment and the measurement techniques used to obtain the data presented in this thesis. The main focus lies on the thermal-conductivity measurements, which will be described in detail.

The magnetization and magnetostriction measurements were performed by M. Hiertz during his diploma thesis [84] and will be described in detail there. The magnetization measurements were done with a home-built force magnetometer which has been built up by D. Loewen and further modified by S. Scharffe during their diploma theses [85, 86]. The magnetostriction measurements were performed with a home-built capacitance dilatometer which has been built by O. Heyer during his diploma thesis [87]. The principle ideas of the capacitance dilatometry are described in Ref. [88].

3.1 Thermal-Conductivity Measurements

The thermal conductivity κ can be measured via the steady-state method, which will be explained in the following. In one dimension, the definition of κ (Eq. 2.1 on page 11) can be rewritten into the form

$$\frac{P}{A} = \kappa \frac{\Delta T}{\Delta x} \,. \tag{3.1}$$

The heat current $j = P/A$ is given by the ratio of the sample-heater power P and the sample cross section A. The temperature gradient $\Delta T/\Delta x$ is assumed to be constant within the sample. Therefore, one needs to measure the temperature difference ΔT between two determined levels of the sample with distance Δx. To ensure a homogeneous heat current within the sample, one needs to chose a suitable sample geometry. The sample should be a thin crystal with the long edge parallel to the heat current.

Fig. 3.1 illustrates the steady-state method to measure the thermal conductivity. In order to measure κ via Eq. (3.1), one needs to know the geometry of the sample, *i.e.* A and Δx, the heating power P, and the temperature difference ΔT. The heating power is the product of the heater current I_{H} and the voltage drop U_{H} over the heater. The temperature difference ΔT can be measured by two different approaches. One can either measure ΔT via a thermocouple or one can measure the absolute values of the temperatures at both levels. The technique including the thermocouple is used in the temperature range between 5 K and 300 K. The method including two thermometers can be used below $\sim 20\,\mathrm{K}$, in

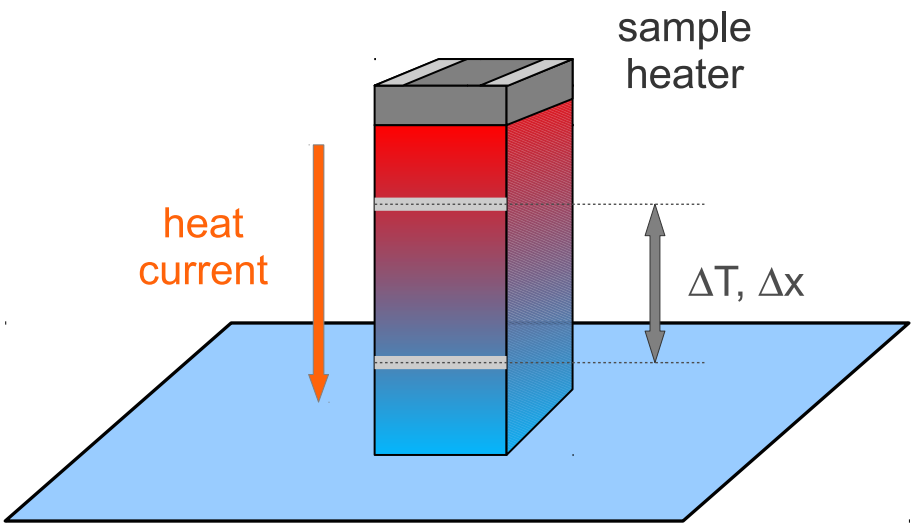

Figure 3.1: Steady-state method to measure the thermal conductivity. The temperature gradient is produced by a sample heater on top of the sample. The temperature difference can either be obtained via a thermocouple or via two thermometers attached at the sample.

principle, down to lowest temperatures. Both techniques will be described in the following.

3.2 Thermal-Conductivity Measurements in the High-Temperature Regime

In the temperature range between 5 K and 300 K, the temperature difference is measured via a thermocouple as shown in Fig. 3.2. The advantage of this measurement technique is that one directly measures the temperature difference ΔT. As a drawback, one cannot directly measure the actual sample temperature as the thermometer is placed on the sample-holder platform. Heating the top of the sample certainly heats up the whole sample. In this temperature regime, the thermal resistance between sample and sample holder usually is rather small, compared to the low-temperature region discussed below. One possibility to directly measure such a heating is to use a second thermocouple which measures the temperature difference between the sample-holder thermometer and the lower end of the primary thermocouple.

The thermocouple used here consists of Chromel[3] and a gold-iron alloy (0.07% iron). This sort of thermocouple has been used within many diploma and PhD theses. The thermocouples used in this thesis are made of one peace of gold (0.07% iron) wire ($\sim 10\,\mathrm{cm}$) and two Chromel wires ($\sim 5\,\mathrm{cm}$). Both wire types

[3]Chromel consists of 90% nickel and 10% chromium.

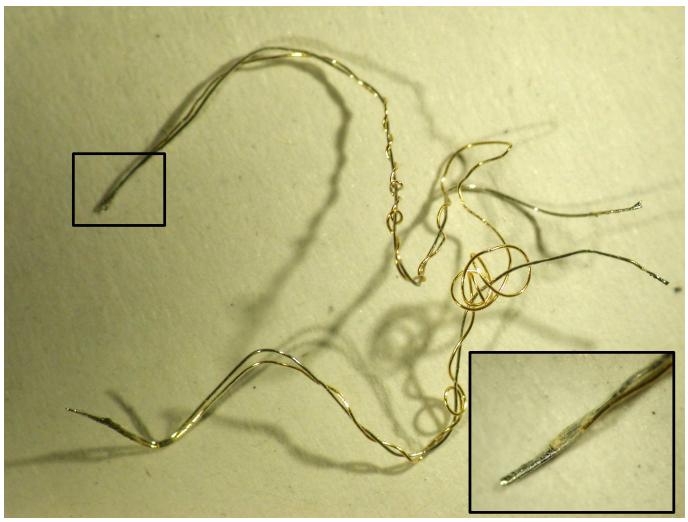

Figure 3.2: Photograph of a thermocouple consisting of chromel and a gold-iron alloy (0.07% iron).

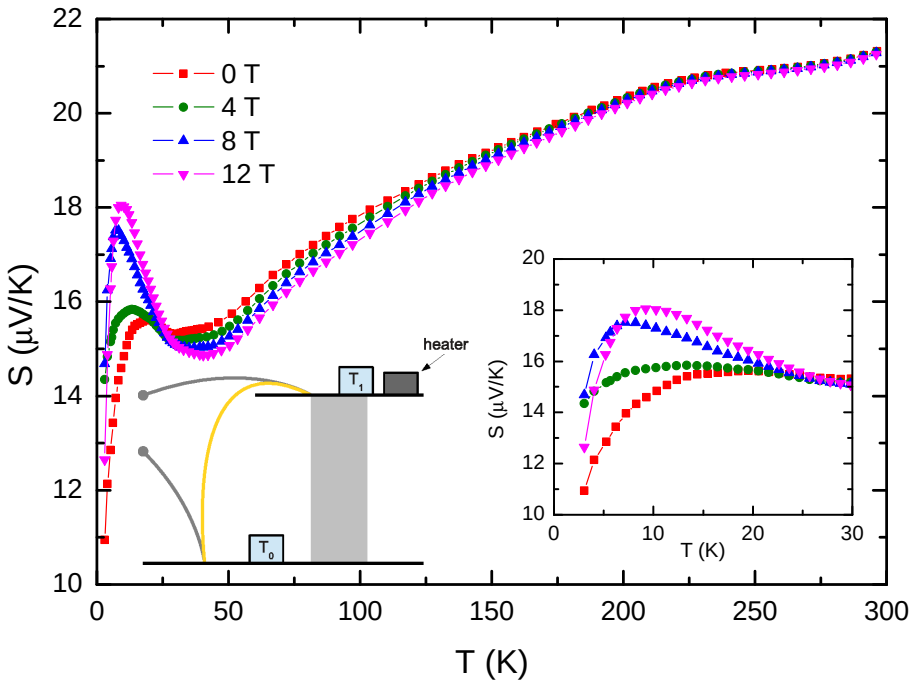

Figure 3.3: Thermopower of the thermocouple used here for various constant magnetic fields. This inset schematically shows the experimental setup used to calibrate the thermocouple.

have a rubber-like cable insulation, which has to be removed at both ends. This can be done with a scalpel. The Chromel wire is rather robust. The gold wire, however, has to be treated very cautiously. Another difficulty is to solder up the ends of the respective wires. To be able to solder the Chromel wire, first, it has be treated with an acid flux. The major problem, however, is to solder the gold wire as it melts quickly at a rather low temperature. This can be best done with solder tin containing lead. This reduces the melting point to ~ 180°C.

The thermocouple has been calibrated for various magnetic fields. The results are shown in Fig. 3.3 for zero field and for three different magnetic fields. Below 60 K, the thermopower strongly depends on the magnetic field. In this temperature region, the thermopower $S(T)$ has been measured for 0 T, 2 T, 4 T, 6 T, 8 T, 10 T, 12 T, 14 T, and 16 T. Above 60 K, the thermopower is hardly field dependent. Here, the $S(T)$ curves are measured in 0 T, 6 T, and 14 T.

The experimental setup to calibrate the thermocouple is schematically illustrated in the inset of Fig. 3.3. It is similar to the calibration setups presented in *e.g.* Refs. [31, 89]. Both ends of the thermocouple are attached at the sample-holder platform and on a sapphire plate with temperatures T_0 and T_1, respectively. The sapphire plate is thermally decoupled from the sample-holder platform via a thick Manganin[4] wire. The temperature difference $\Delta T = T_1 - T_0$ is produced by a heater placed on the sapphire plate.

3.3 Thermal-Conductivity Measurements in the Low-Temperature Regime

Below 5 K, the thermopower of the thermocouple used here rapidly vanishes (see Fig. 3.3). Therefore, one has to measure the temperature difference via two individual thermometers, *i.e.* $\Delta T = T_2 - T_1$. The advantage of this method is the knowledge of the absolute temperatures T_1 and T_2 directly at the sample. Therefore, one can determine the actual sample temperature as the mean value of both temperatures, *i.e.* $T_{\mathrm{sample}} = \frac{1}{2}(T_1 + T_2)$. This is very important as the thermal-contact resistances between the sample holder and the sample often become very large at lowest temperatures.

The challenge is to accurately calibrate both thermometers at the sample. A reasonable temperature difference should be in the order of several percents of the sample temperature. Thus, both thermometers have to provide the same absolute values within a tolerance well below 1 per mill. Therefore, both thermometers have to be calibrated within each measurement run as every cooling of the thermometers leads to a slight change of the $R(T)$ characteristics. A detailed description of the techniques to measure the temperature is given in Sec. 3.5.

The thermometers are calibrated with respect to the sample-holder thermometer. It is important to calibrate both thermometers simultaneously to ensure that

[4]Manganin consists of copper (86%), manganese (12%), and nickel (2%) [90].

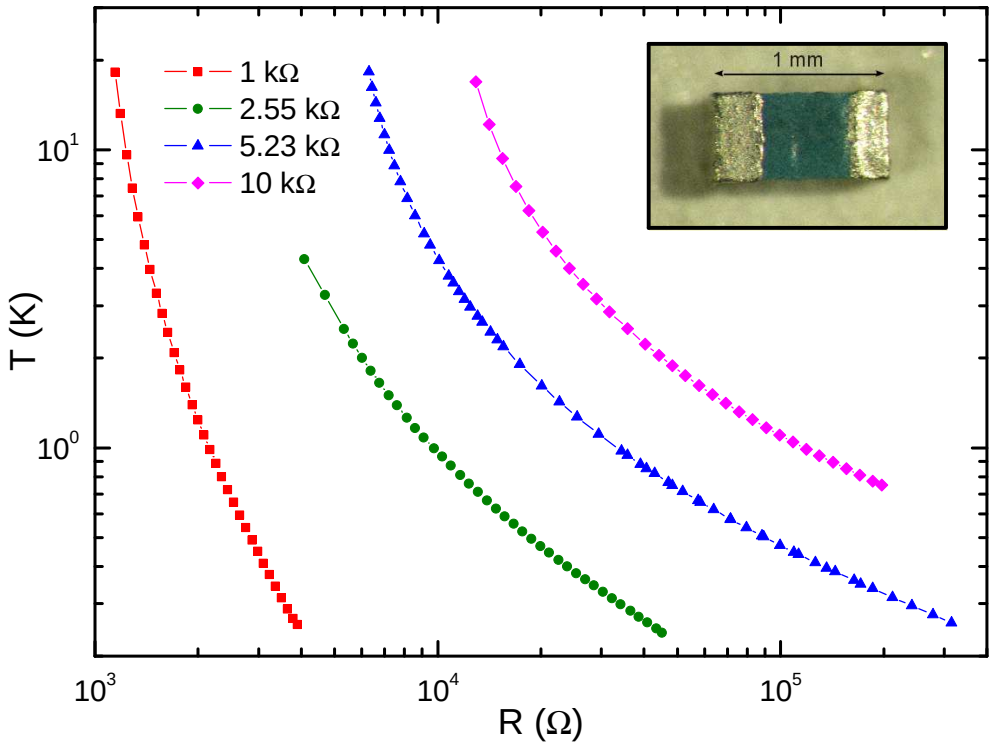

Figure 3.4: Resistance characteristics for different resistor types classified via the room-temperature resistance value. The inset shows a photograph of such a resistor.

both exactly provide the same temperature. The calibration is performed with switched-off heater, *i.e.* with zero sample-heater current. If the sample is a bad thermal conductor, one has to be careful at very low temperatures, as it can actually happen that the sample and, thus, the thermometers heat up, *e.g.* due to radiation.

The thermometers used here are RuO_2 thermometers (inset of Fig. 3.4). The temperature dependent resistance $R(T)$ (Fig. 3.4) shows the typical behavior of a semiconductor. In addition, the resistivity of RuO_2 exhibits a considerable magnetic-field dependence. Fortunately, the field dependence is almost linear. Therefore, it is sufficient to measure the $R(T)$ characteristics for only a few constant magnetic fields. The values for intermediate fields can, hence, be obtained by interpolation.

Fig. 3.4 shows the zero-field resistance characteristics of different RuO_2 thermometer types which are classified via the room-temperature resistances. It turned out that the 5.23 kΩ resistors are best suited for temperature measurements between 0.25 K and ∼ 10 K, *i.e.* for measurements in the ^{3}He cryostat. At temperatures below 0.25 K, *i.e.* in the dilution refrigerator, the 2.55 kΩ resistors were used.

3.4 Sample Wiring

A suitable sample for a thermal-conductivity measurement is bar shaped and rectangular with the long edge parallel to the heat current. Typical sample sizes are of the order of $1 \times 1 \times 3\,\mathrm{mm}^3$. For smaller samples, it is more difficult to attach the required wires and the sample heater. Furthermore, the uncertainties of the geometrical dimensions become rather large. A too large sample, however, exhibits other difficulties. First, the sample has to fit into the sample holder of the cryostat and is, thus, limited to a length of $\sim 10\,\mathrm{mm}$. Another problem arising from too large samples is the increase of relaxation times to establish a static temperature distribution and, thus, a stationary heat current within the sample. This problem becomes more crucial in the low-temperature region where the thermal conductivity of the sample and the sample holder rapidly decreases.

3.4.1 Adhesives

For the thermal-conductivity measurements, several wires, heaters, and thermometers or thermocouples have to be attached directly onto the sample. Therefore, the right choice of the adhesives is a very important point. The choice which adhesive to use depends on the sample properties, in particular, on the compatibility with different solvents. Another important aspect is the electrical conductivity of the sample. For metallic samples, one has to be cautious when attaching the heater on the sample or when mounting the whole sample on the sample holder, which consists of copper. In the following, the different adhesives are presented together with their basic properties.

Silver Glue

The silver glue (*Leitsilber G3303A Plano GmbH* [91]) is a solvent-based adhesive which contains small silver particles. It has a small electrical and thermal resistance and is well suited to attach the wires at the sample which tap the different temperatures (*cf.* Sec. 3.4.2). Moreover, one can use it to glue the entire sample onto the sample holder. The silver glue can easily be solved by acetone and, less well, by ethanol and can residue-free be removed. A disadvantage of the silver glue is the limited mechanical stability.[5] The easiest way to apply the silver glue on the sample is to use a very fine paintbrush, *e.g.* a red marten brush of size 5/0 or 10/0.

Two-Part electrically-conductive Silver Epoxy

The two-part epoxy glue (*Epo-Tek H20E* [92]) is a solvent-free glue which consists of two components which have to be mixed before usage. After mixing, the

[5] The spin ice $Dy_2Ti_2O_7$ could not be fixed on the sample holder with this silver glue as it broke away due to strong torques effected by the magnetic field.

epoxy glue can be handled for several hours. To be hardened, the epoxy glue has to be heated. The duration of hardening depends on the temperature. For a temperature of $\sim 150\,^{\circ}\mathrm{C}$, the glue takes some minutes to harden. After hardening, the silver epoxy has a small electrical and thermal resistance. However, this strongly depends on the heating duration and temperature. The big advantage is the large mechanical stability compared to the solvent-based silver glue. The disadvantage of the silver epoxy is that once it is hardened, it is not solvable and, thus, to remove it from the sample, one has to scrape or polish it off the sample.

GE 7031 Varnish

This varnish (*LakeShore VGE-7031* [93]) is a solvent-based, electrically-insulating varnish. It is solvable by acetone and ethanol and can be removed residue-free from the sample.

Delta Bond 152

This glue (*Wakefield DeltaBond 152* [94]) is a two-part glue. It is electrically insulating and a rather good thermal conductor. After mixing both parts, the glue can be handled for hours. It hardens after approximately 12 hours. When hardened, the adhesive has a very large mechanical stability.

3.4.2 Thermal Contacts and Heat Currents

It is important to tap the correct temperatures at defined levels of the sample. As the sample usually is too small to attach the thermocouple or the thermometers directly at the sample, the temperatures are tapped indirectly by attaching good heat-conducting wires at the sample, *e.g.* copper, platinum, or gold. The thermocouple or the thermometers are, then, sticked on the respective wires (left hand side of Fig. 3.5).

In order to minimize additional thermal resistances when attaching the thermocouple or the thermometers, one can use the silver glue. As the tips of the thermocouple are electrically conducting, one has to use insulated wires (attached at the sample) to avoid thermovoltages which would superimpose the thermovoltages from the thermocouple. The thermometers used for the low-temperature measurements can also be attached by the silver glue. Here, the thermovoltages originating from the sample would disturb the resistivity bridges. To avoid these and, in particular, to avoid an electrical short circuit of the thermometers, the electrical contacts on the backside of the thermometers, first, have to be removed by polishing.

One has to ensure that the heat provided by the heater on top of the sample, indeed, flows through the sample and is not dissipated through the attached wires. It is not possible to perfectly thermally decouple a sample. Therefore, the right choice of cables and adhesives is a very crucial point. It is very important

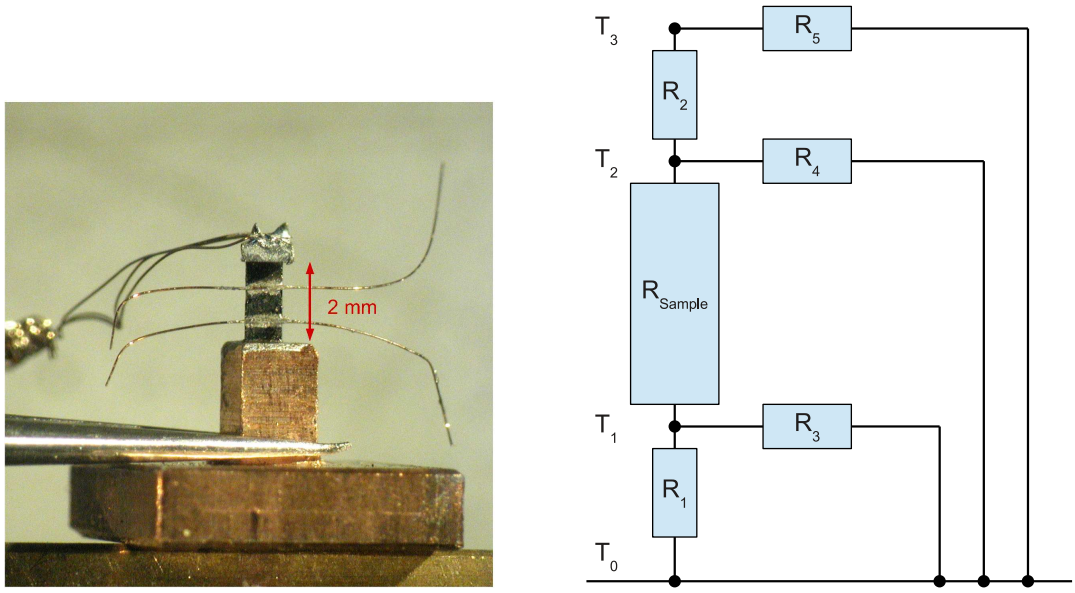

Figure 3.5: Photograph of a $(Ba_{0.9}Sr_{0.1})Co_2V_2O_8$ sample wired for a thermal-conductivity measurement along the [001] direction. The diagram on the right hand side illustrates an equivalent circuit diagram for the steady-state method used for thermal conductivity measurements (Fig. 3.1 on page 24).

that the upper and lower end of the sample are exactly planar. Especially at very low temperatures, the thermal contact resistances usually become very large. To minimize this effect, the concerned surfaces both have to be planar and they should have a maximum contact surface. At very low temperatures, also the pressure with which the two surfaces are pressed together plays an important role.[6]

The left hand side of Fig. 3.5 shows a $(Ba_{0.9}Sr_{0.1})Co_2V_2O_8$ sample wired for a thermal-conductivity measurement. The corresponding equivalent circuit diagram is illustrated on the right hand side. The R_i depict the different thermal resistances. Without heater current ($I_{SH} = 0$) the whole sample is assumed to have a homogeneous temperature, *i.e.* $T_0 = T_1 = T_2 = T_3$.

When turning on a determined heater current I_{SH}, a temperature gradient is built up, *i.e.* $T_0 < T_1 < T_2 < T_3$, where T_3 is assumed to be the temperature of the sample heater and T_0 is the bath temperature. T_1 and T_2 are the temperatures at the attached wires, respectively. R_{Sample} is the thermal resistance of the sample part between the two wires. R_1 and R_2 are the contact resistances together with the upper or lower part of the sample, respectively, *i.e.* above the upper wire and below the lower wire, respectively. The cables providing the sample heater current thermally connect the sample heater to the sample-holder platform via

[6]This effect can be utilized by clamping the lower part of the sample at the sample holder.

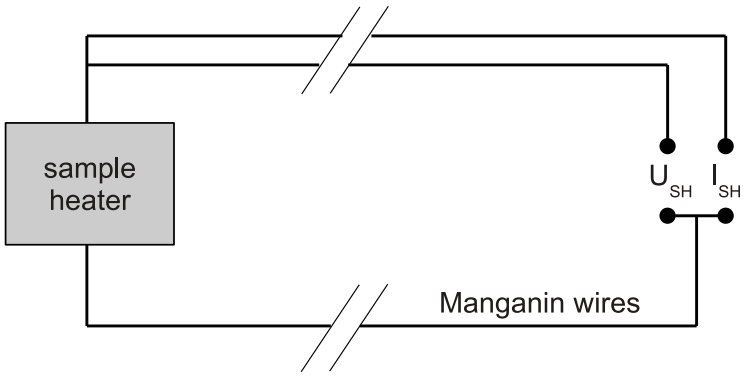

Figure 3.6: Wiring of the sample heater accounting for the heating power produced by the wires.

R_5. The thermocouple or the thermometers attached at the two wires (T_1 and T_2, respectively) thermally connect the sample to the bath (T_0) via R_3 and R_4, respectively.

To minimize the heat current through R_3, R_4, and R_5, the cables should have a rather low thermal conductivity and, in particular, have to be as long as possible. The sample heater and the thermometers are connected via Manganin wires. By spooling the cables, one obtains rather large wires. The drawback of the low thermal conductivity is a rather high electrical resistance. The resistance measurements of the thermometers are not affected, as these are performed with the 4-wire technique and the resistance bridges induce only very small electrical currents. The situation is different for the sample heater. Here, one has to ensure that the resistance of the cables is much smaller compared to the resistance of the sample heater itself. One has to ponder the right choice of the sample heater resistance. It must not be too small, as the cables would also need to have a small electrical resistance. This would result into a too good thermal contact to the bath. A large sample-heater resistance minimizes the heater current. For the measurements presented here, an SMD heater with a resistance of 1 kΩ (at room temperature) was used. The resistance is only weakly temperature dependent.

As the Manganin cables have a rather large resistance (typically $\sim 100\,\Omega$), one cannot avoid a heating power originating from the cables. Therefore, the sample heater is wired as illustrated in Fig. 3.6. This is equivalent to a 4-wire-resistivity measurement of the combination of sample heater together with one (of the three) Manganin cables. One can assume that half the heating power produced by the Manganin cables is transfered to the sample and the other half is dissipated to the bath. Thus, the effective heating power is given by the sum of the power produced by the heater and by two half Manganin wires, *i.e.* by one wire.

3.5 Experimental Environment and Measurement Software

The measurements have been performed within different magnet cryostats of the institute. These are explained in detail in a variety of diploma and PhD theses, *e.g.* [18, 19, 31, 89].

3.5.1 High-Temperature Measurements

The high-temperature measurements were done in home-built cryostat inserts which are in use for many years and, hence, are described in detail within many theses, *e.g.* [19, 89, 95, 96].

The temperature is measured and controlled by a LakeShore 340 temperature controller [93]. The sample-heater current can, in principle, be provided by any current source. Usually a Keithley 6220 precision current source or a Keithley 2400 sourcemeter [97] was used. The voltage drop over the heater and the thermo voltage from the thermocouple are measured by a Keithley 182 or 2182 volt meter.

The measurement is controlled by a software called WLF[7] written in LabView [98]. The functional principle of this software is based on the software called kSR, which has been developed in the institute by C. Zobel [99] and has been advanced by K. Berggold [18, 89]. The main function of WLF is to set the external parameters and to check for stability, *e.g.* the temperature controller and the magnet power supply. After stabilizing the external parameters, first, the offset voltage of the thermocouple has to be determined. This is done with switched-off sample heater. To ensure that there is no temperature gradient over the sample, the temperature has to be highly stable. In a second step, a certain heater current is applied to the sample heater. This builds up a temperature gradient which is measured via the thermocouple.[8] Here also, one has to wait until the temperature is stable over the sample. The corrected thermo voltage is obtained by subtracting the offset voltage from the measured thermo voltage. The calibration of the thermocouple (Fig. 3.3 on page 25) is deposited as a two-dimensional landscape upon the temperature-magnetic-field-plane. As mentioned above, the temperature is only measured at the sample holder and not directly at the sample. One can correct the sample temperature by adding a multiple (geometry factor) of the temperature difference ΔT to the sample-holder temperature. A reasonable correction is given by a factor of 1.5, *i.e.*

$$T_{\text{sample}} = T_{\text{sample holder}} + 1.5 \cdot \Delta T \tag{3.2}$$

[7] WLF is an abbreviation for "Wärmeleitfähigkeit".

[8] One can either manually set a sample-heater current or determine a desired temperature difference as a percentage of the sample-holder temperature. In the high-temperature regime, the temperature difference over the sample should be between 0.2% and 1%.

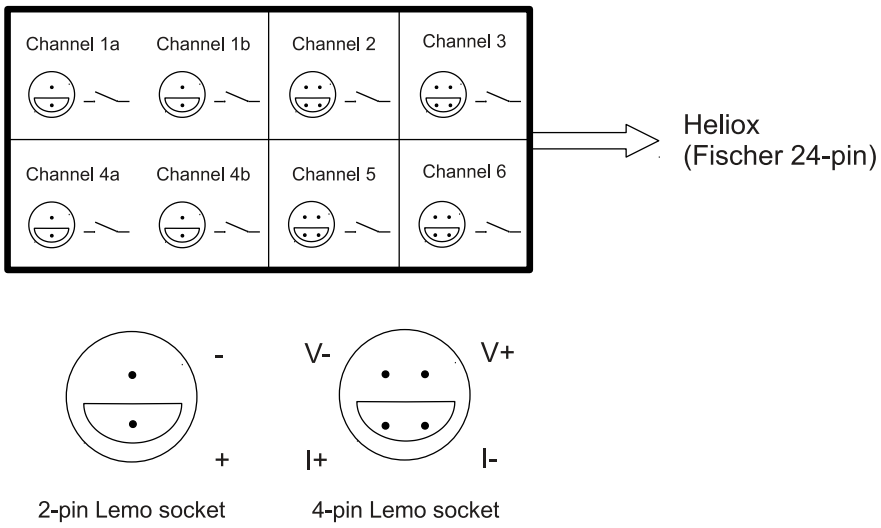

Figure 3.7: Filter box for the Heliox and Kelvinox systems.

3.5.2 Low-Temperature Measurements

The low-temperature thermal-conductivity measurements are far more complicated compared to the high-temperature method. Depending on the temperature range, one can either use a ^{3}He cryostat (Oxford Heliox) or a dilution refrigerator (Oxford Kelvinox) [100]. The Heliox system covers the temperature range between 0.25 K and 10 K. The Kelvinox system can realize temperatures between 0.03 K and 1.2 K.

In the case of the Heliox system, the temperature controlling is done by an ITC-501 temperature controller [100]. The temperature of the Kelvinox system can either be controlled by a Picowatt TS-530A temperature controller [101] or a LakeShore 370 temperature controller [93].

In both cases, Heliox and Kelvinox system, the measurement devices can be connected to the cryostat via a Fisher 24-pin connector. In order to flexibly use different devices, a filter box was built in the electronic workshop of the institute which can be connected to the 24-pin socket at the cryostat (Fig. 3.7).[9] Channels 1a and 1b are reserved for the sample-holder thermometer, which is measured via a LakeShore 370 resistance bridge.

For the thermal-conductivity measurements, the thermometers at the sample are measured either via AVS-47 resistance bridges or via LakeShore 370 resistance bridges. When using an AVS-47, it is useful to grab the resistance from the analog output of the AVS-47, which can be measured by a Keithley 182 or 2182 volt meter. This enhances the accuracy and drastically accelerates the measurement.

[9]The filter box contains low-pass filters and is built in accordance to the construction manual introduced in Ref. [102].

The integration time is, then, limited only by the volt meter.[10]

For the low-temperature measurements, the same software is used (WLF) as for the high-temperature measurements. However, the measurement principle is different. Before starting the main measurement, first, the thermometers have to be calibrated with respect to each other and to the sample-holder thermometer (with switched-off sample heater). To account for the magnetic-field dependence of the thermometer calibration, this has to be done in zero field and for various different magnetic fields. To avoid discontinuities within the temperature calibration, the calibration has to be done for each measuring range of the resistance bridge separately. The advantage of this measurement technique is that the sample heater needs not to be turned off and on at each data point. This drastically accelerates the measurement.

A special procedure to measure the magnetic-field dependence of the thermal conductivity is introduced in the following. The sample-holder temperature is stabilized at a value slightly below the desired sample temperature. The sample heater is controlled by an additional software PID temperature controller which stabilizes the mean value of both temperatures (at the sample) to the desired sample temperature. This ensures that the mean value between both thermometers is exactly constant during the whole measurement, *i.e.* for different magnetic fields. However, one has to ensure that the temperature difference does not become to large with respective to the sample temperature. This can happen if the thermal conductivity has a strong field dependence. In this case, one has to readjust the sample-holder temperature.

This procedure to measure the field dependence of the thermal conductivity can, in principle, be done with a continuously changing magnetic field, *i.e.* with a constant field sweep rate. Problems can occur, for example, when measuring a metallic sample, which is heated due to eddy currents. The main problem is that the system has no time to relax into a stationary state. Therefore, one has to choose a reasonably small field sweep rate.

[10] The measurements here were done with an integration time of 30 ms using a Keithley 182 volt meter.

4 Heat Transport in Spin Ice

4.1 Introduction

Spin ice is a class of geometrically frustrated magnetic systems. The frustration originates from an effective ferromagnetic nearest-neighbor interaction of Ising-like magnetic moments (spins) which are aligned along local easy axes, *i.e.* each spin has only two possible orientations within the spatial lattice. The frustration results in a highly degenerate ground state and, thus, in a residual entropy for $T \to 0$.

The ground state of a spin-ice system is given by the so-called ice rules, which determine the ground-state spin configuration and depend on the actual system. In two dimensions, a spin ice can be realized by a lattice of corner-sharing triangles (Kagomé lattice) with local easy axes pointing from the center of the triangles to the corners. In 3D, a spin ice can be realized by a lattice consisting of corner-sharing tetrahedra (pyrochlore lattice) with local easy axes from the center of the tetrahedra to the corners. In zero field, a 2D spin ice minimizes its magnetic energy when two spins point into and one out of the triangles (or vice versa) and for 3D when two spins point into and two out of the tetrahedra. Breaking the ice rule results in a pair of topological defects, which (in zero magnetic field) can propagate independently[11] upon the lattice without energy loss and, thus, are discussed as magnetic monopoles.

In 2D, a spin ice called artificial spin ice is realized by magnetic nanostructures [103–112]. 3D spin-ice systems are realized by the rare-earth titanates $Dy_2Ti_2O_7$ and $Ho_2Ti_2O_7$ [113]. The rare-earth titanate $Tb_2Ti_2O_7$ was proposed to be a spin-ice system [114]. To my knowledge, however, this could not be experimentally proofed. In this thesis, the 3D spin ice $Dy_2Ti_2O_7$ is studied with respect to its thermal properties in particular to its thermal-transport properties. The main issue will be the study of the ability of the magnetic excitations (monopoles) to carry heat. To answer this question, thermal-conductivity, magnetization, and thermal-expansion measurements were performed on the mother compound $Dy_2Ti_2O_7$ and on the non-magnetic reference system $Y_2Ti_2O_7$ as well as on two doped compounds, $(Dy_{0.5}Y_{0.5})_2Ti_2O_7$ and $Dy_2(Ti_{0.9}Zr_{0.1})_2O_7$. In the case of $(Dy_{0.5}Y_{0.5})_2Ti_2O_7$, 50% of the magnetic Dy ions are replaced by non-magnetic Y ions. In $Dy_2(Ti_{0.9}Zr_{0.1})_2O_7$, 10% of the non-magnetic Ti ions are replaced by (as well non-magnetic) Zr ions, where the magnetic Dy sublattice

[11] The monopole excitations propagate strictly independent only in the case of pure nearest-neighbor interaction, *i.e.* when neglecting the long-range dipolar interaction (*cf.* Sec. 4.2.2).

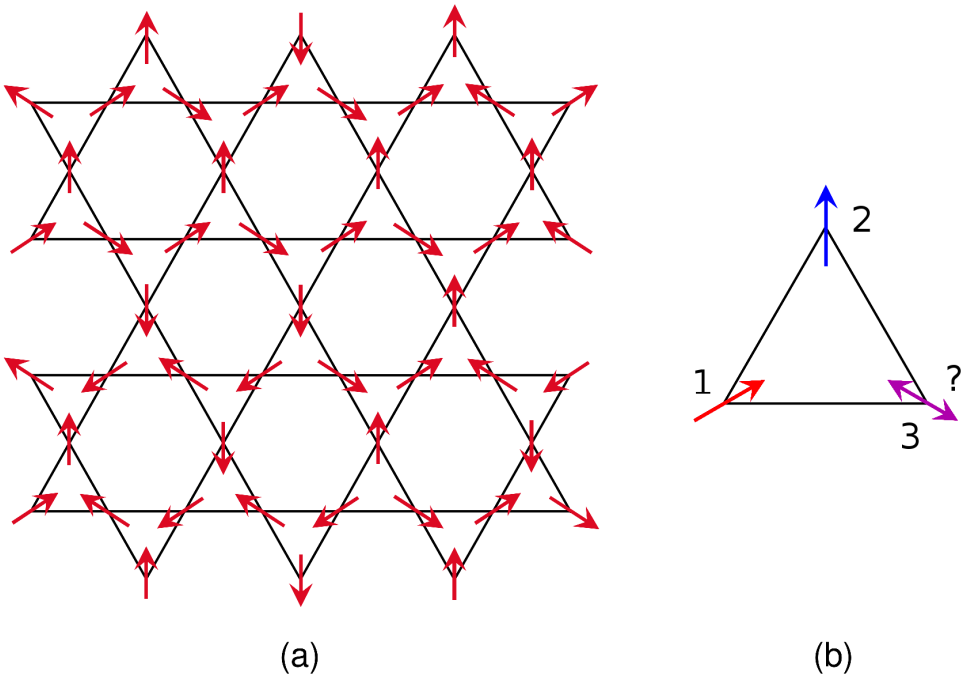

Figure 4.1: (a) Frustrated Kagomé plane consisting of triangles fulfilling the ice rules 2in-1out or 1in-2out. (b) Frustration of Ising spins for ferromagnetic interaction in the case of a single triangle. Each spin has a local easy axis from the center of the triangle to the respective corner.

remains unaffected.

The idea behind these doped compounds is to manipulate either the magnetic or the phononic system. In $(Dy_{0.5}Y_{0.5})_2Ti_2O_7$, the magnetic subsystem is strongly disturbed as, on average, two of four magnetic ions are absent in every tetrahedron. As Y^{3+} and Dy^{3+} have comparable ionic radii, the crystal structure is not (or hardly) effected. In $Dy_2(Ti_{0.9}Zr_{0.1})_2O_7$, the Ti^{4+} ions are replaced by much larger Zr^{4+} ions. This substitution results in a distortion of the crystal and, thus, yields a glassy phononic thermal conductivity [34, 115–119]. A drawback of the Zr doping is that the Dy tetrahedra are also distorted and, as a consequence, the energetic relations within each tetrahedron are disturbed. Thus, doping with Zr also slightly affects the magnetic subsystem (as mentioned above).

4.1.1 Geometric Frustration and Ice Rule

The principle of frustration in spin ice can be illustrated very descriptively for the two-dimensional case. Fig. 4.1(a) shows a frustrated Kagomé lattice. Each triangle fulfills the 2D ice rule 2in-1out or 1in-2out, which originates from the ferromagnetic interaction of Ising spins introduced in the following. The triangle

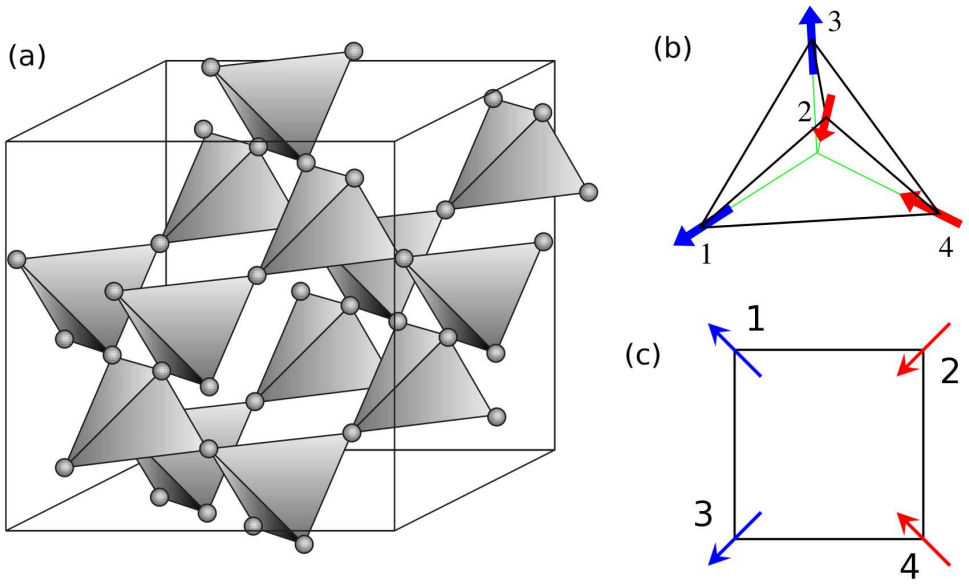

Figure 4.2: (a) Pyrochlore lattice, consisting of corner-sharing tetrahedra (taken from [120]). (b) A single tetrahedron with the local easy axes pointing from the corners to the center (taken from [121]). The shown spin orientation fulfills the ice rule 2in-2out. (c) Schematic 2D mapping of a single tetrahedron with the same spin configuration as shown in panel (b).

in Fig. 4.1(b) illustrates the frustration for a single triangle with ferromagnetically interacting Ising spins with local easy axes from the center of the triangle to the corners. Starting with spin 1, which points into the triangle, the ferromagnetic interaction induces spin 2 to point out of the triangle. The remaining spin 3 is, thus, frustrated as the orientation to one of the other spins is ferromagnetic, but antiferromagnetic with respect to the other one for both spin directions. For symmetry reasons, all three spins are frustrated equally and, as a consequence, the entire Kagomé lattice is frustrated. The particular spin configuration shown in Fig. 4.1(a) is not the unique ground state. The ground-state degeneracy prevents the system from ordering and yields a residual entropy. This is a fundamental property of a spin-ice system.

A pyrochlore lattice (corner-sharing tetrahedra, Fig. 4.2(a)) is a 3D realization of a spin ice. Analogously to the 2D case, the local easy axes point from the corners to the center of the tetrahedra (Fig. 4.2(b)). For the same reason as in the triangle case, the ferromagnetic interaction causes frustration of the spins. For symmetry reasons, again, this results in a frustration of the entire pyrochlore lattice. In its ground state, a tetrahedron fulfills the ice rule 2in-2out, shown in Fig. 4.2(b) and schematically in Fig. 4.2(c). Analogously to the 2D spin ice, this highly degenerate ground state yields a residual entropy and prevents the spin ice

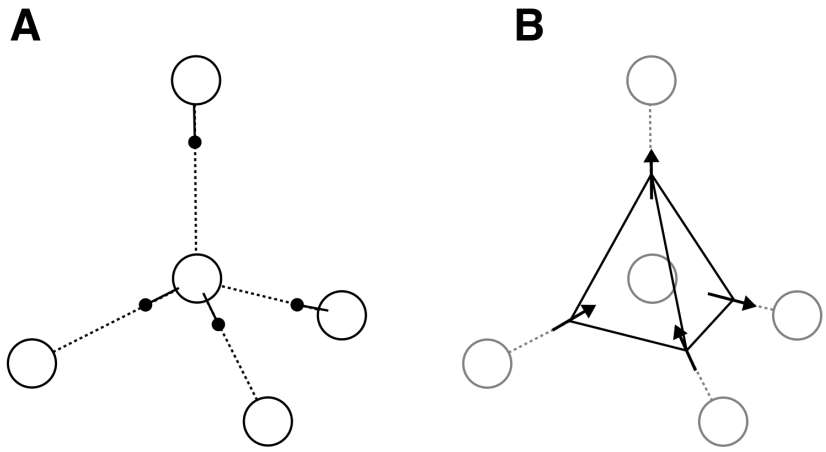

Figure 4.3: (A) Local hydrogen displacement in water ice. (B) Spin orientation of a single tetrahedron obeying the ice rule 2in-2out in the 3D spin-ice system (taken from [123]).

from ordering. For a hypothetical antiferromagnetic interaction, all spins would either point into or out of a tetrahedron (or triangle in the 2D case). Thus, the absence of frustration would cause long-range ordering of the spins.

In this thesis, only 3D spin-ice systems are investigated. To avoid confusion with the 2D spin ice, in the following, the term "Kagomé spin ice" denotes the field-induced ground state of the 3D spin ice for a magnetic field parallel to [111].

4.1.2 Residual Entropy for $T \to 0$

In the 3-dimensional case, the residual entropy $S_0 = S_{T\to 0}$, originating from the ground-state degeneracy, can be illustrated by means of the single-tetrahedron approximation (Sec. 4.2.1). Six out of $2^4 = 16$ possible spin configurations fulfill the ice rule and are, hence, energetically equivalent (Figs. 4.2(b) and (c)). These configurations form a 6-fold-degenerate ground state which results in a residual entropy of [122–125]

$$S_0 = \frac{R}{2} \ln\left(\frac{3}{2}\right) \approx 1.69 \,\frac{\mathrm{J}}{\mathrm{mol\,K}} \quad \text{for} \quad T \to 0 \;, \tag{4.1}$$

where $R = N_\mathrm{A} k_\mathrm{B} \approx 8.314\,\mathrm{J/mol\,K}$ is the gas constant. This ground-state behavior of the spin orientation in the 3D spin ice (Fig. 4.3(B)) is analogous to the hydrogen displacement in water ice [126] (Fig. 4.3(A)). In water ice, every oxygen atom (large white circles) is located in the center of a tetrahedron formed by the four adjacent oxygen atoms. Two of the four hydrogen atoms (small black circles) surrounding an oxygen atom are stronger bound to the atom in the center of the tetrahedron. The two remaining hydrogen atoms are stronger bound to

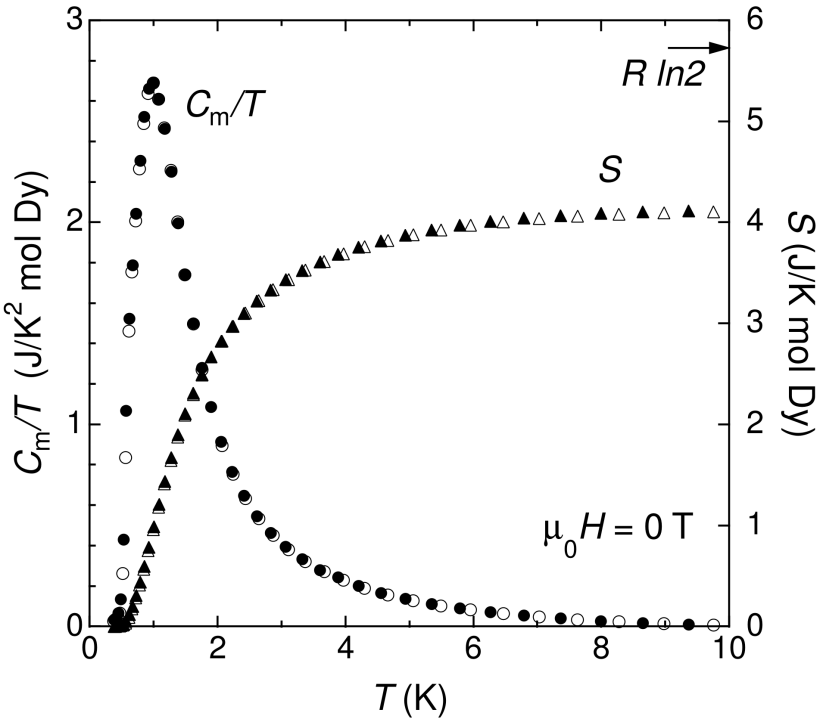

Figure 4.4: Magnetic specific heat and entropy. The open and closed symbols represent measurements on two different samples. $R \ln 2$ is the theoretical value for a two-level system (taken from [124]).

an oxygen atom at one corner of the tetrahedron. This geometrical frustration results in the Pauling's residual entropy of water ice, which has the same value as the residual entropy of the 3D spin-ice system (Eq. 4.1). This analogy to the ice rule 2in-2out is the origin of the name "spin ice" [127, 128].

For $Dy_2Ti_2O_7$, an experimental proof of the residual entropy (Eq. 4.1) has been provided in Ref. [124] by numerical integration of the measured magnetic specific heat C_{mag}/T, *i.e.*

$$S(T) = \int_0^T \frac{C_{mag}(T')}{T'}\,\mathrm{d}T' \,. \tag{4.2}$$

The residual entropy is obtained by subtracting the asymptotic value $S(T \to \infty)$ from the theoretical value for a two-level system $R \ln 2$ (Fig. 4.4). In Ref. [124], a residual entropy $S_0 = 1.66\,\mathrm{J/mol\,K}$ was found. This value is very close to the theoretically predicted value $S_0 = 1.69\,\mathrm{J/mol\,K}$ (Eq. 4.1).

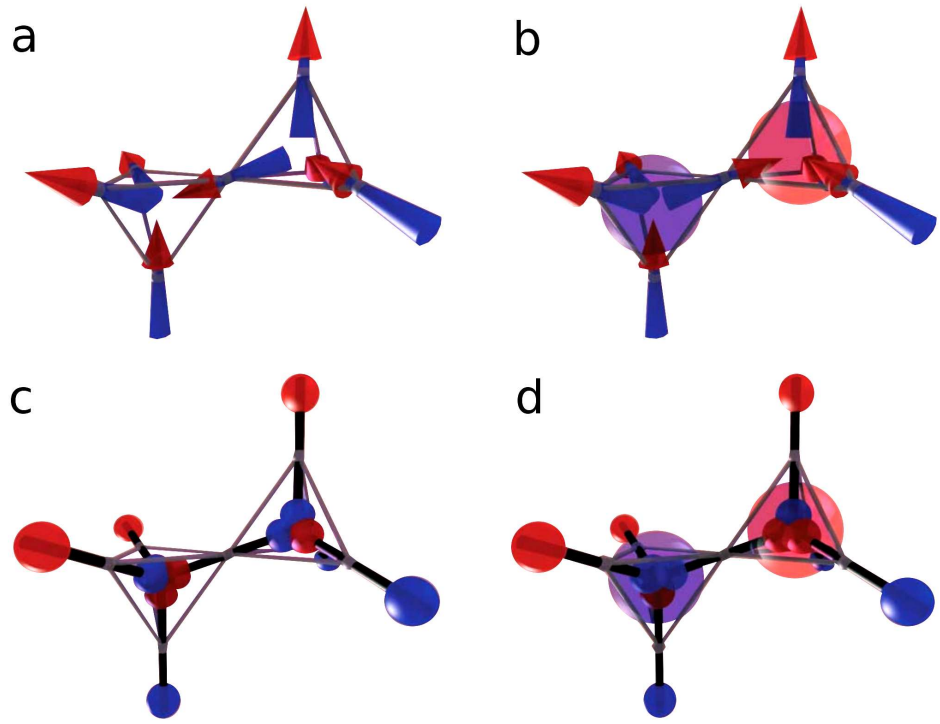

Figure 4.5: a) Two neighboring tetrahedra obeying the ice rule, *i.e.* both tetrahedra have the configuration 2in-2out. b) Creation of a monopole/anti-monopole pair by flipping the spin connecting both tetrahedra. c) 2in-2out configuration within the dumbbell model. d) Monopole/anti-monopole pair within the dumbbell model (taken from [129], recolorized).

4.1.3 Magnetic Monopoles

Elementary excitations in the spin-ice material $Dy_2Ti_2O_7$ were predicted to behave like magnetic monopoles [129, 131, 132]. Such an elementary spin-ice excitation can be created by breaking the ice rule 2in-2out resulting in two tetrahedra with configurations 3in-1out and 1in-3out. Fig. 4.5(a) shows two neighboring tetrahedra obeying the ice rule, *i.e.* being in the ground state. One can create a first excitation by flipping one spin, so that the ice rule is broken in two neighboring tetrahedra. This results in two tetrahedra with the configurations 3in-1out and 1in-3out, respectively (Fig. 4.5(b)).

A fractionized dipole excitation can be regarded as two individual monopoles (monopole/anti-monopole pair). Each monopole (or anti-monopole) can propagate independently within the network of the pyrochlore lattice via single spin flips as follows. One of the in-pointing spins of an excited tetrahedron can be flipped, so that the tetrahedron relaxes back to a 2in-2out configuration, while the 3in-1out excitation has moved to a neighboring tetrahedron. A 1in-3out con-

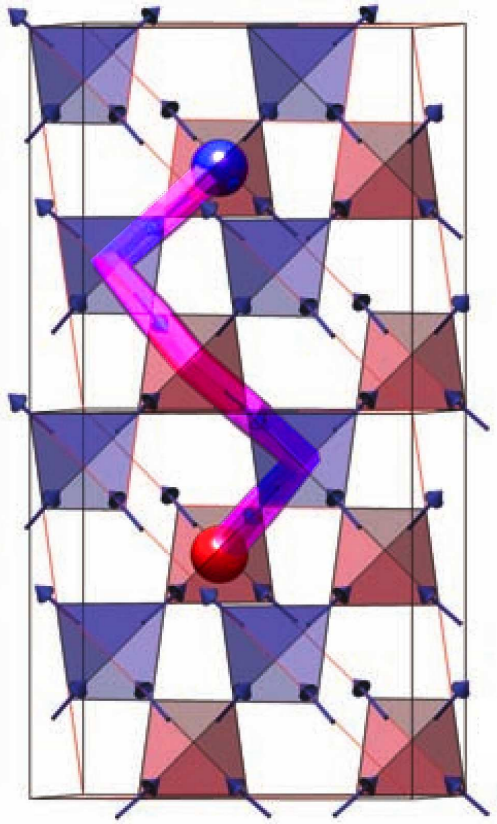

Figure 4.6: A dipole excitation separated into two monopoles (red and blue). The trace connecting the monopoles is called Dirac string (taken from [130], recolorized).

figuration can propagate in the same manner by flipping another out-pointing spin. As long as the ground-state degeneracy is not lifted[12], the energy cost of the created 3in-1out (or 1in-3out) configuration has the same amount as the energy regain of the previous tetrahedron which relaxes back to a 2in-2out configuration. Thus, the monopole excitations can propagate without energy loss and, hence, are not confined. This property is the justification to call these excitations "monopoles". The trace of a monopole excitation and, hence, the connection of the separated dipole excitation is called Dirac string (Fig. 4.6).

The monopole picture can be illustrated by the dumbbell model for a single tetrahedron (Figs. 4.5(c) and (d)). Every spin, represented by an arrow, consists of two isolated magnetic charges at both ends (positive and negative). A tetrahedron fulfilling the ice rule 2in-2out has no net charge (Fig. 4.5(c)). A tetrahedron with configuration 3in-1out (or 1in-3out) has a charge surplus and, thus, represents a magnetic monopole (or anti-monopole) (Fig. 4.5(d)). In Ref. [129],

[12]This is the case in zero magnetic field.

Castelnovo *et al.* predicted an elementary magnetic charge of

$$Q = \pm q_\mathrm{m} = \pm\frac{2\mu}{a_\mathrm{d}} \approx \pm 4.27 \cdot 10^{-13}\,\frac{\mathrm{J}}{\mathrm{T\,m}} \tag{4.3}$$

and, hence, a magnetic Coulomb energy of a separated pair of magnetic monopoles at a distance r of

$$E = -\frac{\mu_0}{4\pi r} q_\mathrm{m}^2\,. \tag{4.4}$$

In the monopole picture, the question whether these excitations behave like (quasi) particles carrying an elementary magnetic charge is still under strong debate [3–5, 133, 134]. These particles should, then, be affected by an external magnetic field and, hence, should be accelerated. To my knowledge, this remains an open question up to now.

4.1.4 $Dy_2Ti_2O_7$

Crystal Structure

In Didysprosium(III)Dititanium(IV)Oxide (Dysprosiumtitanate), the magnetic Dy^{3+} ions form a pyrochlore sublattice, consisting of corner-sharing tetrahedra (Fig. 4.2(a) on page 37). The cubic unit cell has the lattice constant $a \approx 10.14\,\text{Å}$ [135] and contains 16 Dy^{3+} ions. The surrounding O^{2-} ions cause a strong crystal field with an Ising-type $J = 15/2$ doublet forming the ground state of the Dy^{3+} ions and the first excited state well above the ground state. In literature, several values for the first excited doublet state between 140 K and 380 K are reported [136–139]. In the ground state, the total momentum is the sum of spin $S = 5/2$ and orbital momentum $L = 5$, *i.e.* $J = S + L = 15/2$. The total angular momentum is calculated via

$$\mu_J = \mu_S + \mu_L = g_S\mu_\mathrm{B}S + g_L\mu_\mathrm{B}L \approx 2\cdot\mu_\mathrm{B}S + 1\cdot\mu_\mathrm{B}L = 10\mu_\mathrm{B}\,, \tag{4.5}$$

where $g_S \approx 2$ and $g_L = 1$ are the Landé g-factors for the spin and orbital momentum, respectively. Due to the strong crystal field, the magnetic moments $\vec{\mu}$ are aligned along their local easy axes pointing from the center to the corners of the tetrahedra. Thus, every spin[13] in $Dy_2Ti_2O_7$ can point either into or out of a tetrahedron and, hence, $Dy_2Ti_2O_7$ is a good realization of a 3D spin ice.

Exchange Energy and Dipole-Dipole Interaction

For the rare-earth Dy ions, the rather small exchange energies are comparable to the energy scales of the dipole-dipole interaction. Both energy scales are of the order of $\sim 1\,\mathrm{K}$. Thus, we expect the spin-ice physics to take place in this

[13] In the strict sense, one as to consider the magnetic moment, which is antiparallel to the spin, *i.e.* $\mu_z = -g\mu_\mathrm{B}S_z$.

temperature regime. Considering nearest-neighbor antiferromagnetic exchange energies as well as long-range dipole-dipole interaction, we get the Hamiltonian [123, 129, 140]

$$\begin{aligned}\mathcal{H} &= -J \sum_{\langle (i,a),(j,b)\rangle} \vec{S}_i^a \cdot \vec{S}_j^b \\ &\quad + D r_{\mathrm{nn}}^3 \sum_{\substack{i>j \\ a,b}} \frac{\vec{S}_i^a \cdot \vec{S}_j^b}{|\vec{R}_{ij}^{ab}|^3} - \frac{3(\vec{S}_i^a \cdot \vec{R}_{ij}^{ab})(\vec{S}_i^b \cdot \vec{R}_{ij}^{ab})}{|\vec{R}_{ij}^{ab}|^5} \,. \end{aligned} \tag{4.6}$$

Here, the notations of Ref. [140] will be followed. The vectors $\vec{S}_i^a = \sigma_i^a \hat{z}^a$ are the Ising spins of the Dy^{3+} ions, pointing along the local easy axes $\hat{z}^a$ in one of the $\langle 111\rangle$ directions. The $\hat{z}^a$ are normalized, *i.e.* $|\hat{z}^a| = 1$, and the Ising variables $\sigma_i^a = \pm 1$ denote one of the two possible spin orientations. The vectors $\vec{R}_{ij}^{ab}$ point from (the spatial lattice site of) spin $\vec{S}_i^a$ to spin $\vec{S}_j^b$. J is the (antiferromagnetic) exchange-coupling constant and D is the dipole energy scale

$$D = \frac{\mu_0}{4\pi} \frac{\mu^2}{r_{\mathrm{nn}}^3} \,, \tag{4.7}$$

where $r_{\mathrm{nn}} \approx 3.54\,\text{Å}$ is the nearest-neighbor distance between two pyrochlore lattice sites and $\mu = 10\mu_{\mathrm{B}}$ is the magnetic moment of a Dy^{3+} ion (Eq. 4.5).

If we also restrict the dipole-dipole interaction to nearest neighbor[14], the Hamiltonian in Eq. (4.6) can be reduced to an effective ferromagnetic nearest-neighbor spin system. As $\hat{z}^a \cdot \hat{z}^b = -1/3$, the nearest-neighbor exchange coupling is $J_{\mathrm{nn}} = J/3$; and as $(\hat{z}^a \cdot \vec{R}_{ij}^{ab})(\hat{z}^b \cdot \vec{R}_{ij}^{ab}) = -2/3$, the nearest-neighbor dipole-dipole exchange energy is $D_{\mathrm{nn}} = 5D/3 \approx 2.35\,\mathrm{K}$. This results in the effective nearest-neighbor coupling constant

$$J_{\mathrm{eff}} = J_{\mathrm{nn}} + D_{\mathrm{nn}} \,. \tag{4.8}$$

For $Dy_2Ti_2O_7$, the nearest-neighbor exchange coupling was reported to be $J_{\mathrm{nn}} \sim -1.24\,\mathrm{K}$ [141]. Thus, we get a positive (ferromagnetic) effective coupling $J_{\mathrm{eff}} \approx 1.11\,\mathrm{K}$ and an effective Hamiltonian

$$\mathcal{H} = -3\, J_{\mathrm{eff}} \sum_{\langle (i,a),(j,b)\rangle} \vec{S}_i^a \cdot \vec{S}_j^b \,. \tag{4.9}$$

In the presence of an external magnetic field B_{ext}, the Hamiltonian in Eq. (4.6) has to be extended by an additional term considering the energy of a magnetic

[14] For $Dy_2Ti_2O_7$, the antiferromagnetic exchange interaction is generally restricted to nearest neighbors.

dipole in an external magnetic field, *i.e.*

$$\begin{aligned}\mathcal{H} &= -J \sum_{\langle (i,a),(j,b)\rangle} \vec{S}_i^a \cdot \vec{S}_j^b \\ &\quad + Dr_{\mathrm{nn}}^3 \sum_{\substack{i>j \\ a,b}} \frac{\vec{S}_i^a \cdot \vec{S}_j^b}{|\vec{R}_{ij}^{ab}|^3} - \frac{3(\vec{S}_i^a \cdot \vec{R}_{ij}^{ab})(\vec{S}_i^b \cdot \vec{R}_{ij}^{ab})}{|\vec{R}_{ij}^{ab}|^5} \\ &\quad - \mu \sum_i \vec{S}_i \cdot \vec{B}_{\mathrm{ext}} \,. \end{aligned} \tag{4.10}$$

The new term in Eq. (4.10) extends over all Dy sites. The Hamiltonian in Eq. (4.10) will be used to perform Metropolis-like simulations of the dipolar spin ice (Sec. 4.2.2). The effective nearest-neighbor Hamiltonian (Eq. 4.9) also has to be modified to

$$\mathcal{H} = -3\, J_{\mathrm{eff}} \sum_{\langle (i,a),(j,b)\rangle} \vec{S}_i^a \cdot \vec{S}_j^b - \mu \sum_i \vec{S}_i \cdot \vec{B}_{\mathrm{ext}} \,. \tag{4.11}$$

The single-tetrahedron approximation (Sec. 4.2.1) will base on the effective Hamiltonian in Eq. (4.11).

4.1.5 Slow Dynamics

Recently, it has been discovered that anomalous relaxation processes lead to out-of-equilibrium dynamics at temperatures below $\sim 0.6\,\mathrm{K}$ [6, 142–144]. Revealed by a wide range of physical properties of $Dy_2Ti_2O_7$, the measured relaxation times become very large at very low temperatures. However, there is a lot of discrepancy about the absolute values of the (relaxation) time scales. Up to now, this remains under strong debate. In the following, an overview about the present findings will be given.

The observed dominant time scales strongly depend on the measurement techniques used. Measurements of the AC susceptibility provide time scales up to seconds at temperatures around 1 K [139, 143–145], muon spin rotation (μsR) measurements yield time scales in the μs range [3, 146, 147], and neutron spin-echo experiments provide relaxation times down to ns [148].

Moreover, it has been shown [6, 121] that the dynamics of the magnetic system cannot be described by only one single relaxation process at temperatures below $\sim 0.6\,\mathrm{K}$. Klemke *et al.* [6, 121] studied the specific heat and the thermal conductivity of $Dy_2Ti_2O_7$ in zero field and in an external magnetic field parallel to [110]. The specific heat was measured using a temperature-relaxation-based method. Below $\sim 0.6\,\mathrm{K}$, the time-resolved heat relaxation cannot be described by an exponential fit with one or two relaxation times. In Refs. [6, 121], it has been shown that the data can be reasonably fitted by considering at least three relaxation times. The authors explained this by assuming the magnetic system

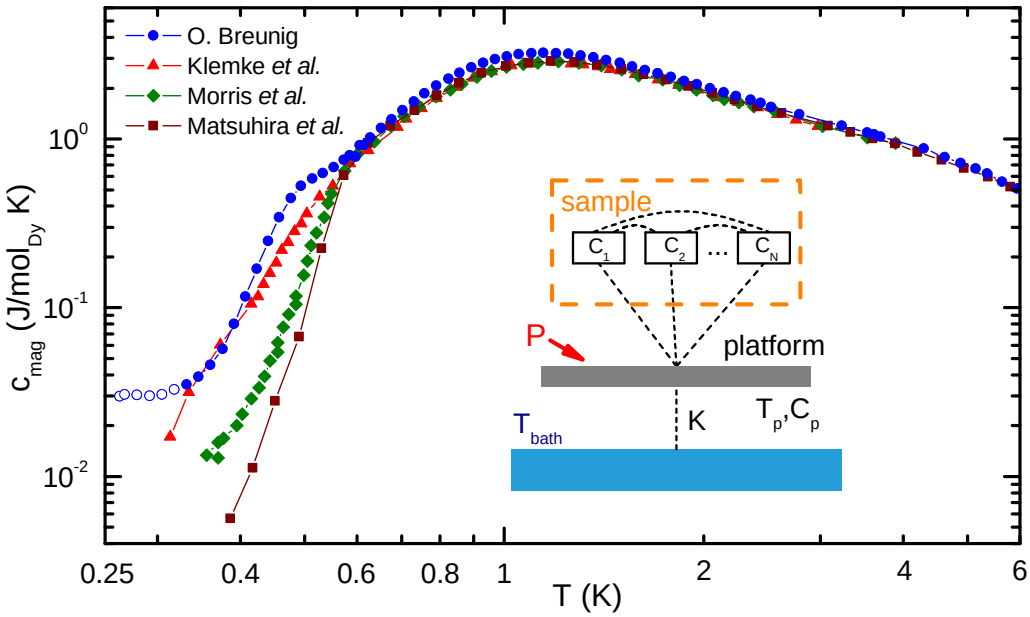

Figure 4.7: Comparison of different literature data of the magnetic specific heat of $Dy_2Ti_2O_7$ [6, 130, 149–151]. The data of Morris *et al.* and Matsuhira *et al.* were obtained via the standard single-relaxation techniques. The data of Klemke *et al.* and O. Breunig were obtained by explicitly taking anomalous relaxation processes into account. Inset: Schematic illustration of the method introduced by O. Breunig.

to consist of different subsystems individually coupled to the platform. Standard methods to measure the specific heat (considering only one single relaxation time) do not account for such dynamics. In Fig. 4.7, four different measurements of the magnetic specific heat of $Dy_2Ti_2O_7$ found in literature are shown. The datasets of Morris *et al.* [130] and Matsuhira *et al.* [149] were measured with the conventional single-relaxation method and, thus, provide too small values below $\sim 0.6\,\mathrm{K}$, whereas the data of Klemke *et al.* [6, 121] were obtained by explicitly accounting for multiple relaxation times and, thus, provide larger values in the low-temperature regime.

An alternative approach to measure the specific heat accounting for sample-internal relaxation dynamics has been introduced by O. Breunig [151]. The inset of Fig. 4.7 shows a schematic illustration of this method. The sample is assumed to consist of any number of subsystems C_i which are not directly linked to the bath, but only to the platform and to each other. The temperature of the platform T_P is measured as a function of time. The measurement starts from equilibrium, *i.e.* $T_\mathrm{sample} = T_\mathrm{P} = T_\mathrm{bath}$, then a constant heating power P is applied to the platform until the entire system is in equilibrium again, *i.e.* $T_\mathrm{sample} \simeq T_\mathrm{P} = T_\mathrm{bath} + \Delta T$. The total heat transformed to the sample is ob-

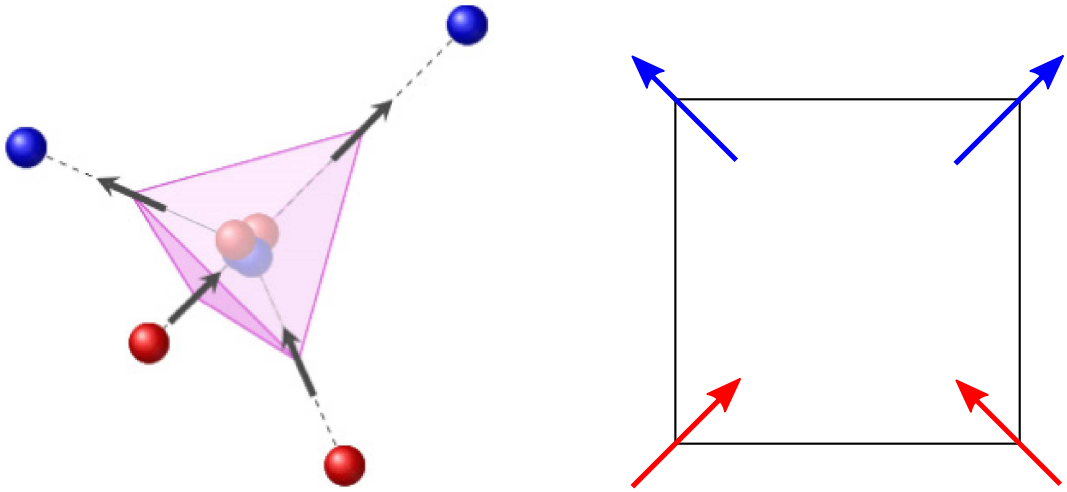

(a) (b)

Figure 4.8: (a) Dumbbell model of a single tetrahedron obeying the ice rule 2in-2out (taken from [139]). (b) Schematic two-dimensional mapping of a single tetrahedron (2in-2out).

tained by subtracting the numerically obtained heat flown via K to the platform from the heat provided by the heater. The results are also shown in Fig. 4.7. For temperatures above $\sim 0.6\,\mathrm{K}$, all methods provide the same values of c_p within 10%. At lower temperatures, the method introduced by O. Breunig provides enhanced c_p values similar to the results of Refs. [6, 121], but without any a-priori assumptions about the subsystems or their corresponding couplings. In addition to [6, 121], the data of Breunig [151] show a shoulder around 0.5 K and a tendency towards saturation below 0.35 K (open symbols). These features most probably arise from nuclear contributions to c_p originating from the isotopes ^{161}Dy and ^{163}Dy [152]. In Refs. [6, 121], a ^{162}Dy-enriched sample was studied.

4.2 Theoretical Approaches

4.2.1 Single-Tetrahedron Approximation

Theoretical Model

A simple but very instructive theoretical model of the magnetic spin-ice system is the single-tetrahedron approximation [134]. Within this model, only one single isolated tetrahedron consisting of four Dy ions with their corresponding local easy-axes in the $\langle 111 \rangle$ directions is considered. Fig. 4.8(a) shows a single tetrahedron obeying the ice rule, *i.e.* two of the four spins point into and the other two out of the tetrahedron. A simple 2D mapping of a tetrahedron with the same spin configuration is shown in Fig. 4.8(b).

The single-tetrahedron approximation is based on the effective nearest-neighbor Hamiltonian (Eq. 4.11) with a ferromagnetic effective coupling constant J_{eff},

$$\mathcal{H} = -3J_{\text{eff}} \sum_{\langle i,j \rangle} \vec{S}_i \cdot \vec{S}_j - \frac{\mu \vec{B}}{2} \sum_{i=1}^{4} \vec{S}_i \,, \tag{4.12}$$

where $\vec{S}_i$ ($i = 1..4$) are the unit vectors pointing along the local easy axes from the corners of the tetrahedron to its center or *vice versa* (Fig. 4.8(a)). The first term in Eq. (4.12) is a summation over all pairs $i \neq j$, where the factor of 3 accounts for the angles of the real local easy axes in the effective ferromagnetic spin-spin interaction. The second term describes the individual coupling to an external magnetic field $\vec{B}$. As every Dy site belongs to two tetrahedra, only half this energy is adjudged to one single tetrahedron. $\mu = 10\,\mu_{\text{B}}$ is the magnetic moment of one Dy ion (Eq. 4.5). The effective coupling constant ($J_{\text{eff}} \approx 1.1\,\text{K}$ in the case of $Dy_2Ti_2O_7$ [134]) is determined by comparing the theoretically obtained magnetization $M(B)$ with experimental data for $\vec{B} \,||\, [111]$. For this field direction, the $M(B)$ data exhibit a prominent steplike feature (see discussions on page 50).

The difference of the Hamiltonian in Eq. (4.12) from that introduced before in Eq. (4.11) is the consideration of only one single tetrahedron, *i.e.* of only four spins. Thus, every spin has only 3 neighbors. In Eq. (4.11), every spin has 6 neighbors. In Sec. 4.2.2, Metropolis-like simulations of the dipolar and the nearest-neighbor spin ice are introduced. It turns out that numerical calculations on a nearest-neighbor level and the single-tetrahedron approximation provide the same results in zero magnetic field, whereas there are slight differences when including an external magnetic field.

Energy-Levels and Ground-State Degeneracy

Within the single-tetrahedron approximation, an isolated tetrahedron has $2^4 = 16$ possible spin configurations which are highly degenerate in zero magnetic field (Fig. 4.9). In the absence of an external magnetic field, six energetically equivalent 2in-2out configurations form the ground state. The first excited state, 2.2 K above the ground state, is 8-fold degenerate and consists of tetrahedra breaking the ice-rule (3in-1out or 1in-3out). These excitations are discussed as magnetic monopoles (Sec. 4.1.3). The energy of the two remaining configurations (4in-0out and 0in-4out) is 4 times larger than for the first excited state and will mostly be neglected in the following chapters.

The single-tetrahedron model, being a 16-level system, can be solved analytically. At a given temperature T, the different spin configurations are populated according to the Boltzmann distribution (in thermal equilibrium):

$$p_n = \frac{1}{Z} \exp\left(-\frac{E_n}{k_{\text{B}}T}\right) \quad \text{with} \quad Z = \sum_{k=1}^{16} \exp\left(-\frac{E_k}{k_{\text{B}}T}\right) . \tag{4.13}$$

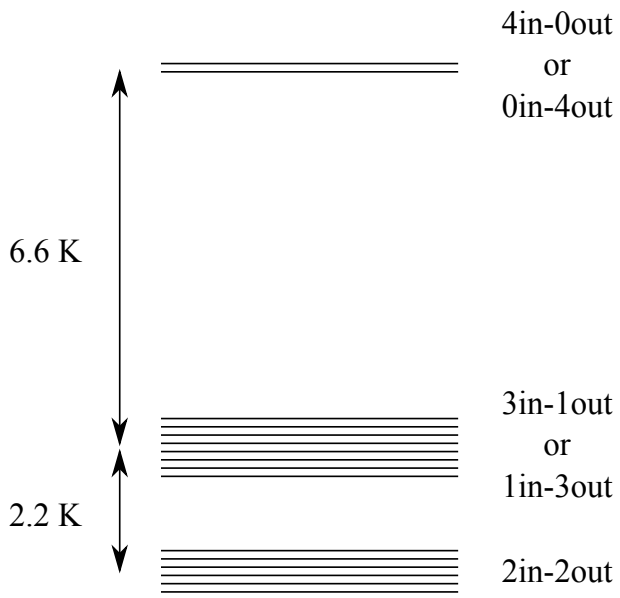

Figure 4.9: Energy levels of a single tetrahedron with effective coupling $J_{\text{eff}} = 1.1\,\text{K}$ [134] in zero magnetic field.

One can use the partition function Z to calculate several thermodynamic quantities, *e.g.* specific heat

$$C = \frac{R}{2} T \frac{\partial^2}{\partial T^2} (T \ln Z) \qquad \left([C] = \frac{\text{J}}{\text{K} \cdot \text{mol Dy}} \right) \tag{4.14}$$

and entropy

$$S = \frac{R}{2} \frac{\partial}{\partial T} (T \ln Z) = \int_0^T \frac{C}{T'} \, \mathrm{d}T' \qquad \left([S] = \frac{\text{J}}{\text{K} \cdot \text{mol Dy}} \right) . \tag{4.15}$$

Fig. 4.10 shows C/T and the integral $S(T)$, calculated via Eqs. (4.14) and (4.15). The difference between the asymptotic value $S_{T\to\infty}$ and the theoretical value $R \ln 2$ for a two-level system yields the residual entropy $S_0 = 1.69\,\text{J/mol K}$. This is exactly the theoretical prediction of Pauling's entropy of water ice (Eq. 4.1).

One has to keep in mind that the single-tetrahedron approximation (Eq. 4.12) is a strong simplification which neglects the long-range dipolar interaction. Furthermore, it only describes a system in thermal equilibrium. For low temperatures and small magnetic fields, however, the spin ice is dominated by non-equilibrium processes [6, 143, 144]. Nevertheless, the single-tetrahedron model is a very instructive approach, in particular, when including an external magnetic field.

Single Tetrahedron in an external magnetic Field

In the following, the single-tetrahedron approximation is discussed for different

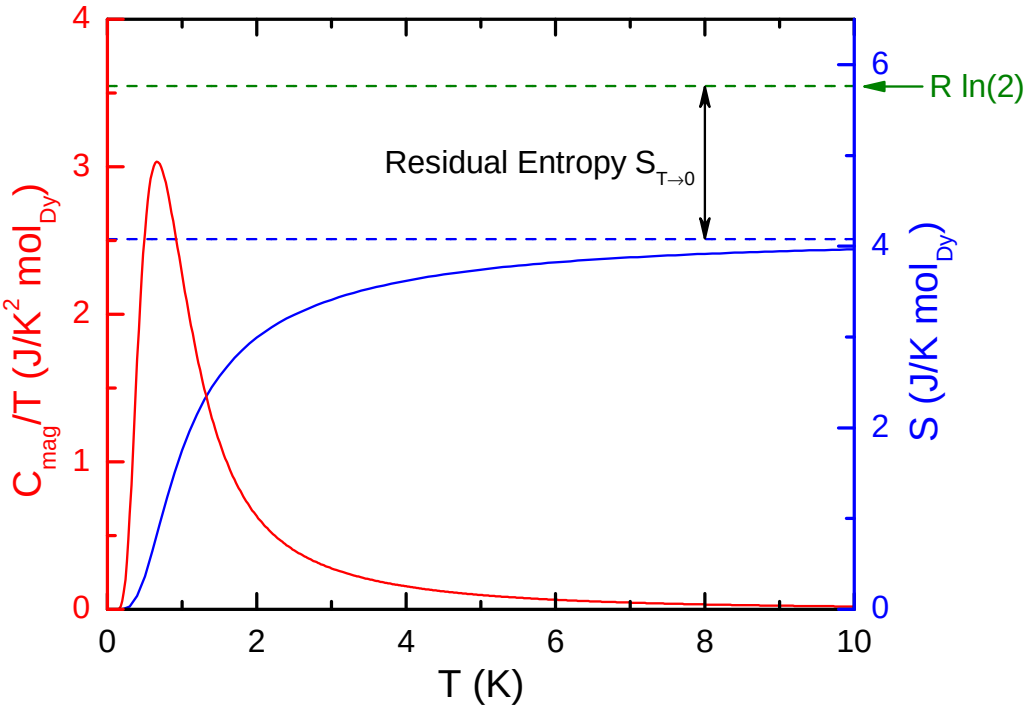

Figure 4.10: C/T and the entropy S of the spin ice calculated with the single-tetrahedron model in zero magnetic field. The residual entropy S_0 is obtained by subtracting the asymptotic value $S_{T\to\infty}$ from the theoretical value $R \ln 2$ for a two-level system. The theoretical curves have similarities to the experimental data shown in Fig. 4.4 on page 39.

magnetic-field directions. The external magnetic field competes with the internal magnetic interaction and, thus, has a strong influence on the energy levels of the different spin configurations calculated via Eq. (4.12). Moreover, the preferential direction of each spin, due to the magnetic field, causes a lifting of the ground-state degeneracy. For the special geometrical arrangement of the pyrochlore lattice, together with the local easy axes of the Dy momenta, three magnetic-field directions ([001], [111], and [110]) are of particular interest and will be discussed here. These field directions yield different field-induced ground states. These particular field directions, compared to the orientation of the tetrahedra within the pyrochlore lattice, are illustrated in Fig. 4.11. In the following, the influence of a magnetic field on the energy levels for these three field directions is discussed.

For $\vec{B}$ || [001], the magnetic field causes a preference of one particular 2in-2out configuration for which all spins have a positive component parallel to $\vec{B}$. This results in a non-degenerate field-induced 2in-2out ground state (Fig. 4.12(a)). As all spins have the same component in [001] direction, all of them are affected equally, and for symmetry reasons, the field-induced energy splitting shows a monotonic behavior. As the gap to the next energy level becomes larger with in-

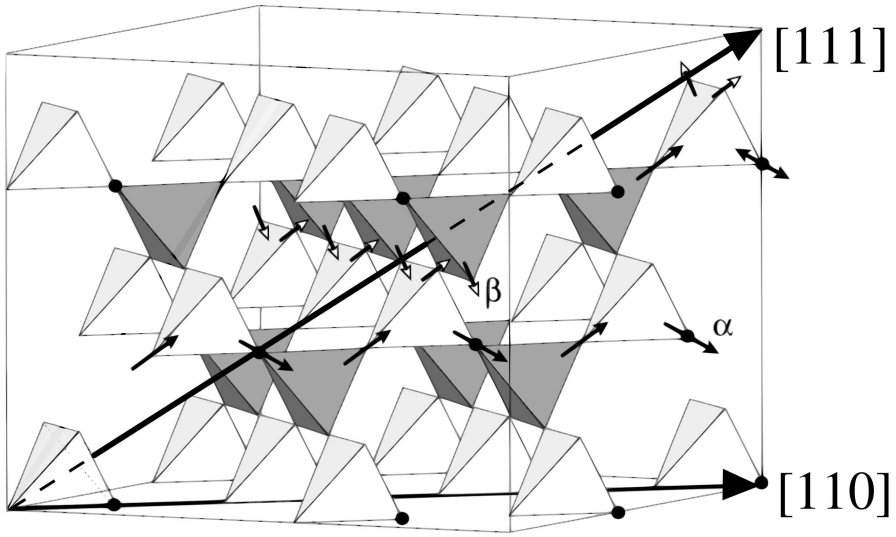

Figure 4.11: Orientation of the magnetic-field directions discussed here within the pyrochlore lattice. The [110] direction exhibits the peculiarity that an applied magnetic field along this direction divides the pyrochlore lattice into α chains (black arrowheads, parallel to $\vec{B}$) and β chains (white arrowheads, perpendicular to $\vec{B}$) (taken from [121]).

creasing field, the non-degenerate ground state will be more stabilized the larger the magnetic field is. For $T \to 0$, an infinitesimally small magnetic field should cause a population only of the non-degenerate ground state and, thus, a sharp jump of the magnetization at infinitesimally small fields, as expected for a paramagnet. However, the slow dynamics at low temperatures (Sec. 4.1.5) prevent the magnetic system from behaving like a usual paramagnet but rather like a ferromagnet with a remnant magnetization at zero field. This special behavior at low temperatures cannot be reflected by the single-tetrahedron approximation as it only describes the system in thermal equilibrium.

The field direction $\vec{B} \,||\, [111]$ affects the spins unequally. This particular field direction is parallel to one of the local easy axes at one corner of the tetrahedron (Fig. 4.12(b)). Thus, this particular spin (parallel to $\vec{B}$) can gain the most dipole energy (compared to the other three spins) when pointing parallel to the magnetic field. As a consequence, it will be easily aligned along $\vec{B}$ already for rather small fields at low temperatures. The three remaining spins of the tetrahedron have the same component parallel to $\vec{B}$. Thus, as long as the internal interaction prevents these spins from aligning parallel to $\vec{B}$, which is the case for magnetic fields below 1 T, the field-induced ground state is degenerate, consisting of three energetically equivalent 2in-2out configurations. The phase achieved below 1 T

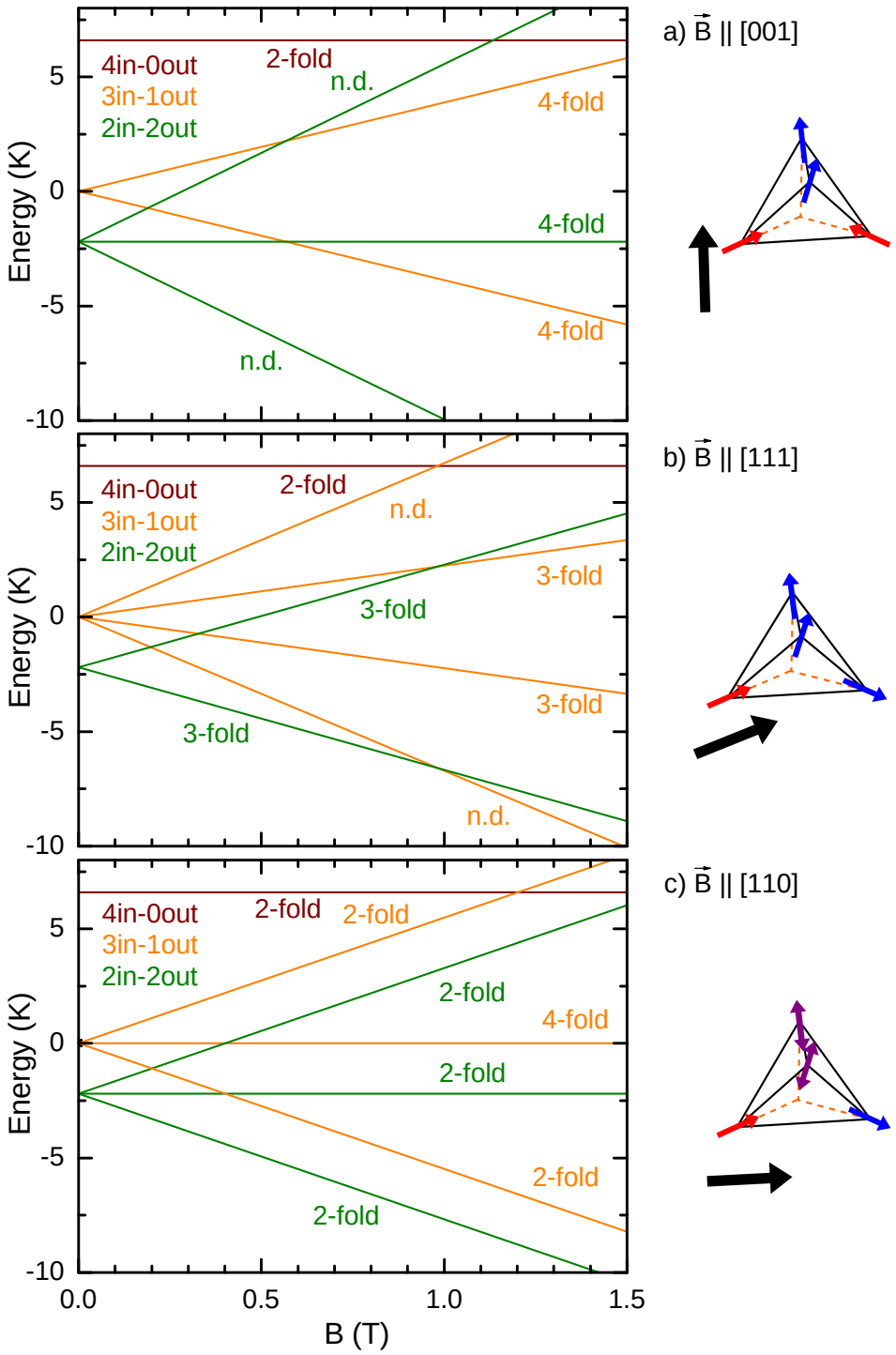

Figure 4.12: Field-dependent energy splitting of the configurations of a single tetrahedron for a) $\vec{B} \,||\, [001]$, b) $\vec{B} \,||\, [111]$, and c) $\vec{B} \,||\, [110]$ (n.d. = non degenerate). The tetrahedra images on the right-hand side (taken from [121]) show the field-induced ground states (for $\vec{B} \,||\, [111]$, the ground state above 1 T).

is called Kagomé-ice state[15] [120, 124, 153, 154]. For magnetic fields above 1 T, the energy of the external field exceeds the internal energies, and all spins tend to point along the magnetic field $\vec{B}$. This change to a non-degenerate 3in-1out ground state at 1 T (Fig. 4.12(b)) is accompanied by a sharp steplike increase of the magnetization $M(B)$ at low temperatures (Fig. 4.15).

For $\vec{B} \,||\, [110]$, two of the four spins per tetrahedron are perpendicular to the applied magnetic field (Fig. 4.12(c)) and are, thus, not affected. As a consequence, the field-induced ground state remains 2-fold degenerate, even for high magnetic fields.[16] This particular field direction exhibits another peculiarity. As shown in Fig. 4.11 on page 50, the magnetic field divides the pyrochlore lattice into two disjunct classes, the α chains (parallel to $\vec{B}$) and the β chains (perpendicular to $\vec{B}$). For high magnetic fields, the spins of the α chains tend to align along the applied field, whereas the spins of the β chains have two possible equivalent spin configurations (taking the ice rule into account). This energetic equivalence is only valid for a local consideration (as it is the case in the single-tetrahedron approximation). As the spins of the neighboring tetrahedra also influence the spin state of one particular tetrahedron, the β chains should also form (at least domains of) ferromagnetic chains.

4.2.2 Numerical Simulations

System Parametrization and numerical Model

In the framework of this thesis, a PYTHON-script [156] was written to simulate the dynamics of the magnetic spin-ice system using a single-spin-flip Metropolis-like algorithm. A detailed review about Metropolis-like Monte Carlo studies of $Dy_2Ti_2O_7$ can be found in Ref. [140].

The pyrochlore lattice is a cubic system with a cubic unit cell containing 16 lattice sites. Fig. 4.13 illustrates the parametrization of the cubic unit cell by dividing it into four layers of 4×4 square lattices. The size of the parametrized pyrochlore lattice is determined by the edge length L which is an integer number and determines the number of cubic unit cells in a row. Thus, the whole lattice consists of L^3 cubic unit cells with 16 lattice sites in each unit cell, *i.e.* of $16\,L^3$ sites. After several test runs, it turned out that a reasonable balance between numerical precision, due to finite-size effects, and computational efficiency is given for a lattice size of $L = 4$, *i.e.* for 1024 sites. All calculations presented here were performed with this particular lattice size. To avoid boundary effects, the parametrized lattice is treated with periodic boundary conditions.

[15] The Kagomé-ice state within the 3D spin ice is not equivalent to the 2D spin ice (Fig. 4.1 on page 36). In 3D, the local easy axes of the Dy ions within the Kagomé planes have a component perpendicular to the plane. Thus, the different spin configurations of the triangles are not energetically equivalent.

[16] Monte Carlo simulations presented in Ref. [155] predict an ordered phase for high magnetic fields and low temperatures.

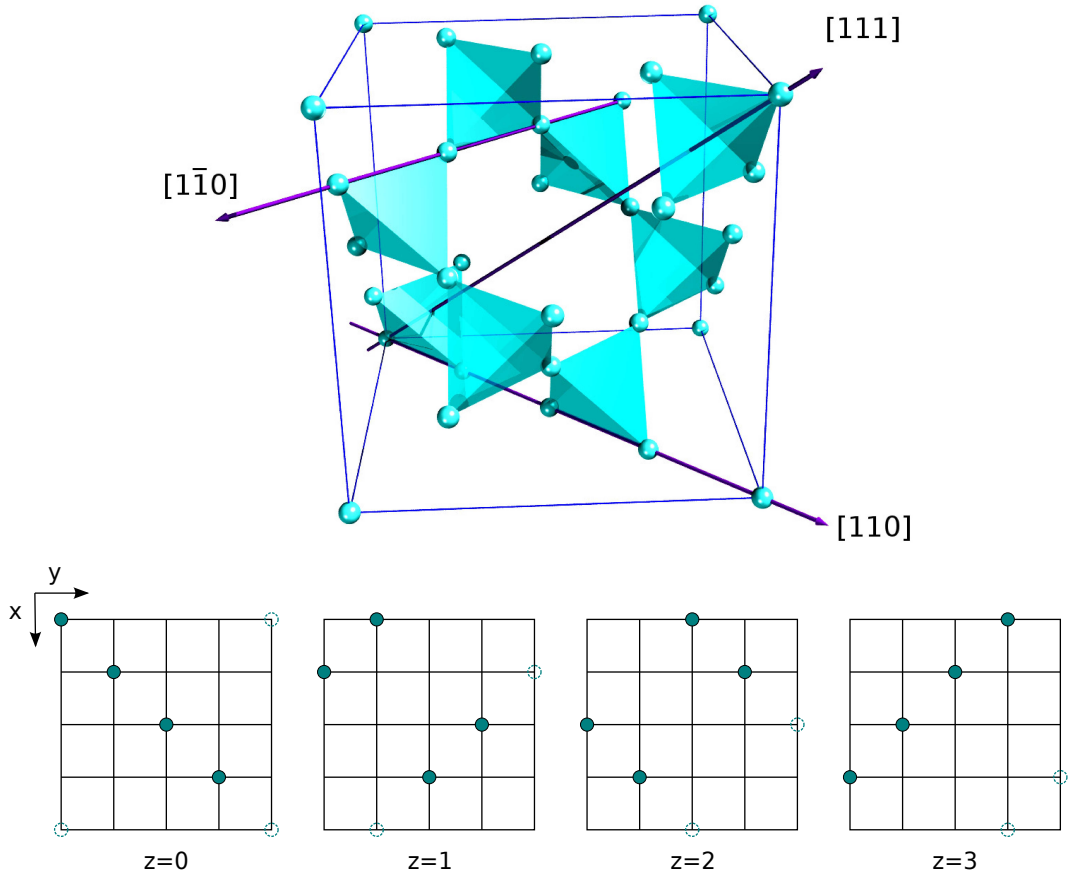

Figure 4.13: Cubic unit cell of the pyrochlore lattice, containing 16 lattice sites (blue spheres). The crystallographic directions [111], [110], and [1$\bar{1}$0] are inserted to facilitate the 3D imagination. The square panels illustrate the parametrization of the cubic unit cell (explained in the text). The open dashed circles depict lattice sites which arise from the periodicity of the lattice.

The magnetic moment of Dy^{3+} is $\mu = 10\mu_B$, but one can also choose an individual value for μ. For a fixed μ, the lattice can be further modified in order to simulate a dilute spin ice, *i.e.* doping with non-magnetic ions, *e.g.* Yttrium (Y) (Sec. 4.2.2). Within the simulation, the doping is realized as follows. The magnetic moment of every single ion (every lattice site) is randomly set to zero according to a given probability between 0 and 1. The advantage is that the non-magnetic defect sites are randomly distributed and do not form a superstructure. As a drawback, the actual doping ratio with defect sites is not exactly the predefined value. For a lattice size of 1024 ions, however, this deviation causes no considerable error.

The main function of the simulation software works as follows. The energy E of one particular ion is calculated according to its magnetic moment as a sum-

mation of (i) the exchange energy (spin-spin interaction), (ii) the long-range dipole-dipole interaction, and (iii) the dipole energy with respect to the external magnetic field (Eq. 4.10 on page 44). Due to its local easy axis, every spin has only two possibilities of orientation and can, hence, be regarded as a two-level system with an energy gap $\Delta = 2E$. The spin orientation is then determined by the distribution

$$p = \frac{\exp(-2E/k_\mathrm{B}T)}{1+\exp(-2E/k_\mathrm{B}T)}\,. \tag{4.16}$$

In order to implement thermal fluctuations, the spin orientation is randomly determined with a probability weight according to Eq. (4.16). This procedure is sequentially done for every single ion of the lattice. To avoid systematical errors, the order of processing is randomly generated at the beginning of each simulation step. For each decision whether to flip a spin or not only the present spin configuration is base of calculation not the history. During one simulation step (processing all spins), the external parameters (temperature and magnetic field) are kept fixed. After each simulation step, the external parameters are only slightly changed. This inhibits the system to go too far from thermal equilibrium. The smaller the change of parameter, the closer the system is at thermal equilibrium after the step.

Typically, a simulation starts with randomly distributed spin orientations. Thus, it is convenient to start a simulation at a rather high temperature above $\sim 2\,\mathrm{K}$. Here, thermal fluctuations are large enough to ensure that the system rapidly reaches thermal equilibrium, *i.e.* after a few steps. Temperature-dependent simulations start from high temperatures and are performed by lowering the temperature by a small amount at each simulation step. Before starting a field-dependent simulation, the system needs to be cooled down slowly (*i.e.* with a small step size) at a fixed magnetic field. This ensures that the system stays in its ground state, especially for field-depended simulations at rather low temperatures (below 0.6 K). When changing the magnetic field at very low temperatures, it is not ensured that the system reaches thermal equilibrium, even for a very small step size of the magnetic-field change. This results in a hysteretic behavior, discussed in Sec. 4.2.2.

The temperature-dependent simulations, introduced here, were performed by decreasing temperature with temperature steps of $\Delta T = 0.2\,\mathrm{mK}$. The field-dependent data were simulated with field steps of $\Delta B = 0.5\,\mathrm{mT}$.

Nearest-Neighbor Spin-Ice Simulation

First, the case of pure nearest-neighbor interaction (Eq. 4.11) is discussed. Fig. 4.14 shows the simulated temperature dependence of the energy of the spin-ice system in zero field for pure nearest-neighbor interaction (orange line). The analytically obtained energy of a single tetrahedron (dashed line, Sec. 4.2.1) perfectly matches the simulated data. This shows that both approaches are

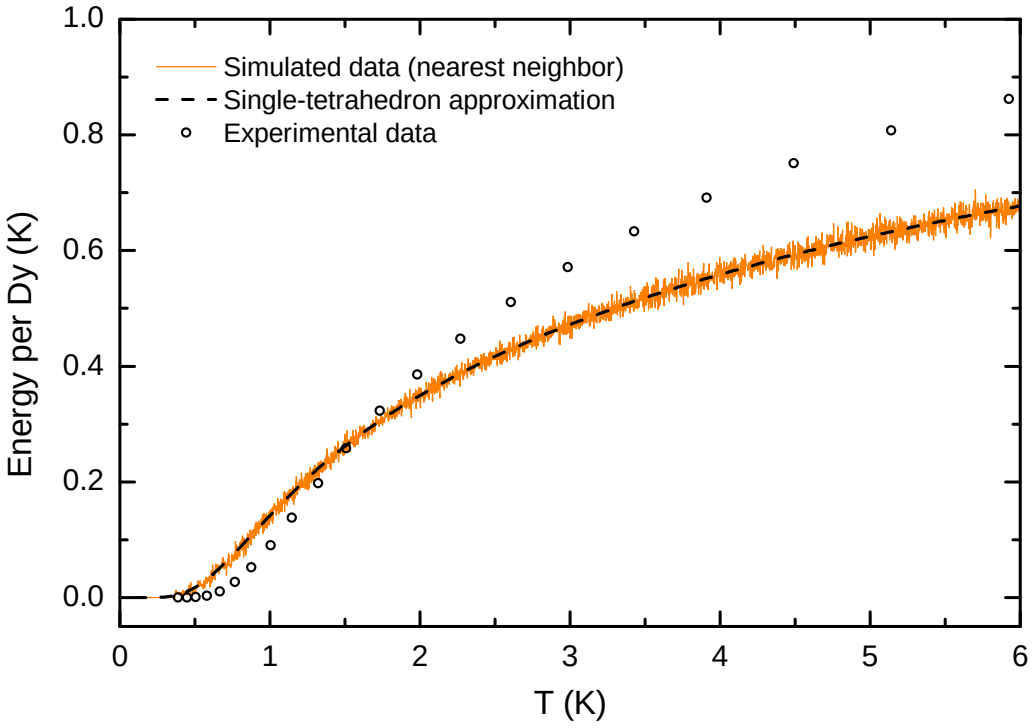

Figure 4.14: Zero-field temperature dependence of the energy per Dy ion of the magnetic spin-ice system. The experimental data were obtained by numerical integration of specific heat data of $Dy_2Ti_2O_7$ (digitized from [124]).

equivalent in zero field. However, the poor agreement with experimental data (open black circles) shows that restricting to nearest-neighbor interaction provides a strongly oversimplified approximation, which can be used only on a qualitative level.

This can also be observed when simulating the field-dependent magnetization $M(B)$. Fig. 4.15 compares the simulated magnetization for $\vec{B} \,||\, [111]$ at 0.4 K (nearest neighbor) with the magnetization of a single tetrahedron and experimental data [84]. The curves resemble each other only on a qualitative level. In the presence of an external magnetic field, the single-tetrahedron calculations are different from the simulated magnetization. Furthermore, the sharp steplike feature, clearly observed in the experimental data, is much broader in both theoretical approaches. It is notable that both data (simulated and experimental) are not hysteretic at 1 T. At low fields, however, the experimental data exhibit a clear hysteresis, indicated by arrows in Fig. 4.15, which is absent in the theoretical curves.

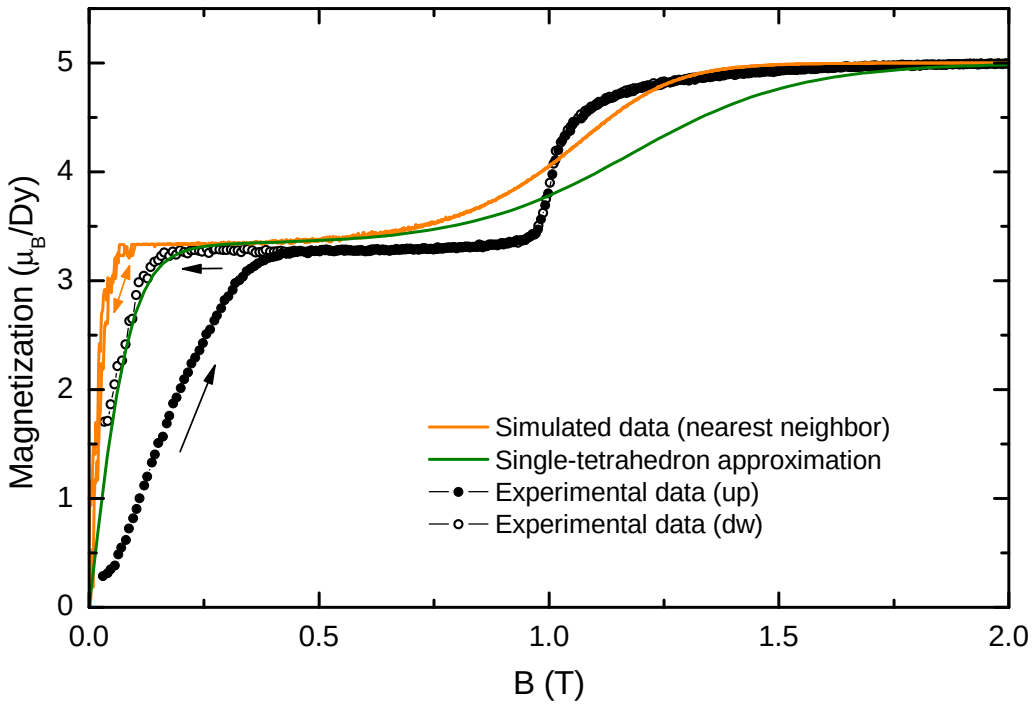

Figure 4.15: Magnetization for $\vec{B} \,||\, [111]$ at 0.4 K. Comparison of simulated data for nearest neighbor interaction (orange), single-tetrahedron approximation (green), and experimental data of $Dy_2Ti_2O_7$ (black circles [84]). The simulation started after slowly cooling down the spin system in zero magnetic field.

Dipolar Spin-Ice Simulation

For a more quantitative treatment of the spin ice, the long-range dipolar interaction has to be taken into account. This model is called dipolar spin ice. For the short-range exchange energy, only the 6 nearest neighbors have to be considered. The long-range dipolar interaction, however, has to be cut off at a reasonable distance. Although the dipole field decays rather fast[17], it turns out that the long-range interaction has a considerable influence on the magnetic system. The long-range dipolar interaction can be calculated via Ewald summation techniques [14, 140, 157–159]. In the calculations presented here the dipolar interaction is calculated explicitly for a given number of neighbors, *i.e.* it is cut off at a suitable distance. In this framework, the number of considered neighbors can be treated as a free parameter of the simulated system. It turned out that $n = 222$ is a reasonable number of neighbors to achieve a good agreement between experimental

[17] proportional to $1/r^3$ for large distances r.

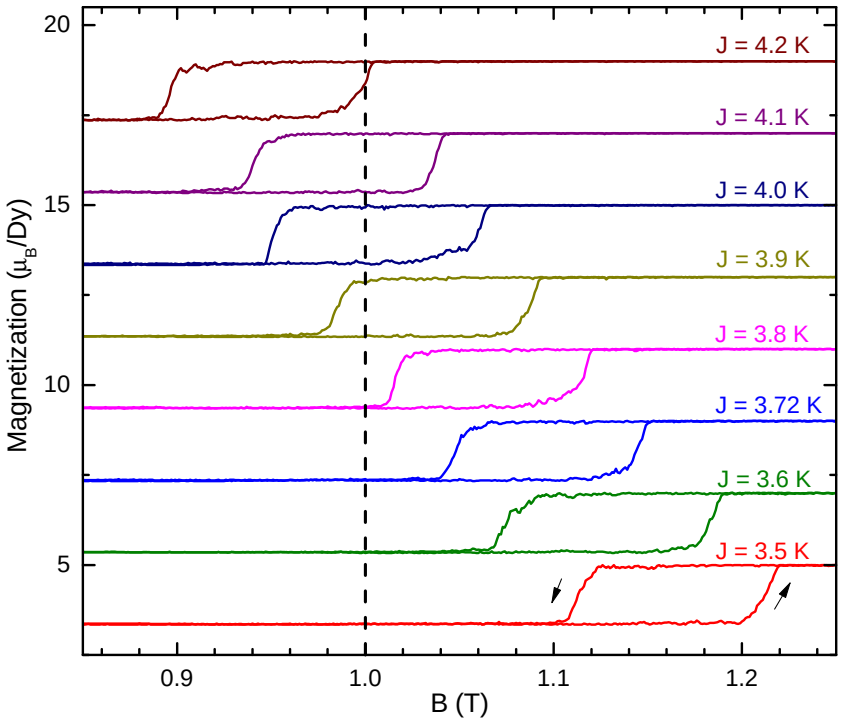

Figure 4.16: Simulation of the field dependence of the magnetization $M(B)$ parallel to [111] for various exchange couplings J at $T = 0.4\,\mathrm{K}$. The simulations started after slowly cooling down at a field of 0.75 T. The dipolar interaction is taken into account for the next $n = 222$ neighbors. The different curves are shifted by $2\mu_\mathrm{B}$ with respect to each other. The arrows indicate the direction of the field change, exemplarily for $J = 3.5\,\mathrm{K}$.

data and simulation.[18]

As the dipolar-interaction coupling $D \approx 1.40\,\mathrm{K}$ in Eq. (4.10) is determined via Eq. (4.7), the only remaining free parameter of the simulated spin system is the exchange coupling constant J. The effective nearest-neighbor coupling constant J_eff (Eq. 4.8) and, thus, the nearest-neighbor coupling $J_\mathrm{nn} = J/3 = -1.24\,\mathrm{K}$ (*i.e.* $J = 3.72\,\mathrm{K}$) have been fixed by comparing the simulated magnetization data with experimental results for a magnetic field $\vec{B}\,||\,[111]$ (Sec. 4.2.1). As more neighbors are taken into account within the dipolar spin-ice simulation, the exchange coupling J needs to be slightly corrected as follows. The magnetization $M(B)$ was simulated with different values for J from 3.5 K to 4.2 K (Fig. 4.16). The dashed line indicates the experimentally observed position of the steplike increase of $M(B)$ (Fig. 4.15). The simulated magnetization exhibits a clear hysteresis at this transition, which is independent of J. Such a hysteresis is not

[18] As the exchange-coupling constant J will be determined in the following paragraph, the number $n = 222$ will be justified afterwards.

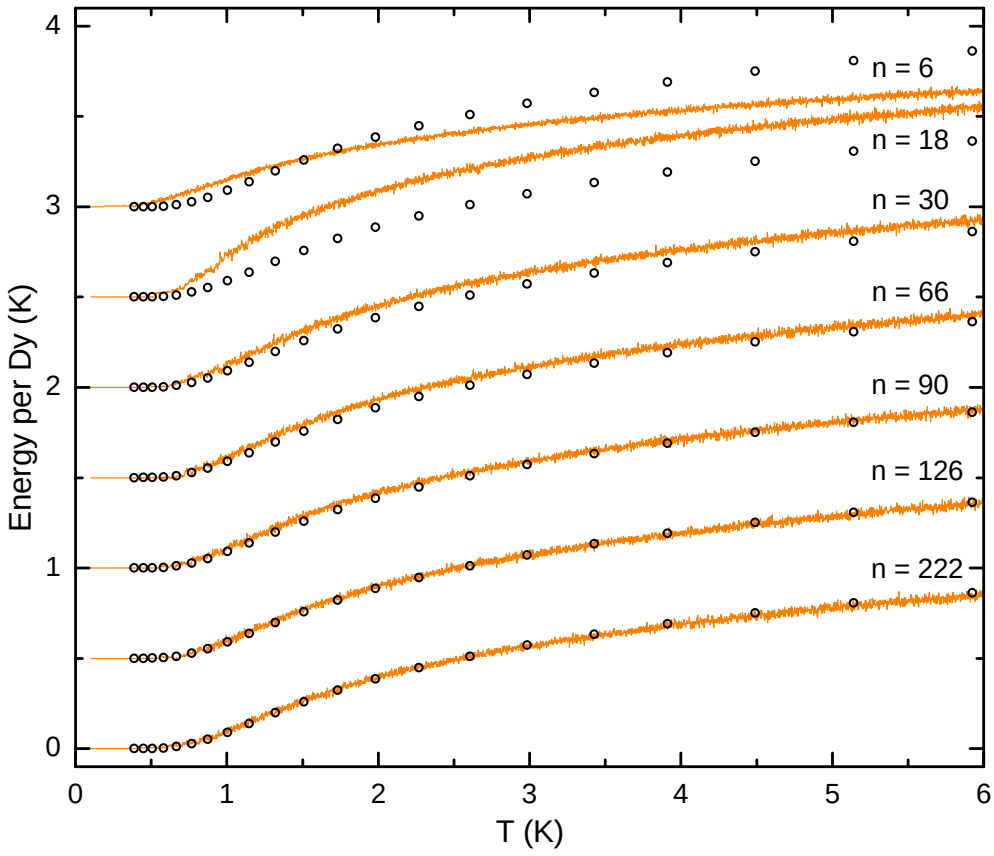

Figure 4.17: Simulation of the temperature dependence of the energy per Dy ion for various numbers of neighbors n at zero field (orange line). The black circles depict experimental data, obtained by integrating the measured specific heat (digitized from [124]). The different curves are shifted with respect to each other.

observed in the experimental data (Fig. 4.15) and shows that the magnetic system has not reached thermal equilibrium within the hysteresis (*cf.* discussion in Sec. 4.2.2). Despite this difference, one can clearly see that for $J = 4\,\mathrm{K}$ the two critical fields (up and down) lie almost symmetrically around the expected value of 1 T. By this criterion, we determine the exchange coupling $J = 4\,\mathrm{K}$ for calculations of the dipolar spin ice.

In the following, the dependence of the spin-ice energy on the number of considered neighboring ions in the dipolar spin-ice system is investigated. The ions taken into account for the dipolar interaction are chosen spherically symmetrically around the considered central ion. This results in the following possible numbers of neighbors,

$$n = 6,\ 18,\ 30,\ 66,\ 90,\ 126,\ 222,\ \ldots\ , \tag{4.17}$$

where these numbers of neighbors correspond to spheres with radii

$$r/r_{\mathrm{nn}} = 1,\ 1.8,\ 2,\ 2.7,\ 3,\ 3.5,\ 4.2,\ \ldots\ , \tag{4.18}$$

respectively. Due to the periodic boundary conditions, it is obvious that a magnetic ion feels its own influence if considering too many neighbors.

Fig. 4.17 shows the simulated temperature dependence of the total energy per Dy ion of the spin system for various numbers of neighbors n (orange line). For $n = 222$, one gets a quite good agreement of simulation and experimentally obtained data. This proves that the nearest-neighbor Hamiltonian and, thus, the single-tetrahedron approximation is only a rough approximation. The long-range dipolar interaction turns out to be very essential, and a rather large number of neighboring spins have to be taken into account to describe the spin system properly.

Dipolar Spin Ice in an external magnetic Field

To check the applicability of the dipolar-spin-ice simulation in the presence of an external magnetic field, the temperature dependence of the simulated spin system is compared to experimental data obtained for various magnetic-field strength along different field directions. The simulations were performed by slowly lowering the temperature from 6 K down to 0.1 K at a fixed magnetic field.

Figs. 4.18 and 4.19 show the temperature-dependent energy of the spin system for external magnetic fields parallel to [111], [001], and [110], respectively. The simulated data (orange curves) are compared with experimental data obtained by numerical integration of the measured specific heat. For $\vec{B} \,||\, [111]$ and $\vec{B} \,||\, [001]$, the specific heat data was digitized from [124]. For $\vec{B} \,||\, [110]$, the specific heat was measured by O. Breunig [151], where the measurements for $\vec{B} \,||\, [110]$ have been scaled by 10% to adjust the data with respect to literature data [124, 160].

The theoretical data were simulated for the corresponding magnetic fields of the experimental datasets (denoted within the figures). In some cases, marked by a star (*), a simulation at a slightly different magnetic field provides better coincidence with experimental data. In Fig. 4.19(a), the 0.5 T as well as the 1 T datasets are better described by simulations at 0.7 T and 1.1 T, respectively. A reason for this discrepancy could be an increase of the internal magnetic field inside the sample due to an increasing magnetization which is not taken into account within the simulation.

In sum, the simulation of the dipolar spin ice provides a rather good quantitative agreement with experimental data for three different field directions and a variety of magnetic fields strengths.

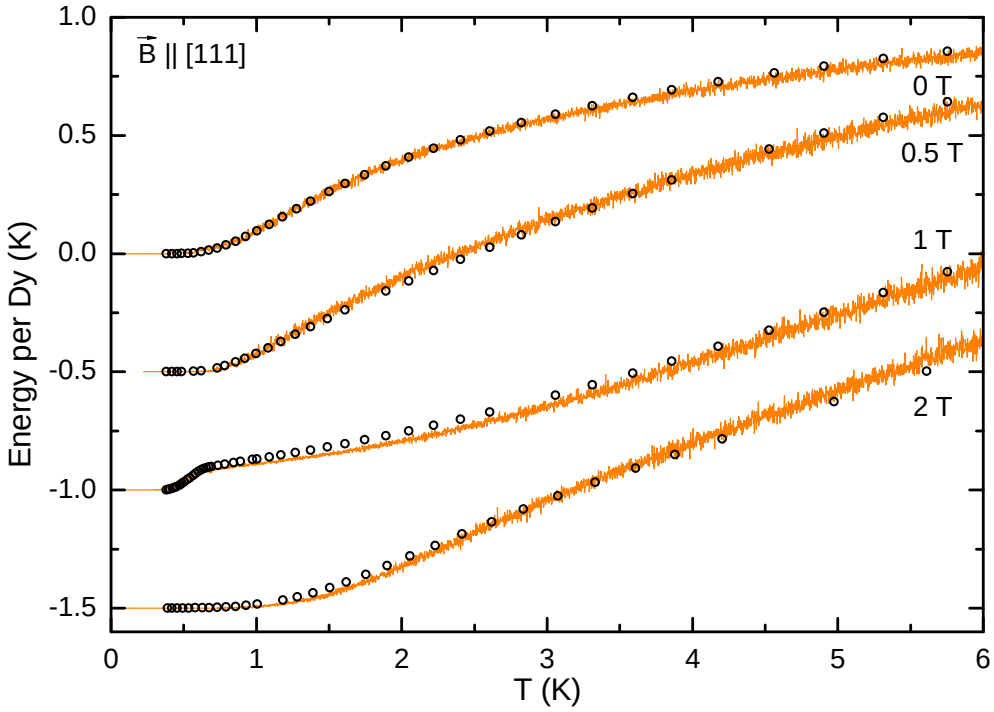

Figure 4.18: Simulation of the temperature dependence of the energy per Dy ion for a magnetic field parallel to [111] (orange line). The black circles depict experimental data, obtained by integrating the measured specific heat (digitized from [124]). The different curves are shifted with respect to each other.

Out-of-Equilibrium Processes

The dipolar-spin-ice simulations presented in Figs. 4.18 and 4.19 were performed by cooling very slowly in the presence of a fixed magnetic field (field cooled). Therefore, it is ensured that the system has the possibility to condense into the field-induced ground state. When the field is changed at low temperatures (after cooling at a fixed field or in zero field), however, the system possibly needs a long time scale to relax back into thermal equilibrium. In the context of numerical simulation, this means that a large number of simulation steps is probably needed. A suitable test to check for equilibrium is to simulate with increasing field followed by a simulation with decreasing field. A hysteresis, as observed in Fig. 4.16 on page 57, indicates that the system did not have enough time (or number of steps) to minimize its energy, *i.e.* to find thermal equilibrium.

Fig. 4.20 shows the magnetic-field dependence of the simulated magnetization for $\vec{B} \,||\, [111]$ at various temperatures. One can clearly see, that the hysteresis around 1 T disappears above $\sim 0.6\,\mathrm{K}$. Within the hysteretic region around 1 T, the magnetic system stays in a meta-stable state. Here, the thermal activation

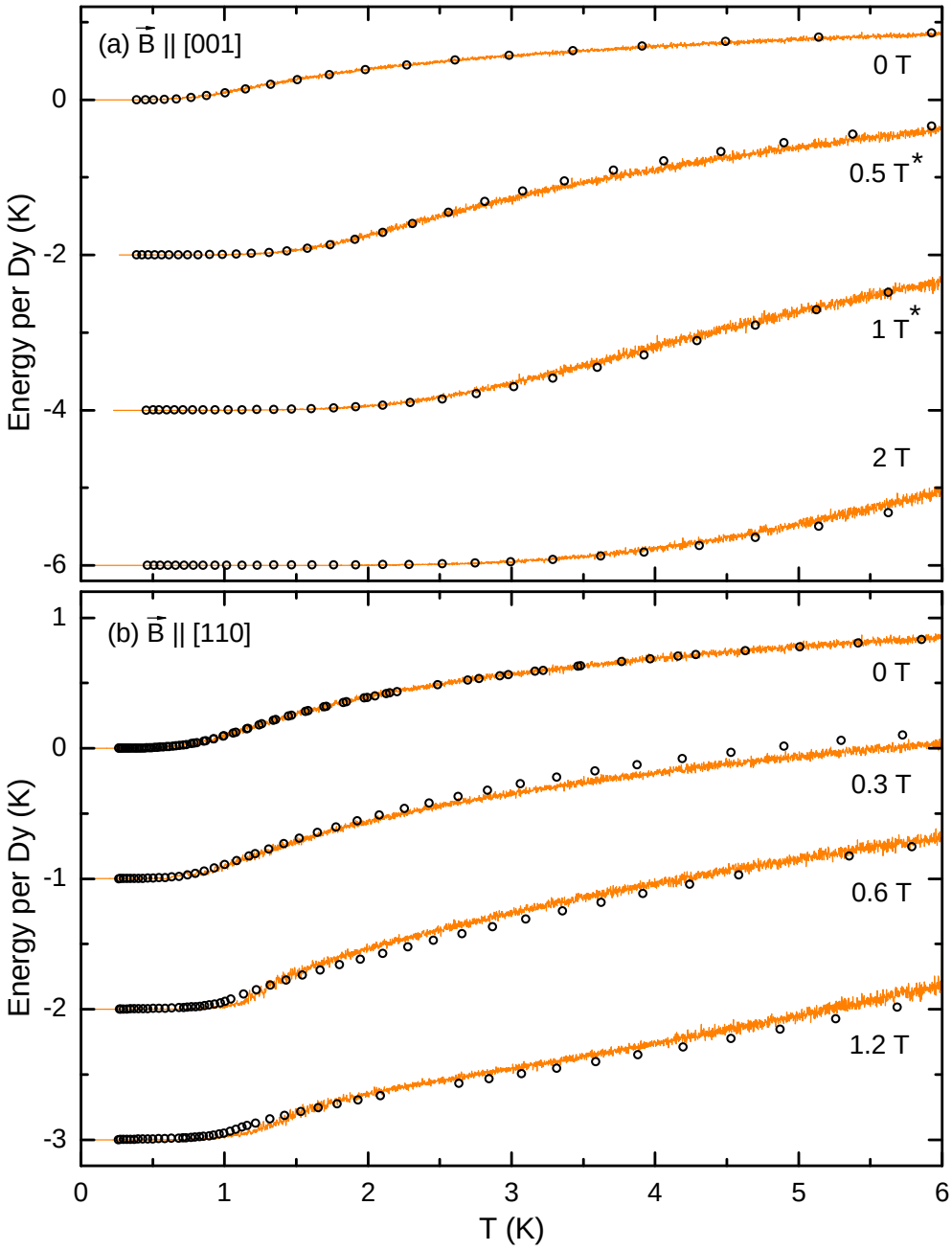

Figure 4.19: Simulated temperature dependence of the energy per Dy ion for magnetic fields parallel to (a) [001] and (b) [110] (orange line). The black circles depict experimental data, obtained by integrating the measured specific heat (from [124] and [151] for $\vec{B} \,||\, [001]$ and $\vec{B} \,||\, [110]$, respectively). The different curves are shifted with respect to each other.

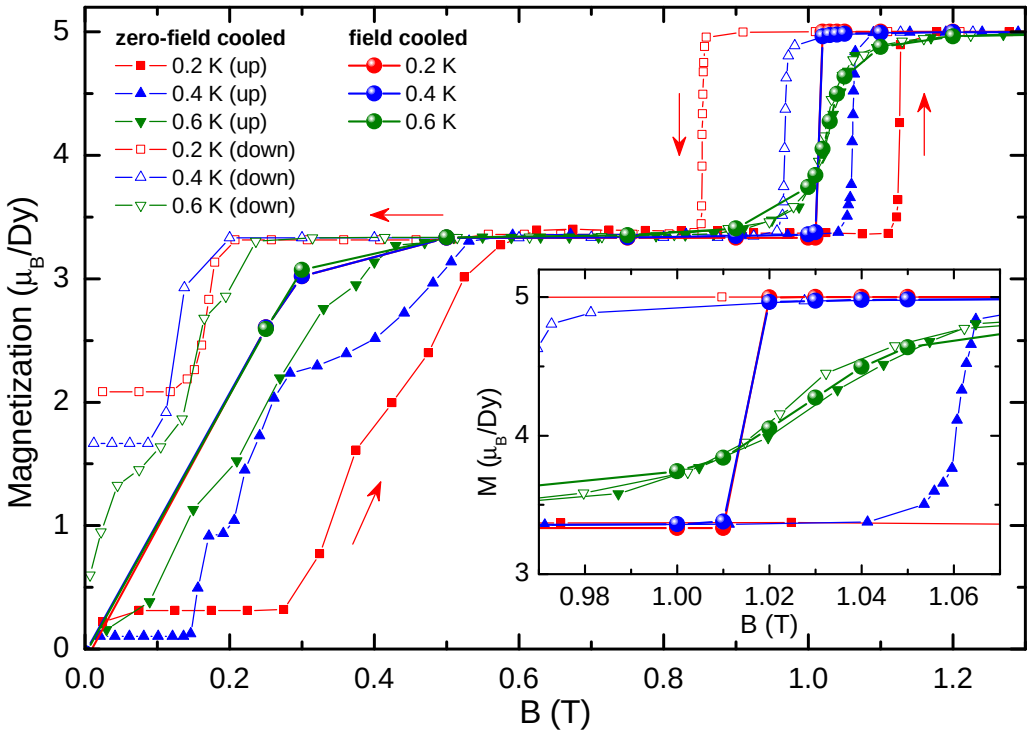

Figure 4.20: Simulations of the magnetic-field dependence of the magnetization of the dipolar spin ice at temperatures between 0.2 K and 0.6 K. The field-cooled data were obtained by slowly cooling the spin ice at a certain fixed magnetic field. The zero-field-cooled data were obtained by first cooling in zero field, followed by a simulation with increasing field (up), and subsequently with decreasing field (down). The inset shows an enlargement of the region around the transition at 1 T.

energy of a single spin flip is not sufficiently large to rearrange the spins in order to achieve the energetically most favorable state. This would require a large number of simultaneous spins flips. This hysteresis at 1 T is not observed in experiments, at least not for temperatures above 0.2 K.[19] The correct field-induced ground state can be achieved by slowly cooling in the presence of a constant magnetic field. Below 0.6 K, the simulated field-cooled magnetization data (circles in Fig. 4.20) show a sharp step at $\sim 1\,\mathrm{T}$. For higher temperatures, this step broadens and the hysteresis observed for the zero-field cooled data vanishes. This indicates that the system stays in thermal equilibrium when changing the magnetic field above 0.6 K. The hysteresis at low fields in Fig. 4.20 is, indeed, observed in experimental data. This meta-stable magnetization leads to a ferromagnetic-like hysteretic magnetization $M(B)$ [145].

A possible explanation for the out-of-equilibrium processes and, thus, the phe-

[19] In Ref. [125], a slight hysteresis was observed for lower temperatures.

nomenon of slow dynamics at low temperatures (Sec. 4.1.5) is the small number of thermally excited monopoles in the low-temperature region (Sec. 4.2.2). Within a model considering only single-spin-flip processes, a rearrangement of the spin system is only possible in the presence of monopoles (topological defects). If simultaneous spin flips are forbidden, a 2in-2out tetrahedron only can change into another 2in-2out configuration when a monopole passes through it. As a consequence, the magnetic system needs more time to relax into thermal equilibrium the smaller the monopole number is.

Note, that the simulation algorithm makes no assertion about the absolute time scale. Thus, the slow-dynamic behavior (Sec. 4.1.5) can only be explained on a qualitative level. At very low temperatures, moreover, finite-size effects of the simulated lattice become more and more crucial as it can actually happen that no monopoles are present at all. If this happens, one has to wait until a monopole is created due to thermal fluctuations, which becomes more unlikely the lower the temperature is.

Monopole Density

After each simulation step, the number of tetrahedra with a particular configuration is counted. The 16 types of single-tetrahedron configurations are classified into three different subsets representing the energetically equivalent configurations (in zero field). In this sense, all tetrahedra with configuration 3in-1out or 1in-3out are summarized as 3in-1out (monopoles) as a collective term. Both remaining configurations 4in-0out and 0in-4out are summarized as 4in-0out.

Fig. 4.21 shows the density of each tetrahedron class calculated by different theoretical approaches. The light-green, the light-blue, and the orange data are simulations of the effective nearest-neighbor (nn) spin-ice model. The dashed lines are calculations of the single-tetrahedron approximation, which perfectly agree with the nearest-neighbor simulations. The dark-green, the red, and the dark-blue data are simulations of the dipolar spin ice. As already mentioned, the 4in-0out tetrahedron density is rather small and can be neglected at low temperatures. For temperatures above 5 K, the spin ice is dominated only by the nearest-neighbor interaction, whereas the long-range interaction does not play an essential role. Here, the 2in-2out and the (thermally excited) 3in-1out tetrahedra are almost equally distributed. In the low-temperature regime, the long-range interaction stabilizes the 2in-2out ground state. The monopoles are more rarefied compared to the density one would expect from nearest-neighbor interaction only. At 1 K, the monopole density is about 5% but increases for higher temperatures. For lower temperatures, the monopole density rapidly decreases. For very low temperatures ($T \to 0$), the dipolar spin-ice model results in the same ground state as the nearest-neighbor model, *i.e.* the spin ice consists only of 2in-2out tetrahedra. Therefore, one can conclude that the long-range interaction does not affect the residual entropy (Sec. 4.1.2).

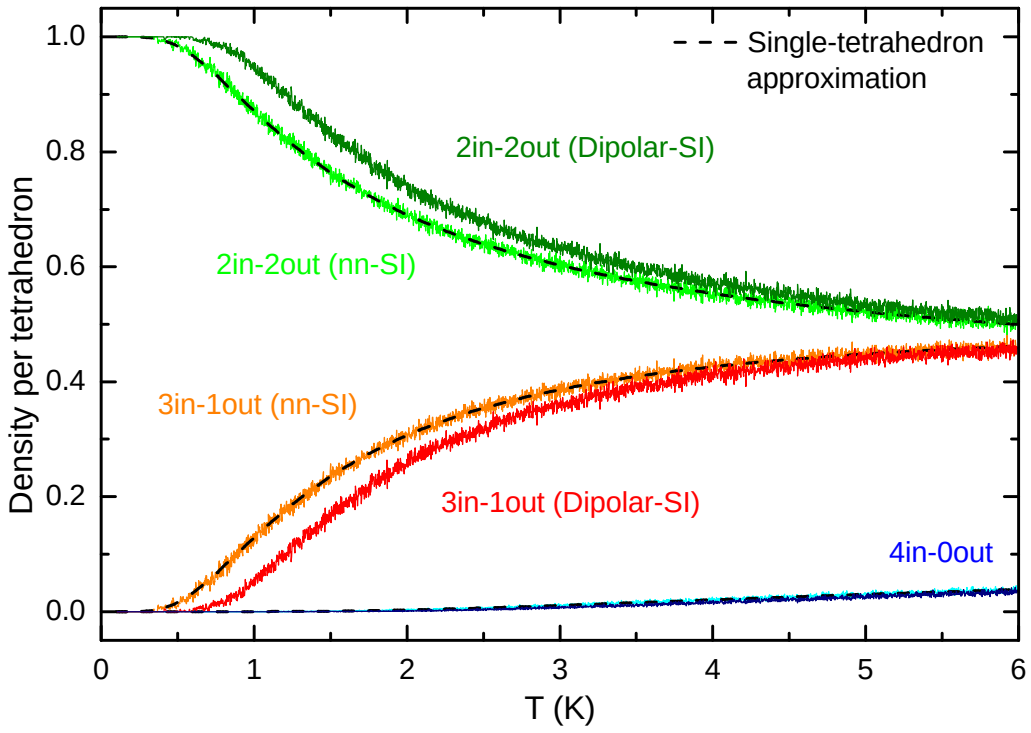

Figure 4.21: Temperature-dependent density of the different spin configurations for nearest-neighbor (nn) and for dipolar spin-ice simulations as well as for the single-tetrahedron approximation.

$(Dy_{1-x}Y_x)_2Ti_2O_7$

In $(Dy_{1-x}Y_x)_2Ti_2O_7$, magnetic Dy ions are partially replaced by non-magnetic Y ions. The non-magnetic reference compound $Y_2Ti_2O_7$ can be regarded as the high-doping limit of $(Dy_{1-x}Y_x)_2Ti_2O_7$. Low doping with Y should only produce spatially dilute defects of the pyrochlore lattice, and the spin-ice properties, as introduced in the previous paragraphs, should hardly be affected. $(Dy_{1-x}Y_x)_2Ti_2O_7$ in the low-doping limit is called "dilute spin ice". With increasing doping level, the correlation of the remaining magnetic ions should decay. As a consequence, $(Dy_{1-x}Y_x)_2Ti_2O_7$ should behave more and more like a usual paramagnet.

The influence of the doping level can be investigated by simulating the magnetic-field dependence of the magnetization $M(B)$ for $\vec{B} \,||\, [111]$. For this particular field direction, the correlation of the magnetic moments leads to a plateau in the magnetization data followed by a sharp steplike increase at 1 T. The step around 1 T is very sharp at lowest temperatures and broadens at higher temperatures (Figs. 4.15 and 4.20 on page 56 and 62, respectively). The field dependence of the simulated magnetization for $\vec{B} \,||\, [111]$ is shown in Fig. 4.22 for a variety of doping levels at a fixed temperature of 0.4 K.

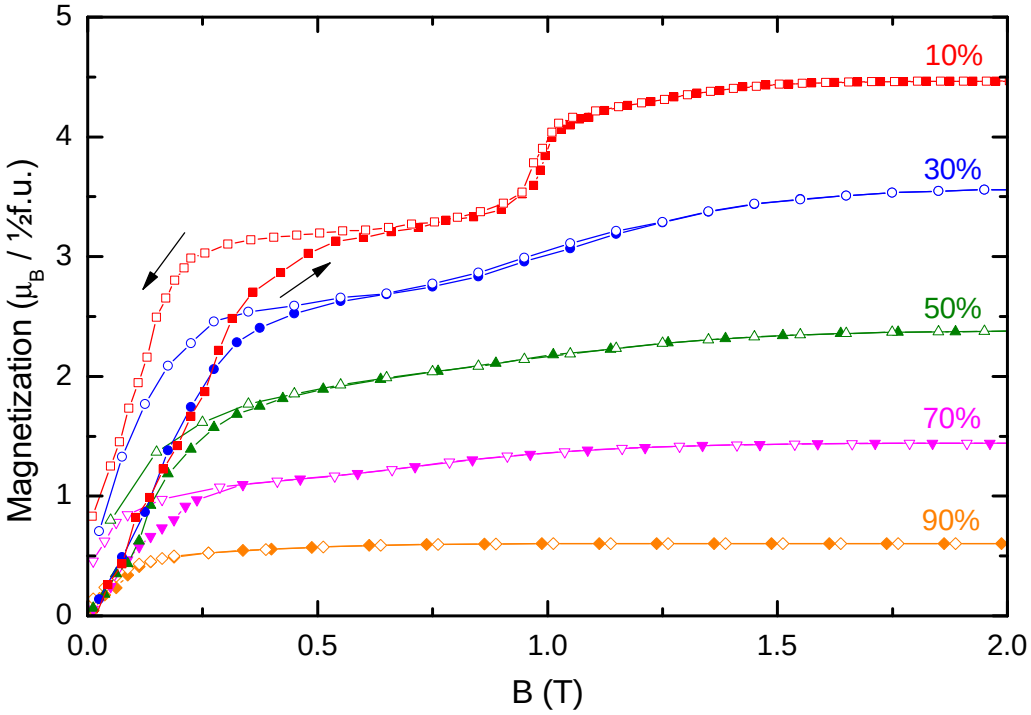

Figure 4.22: Field dependence of the magnetization of $(Dy_{1-x}Y_x)_2Ti_2O_7$ for $\vec{B} \,||\, [111]$ and doping levels x between 10% and 90%. The data were obtained by simulations of the dipolar spin ice. The unit of the magnetization is related to the lattice site, *i.e.* to the sum of magnetic and non-magnetic ions (1/2 f.u.). The arrows indicate the hysteretic behavior exemplary for $x = 10\%$.

In the low-doping case ($x = 10\%$), the simulated magnetization shows a behavior similar to the undoped compound $Dy_2Ti_2O_7$. The sharp feature at 1 T is broadened weakly. Note, that the hysteresis at 1 T completely vanishes already in the low-doping case. The hysteresis in $M(B)$ for low fields, however, is conserved, even for high doping. With increasing doping, the spin-ice features of the magnetization die out very fast and $(Dy_{1-x}Y_x)_2Ti_2O_7$ behaves more and more like a usual paramagnet, as expected.

Fig. 4.23 shows the influence of Y doping on the residual entropy. The data are obtained by simulating the Y-doped dipolar spin ice. The entropy $S(T)$ is calculated by integration of $c(T)/T$. The specific heat $c(T)$ is obtained by differentiating the energy of the magnetic system in $(Dy_{1-x}Y_x)_2Ti_2O_7$. The residual entropy ΔS is the difference between the high-temperature limit of $S(T)$ and the entropy $R \ln 2$ of a two-level system. The inset of Fig. 4.23 shows the residual entropy ΔS of $(Dy_{1-x}Y_x)_2Ti_2O_7$ as a function of the doping level x. ΔS decreases nearly linearly with increasing x and practically vanishes for $x = 90\%$. Note, that the entropy data in Fig. 4.23 are simulated only up to 6 K. At least in the

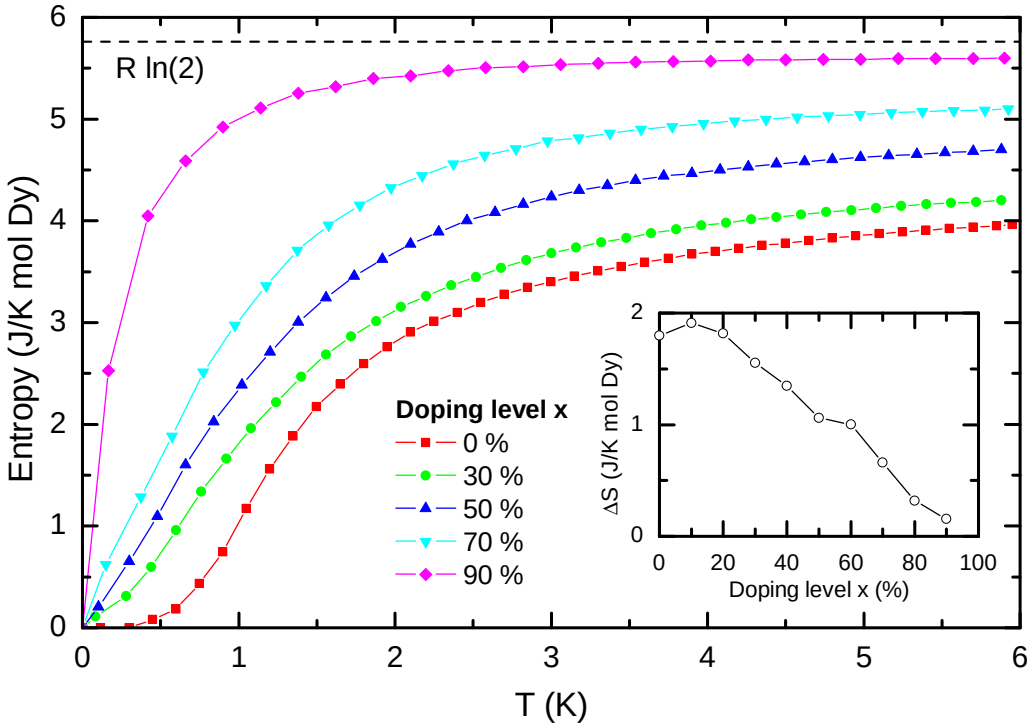

Figure 4.23: Entropy of $(Dy_{1-x}Y_x)_2Ti_2O_7$ for various doping levels x. The data were obtained by simulations of the Y-doped dipolar spin ice. The inset shows the residual entropy ΔS as a function of the doping level x.

low-doping limit, $S(T)$ is not saturated at 6 K. Thus, the ΔS data is slightly overestimated for low doping.

In sum, one can tune the spin-ice behavior by varying the doping level x. In Secs. 4.4.2, 4.5.2, and 4.6.2, the half-doped $(Dy_{0.5}Y_{0.5})_2Ti_2O_7$ (*i.e.* $x = 50\%$) is investigated as a magnetic reference system with strongly suppressed spin-ice signatures. The advantage of this particular doping level is that although the spin-ice system is strongly disturbed, the sample remains strongly magnetic. Therefore, this doped compound will be used to analyze magnetic-field dependent properties of $Dy_2Ti_2O_7$ which do not originate from the magnetic spin-ice system.

4.2.3 Debye-Hückel Theory

An alternative theoretical approach to describe the spin-ice model makes use of the framework of the Debye-Hückel theory [161, 162]. This theory describes the electrostatic interaction of charged particles in an electrolyte solution. Within the monopole picture, the excited tetrahedra (3in-1out and 1in-3out) are supposed to act like particles carrying an elementary magnetic charge (Sec. 4.1.3). Within this framework, the Debye-Hückel theory is implemented by replacing the

electric charges by magnetic charges (monopoles). A detailed review of the applicability of the Debye-Hückel theory on the spin ice can be found in Ref. [134]. In this chapter, the essential points of the discussion in Ref. [134] will be briefly summarized.

The Debye-Hückel Hamiltonian reads

$$H = \frac{\mu_0}{4\pi} \sum_{i<j} \frac{q_i q_j}{r_{ij}} + \Delta \sum_i \left(\frac{q_i}{2\mu/a_\mathrm{d}} \right)^2 \quad \text{where} \quad q = \pm \frac{2\mu}{a_\mathrm{d}} \,. \tag{4.19}$$

The first term describes the Coulomb interaction between particles carrying an elementary magnetic charge q and Δ is the energy cost of an isolated monopole. First, an expression for the monopole density per tetrahedron in the absence of a Coulomb-like interaction (non-interacting monopoles) is obtained by minimizing the free energy per tetrahedron $U/N_\mathrm{t} = \rho\Delta$,

$$\rho_\mathrm{nn} = \frac{2\exp(-\Delta/T)}{1+2\exp(-\Delta/T)} \,. \tag{4.20}$$

The energy cost of creating a monopole $\Delta = 4.35\,\mathrm{K}$ can be estimated by the nearest-neighbor coupling [134]. In contrast to Eq. (4.20), the monopole density per tetrahedron including Debye-Hückel contributions (interacting monopoles) cannot be written as an analytical expression. The Debye-Hückel monopole density can only be numerically calculated via the following recursive approach

$$\begin{aligned} \rho_0 &= \rho_\mathrm{nn} = \frac{2\exp(-\Delta/T)}{1+2\exp(-\Delta/T)} \\ \rho_{\ell+1} &= \frac{2\exp\left[-\left(\frac{\Delta}{T} - \frac{E_\mathrm{nn}}{2T}\frac{\alpha\sqrt{\rho_\ell}}{1+\alpha\sqrt{\rho_\ell}}\right)\right]}{1+2\exp\left[-\left(\frac{\Delta}{T} - \frac{E_\mathrm{nn}}{2T}\frac{\alpha\sqrt{\rho_\ell}}{1+\alpha\sqrt{\rho_\ell}}\right)\right]} \end{aligned} \tag{4.21}$$

$$\alpha(T) = \sqrt{\frac{3\sqrt{3}\pi E_\mathrm{nn}}{2T}} \quad \text{and} \quad E_\mathrm{nn} = \frac{\mu_0 q^2}{4\pi a_\mathrm{d} k_\mathrm{B}} \,, \tag{4.22}$$

where $q = 2\mu/a_\mathrm{d}$ is the magnitude of the monopole charge, $\mu = 10\mu_\mathrm{B}$ is the magnetic moment of a Dy ion, and $a_\mathrm{d} = 4.34\,\text{Å}$ is the distance between two neighboring tetrahedra. Eq. (4.21) converges to the Debye-Hückel monopole density ρ_DH, where it turns out that one obtains a suitable accuracy after 5 steps [134], *i.e.*

$$\rho_\mathrm{DH} = \rho_{\ell\to\infty} \simeq \rho_5 \,. \tag{4.23}$$

Fig. 4.24 compares the monopole density per tetrahedron for different theoretical models with numerical simulations of the dipolar spin ice (Sec. 4.2.2). At temperatures below $\sim 1.5\,\mathrm{K}$, the density calculated via the Debye-Hückel the-

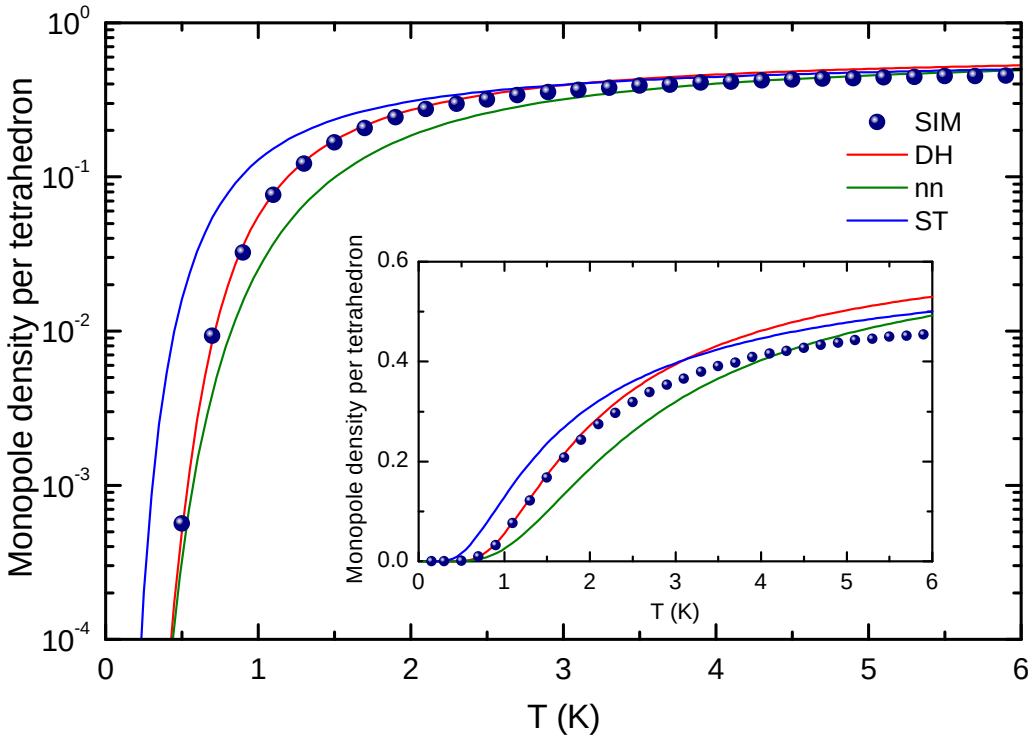

Figure 4.24: Comparison of the monopole density per tetrahedron, obtained by numerical simulation (SIM) of the dipolar spin ice with the density, calculated with Debye-Hückel theory (DH), the theory of non-interacting (nn) monopoles, and the single-tetrahedron (ST) approximation, respectively. The inset shows the same data on a linear scale.

ory almost perfectly matches the numerical simulation, whereas the model of non-interacting monopoles and the single-tetrahedron approximation yield very poor agreement. At higher temperatures, however, none of the models describes the spin ice properly (inset of Fig. 4.24). In Ref. [134], the authors argue that the Debye-Hückel theory can only be applied for temperatures below $\sim 1\,\mathrm{K}$ as the screening length becomes shorter than the lattice spacing at higher temperatures.

Within the Debye-Hückel theory, one can calculate the specific heat via

$$c_{\mathrm{DH}} = -RT\frac{\partial^2}{\partial T^2}\left(\frac{F}{N_{\mathrm{s}}k_{\mathrm{B}}}\right) \tag{4.24}$$

with the Debye-Hückel free energy per spin

$$\begin{aligned}\frac{F}{N_{\mathrm{s}}k_{\mathrm{B}}} &= \frac{\rho}{2}\Delta + \frac{T\rho}{2}\ln\left(\frac{\rho/2}{1-\rho}\right) + \frac{T}{2}\ln(1-\rho) \\ &\quad -\frac{T}{3\sqrt{3}\pi}\left\{\frac{\alpha^2(T)\rho}{2} - \alpha(T)\sqrt{\rho} + \ln\left[1+\alpha(T)\sqrt{\rho}\right]\right\}, \end{aligned} \tag{4.25}$$

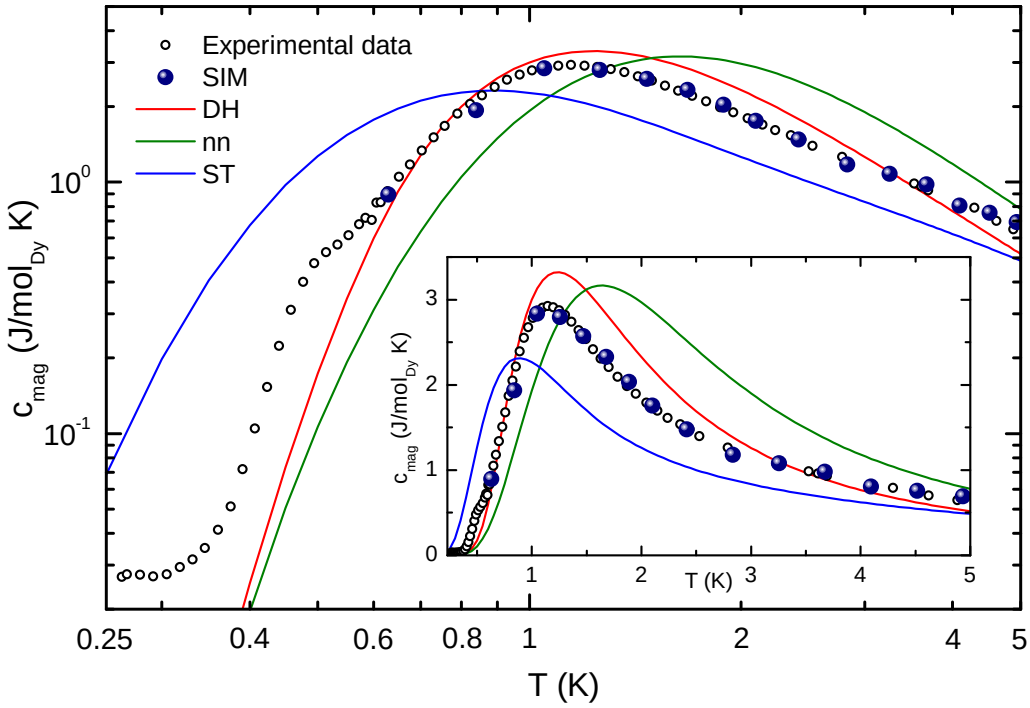

Figure 4.25: Comparison of experimental data of the specific heat [151] with theoretical data obtained by numerical simulations (SIM), Debye-Hückel (DH), non-interacting monopoles (nn), and the single-tetrahedron approximation (ST). The specific-heat data is scaled by 10%. The inset shows the same data on a linear scale.

where $\alpha(T)$ and E_{nn} are given by Eq. (4.22). Fig. 4.25 compares the experimental data of the magnetic specific heat c_{mag} (open black circles [151]) with the theoretical approaches introduced in this chapter. The specific-heat data were scaled by 10% to adjust the measurements to literature data [124]. The numerical simulation perfectly matches the experimental data in the whole temperature range. Below 0.6 K, however, the specific heat could not be calculated due to finite-size effects of the simulated lattice (*cf.* discussion in Sec. 4.2.2). The theoretical curves obtained by Debye-Hückel (DH), non-interacting monopoles (nn), and the single-tetrahedron approximation (ST) describe the measured specific heat only on a qualitative level (*cf.* discussion above). The best agreement of theory and experimental data is provided by the Debye-Hückel model between $\sim 0.6\,\mathrm{K}$ and $\sim 1\,\mathrm{K}$. In the temperature range below 0.6 K, the spin ice enters a region of slow dynamics (Sec. 4.1.5). Here, theory and experiments strongly deviate.

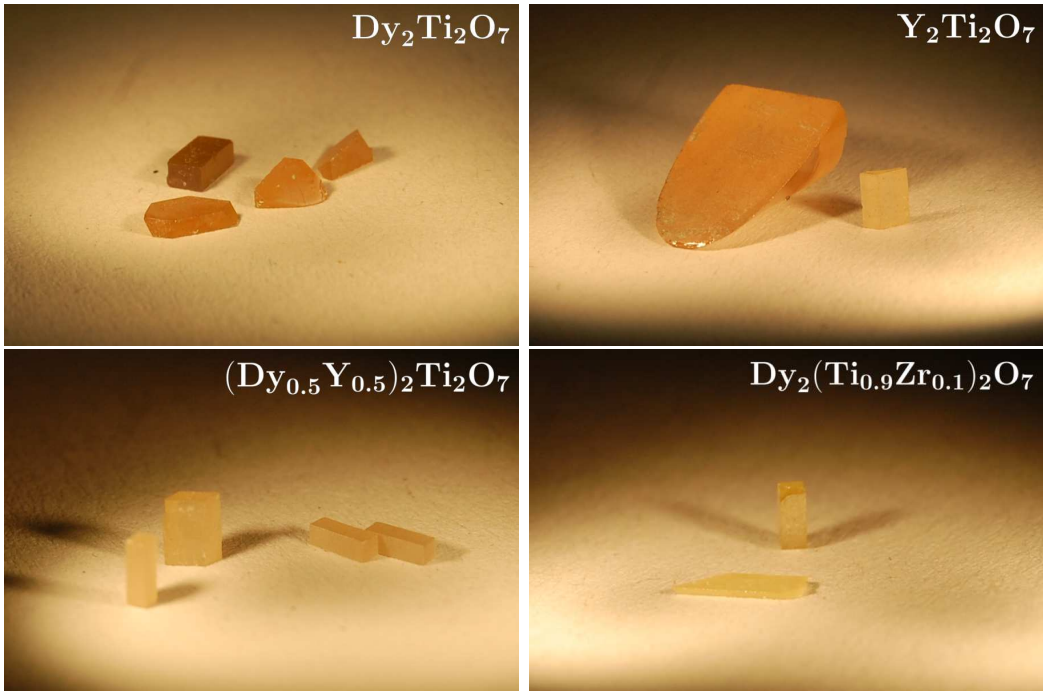

Figure 4.26: Single crystals of $Dy_2Ti_2O_7$, $Y_2Ti_2O_7$, $(Dy_{0.5}Y_{0.5})_2Ti_2O_7$, and $Dy_2(Ti_{0.9}Zr_{0.1})_2O_7$.

4.3 Samples and Characterization

The measurements presented in this chapter were done on single crystals grown by M. Valldor and J. Frielingsdorf [163]. For the crystal growth, a floating zone technique was applied inside a mirror image furnace to acquire centimeter sized crystals. To obtain crystals without cracks, the floating zone was run twice trough the bars. The pale yellow crystals exhibit high reflectance at a grazing angle but otherwise full transparency. $Dy_2Ti_2O_7$ is slightly more yellow than the other compounds $Y_2Ti_2O_7$, $(Dy_{0.5}Y_{0.5})_2Ti_2O_7$, and $Dy_2(Ti_{0.9}Zr_{0.1})_2O_7$.

Magnetization and magnetostriction measurements shown in the following chapters were done by M. Hiertz on single crystals obtained from the same bars as the crystals used for thermal-conductivity measurements, which will be presented in the following chapters. Details of the magnetization and magnetostriction measurements can be found in Ref. [84].

The thermal conductivity of the compounds presented in this chapter were measured on two different sample-geometry types. Samples of type I (Fig. 4.27(a)) are rectangular with the long edge parallel to [111]. Fig. 4.27(b) shows sample type II. This sample type is bar shaped with the long edge parallel to $[1\bar{1}0]$. The cross section is a parallelogram with an angle of 55°. The surfaces of this sample are orientated along $[1\bar{1}0]$, [111], and [001]. Thus, one can easily

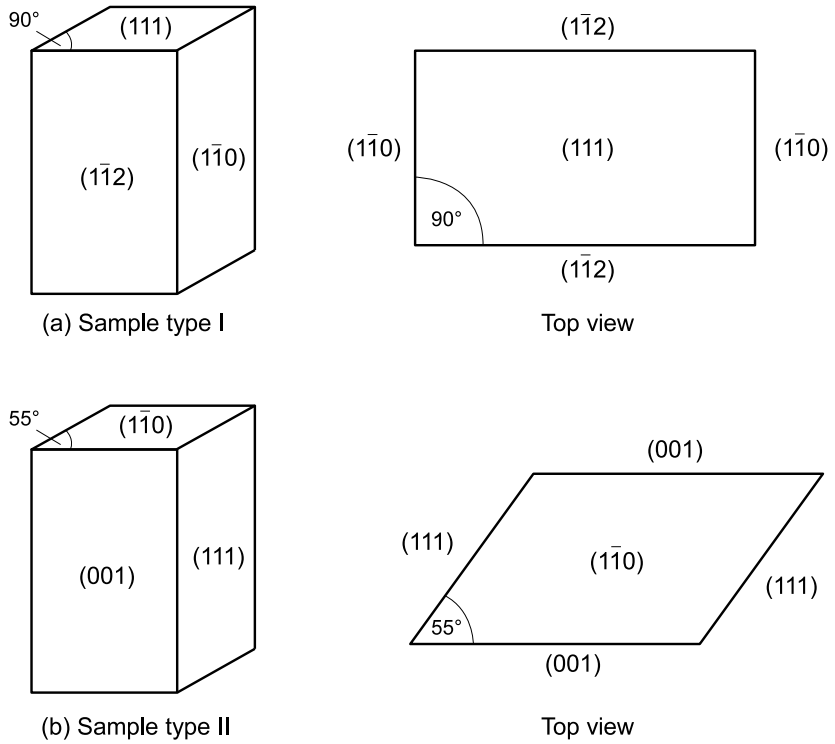

Figure 4.27: Geometry types of samples used for thermal-conductivity measurements on $Dy_2Ti_2O_7$, $Y_2Ti_2O_7$, $(Dy_{1-x}Y_x)_2Ti_2O_7$, and $Dy_2(Ti_{0.9}Zr_{0.1})_2O_7$.

apply the external magnetic field along one of these directions (perpendicular to the respective surfaces). This sample type is used for thermal-conductivity measurements along $[1\bar{1}0]$.

4.3.1 $Dy_2Ti_2O_7$

Literature Data

For $Dy_2Ti_2O_7$, several articles presenting magnetization data were published. Here, a brief overview is given. In Ref. [145], the magnetic-field dependence of the magnetization was measured on a polycrystalline sample at temperatures below 1 K. In the presented temperature range, the magnetization saturates above $\sim 0.5\,\mathrm{T}$. Below 0.65 K, the magnetization is strongly hysteretic and shows a ferromagnetic-like behavior. Most likely, this originates from the slow-dynamic behavior of the spin ice at low temperatures (Sec. 4.1.5). Similar results were reported for the Ho-based spin-ice compounds $Ho_2Sn_2O_7$ and $Ho_2Ti_2O_7$ [164].

An overview of the magnetization $M(B)$ of $Dy_2Ti_2O_7$ measured on single crystals for different magnetic-field directions has been published in [165]. Fig. 4.28 shows the magnetization at a temperature of 1.8 K. The theoretically expected

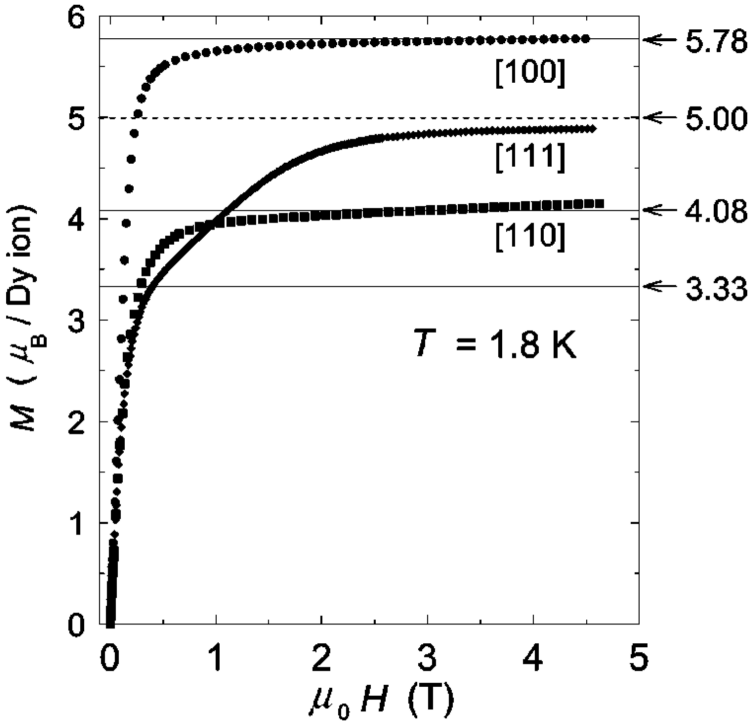

Figure 4.28: Comparison of the magnetization $M(B)$ for different magnetic-field directions at $T = 1.8\,\mathrm{K}$ (taken from [165]). The values at the right hand side depict the theoretically obtained saturation values of the magnetization for the different field directions.

saturation values for the different field directions (right hand side of Fig. 4.28) can be calculated via the single-tetrahedron approximation (Sec. 4.2.1).

Magnetization data of $Dy_2Ti_2O_7$ for $\vec{B} \,||\, [001]$ below 1.8 K were presented in Ref. [130]. Unfortunately, only measurements with increasing magnetic field are presented there. The corresponding magnetization data presented in this thesis (Figs. 4.30 and 4.33) clearly show a hysteretic behavior at temperatures below 0.6 K.

The magnetization of $Dy_2Ti_2O_7$ for $\vec{B} \,||\, [111]$ was presented in Refs. [124, 125, 149] (Fig. 4.29). At low temperatures, $M(B)$ exhibits a plateau followed by a sharp steplike increase at 1 T, which is broadened at higher temperatures (Fig. 4.28). In Ref. [125], the anomaly at 1 T is interpreted as a first-order liquid-gas transition of the monopole excitations with a critical endpoint at 0.36 K. In addition, one can clearly observe a hysteresis below 0.6 K which, most likely, has the same origin as the hysteresis for $\vec{B} \,||\, [001]$.

To my knowledge, up to now, no magnetization data of $Dy_2Ti_2O_7$ for $\vec{B} \,||\, [110]$ in the low-temperature regime has been published.

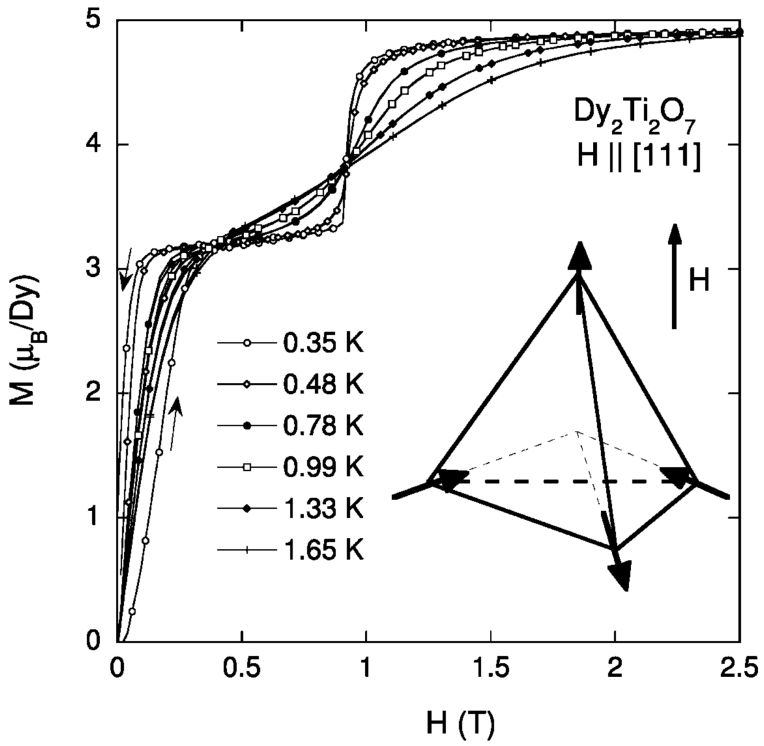

Figure 4.29: Magnetization of $Dy_2Ti_2O_7$ for $\vec{B} \,||\, [111]$ (taken from [125]).

Magnetization

All field-dependent magnetization measurements presented here were performed after slowly cooling in zero-field. Fig. 4.30 shows the field-dependence of the magnetization $M(B)$ of $Dy_2Ti_2O_7$ for $\vec{B} \,||\, [001]$ at temperatures between 0.4 K and 2 K. In the considered temperature range, the magnetization reaches the theoretically predicted saturation value of $\sim 5.7\,\mu_B$/Dy. This saturation value corresponds to a fully polarized spin ice which consists of only one type of 2in-2out configuration. When lowering the temperature, the increase towards saturation becomes steeper. In the slow-dynamic regime below $\sim 0.6\,$K, $M(B)$ exhibits a clear hysteresis which becomes wider the lower the temperature is.

The magnetization data for $\vec{B} \,||\, [111]$ (Fig. 4.31) nicely reproduces the literature data shown in Fig. 4.29. The discontinuous jump of the 0.25 K curve at $\sim 0.2\,$T (up, closed red squares) most likely originates from a too large sweeping rate (0.02 T/min). This effect was also observed in Ref. [166] and is discussed for $\vec{B} \,||\, [001]$ in the following paragraph. On the plateau below 1 T, the triangular planes of the pyrochlore lattice are polarized. Within the Kagomé planes, one spin per triangle points parallel to the magnetic field and the other two point antiparallel to $\vec{B}$. This 3-fold-degenerate ground state is called Kagomé-ice state. All these three tetrahedron configurations have the same magnetization component

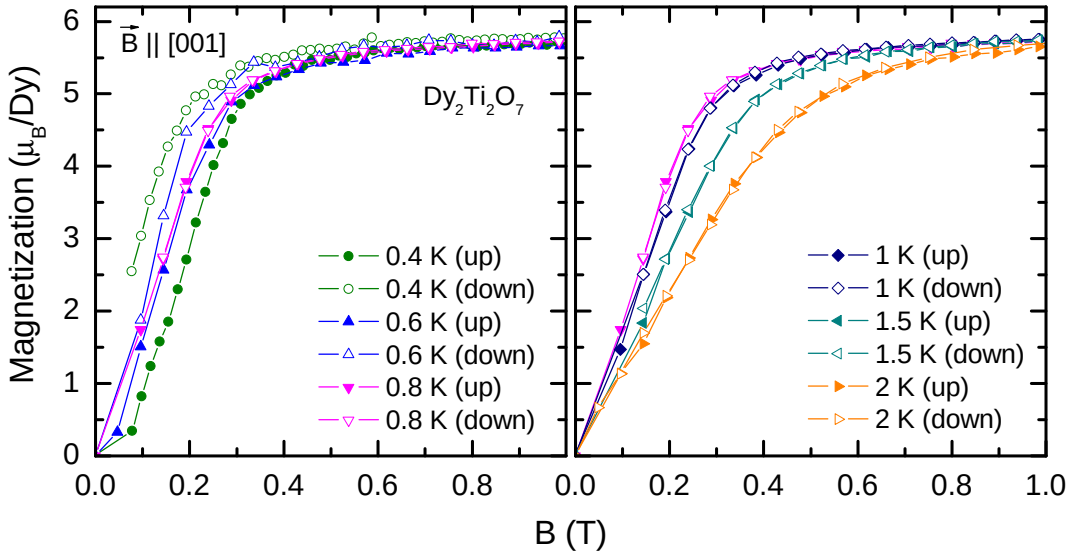

Figure 4.30: Magnetization of $Dy_2Ti_2O_7$ for $\vec{B} \,||\, [001]$.

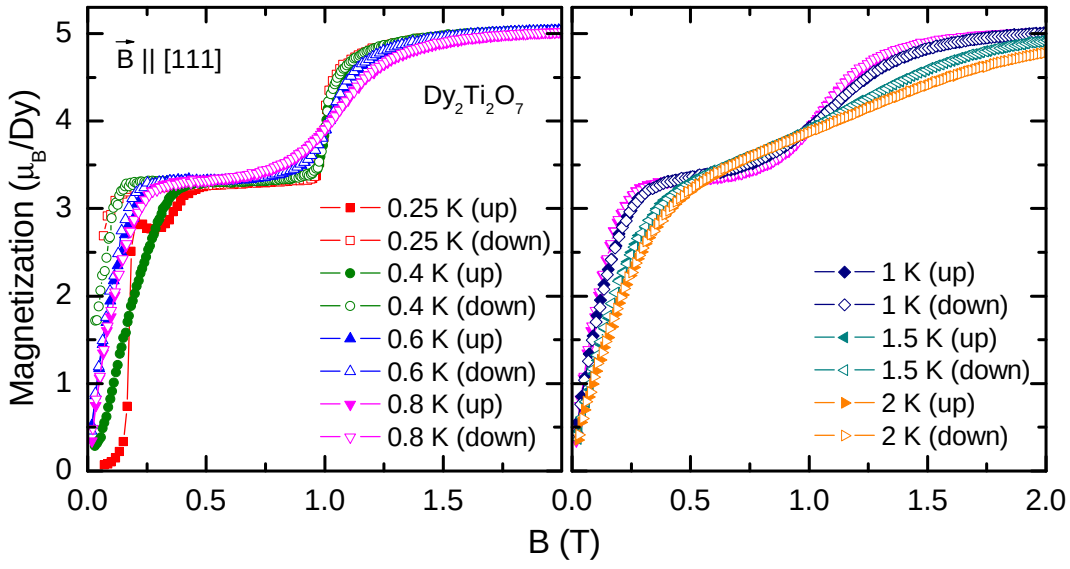

Figure 4.31: Magnetization of $Dy_2Ti_2O_7$ for $\vec{B} \,||\, [111]$.

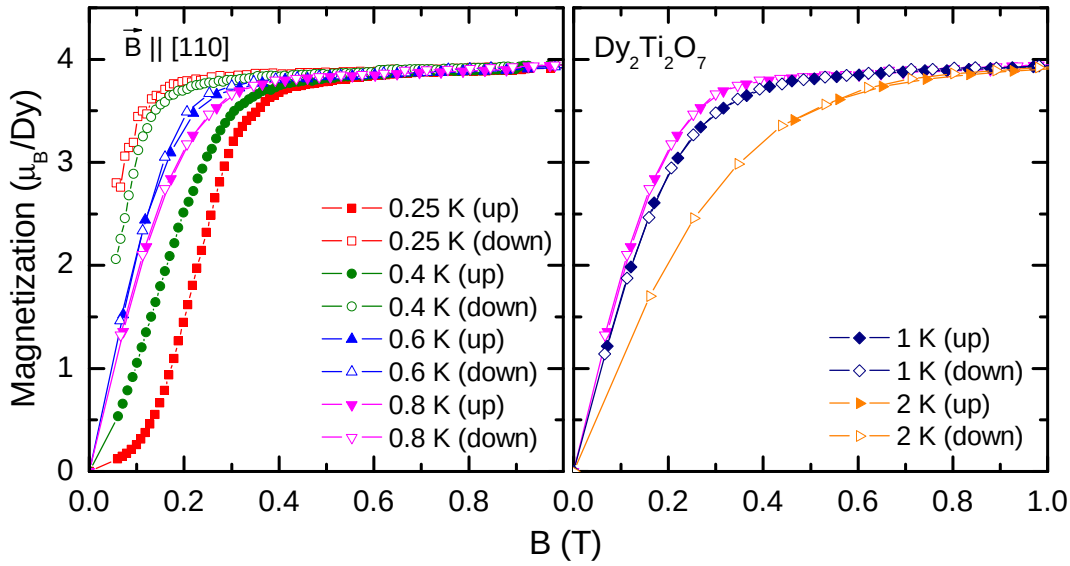

Figure 4.32: Magnetization of $Dy_2Ti_2O_7$ for $\vec{B} \,||\, [110]$.

parallel to $\vec{B}$, namely $3.33\,\mu_B$/Dy. Thus, from the magnetization data only, one cannot distinguish these three tetrahedron configurations. The saturation value of $5\,\mu_B$/Dy corresponds to the non-degenerate ground state above 1 T. Here, all tetrahedra have an alternating spin configuration 3in-1out or 1in-3out.

Fig. 4.32 shows the magnetization of $Dy_2Ti_2O_7$ for $\vec{B} \,||\, [110]$. $M(B)$ reaches the saturation value $4\,\mu_B$/Dy, close to the theoretically expected value of $4.08\,\mu_B$/Dy. The saturation value corresponds to a 2-fold-degenerate ground state. Two spins per tetrahedron are perpendicular to $\vec{B}$ and, thus, have no magnetization component. The data are very similar to the data obtained for $\vec{B} \,||\, [001]$. In the region of slow dynamics below 0.6 K, $M(B)$ is hysteretic with respect to the field-sweep direction. The hysteresis width increases with decreasing temperatures.

Dependency on the Field Sweep Rate

In the low-field region, the magnetization is strongly hysteretic. The hysteresis width increases with decreasing temperature. At temperatures below ~ 0.3 K, the field-dependent magnetization $M(B)$ also strongly depends on the field sweep rate. Fig. 4.33 shows the magnetic-field dependence $M(B)$ at 0.25 K for $\vec{B} \,||\, [001]$. In order to obtain a smooth magnetization curve, the measurement has to be performed with a very slow field sweep rate of 0.003 T/min (red squares in the main panel). $Dy_2Ti_2O_7$ does not behave like a usual paramagnet for which the magnetization increase is expected to become sharper for lower temperatures. For $T \to 0$, the magnetization should actually jump discontinuously to the satu-

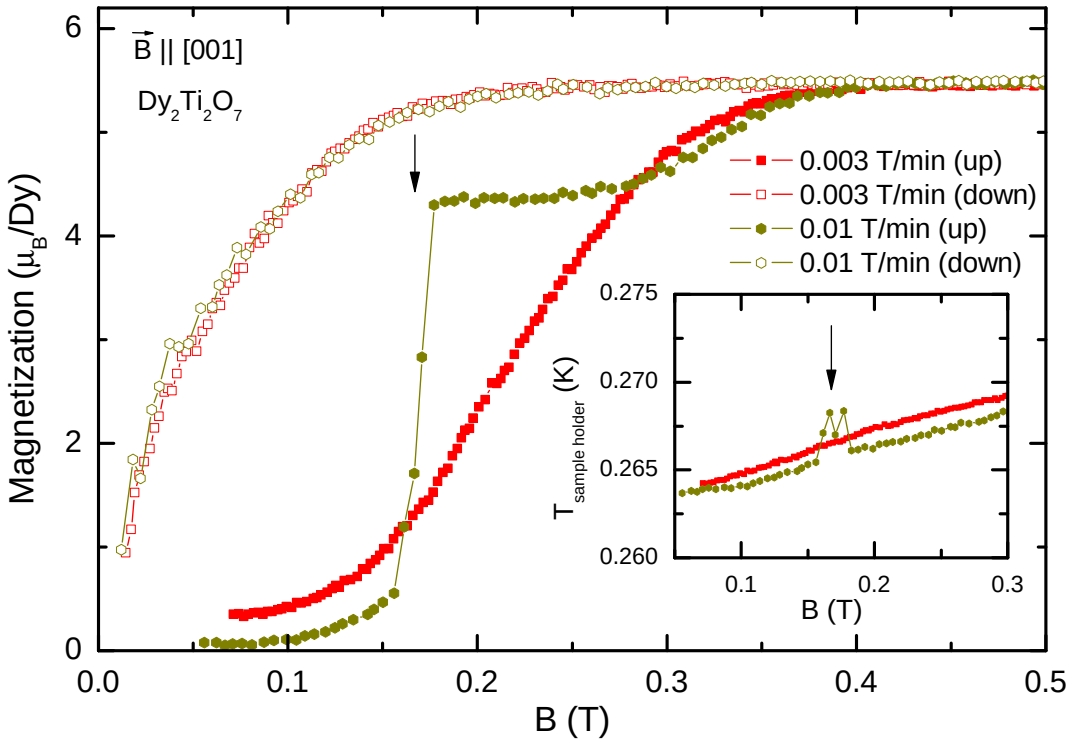

Figure 4.33: Magnetization of $Dy_2Ti_2O_7$ ($\vec{B} \,||\, [001]$) at 0.25 K for different field-sweep rates. Inset: Sample-holder temperature. The arrows within main panel and inset indicate corresponding magnetic fields.

ration value for an infinitesimally small magnetic field. Here, the magnetization remains almost zero up to a critical magnetic field. For higher fields, $M(B)$ increases towards saturation. When lowering the temperature, the critical field is shifted towards higher fields. For a paramagnet, one would expect the contrary.

For a larger sweep rate of 0.01 T/min (dark-yellow circles), $M(B)$ abruptly jumps to a value of $\sim 4.5\,\mu_B$/Dy at ~ 0.15 T and almost remains constant up to a certain field, where the curve joins up the dataset measured with slower rates. This discontinuous step in $M(B)$ is accompanied by an abrupt increase of the sample temperature which, immediately afterwards, decreases back to its initial value as the heat is dissipated to the bath (sample holder) (inset of Fig. 4.33). The temperature shown here is not the actual sample temperature as it is measured at the sample holder and not directly at the sample. In Ref. [166], similar measurements were presented where an additional thermometer was attached directly on the sample. The authors name this effect "thermal runaway" and report an increase of the sample temperature up to 0.6 K. Note, that the measurements with decreasing field do not depend on the sweep rate.

A possible explanation of this effect can be derived by energy considerations of the single-tetrahedron approximation (Sec. 4.2.1). For temperatures below

$\sim 0.4\,\mathrm{K}$, the dynamics of the magnetic system of $Dy_2Ti_2O_7$ freeze, *i.e.* the system is dominated by very long relaxation times. As the magnetization measurements shown in Fig. 4.33 were performed after cooling very slowly in zero magnetic field, the $M(B)$ curves start from a state consisting of equally distributed 2in-2out tetrahedra, *i.e.* the spin system stays in (or is at least very close to) a 6-fold degenerate ground state (Fig. 4.12). When increasing the magnetic field, the ground-state degeneracy is lifted, *i.e.* the energy levels split up. Due to large relaxation times, the system requires much time to reach the field-induced ground state. When changing the magnetic field too fast, a considerable number of 2in-2out tetrahedra remain in their energetically unfavorable state. As the energy gap increases with increasing field, the Zeeman energy piles up until these tetrahedra avalanche-like change into the energetically lower level by flipping one (or more) spin(s). This stored energy is transfered to the phononic system and, thus, results in a heating-up of the whole sample. In Fig. 4.33, this can be observed indirectly via the sample-holder temperature, which measures the bath temperature. In Ref. [166], temperatures up to $\sim 0.6\,\mathrm{K}$ were observed directly at the sample.

This also explains why this anomaly is not observed in the measurements with decreasing field. Coming from high fields, the system starts from a non-degenerate ground state. When approaching smaller fields, the energy gap to other 2in-2out configurations diminishes and, thus, other 2in-2out states are populated. As indicated by the hysteresis, this process is also suppressed due to the slow dynamic behavior in the frozen spin-ice state.

4.3.2 $(Dy_{0.5}Y_{0.5})_2Ti_2O_7$

The complete substitution of the magnetic Dy^{3+} ions in $Dy_2Ti_2O_7$ by non-magnetic Y^{3+} ions results in the non-magnetic reference compound $Y_2Ti_2O_7$, which is a non-magnetic phononic reference system to $Dy_2Ti_2O_7$. However, the influence of the magnetic-field on the phononic properties of $Dy_2Ti_2O_7$ cannot by studied by a non-magnetic compound like $Y_2Ti_2O_7$. In $(Dy_{0.5}Y_{0.5})_2Ti_2O_7$, 50% of the magnetic Dy ions are replaced by non-magnetic Y ions. This compound certainly remains magnetic. The spin-ice features, however, should be suppressed as, in average, two of the four Dy ions are missing in each tetrahedron. Numerical simulations (Sec. 4.2.2) predict the spin-ice features to die out when increasing the doping level x. In the following chapters, the thermal conductivity of $(Dy_{0.5}Y_{0.5})_2Ti_2O_7$ is studied as a magnetic reference compound to $Dy_2Ti_2O_7$ with suppressed spin-ice features. Concerning the heat transport, the idea is to suppress the magnetic contribution κ_{mag} while conserving the field-dependent phononic background κ_{ph}.

Fig. 4.34 shows the field-dependent magnetization $M(B)$ of $(Dy_{0.5}Y_{0.5})_2Ti_2O_7$ for $\vec{B}\,||\,[001]$ at various constant temperatures between 0.25 K and 2 K. The data show a paramagnetic-like behavior. The magnetization increases rapidly

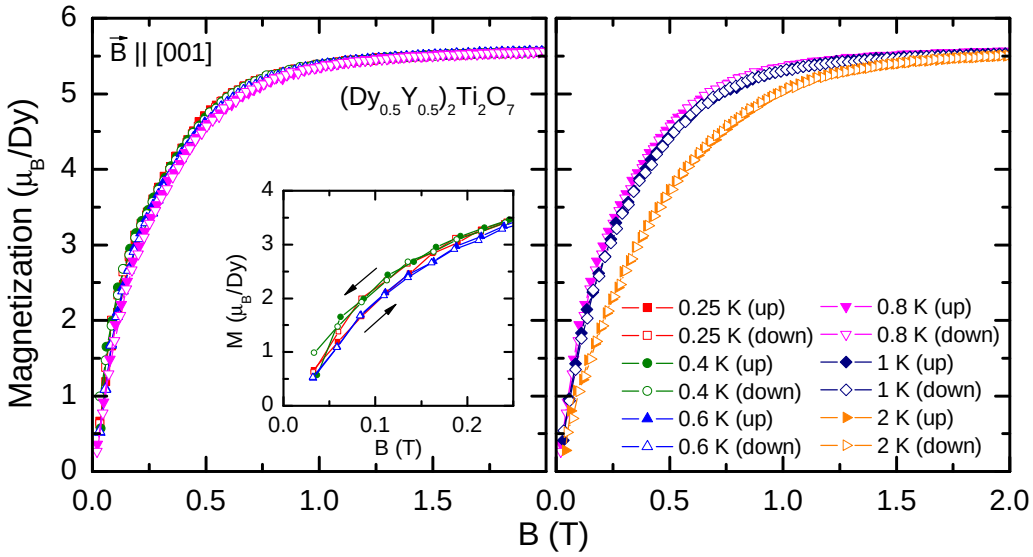

Figure 4.34: Magnetization of $(Dy_{0.5}Y_{0.5})_2Ti_2O_7$ for $\vec{B} \,||\, [001]$.

towards its saturation value of $\sim 5.6\,\mu_B$/Dy, close to the theoretically predicted value of $\sim 5.8\,\mu_B$/Dy. This increase sharpens towards lower temperatures. Below ~ 0.8 K, however, $M(B)$ is hardly temperature dependent. For a paramagnet, the tendency of the $M(B)$ curves to become sharper should be observable down to lowest temperatures. This shows that correlations between the Dy ions are still present in $(Dy_{0.5}Y_{0.5})_2Ti_2O_7$ and, hence, some spin-ice features should still be observable, even if (strongly) suppressed.

The main difference between the magnetization of $(Dy_{0.5}Y_{0.5})_2Ti_2O_7$ (Fig. 4.34) and of the mother compound $Dy_2Ti_2O_7$ (Fig. 4.33) is the absence of a hysteresis in $(Dy_{0.5}Y_{0.5})_2Ti_2O_7$. For $Dy_2Ti_2O_7$, a large hysteresis is observed in the magnetization data at lowest temperatures (0.25 K), which strongly depends on the field-sweep rate. As can be seen in the inset of Fig. 4.34, $M(B)$ of $(Dy_{0.5}Y_{0.5})_2Ti_2O_7$ exhibits no significant hysteresis, even at the lowest temperatures.

The magnetization $M(B)$ of $(Dy_{0.5}Y_{0.5})_2Ti_2O_7$ for $\vec{B} \,||\, [111]$ is illustrated in Fig. 4.35. The data show a small kink around 0.5 T, which, presumably, is a remain of the magnetization plateau observed in $Dy_2Ti_2O_7$ (Fig. 4.31 on page 74). The saturation magnetization of $\sim 4.8\,\mu_B$/Dy is close to the theoretical value of $5\,\mu_B$/Dy. The feature around 0.5 T is hardly temperature dependent below 0.8 K, analogous to the situation for $\vec{B} \,||\, [001]$ (discussed above). At lowest temperatures (inset of Fig. 4.35), a small hysteresis is observed, which is much less pronounced compared to the mother compound $Dy_2Ti_2O_7$ (Fig. 4.31). The steplike feature at 1 T in the $Dy_2Ti_2O_7$ data is missing in the $(Dy_{0.5}Y_{0.5})_2Ti_2O_7$ data. A small feature at 0.5 T, however, is still observable for $(Dy_{0.5}Y_{0.5})_2Ti_2O_7$. This is a

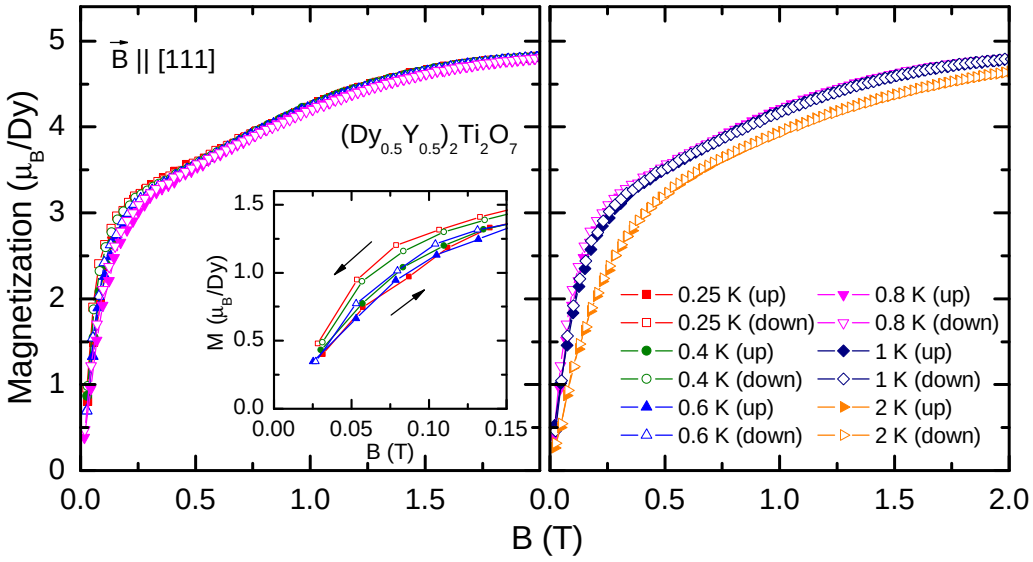

Figure 4.35: Magnetization of $(Dy_{0.5}Y_{0.5})_2Ti_2O_7$ for $\vec{B}\,||\,[111]$.

further indication that some spin-ice features still remain in $(Dy_{0.5}Y_{0.5})_2Ti_2O_7$, in particular, as the kink around 0.5 T is not observed for $\vec{B}\,||\,[001]$ (Fig. 4.34).

Fig. 4.36 illustrates the magnetization $M(B)$ of $(Dy_{0.5}Y_{0.5})_2Ti_2O_7$ for a magnetic field in [110] direction. The data have similarities to those for $\vec{B}\,||\,[001]$ (Fig. 4.34). They show a paramagnetic-like behavior with a saturation magnetization of $\sim 4\,\mu_B$/Dy, close to the theoretical value of $4.08\,\mu_B$/Dy. Here again, the $M(B)$ curves are temperature independent below 0.8 K and only show a small hysteresis at lowest temperatures.

4.3.3 $Dy_2(Ti_{0.9}Zr_{0.1})_2O_7$

Partially substituting Ti by Zr causes non-magnetic defects as the Zr ions are significantly larger than the Ti ions. The magnetic Dy sublattice is not (or only hardly) affected by Zr doping. Thus one expects the spin-ice properties to be essentially conserved.

In the following chapters, the thermal conductivity of $Dy_2(Ti_{0.9}Zr_{0.1})_2O_7$ is analyzed. The additional defect scattering on the Zr ions is supposed to suppress the phononic thermal conductivity, while essentially conserving the magnetic contribution κ_{mag}. Fig. 4.37 shows the field-dependent magnetization of $Dy_2(Ti_{0.9}Zr_{0.1})_2O_7$ for $\vec{B}\,||\,[111]$ at temperatures between 0.25 K and 2 K. The plateau within the Kagomé-ice phase is less pronounced compared to $Dy_2Ti_2O_7$ (Fig. 4.31 on page 74), *i.e.* the magnetization is not constant but exhibits a linear increase up to the transition at 1 T. In addition, the step at 1 T is broadened compared to the data obtained for $Dy_2Ti_2O_7$, and the $M(B)$ curves saturate at

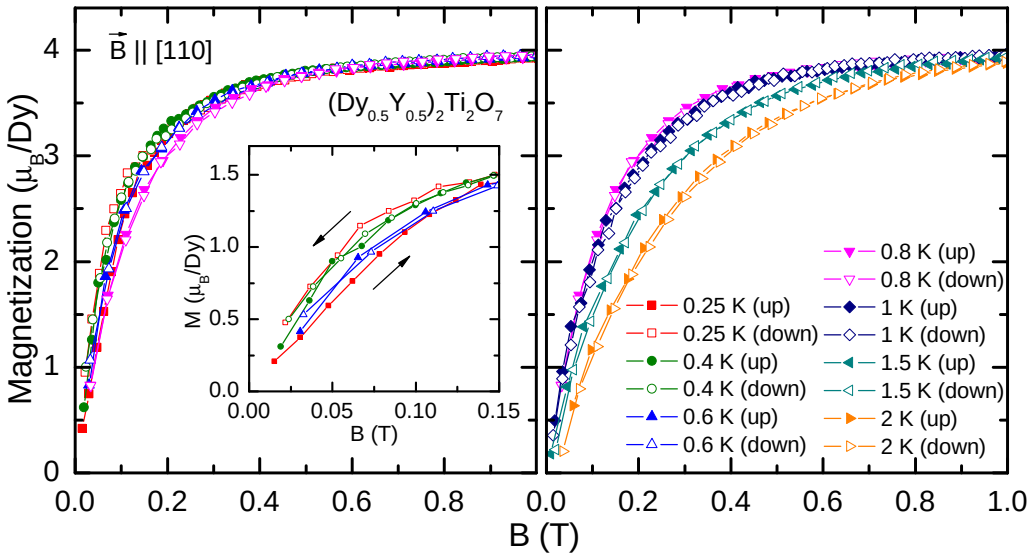

Figure 4.36: Magnetization of $(Dy_{0.5}Y_{0.5})_2Ti_2O_7$ for $\vec{B} \,||\, [110]$.

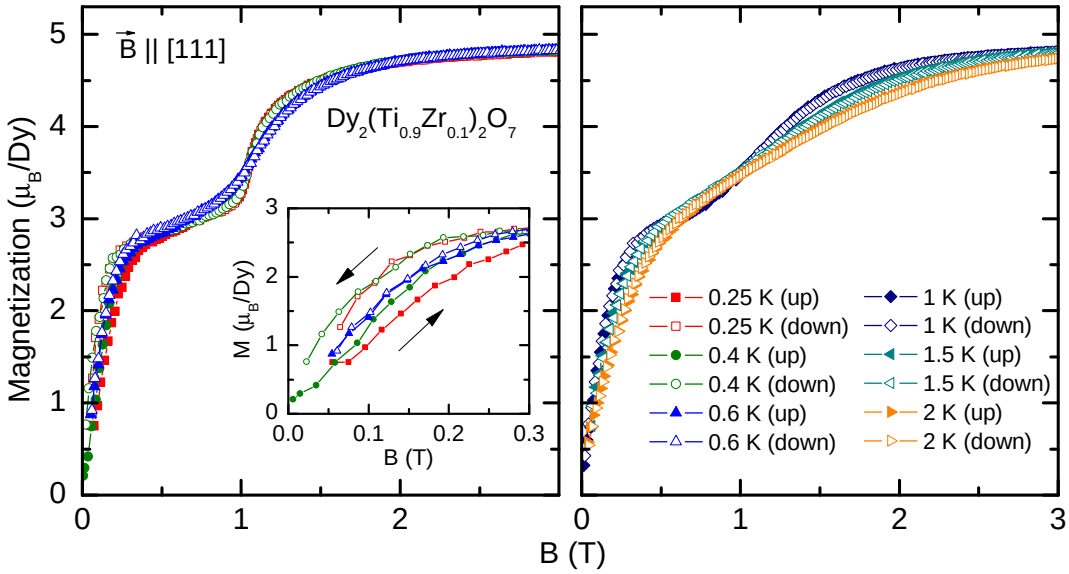

Figure 4.37: Magnetization of $Dy_2(Ti_{0.9}Zr_{0.1})_2O_7$ for $\vec{B} \,||\, [111]$.

higher fields than for $Dy_2Ti_2O_7$. The saturation value for $Dy_2(Ti_{0.9}Zr_{0.1})_2O_7$ is close to the expected value of $5\mu_B$/Dy. Furthermore, the hysteresis observed in the low-field region at low temperatures is less pronounced. At higher temperatures, the $M(B)$ curves broaden, as expected.

The magnetization data of $Dy_2(Ti_{0.9}Zr_{0.1})_2O_7$ show that the essential spin-ice features are still present. However, these features are broadened compared to the undoped $Dy_2Ti_2O_7$. These differences most likely originate from local lattice distortions due to the different ionic radii of Ti^{4+} and Zr^{4+}. This distortion results in a distortion of the Dy sublattice and, hence, in a distortion of the Dy tetrahedra. As a consequence, the distances and, thus, the energetic interaction within the tetrahedra are no longer equivalent. As the Zr defects are randomly distributed, the tetrahedra are not distorted regularly. Thus, the lattice consists of a variety of slightly different Dy tetrahedra. This explains the increasing magnetization on the plateau below 1 T as the different tetrahedra are not energetically equivalent, as it is the case for $Dy_2Ti_2O_7$. In addition, the broadening of the step at 1 T can also be explained by distorted tetrahedra.

4.4 Thermal Transport for $\vec{B}\,||\,[001]$

The following chapters concern the thermal-transport properties of the spin-ice compound $Dy_2Ti_2O_7$ and the related compounds $Y_2Ti_2O_7$, $(Dy_{0.5}Y_{0.5})_2Ti_2O_7$, and $Dy_2(Ti_{0.9}Zr_{0.1})_2O_7$. The main focus lies on the dynamics of the magnetic excitations, the magnetic monopoles (Sec. 4.1.3). Measurements of the thermal conductivity are a suitable probe to study the dynamics of magnetic excitations (*cf.* Sec. 2.1.5).

The studies presented in this chapter will restrict to the magnetic-field direction parallel to [001]. The subsequent chapters will investigate thermal-transport properties for magnetic fields parallel to [111] and [110]. The field direction parallel to [001] has several peculiarities. It is highly symmetric with respect to the local easy axes of the Dy momenta.[20] A magnetic field parallel to [001] results in a non-degenerate field-induced 2in-2out ground state, for which all Dy momenta have a positive non-vanishing component parallel to $\vec{B}$ (Fig. 4.12 on page 51).

The question whether magnetic excitations in spin ice (monopoles) contribute to the heat transport will be the main issue of this chapter. As a magnetic field parallel to [001] lifts the ground-state degeneracy, the magnetic excitations (monopoles) are expected to entirely vanish. Hence, a magnetic contribution κ_{mag} is expected to vanish when applying a field in [001] direction.

The phononic (κ_{ph}) and the magnetic (κ_{mag}) contributions are investigated by means of the different reference compounds $Y_2Ti_2O_7$, $(Dy_{0.5}Y_{0.5})_2Ti_2O_7$, and $Dy_2(Ti_{0.9}Zr_{0.1})_2O_7$.

[20] Each local easy axis has the same projection to the field direction [001].

The thermal conductivity of $Y_2Ti_2O_7$ certainly is purely phononic. However, it does not reflect a magnetic-field-dependent phononic background of the magnetic compound $Dy_2Ti_2O_7$. In the magnetic reference compound $(Dy_{0.5}Y_{0.5})_2Ti_2O_7$, a magnetic contribution κ_{mag} is supposed to be suppressed. Hence, the thermal conductivity of $(Dy_{0.5}Y_{0.5})_2Ti_2O_7$ should essentially reflect the field-dependent phononic background of $Dy_2Ti_2O_7$. In $Dy_2(Ti_{0.9}Zr_{0.1})_2O_7$, the phononic contribution is expected to be suppressed, whereas κ_{mag} is supposed to be unaffected. Thermal-conductivity measurements of $Dy_2(Ti_{0.9}Zr_{0.1})_2O_7$ have been performed for $\vec{B} \,||\, [111]$ (Sec. 4.5).

4.4.1 $Dy_2Ti_2O_7$

Literature Data

To my knowledge, only one experimental study of the thermal conductivity of $Dy_2Ti_2O_7$ has been published up to now [6].[21] This study focuses on the anomalous relaxation times in the low-temperature regime which are studied by analyzing the temperature dependence of the specific heat and the thermal conductivity of $Dy_2Ti_2O_7$ for various magnetic-field strengths $\vec{B} \,||\, [110]$.

Below $\sim 0.6\,\mathrm{K}$, the time-dependent temperature curves of the specific-heat measurement do not behave like exponential relaxation processes concerning one single relaxation time. In Ref. [6], the exponential time evolution with multiple relaxation times was interpreted as the magnetic system consisting of different subsystems with different relaxation times. Taking this into account, the authors obtained enhanced values of the specific heat (Fig. 4.7 on page 45).

Furthermore, the thermal conductivity was investigated applying a heat pulse technique where the temperature gradient was measured as a function of time. The thermal conductivity was interpreted as purely phononic and the temperature dependence of $\kappa(T)$ was attributed to phonon scattering on magnetic excitations (monopoles). As will be discussed below, this interpretation is not supported by our data.

Low-Field Thermal Conductivity

Fig. 4.38 shows the temperature dependence of the thermal conductivity of $Dy_2Ti_2O_7$ for zero field and for 0.5 T together with the thermal conductivity of the non-magnetic, iso-structural reference system $Y_2Ti_2O_7$.[22] In both cases, the heat current is directed along the crystallographic $[1\bar{1}0]$ direction (within the

[21] This article mainly summarizes the PhD thesis of B. Klemke [121].

[22] Around the low-temperature maximum, the thermal conductivity of $Y_2Ti_2O_7$ is 6 times larger compared to literature data presented in Ref. [167]. At room temperature, both datasets yield comparable values. This shows the high purity of the single crystal used here.

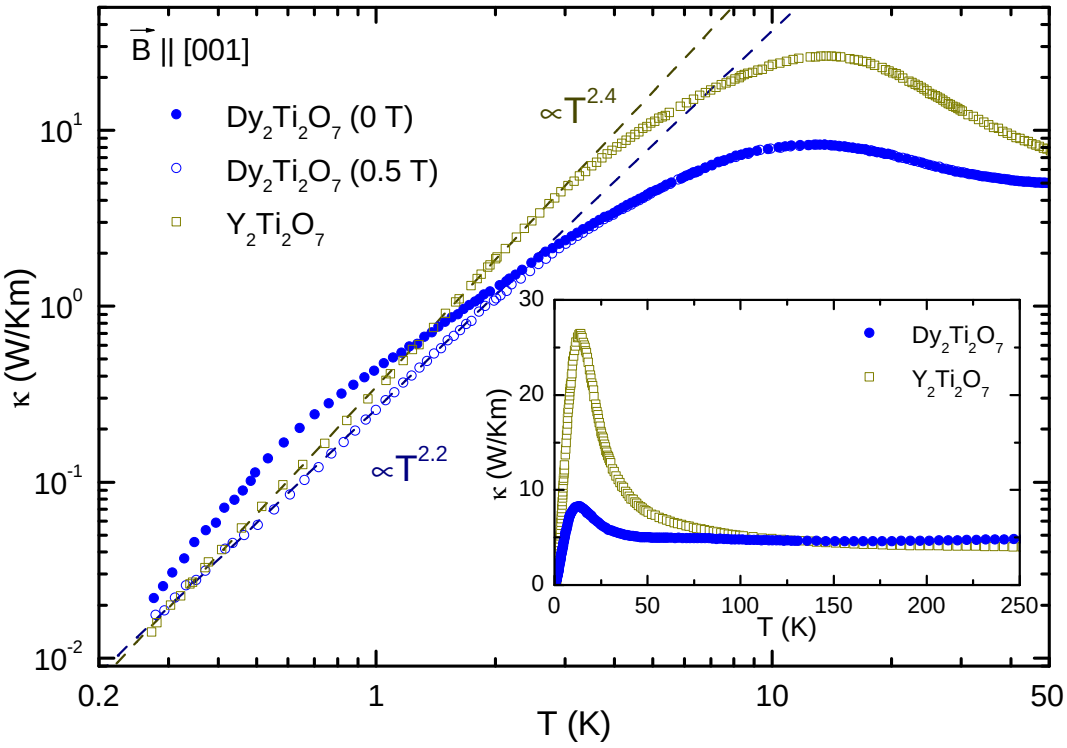

Figure 4.38: Thermal conductivity of $Dy_2Ti_2O_7$ ($\vec{B}\,||\,[001]$) for zero field and for 0.5 T (closed and open blue circles) and the thermal conductivity of the non-magnetic reference compound $Y_2Ti_2O_7$ (dark yellow). The 0.5 T curve was measured in an external field of 1 T which is strongly reduced due to demagnetization effects. Inset: Same data on linear scales.

Kagomé planes), perpendicular to the magnetic field parallel to [001].[23]

The thermal conductivity κ of $Dy_2Ti_2O_7$ shows no field dependence above 4 K. At lower temperatures, κ is strongly suppressed by the magnetic field. As can be seen in the inset of Fig. 4.38, the thermal conductivity of the non-magnetic $Y_2Ti_2O_7$ is comparable to $Dy_2Ti_2O_7$ for temperatures above $\sim 100\,\mathrm{K}$, whereas $\kappa(T)$ of $Dy_2Ti_2O_7$ is strongly suppressed below 100 K. This differences probably originate from a structural instability in $Dy_2Ti_2O_7$, which is observed in Raman scattering data of $Dy_2Ti_2O_7$, but absent in the non-magnetic, iso-structural compound $Lu_2Ti_2O_7$ [168, 169]. Moreover, the phononic thermal conductivity of $Dy_2Ti_2O_7$ also can be reduced by phonon scattering on crystal-field excitations of the 4f electrons of the Dy ions (Sec. 4.7.3).

For temperatures below $\sim 3\,\mathrm{K}$, the $Y_2Ti_2O_7$ curve resembles the 0.5 T curve

[23] This configuration is similar to the case of a cigar-shaped sample with the magnetic field perpendicular to the long edge (semi major axis), see Fig. 2.4. Hence, a considerable demagnetization field has to be subtracted from the applied magnetic field. The 0.5 T curve has been measured in an external field of 1 T.

of $Dy_2Ti_2O_7$. Both datasets exhibit a power-law behavior in a rather large temperature region up to $\sim 3\,\mathrm{K}$ with a comparable exponent. The zero-field data of $Dy_2Ti_2O_7$, however, show a clear shoulder around 1 K and do not follow such a simple power law. The qualitative similarity of the thermal conductivity of $Y_2Ti_2O_7$ and the field data of $Dy_2Ti_2O_7$ gives rise to the interpretation of an additional magnetic contribution κ_{mag} for $Dy_2Ti_2O_7$ in zero field on top of the phononic background κ_{ph}, which is basically given by the $\kappa(T)$ data at 0.5 T.

This assertion is supported by measurements of the magnetic-field dependence of $\kappa(B)$ at various constant temperatures. First, the results for magnetic field strengths up to 0.5 T (Fig. 4.39) will be discussed. The studies of higher magnetic fields up to 7 T will be introduced in Sec. 4.4.1. Below 4 K, $\kappa(B)$ steplikely decreases at $\sim 0.2\,\mathrm{T}$ (Fig. 4.39(a)). Above 0.6 K, the step is followed by a weak decrease of κ. At lower temperatures, $\kappa(B)$ remains almost constant above the step. The relative reduction κ/κ_0 is maximal for 0.6 K and basically vanishes above 4 K. The decrease of $\kappa(B)$ correlates with the increase of $M(B)$, shown exemplarily in Figs. 4.39(b) - (e) at temperatures between 0.4 K and 0.7 K, respectively. The steplike change of $\kappa(B)$ exhibits a clear hysteresis below 0.6 K with different critical fields for different field-sweep directions, which is also observed in the magnetization data. With decreasing temperature, the hysteresis width of $\kappa(B)$ and $M(B)$ increase in the same manner.

The observed correlation of $\kappa(B)$ and $M(B)$ can be explained by the occurrence of an additional magnetic contribution κ_{mag} on top of the phononic background κ_{ph}, *i.e.*

$$\kappa = \kappa_{\mathrm{mag}} + \kappa_{\mathrm{ph}}\,, \tag{4.26}$$

where the magnetic contribution depends on the ground-state degeneracy and is, thus, suppressed by the magnetic field parallel to [001], which lifts the ground-state degeneracy of the spin ice. A microscopic model explaining the magnetic heat transport in $Dy_2Ti_2O_7$ including a quantitative analysis is introduced in Sec. 4.7.1.

Slow Dynamics

Below 0.5 K, an additional feature is observed in the $\kappa(B)$ data (Figs. 4.39(e) and (f)). Starting the measurement from zero field (after zero-field cooling), $\kappa(B)$ decreases to a certain saturation value (curve 1). After subsequently measuring with decreasing field back to zero field (curve 2), $\kappa(B)$ only recovers 90% of its initial zero-field value (after zero-field cooling) at 0.35 K (95% at 0.4 K). Repeating this measurement, one obtains curves 3 and 4 with coinciding endpoints, where curve 2 and 4 perfectly match each other. The reduced zero-field value of κ slowly relaxes back to its initial zero-field value (after zero-field cooling). Fig. 4.40(a)

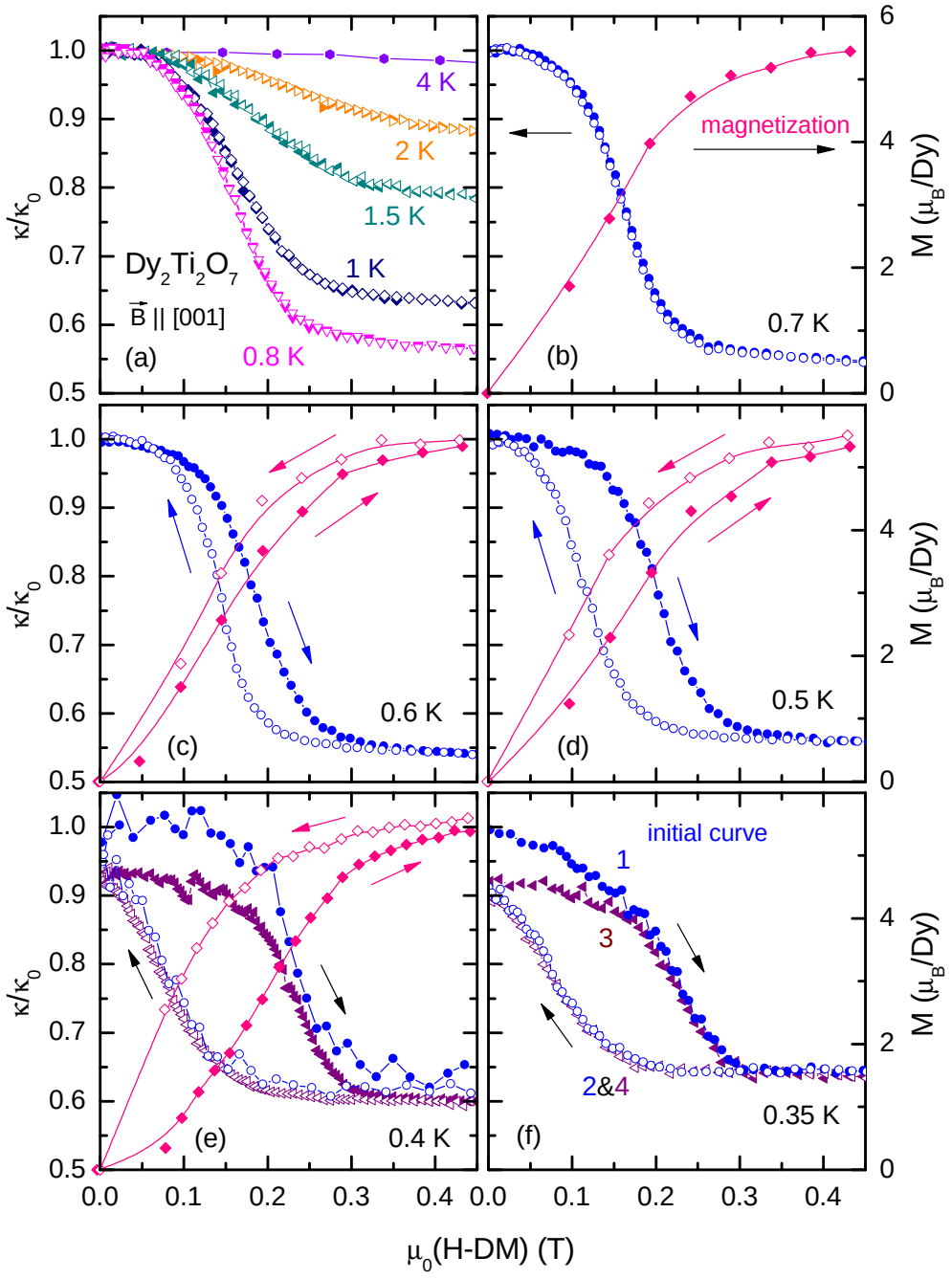

Figure 4.39: Magnetic-field dependence of $\kappa(B)/\kappa(0\,\mathrm{T})$ of $Dy_2Ti_2O_7$ for $\vec{B}\,||\,[001]$. All curves were measured after zero-field cooling. The magnetic field is rescaled with respect to demagnetization effects. Panels (b) - (e) additionally contain the magnetization data $M(B)$. The arrows indicate the field-sweep direction.

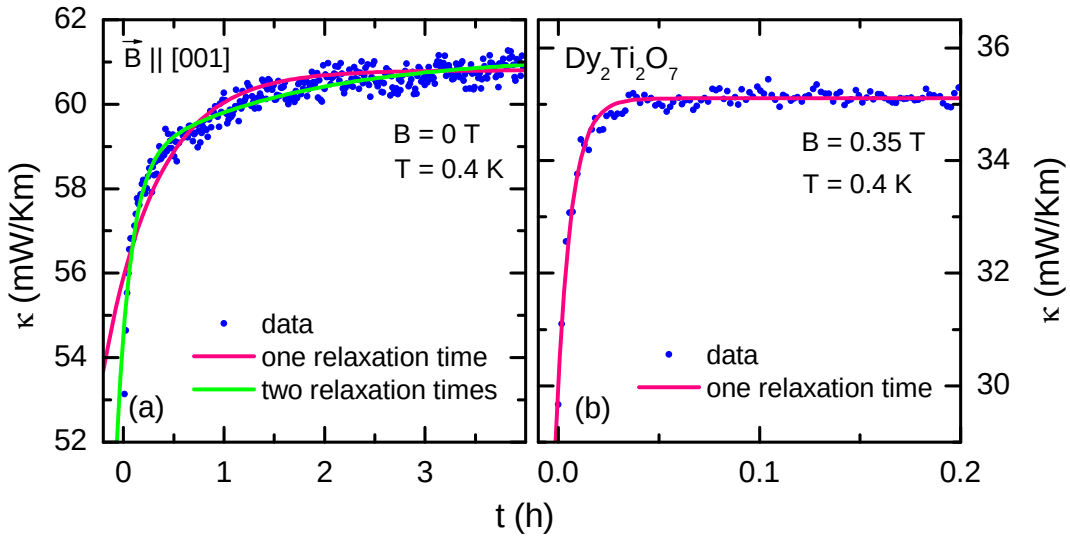

Figure 4.40: Time-dependent relaxation $\kappa(t)$ at 0.4 K for (a) zero field and (b) for 0.35 T. In both cases, the measurement started after decreasing the magnetic field from $\sim 1\,\mathrm{T}$. In zero field, an exponential fit with two (large) relaxation times is needed to match the data, whereas for 0.35 T, only one single (small) relaxation time is needed.

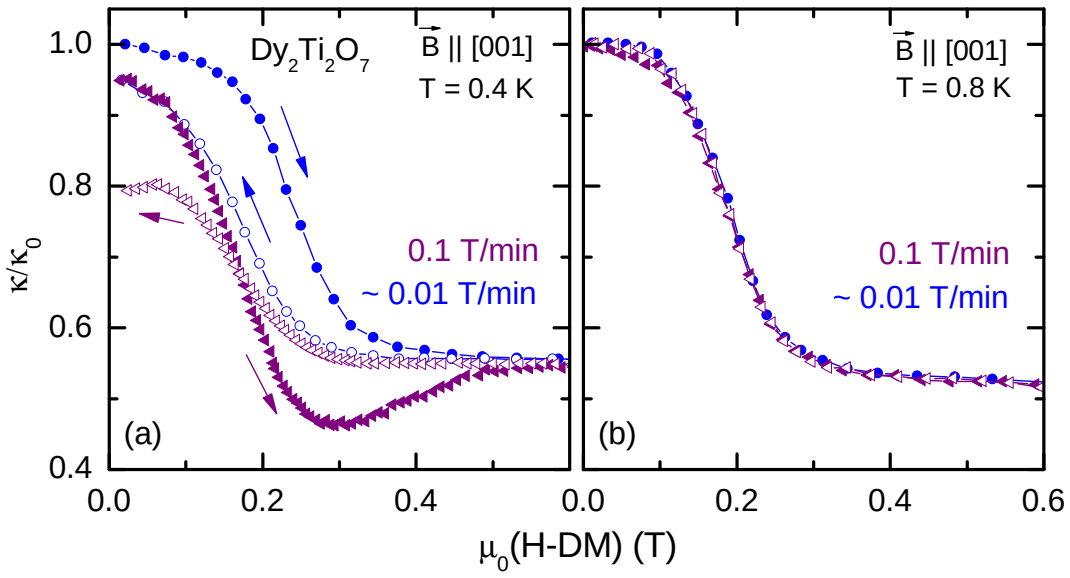

Figure 4.41: Relative change $\kappa(B)/\kappa(0\,\mathrm{T})$ ($\vec{B} \,||\, [001]$) of $Dy_2Ti_2O_7$ for different magnetic-field sweep rates at 0.4 K and 0.8 K. Demagnetization effects are taken into account.

shows the zero-field relaxation-process at 0.4 K.[24,25] The relaxation process cannot be described by an exponential fit with only one single relaxation time (red curve). At least two relaxation times are needed to match the experimental data properly (green curve), *i.e.*

$$\kappa(t) = a_0 + a_1\left(1 - \mathrm{e}^{-t/\tau_1}\right) + a_2\left(1 - \mathrm{e}^{-t/\tau_2}\right) . \tag{4.27}$$

The relaxation fit of Fig. 4.40(a) yields large relaxation times $\tau_1 \simeq 8\,\mathrm{min}$ and $\tau_2 \simeq 100\,\mathrm{min}$. As every data point in Fig. 4.39 was measured after stabilizing several minutes, the different zero-field values in Figs. 4.39(e) and (f) originate from the large relaxation time τ_2.

For comparison, Fig. 4.40(b) shows the relaxation $\kappa(t)$ at 0.35 T, where the magnetization is almost saturated. The time-resolved measurement started directly after decreasing the field from $\sim 1\,\mathrm{T}$ down to 0.35 T with relaxed stabilization criteria as explained above. At 0.35 T, the relaxation $\kappa(t)$ can be well described by an exponential fit with one single relaxation time. The fit yields a rather small relaxation time $\tau \simeq 30\,\mathrm{sec}$.

Different time-dependent relaxation processes are also observed when measuring $\kappa(B)$ with different field-sweep rates. Fig. 4.41(a) shows the field dependence of κ/κ_0 at 0.4 K for 0.1 T/min and for 0.01 T/min. After zero-field cooling, a stabilized measurement with increasing field (approximately $\sim 0.01\,\mathrm{T/min}$) was performed (closed blue circles). The subsequent measurement with decreasing field (open blue circles) ends at 95% of the zero-field value (*cf.* Fig 4.39(e)). Starting from this zero-field value, a measurement with a continuous sweep rate of 0.1 T/min was performed (closed purple triangles). This curve shows a clear minimum around 0.3 T and ends up at the same value above 0.5 T as the stabilized (slow) measurement. The measurement with decreasing field (down) and a sweep rate of 0.1 T/min (open purple triangles) ends at only 80% of the initial zero-field value. Fig. 4.41(b) shows κ/κ_0 at 0.8 K for 0.1 T/min and 0.01 T/min. In contrary to the data at 0.4 K, the measurement at 0.8 K is neither hysteretic, nor does it depend on the field sweep rate.

High-Field Thermal Conductivity

In a second measurement run, the κ data were extended towards higher fields. Fig. 4.42 shows κ/κ_0 for magnetic fields up to 7 T. Beside the field dependence for magnetic fields below 0.5 T (discussed above), $\kappa(B)$ exhibits an additional steplike decrease at $\sim 2\,\mathrm{T}$. The position of this step is temperature independent and is observed in the whole measured temperature range up to 8 K. As shown exemplarily for 0.4 K (Fig. 4.42(b)), the magnetization has no feature

[24] This measurement is part of another measurement run including the high-field regime up to 8 T.

[25] To obtain a sufficiently large number of data points, the stabilization criteria were reduced in these measurements.

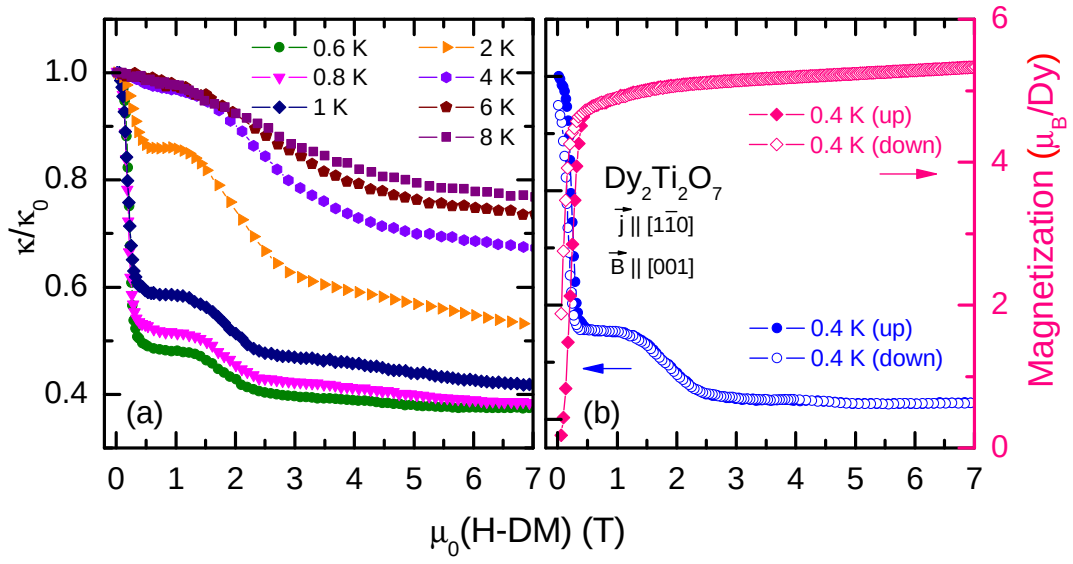

Figure 4.42: Relative change $\kappa(B)/\kappa(0\,\mathrm{T})$ of $Dy_2Ti_2O_7$ for magnetic fields up to 7 T parallel to [001]. The datasets between 0.6 K and 8 K are displayed in panel (a). Panel (b) shows κ/κ_0 together with the magnetization (the inset shows an enlargement of the low-field region). Demagnetization effects are taken into account.

at this particular magnetic field. For the lowest measured temperatures, $\kappa(B)$ stays basically constant above the step at 2 T, whereas for higher temperatures (Fig. 4.42(a)), $\kappa(B)$ linearly decreases above the step (at least up to 7 T).

Within the proposed interpretation of $\kappa(B)$ given in the previous paragraphs, the magnetic contribution κ_{mag} vanishes completely for magnetic fields above the saturation of the magnetization $M(B)$, *i.e.* above $\sim 0.5\,\mathrm{T}$ (depending on temperature). Hence, the feature in $\kappa(B)$ around 2 T and the decrease above 3 T (Fig. 4.42) cannot be explained by a magnetic contribution as introduced above. However, scattering on magnetic excitations can also be excluded, as $M(B)$ is saturated above $\sim 0.5\,\mathrm{T}$. A possible interpretation is to attribute the field dependence of $\kappa(B)$ for magnetic fields above 1 T to a field-dependent phononic background $\kappa_{\mathrm{ph}}(B)$. In the following, this field dependence is analyzed via magnetostriction measurements of $Dy_2Ti_2O_7$ and thermal-conductivity measurements of $(Dy_{0.5}Y_{0.5})_2Ti_2O_7$.

Magnetostriction

In this paragraph, the magetostriction of $Dy_2Ti_2O_7$ parallel to $\vec{B}\,||\,[001]$ is investigated. Fig. 4.43 shows the relative length change $\Delta L/L$ of $Dy_2Ti_2O_7$ parallel to [001] (inset (b)). For a magnetic field $\vec{B}\,||\,[001]$, $\Delta L/L$ shows a sharp anomaly below $\sim 0.5\,\mathrm{T}$. For higher fields, $\Delta L/L$ increases almost linearly. This behavior

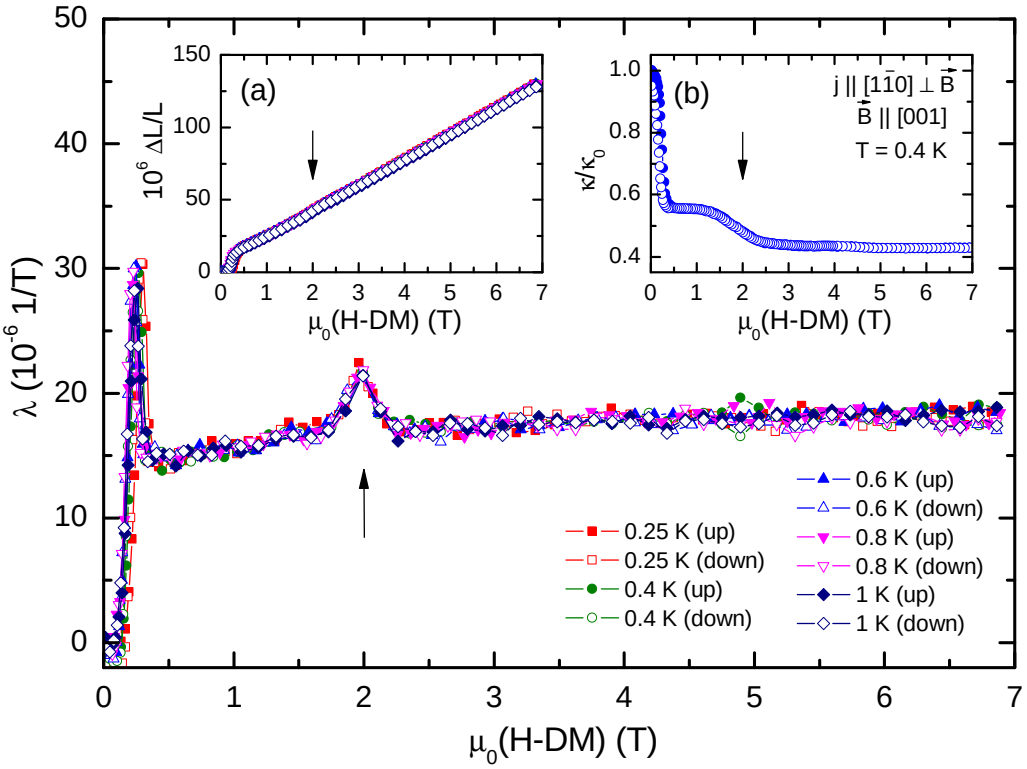

Figure 4.43: Magnetostriction of $Dy_2Ti_2O_7$ parallel to $\vec{B}\,||\,[001]$ at various constant temperatures between 0.25 K and 1 K. Inset (a) shows the field-induced length change. Inset (b) shows the relative change $\kappa(B)/\kappa(0\,\mathrm{T})$ for the same field direction at 0.4 K. For all shown datasets, demagnetization effects are taken into account.

is essentially temperature independent. Upon this linear increase of $\Delta L/L$, an additional anomaly around 2 T can be observed, which can be better visualized via the derivative of $\lambda = (1/L)\,\partial/\partial B(\Delta L)$ (main panel of Fig. 4.43).

The anomaly below 0.5 T can be attributed to the field-induced change of the magnetization $M(B)$. Above 0.5 T, the magnetization of $Dy_2Ti_2O_7$ is saturated (at least at lowest temperatures). The saturated magnetization indicates that the fully polarized spin ice consists of only one particular 2in-2out configuration forming the non-degenerate field-induced ground state. Above $\sim 0.5\,\mathrm{T}$, spin-ice excitations (monopoles) are expected to completely vanish. Hence, the linear increase of $\Delta L/L$, *i.e.* the elongation of the sample, and the anomaly around 2 T cannot originate from the monopole excitations in $Dy_2Ti_2O_7$.

The data shown in Fig. 4.43 were measured on a sample shaped as a thin plate of thickness 0.25 mm with the short edge parallel to [001]. This geometry leads to a rather large demagnetization field. Above $\sim 0.5\,\mathrm{T}$, the magnetization is saturated and, hence, the demagnetization field is constant. Thus, the shape of

the peak at 2 T (Fig. 4.43) is not affected. The situation is much more complex for magnetic fields below 1 T as demagnetization causes not only a simple shift or linear scaling of the magnetic-field axis. The slope and, thus, the derivative $\lambda(B)$ is very sensitive to the demagnetization correction. The data in Fig. 4.43 were obtained by first calculating the derivative. The demagnetization corrections were applied afterwards.[26]

The magnetostriction data can be interpreted qualitatively by assuming that the magnetic moments at the corners of the tetrahedra are canted towards the external magnetic field. The torque effected by the external field causes a tilting of the local easy axes and, thus, a distortion of the surrounding oxygen ions. This leads to a distortion of the entire cubic cell and is supposed to suppress the phononic thermal conductivity. This also explains the temperature independence of the magnetostriction as the torque caused by an external magnetic field is temperature independent at low temperatures and high magnetic fields, where $M(B)$ is saturated. As the phononic thermal conductivity is strongly temperature dependent, the effect of a lattice distortion on κ_{ph} certainly will depend on temperature.

The continuous lattice distortion can be understood by the torque affecting the Dy momenta, but the origin of the anomaly around 2 T is unclear. At this particular field of 2 T, one can observe an anomaly in the field-dependent thermal conductivity $\kappa(B)$, which also shows a steplike anomaly around 2 T (Fig. 4.43(b)). This qualitative comparison gives rise to the assumption that the anomaly at 2 T in the $\kappa(B)$ data can be attributed to the phononic background κ_{ph} rather than to the magnetic spin-ice system.

4.4.2 $(\mathbf{Dy_{0.5}Y_{0.5}})_2\mathbf{Ti_2O_7}$

The temperature dependence of the zero-field thermal conductivity $\kappa(T)$ of $(Dy_{0.5}Y_{0.5})_2Ti_2O_7$ is illustrated in Fig. 4.44. The data of $(Dy_{0.5}Y_{0.5})_2Ti_2O_7$ show a power-law behavior up to $\sim 2\,\mathrm{K}$ with an exponent close to 2.1, which is comparable to the 0.5 T data of $Dy_2Ti_2O_7$, also depicted in this plot. Compared to the thermal conductivity of $Dy_2Ti_2O_7$, $\kappa(T)$ of $(Dy_{0.5}Y_{0.5})_2Ti_2O_7$ is slightly larger below 1.5 K and smaller for higher temperatures. The qualitative similarity gives rise to the interpretation that the zero-field thermal conductivity of $(Dy_{0.5}Y_{0.5})_2Ti_2O_7$ essentially represents the phononic background κ_{ph} of $Dy_2Ti_2O_7$ (*cf.* the comparison of $Dy_2Ti_2O_7$ and $Y_2Ti_2O_7$ in Fig. 4.38 on page 83).

In contrast to $Y_2Ti_2O_7$, $(Dy_{0.5}Y_{0.5})_2Ti_2O_7$ is a magnetic compound with a magnetic-field dependent thermal conductivity. Fig. 4.45 shows the field dependence of $\kappa(B)$ of $(Dy_{0.5}Y_{0.5})_2Ti_2O_7$ together with $\kappa(B)$ of the mother com-

[26] The analysis discussed in this paragraph focuses on the magnetic-field region above 1 T. A Detailed discussion of thermal expansion and magnetostriction also including the low-field region can be found in Ref. [84].

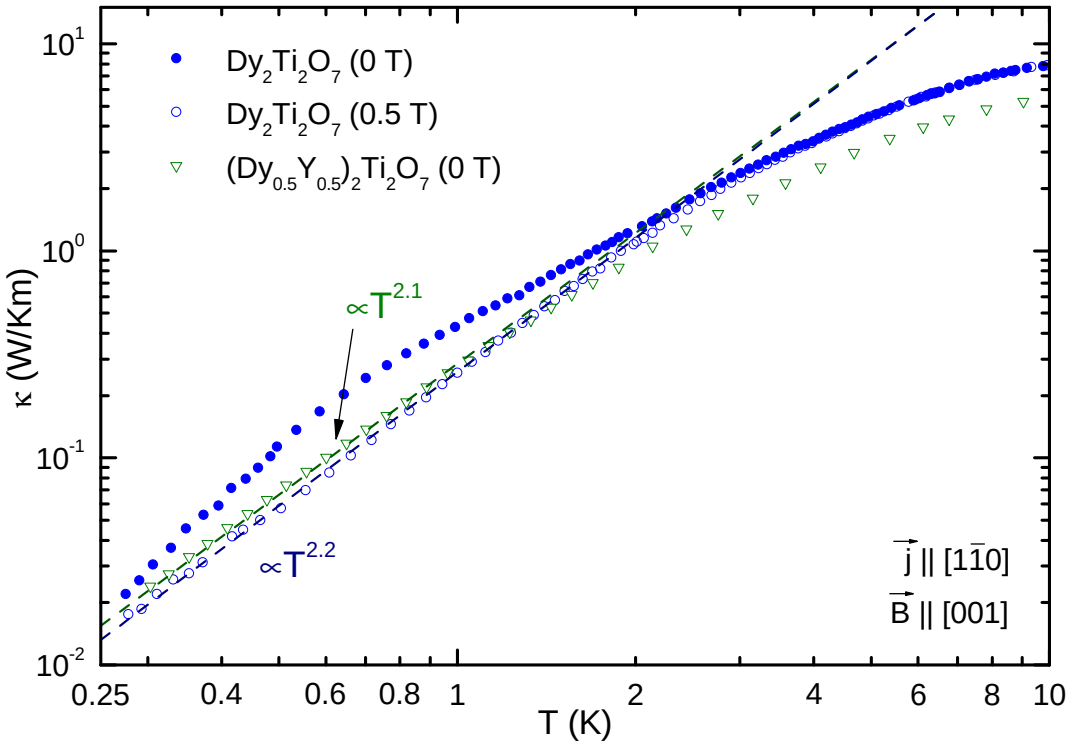

Figure 4.44: Thermal conductivity of $Dy_2Ti_2O_7$ in zero-field and for 0.5 T (blue circles) and the zero-field thermal conductivity of $(Dy_{0.5}Y_{0.5})_2Ti_2O_7$ (green triangles). In both cases, the heat current is directed along the crystallographic $[1\bar{1}0]$ direction.

pound $Dy_2Ti_2O_7$. Note, that the thermal-conductivity data shown in Fig. 4.45 are absolute values. Contrary to $Dy_2Ti_2O_7$, the thermal conductivity $\kappa(B)$ of $(Dy_{0.5}Y_{0.5})_2Ti_2O_7$ is not hysteretic (not shown).

At 4 K, the magnetic contribution κ_{mag} of $Dy_2Ti_2O_7$ is expected to vanish. At this temperature, the thermal conductivity of both compounds show a very similar behavior, where the values of $Dy_2Ti_2O_7$ are slightly larger. At 2 K, however, the additional step in the $Dy_2Ti_2O_7$ data for fields below 0.5 T is not observed in the $(Dy_{0.5}Y_{0.5})_2Ti_2O_7$ data. Even at lower temperatures where this low-field step becomes more pronounced no corresponding feature is observed in the $(Dy_{0.5}Y_{0.5})_2Ti_2O_7$ data. The high-field behavior of $(Dy_{0.5}Y_{0.5})_2Ti_2O_7$, however, is very similar to the field dependence of $Dy_2Ti_2O_7$. Note that the $\kappa(B)$ data shown in Fig. 4.45 are not scaled to match each other.

The main difference between the thermal conductivity $\kappa(B)$ of $Dy_2Ti_2O_7$ and of $(Dy_{0.5}Y_{0.5})_2Ti_2O_7$ is the correlation with the magnetization $M(B)$. Fig. 4.39 on page 85 clearly shows that for $Dy_2Ti_2O_7$, the increase of $M(B)$ directly correlates with the decrease of $\kappa(B)$. This correlation is interpreted as a suppression of the magnetic thermal conductivity κ_{mag} due to the lifting of the ground-state

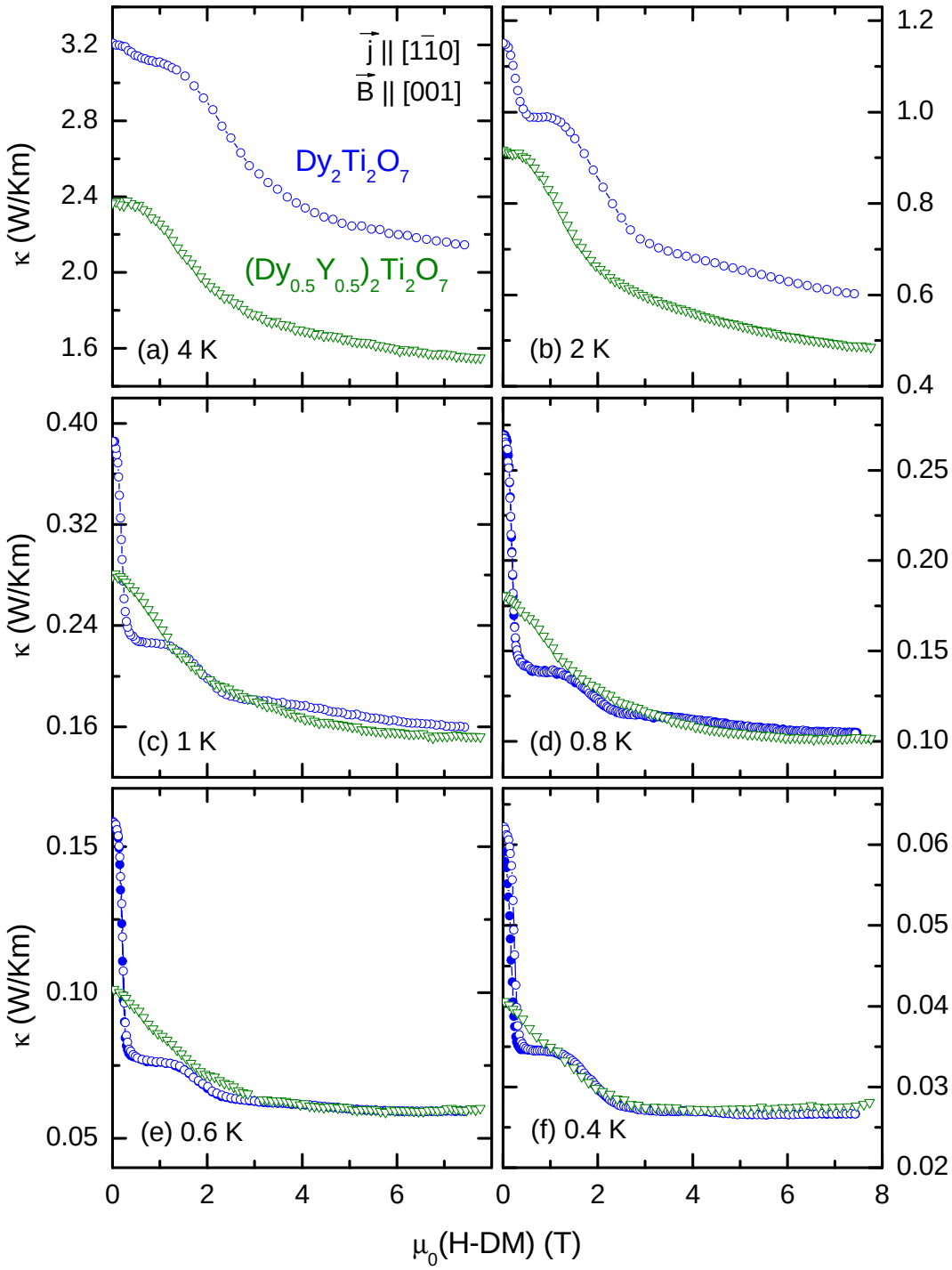

Figure 4.45: Field dependence of the thermal conductivity $\kappa(B)$ of $(Dy_{0.5}Y_{0.5})_2Ti_2O_7$ (green triangles) and of the spin ice $Dy_2Ti_2O_7$ (blue circles) at various constant temperatures between 0.4 K and 4 K for $\vec{B} \,||\, [001]$. In both cases, demagnetization effects are taken into account.

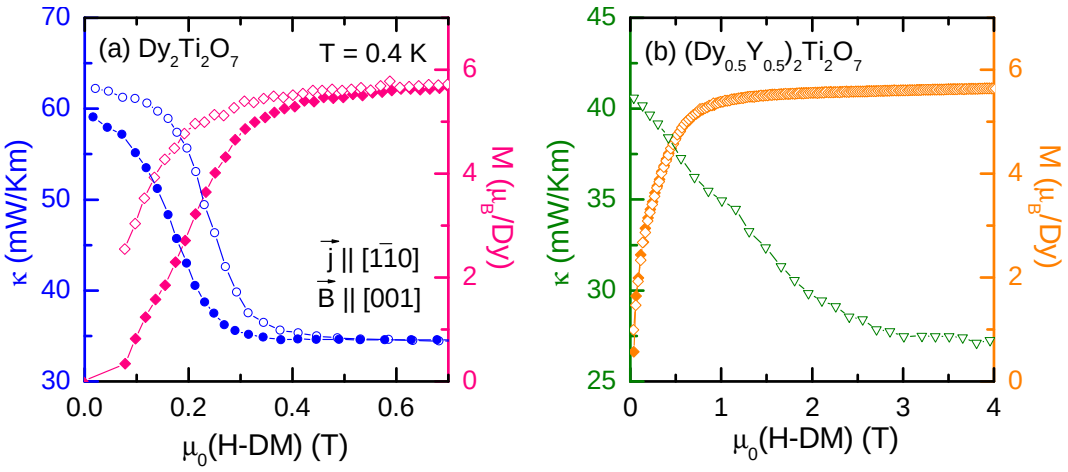

Figure 4.46: Comparison of thermal conductivity $\kappa(B)$ with magnetization $M(B)$ of $Dy_2Ti_2O_7$ and of $(Dy_{0.5}Y_{0.5})_2Ti_2O_7$ at 0.4 K for $\vec{B}\,||\,[001]$. Demagnetization effects are taken into account.

degeneracy by a magnetic field parallel to [001]. Fig. 4.46 compares the correlation of $\kappa(B)$ and $M(B)$ for $Dy_2Ti_2O_7$ and $(Dy_{0.5}Y_{0.5})_2Ti_2O_7$, at 0.4 K. Panel (a) shows this correlation for $Dy_2Ti_2O_7$, where even the hysteretic behavior is observed in both datasets. The data are only shown below 0.7 T, as the magnetization is fully saturated above $\sim 0.5\,\mathrm{T}$. Fig. 4.39(b) shows $\kappa(B)$ and $M(B)$ for $(Dy_{0.5}Y_{0.5})_2Ti_2O_7$ up to 4 T. The magnetization saturates above 1 T and remains almost constant for higher fields. The field dependent $\kappa(B)$ decreases with increasing field up to $\sim 3\,\mathrm{T}$ and remains almost constant for higher fields. The direct comparison of $Dy_2Ti_2O_7$ and $(Dy_{0.5}Y_{0.5})_2Ti_2O_7$ in Fig. 4.39 shows that the field-induced suppression of the thermal conductivity originates from different causes. Contrary to the case for $Dy_2Ti_2O_7$, the field dependence of $\kappa(B)$ of $(Dy_{0.5}Y_{0.5})_2Ti_2O_7$ does not correlate with the magnetization and, hence, not with the degeneracy of the field-induced ground state.

The similarity of the field dependence of $\kappa(B)$ of $(Dy_{0.5}Y_{0.5})_2Ti_2O_7$ and of $Dy_2Ti_2O_7$ for high magnetic fields (above $\sim 1\,\mathrm{T}$) supports the interpretation of the high-field dependence of $\kappa(B)$ of $Dy_2Ti_2O_7$ as the field-dependent phononic background κ_{ph}, which is essentially given by the field dependence of $\kappa(B)$ of $(Dy_{0.5}Y_{0.5})_2Ti_2O_7$. Above $\sim 1\,\mathrm{T}$, even the absolute values are rather close to each other. It is obvious, however, that one cannot identify the zero-field κ data of $(Dy_{0.5}Y_{0.5})_2Ti_2O_7$ directly as the zero-field phononic background κ_{ph} of $Dy_2Ti_2O_7$. Below 1 K, the estimated κ_{ph} of $Dy_2Ti_2O_7$ is smaller than the zero-field values of $(Dy_{0.5}Y_{0.5})_2Ti_2O_7$. A possible explanation could be a magnetic contribution for $(Dy_{0.5}Y_{0.5})_2Ti_2O_7$ which is more pronounced at lower temperatures. Compared to $Dy_2Ti_2O_7$, this presumable magnetic contribution would be significantly smaller, as expected for a doping level of 50%.

4.4.3 Conclusion

In conclusion, the thermal conductivity data of $Dy_2Ti_2O_7$ and the related compounds $Y_2Ti_2O_7$ and $(Dy_{0.5}Y_{0.5})_2Ti_2O_7$ provide clear evidence for a considerable magnetic contribution $\kappa_{\rm mag}$ for the spin-ice compound $Dy_2Ti_2O_7$ on top of the phononic background $\kappa_{\rm ph}$. The magnetic contribution $\kappa_{\rm mag}$ is maximum in zero field and is strongly suppressed by an external field parallel to [001] which lifts the ground-state degeneracy.

The high-field dependence of $\kappa(B)$ of $Dy_2Ti_2O_7$ is identified as the field-dependent phononic background $\kappa_{\rm ph}(B)$, which originates from lattice distortions due to torques of the Dy momenta effected by the external magnetic field. This interpretation is supported by measurements of the field-induced length change $\Delta L/L$ of $Dy_2Ti_2O_7$, which shows that the $Dy_2Ti_2O_7$ crystal almost linearly elongates with increasing field. Moreover, $\kappa(B)$ and $\Delta L/L$ exhibit anomalies at a comparable magnetic field around 2 T, which can, thus, be attributed to $\kappa_{\rm ph}(B)$.

A more quantitative study of the field-dependent phononic background $\kappa_{\rm ph}(B)$ is provided by thermal-conductivity measurements of $(Dy_{0.5}Y_{0.5})_2Ti_2O_7$. Here, the spin-ice features are strongly suppressed and, hence, the thermal conductivity is supposed to be essentially of phononic origin. The field dependence of $\kappa(B)$ of $(Dy_{0.5}Y_{0.5})_2Ti_2O_7$ essentially reflects $\kappa_{\rm ph}(B)$ of $Dy_2Ti_2O_7$. Hence, one can separate the magnetic from the phononic contribution. A detailed study of $\kappa_{\rm mag}$ including a microscopic model will be introduced in chapter 4.7.1.

An alternative approach to separate the different contributions of κ is to partly replace Ti by Zr. This substitution essentially conserves the spin-ice behavior, but suppresses the phononic thermal conductivity due to additional Zr defects. Thermal-conductivity measurements of $Dy_2(Ti_{0.9}Zr_{0.1})_2O_7$ for $\vec{B}\,||\,[111]$ are presented in Sec. 4.5.3.

4.5 Thermal Transport for $\vec{B}\,||\,[111]$

In the previous chapter, thermal-transport properties of the spin ice $Dy_2Ti_2O_7$ and its related compounds were discussed for a magnetic field parallel to [001]. This chapter concerns the spin ice with a field applied parallel to the [111] direction. This field direction provides several particularities. It is parallel to the easy axis of one of the four Dy momenta per tetrahedron. This particular spin can easily be aligned parallel to $\vec{B}$. For symmetry reasons, the field-induced ground state is 3-fold degenerate for magnetic fields below 1 T. For larger fields, the spin ice is fully polarized and the ground-state degeneracy is lifted. At very low temperatures, the degeneracy in the field range below 1 T results in a magnetization plateau followed by a sharp step at 1 T. This property of a magnetic field parallel to [111] allows to tune the degree of degeneracy by variation of the magnetic field

strength, *i.e.* one can realize different degrees of degeneracy.[27]

In the following, the magnetic contribution κ_{mag} and the phononic background κ_{ph} of $Dy_2Ti_2O_7$ are analyzed for $\vec{B}\,||\,[111]$, analogously to the previous chapter.

4.5.1 $Dy_2Ti_2O_7$

The thermal conductivity of $Dy_2Ti_2O_7$ was measured for $\vec{B}$ parallel to [111] with the heat current $\vec{j}$ either along [111] (parallel to $\vec{B}$) or along $[1\bar{1}0]$ (perpendicular to $\vec{B}$). The field dependence of κ/κ_0 for $\vec{j}\,||\,[1\bar{1}0]$ is presented in Fig. 4.47. Analogous to the magnetization data for $\vec{B}\,||\,[111]$ (Fig. 4.31 on page 74), $\kappa(B)$ exhibits a plateau below 1 T which sharpens when lowering the temperature. Below 0.6 K (Fig. 4.47(c)), $\kappa(B)$ is hysteretic within the Kagomé-ice phase (below 1 T) with respect to the field sweep direction. For temperatures below 0.4 K (Figs. 4.47(d) and (e)), the measurements with decreasing field (open circles) end in a reduced zero-field value of κ, as was also observed for $\vec{B}\,||\,[001]$ (Figs. 4.39(e) and (f) on page 85). In this low-temperature regime, the measurements with increasing field exhibit an additional feature. Around the phase transition at 1 T, $\kappa(B)$ has a maximum followed by a sharp decline. At $\sim 1.1\,\mathrm{T}$, $\kappa(B)$ exhibits a small shoulder and a clear kink at 1.5 T. Above this field, $\kappa(B)$ decreases slowly and remains almost constant above 6 T (Fig. 4.39(e)). As can be seen in the inset of Fig. 4.39(e), the magnetization $M(B)$ shows no features above 1 T.

It is notable that the magnetization shows no hysteresis on the plateau within the Kagomé-ice phase. As mentioned above, the ground state within the Kagomé-ice phase is 3-fold degenerate. Within the single-tetrahedron approximation, the ground state is realized by 3 equivalent 2in-2out configurations which have in common that the spin of the triangle plane is polarized by the magnetic field. The magnetization of these three spin configurations have the same component parallel the [111] direction. As one can only measure the projection of the actual magnetization on the magnetic-field direction, these three configurations look the same in the magnetization measurements parallel to [111]. Hence, by magnetization measurements only, one cannot decide which ground state is actually realized. The thermal conductivity within the Kagomé-ice phase is discussed in detail in the following paragraph.

The field dependence of κ/κ_0 for $\vec{j}\,||\,\vec{B}\,||\,[111]$ (Fig. 4.48) shows a similar behavior as the measurements with heat current directed along $[1\bar{1}0]$. The absolute values of κ are 30% larger for $\vec{j}\,||\,[111]$ (not shown). In contrast to the data for $\vec{j}\,||\,[1\bar{1}0]$, the maximum at lowest temperatures around 1 T is significantly higher and the following decline is sharper.

The differences in the field dependencies for $\vec{j}\,||\,[111]$ and $\vec{j}\,||\,[1\bar{1}0]$ most likely originate from small misalignments of the magnetic field. Fig. 4.49 shows the $\kappa(B)$

[27] In contrast to the field direction parallel to [001] where the degeneracy is lifted in one single step.

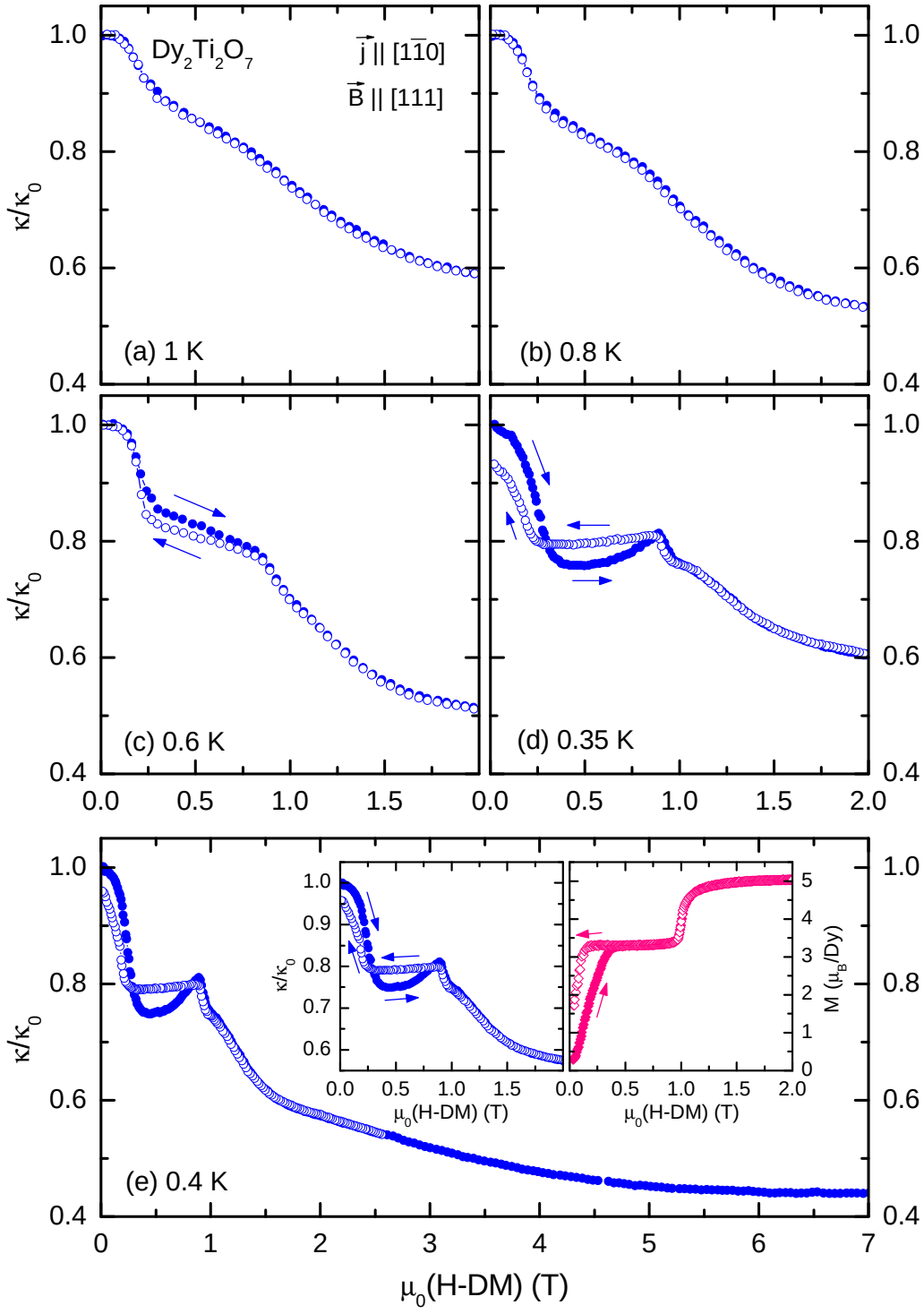

Figure 4.47: Relative change $\kappa(B)/\kappa(0\,\mathrm{T})$ of $Dy_2Ti_2O_7$ for $\vec{B} \,||\, [111]$ and $\vec{j} \,||\, [1\bar{1}0] \perp \vec{B}$. The inset of panel (e) shows the comparison of κ/κ_0 and the magnetization $M(B)$ at 0.4 K. Demagnetization effects are taken into account. The arrows indicate the field sweep direction.

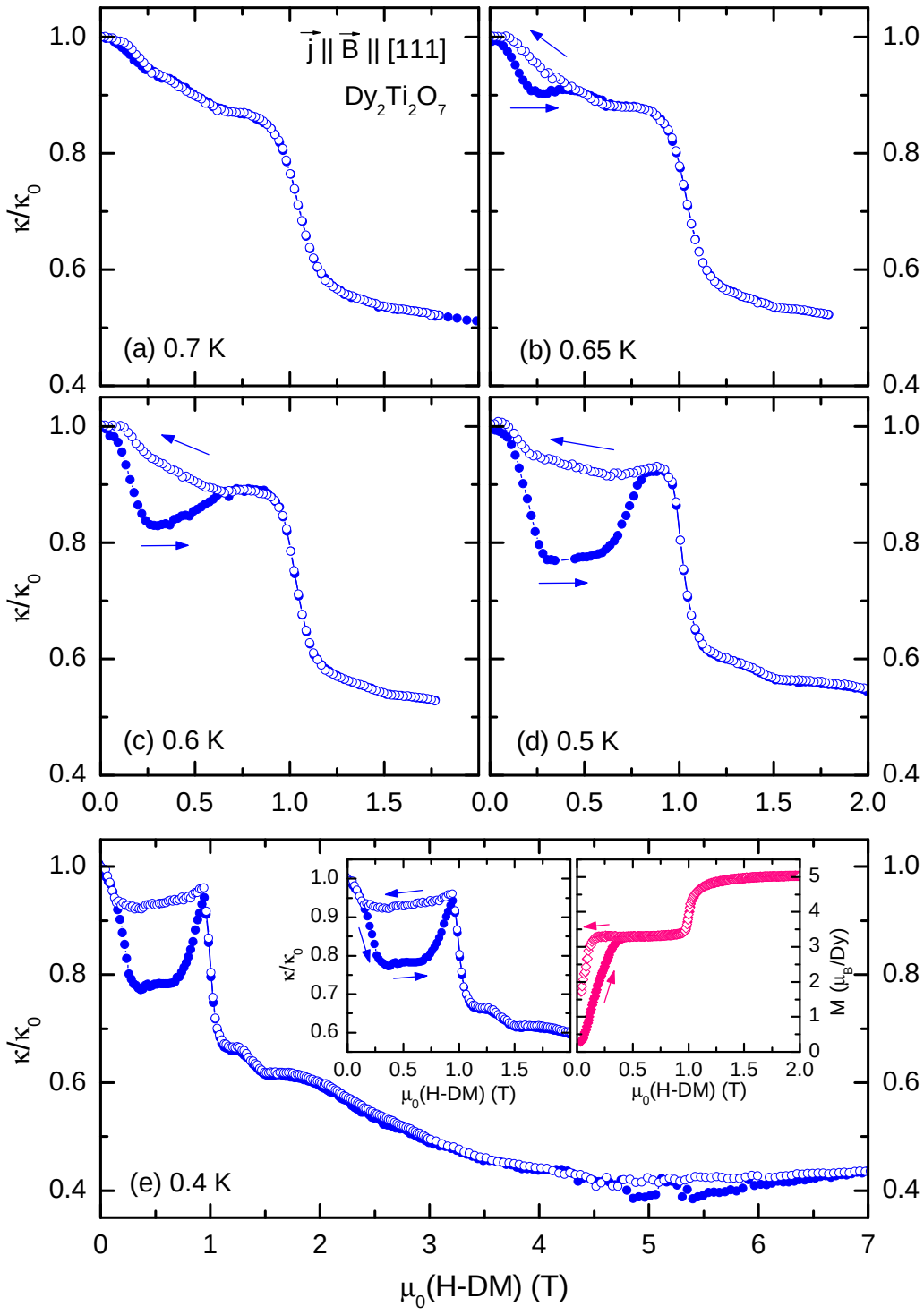

Figure 4.48: Relative change $\kappa(B)/\kappa(0\,\mathrm{T})$ of $Dy_2Ti_2O_7$ for $\vec{j} \,||\, \vec{B} \,||\, [111]$. The inset of panel (e) shows the comparison of κ/κ_0 and the magnetization $M(B)$ at 0.4 K. Demagnetization effects are taken into account. The arrows indicate the field sweep direction.

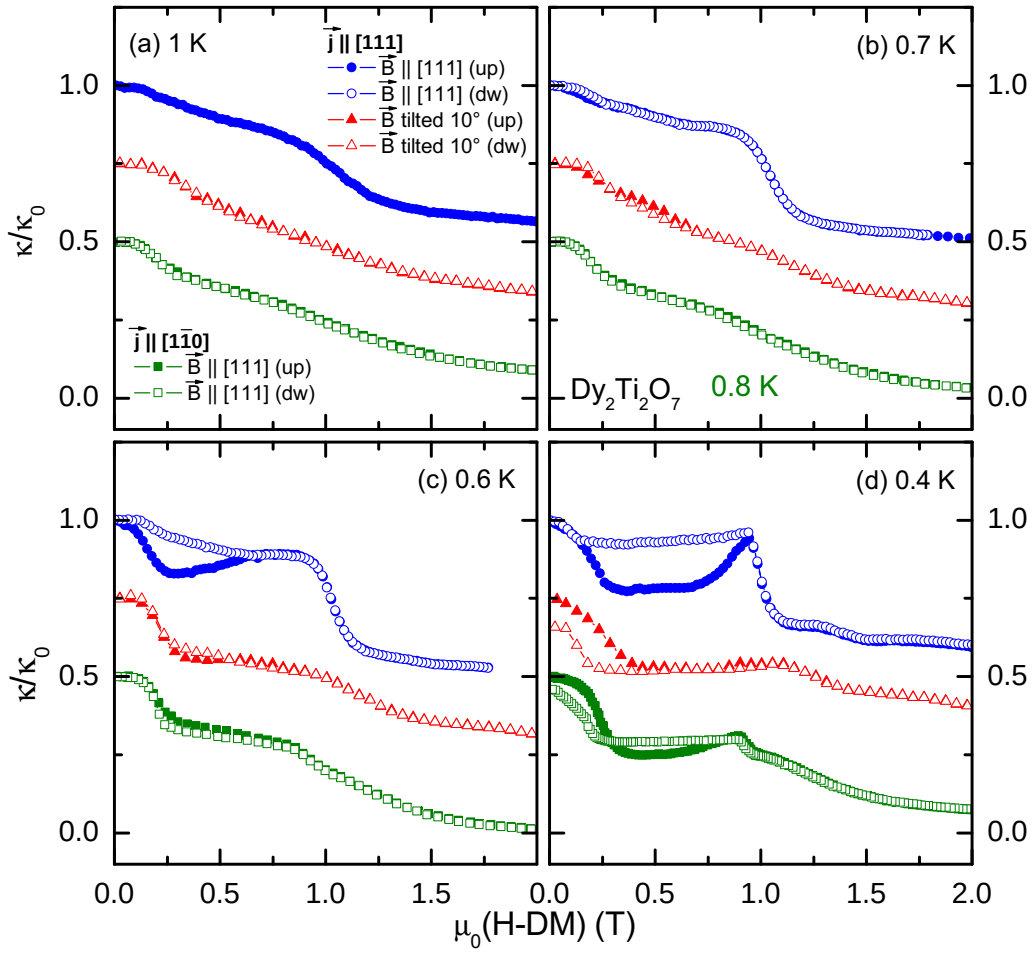

Figure 4.49: Comparison of $\kappa(B)/\kappa(0\,\mathrm{T})$ of $Dy_2Ti_2O_7$ with $\vec{j}\,||\,[111]$ and $\vec{B}\,||\,[111]$ as well as for a 10°-tilted magnetic field, together with the data for $\vec{j}\,||\,[1\bar{1}0]$ and $\vec{B}\,||\,[111]$. Demagnetization effects are taken into account. The different datasets are shifted by 0.25 with respect to each other.

data for both heat-current directions together with data obtained for $\vec{j}\,||\,[111]$ and a tilted magnetic field (by 10° from the [111] direction). One can clearly see that the data obtained for $\vec{j}\,||\,[1\bar{1}0]$ have much more similarities with the data for $\vec{j}\,||\,[111]$ measured with a tilted field, rather than with the data for the untilted field. Another explanation could be a misaligned magnetic field originating from a non-homogeneous demagnetization of the sample. For $\vec{j} \perp \vec{B}$, the demagnetization effect is much more pronounced, and as the sample has sharp edges and corners, the demagnetization field is certainly not homogeneous. For $\vec{j}\,||\,\vec{B}$, the demagnetization effect, as a whole, is less pronounced and, thus, a non-homogeneous inner magnetic field plays a less important role.

The zero-field values for $\vec{j}\,||\,[111]$ after cooling in zero-field coincide with the

values obtained after increasing and subsequently decreasing the magnetic field. This is different from the situation for $\vec{j} \,||\, [1\bar{1}0]$ where the zero-field data do not match. Hence, the slow relaxation processes observed for $\vec{j} \,||\, [1\bar{1}0]$ (Fig. 4.40 on page 86) are not observed for the heat current parallel to [111], at least in the measured temperature range down to 0.4 K. However, the situation is not exactly the same for both heat-current directions as the measurements with decreasing field for $\vec{j} \,||\, [111]$ ends in a significantly larger zero-field value than the corresponding value for $\vec{j} \,||\, [1\bar{1}0]$.

Heat Transport in the Kageomé-Ice Phase

The hysteresis of $\kappa(B)$ at lowest temperatures within the Kagomé-ice phase (Figs. 4.47(e) and 4.48(e)) is of particular interest as there is no corresponding hysteresis in the magnetization data (insets of Figs. 4.47(e) and 4.48(e)). Below 0.7 K, the thermal conductivity within the Kagomé-ice phase depends on whether the measurement is performed with increasing field starting after zero-field cooling or with decreasing field starting from high magnetic fields. Starting after zero-field cooling, $\kappa(B)$ is lower than the data obtained from the measurement starting at high fields. Figs. 4.48(a) - (d) show the evolution of the hysteresis for different temperatures. At 0.4 K, the hysteresis has a maximum width from $\sim 0.1\,\mathrm{T}$ up to 1 T. When increasing the temperature, the hysteresis becomes smaller. The upper critical field of the hysteresis shifts towards lower fields, whereas the lower critical field essential stays constant. Between the upper critical field and the transition at 1 T, $\kappa(B)$ is almost constant and the measurements for both field sweep directions coincide. At 0.7 K, the hysteresis finally vanishes. The step at 1 T and the plateau below, however, are still well observable.

A possible explanation of this feature is an eventual dependence of $\kappa(B)$ on an ordered (or disordered) Kagomé ice. When starting a field-dependent measurement at low temperatures, *e.g.* at 0.4 K after zero-field cooling, the spin-ice system starts from an entropic ground state. When entering the Kagomé-ice phase at $\sim 0.2\,\mathrm{T}$, the ground state is 3-fold degenerate (as discussed above). However, as the measurement starts from an entropic state, flipping the spins of the triangular planes can cause 3in-1out or 1in-3out defects within the Kagomé planes. As the spin-ice dynamics are very slow in this low-temperature regime and the monopole density is rather small, a reorientation of the tetrahedra is very unlikely. When approaching the phase transition at 1 T, the monopole density increases significantly and, hence, a rearrangement is much more likely. This can be understood by means of the single-tetrahedron approximation as the energy gap from the 3-fold degenerate 2in-2out ground state to the first excited 3in-1out (or 1in-3out) state vanishes at this particular field. Above 1 T, the excitations die out as the field-induced ground state consists only of fully polarized 3in-1out and 1in-3out tetrahedra (depending on the orientation of each tetrahedron with respect to the external field). This is consistent with the observed temperature

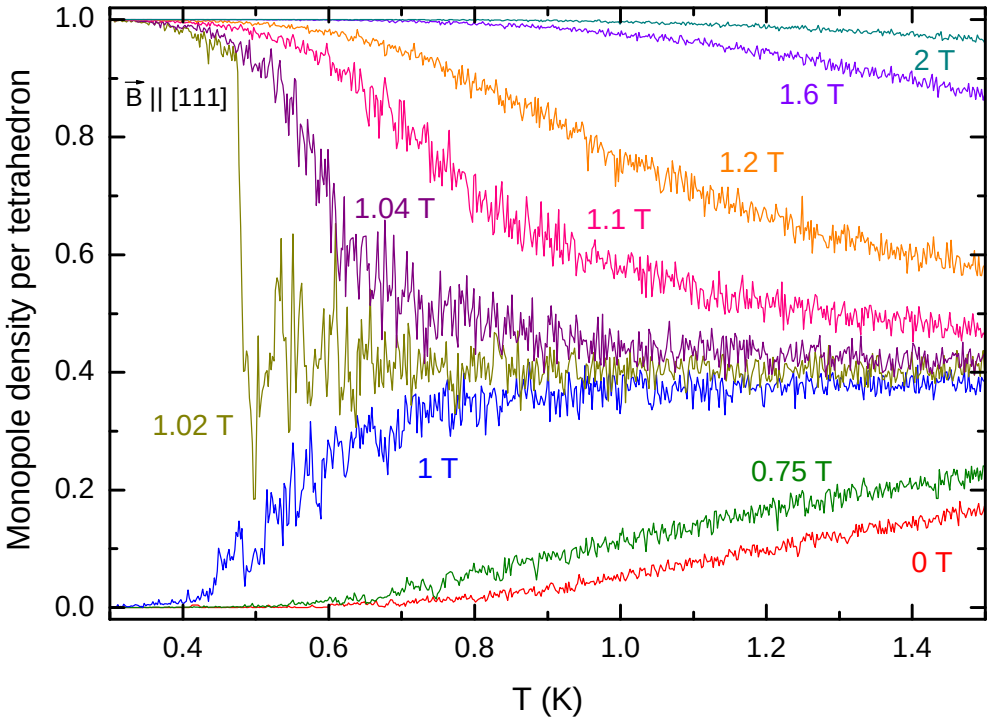

Figure 4.50: Simulation of the temperature dependence of the monopole density per tetrahedron of the dipolar spin ice for various magnetic fields parallel to [111]. All curves were obtained by slowly cooling at a constant magnetic field.

dependence of the upper critical field. At higher temperatures, the rearrangement of the Kagomé planes is possible for even lower fields due to a larger number of thermally excited monopoles.

This interpretation is supported by numerical studies of the dipolar spin ice. Fig. 4.50 shows the monopole density obtained by numerical calculations of the dipolar spin ice (Sec. 4.2.2). The curves were obtained by slowly cooling at a constant magnetic field parallel to [111]. For fields above 1 T, the monopole density converges to 1 when lowering the temperature. For lower fields, the monopole density vanishes at lowest temperatures. At a critical field of $\sim 1.02\,\mathrm{T}$, the monopole density almost stays constant and jumps either to 0 or 1 at a critical temperature $T_\mathrm{C} \sim 0.45$ K. This chaotic behavior can be understood by the step in the magnetization data at 1 T which becomes infinitesimally sharp for $T \to 0$ (Fig. 4.20 on page 62). Around the critical field of $\sim 1.02\,\mathrm{T}$, the monopole density strongly fluctuates at low temperatures.

When entering the Kagomé-ice phase from higher magnetic fields, the situation is different from the case of an increasing field. At higher fields (above 1 T), the measurement starts from a fully ordered phase. Below 1 T, the spins

within the Kagomé planes start to flip in order to achieve one of the energetically suitable 2in-2out configurations. As the spin ice is fully ordered above 1 T, when entering the Kagomé-ice phase the rearrangement of the spins of the Kagomé planes causes no 3in-1out or 1in-3out defects (or at least less than for the case of an increasing field).

Above 1 T, the measurements with different field-sweep directions (up and down) match each other, as in the fully polarized state above 1 T, the field-induced ground state degeneracy is lifted. This situation is analogous to the case of $\vec{B} \,||\, [001]$ (presented in the previous chapter).

A possibility to lift the degeneracy within the Kagomé-ice state is a slight deviation of the applied magnetic-field direction. In Ref. [170], the entropy is predicted to vanish for a small tilting from the [111] direction. Fig. 4.49 on page 98 shows the comparison of the $\kappa(B)$ data for $\vec{B} \,||\, [111]$ (blue circles) and for a 10°-tilted field (red triangles). In both measurements, the direction of the heat-current $\vec{j}$ has been kept fix along [111]. One can clearly see that the step-like feature at 1 T broadens when tilting the field. Furthermore, the hysteresis in the Kagomé-ice phase and the maximum around 1 T almost completely vanishes. The absence of the hysteresis in the data with tilted field can be explained via the single-tetrahedron approximation. Due to a tilted magnetic field, one of the three tetrahedron configurations forming the 3-fold degenerate Kagomé-ice ground state is energetically favorable compared to the others. Furthermore, the absence of a hysteresis indicates that the system is close to equilibrium below 1 T.

Analogously to the [001] field direction, the $\kappa(B)$ curves for $\vec{B} \,||\, [111]$ and $\vec{j} \,||\, [1\bar{1}0]$ also show a hysteretic behavior with slow relaxation processes (Fig. 4.51).[28] The zero-field value after decreasing the magnetic field is reduced compared to the value obtained after cooling in zero field. The reduced zero-field value slowly relaxes back to the initial value (not shown), analogously to the case for $\vec{B} \,||\, [001]$ (Figs. 4.39 and 4.40 on page 85 and 86, respectively).

Within the Kagomé-ice phase (at 0.4 K) including its hysteretic behavior, $\kappa(B)$ also depends on whether the curve started after zero-field cooling (red curve, part 1) or from the reduced zero-field value (green curve, part 3). The different curves with decreasing field (open red and green symbols, respectively) almost stay constant right at the value where the measurement started. At zero field, the green curve starts from a lower value and remains below the green curve, also in the Kagomé-ice phase up to the turning point of the field at 0.8 T. Within

[28] As shown in Fig. 4.48(e) on page 97, the zero-field values after zero-field cooling and after decreasing the magnetic field match each other for $\vec{j} \,||\, \vec{B} \,||\, [111]$, *i.e.* no slow relaxation is observed. The origin of the different behavior is unclear. A possible explanation could be the larger values of $\kappa(B)$ for a decreasing field within the Kagomé-ice phase compared to the data obtained for $\vec{j} \,||\, [1\bar{1}0]$. This can also be observed in the data for a 10° tilted field (Fig. 4.49 on page 98), which in contrast to the measurements with an untilted field, show lower values below 1 T and, in particular, show a slow relaxation at zero field.

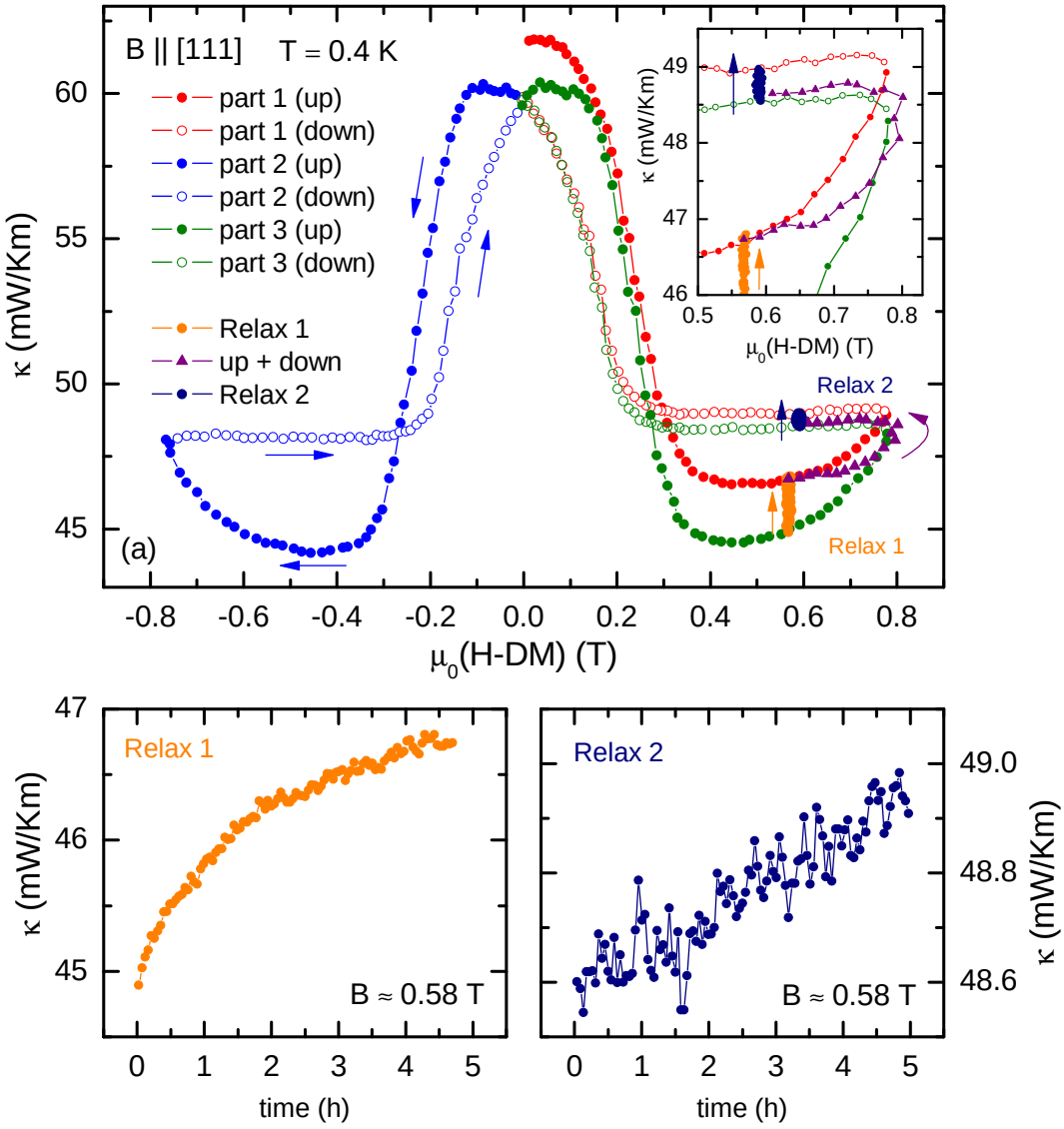

Figure 4.51: Hysteretic behavior of $\kappa(B)$ of $Dy_2Ti_2O_7$ for $\vec{j} \,||\, [1\bar{1}0]$ and $\vec{B} \,||\, [111]$ at 0.4 K. The hysteresis loop consists of three parts, also including the negative field range (part 2). The two different relaxation curves were measured at the same field with different starting conditions, *i.e.* starting from the up curve (orange, relax 1) and from the down curve (dark blue, relax 2). Demagnetization effects are taken into account.

the Kagomé-ice phase, the $\kappa(B)$ values slowly drift towards higher values. This strongly depends on whether one starts from the lower or from the upper part of the hysteresis. In Fig. 4.51, two different relaxation processes are shown at the same magnetic field of $\sim 0.58\,\mathrm{T}$ but starting from different κ values. The orange curve starts from the curve with increasing field (closed green symbols, part 3). The time resolved $\kappa(t)$ data (Fig. 4.51(b)) show the relaxation process for up to 5 hours. The relaxation curve ends at the closed red symbols (part 1). However, the relaxation curve exhibits a considerable drift even after 5 hours. Hence, one cannot decide by means of this data to which equilibrium value the $\kappa(t)$ values will converge. From the end point of the first relaxation (orange symbols, relax 1) the measurement continues towards the turning point at 0.8 T, and directly afterwards back again to 0.58 T (purple symbols). Although starting on the red curve (part 1), the data do not follow the red points when increasing the field, but rather return to the green curve (part 3), even when decreasing the field back to 0.58 T. Starting from this point, the κ values again start to drift upwards (Fig. 4.51(c), relax 2). Compared to the relaxation shown in panel (b) this relation is significantly slower and also does not reach equilibrium even after 5 hours.

In sum, the field dependence of $\kappa(B)$ for $\vec{B} \,||\, [111]$ shows a hysteretic behavior within the Kagomé-ice phase with very slow relaxation processes, even for a non-zero magnetic field. Due to the very large relaxation times, it is not possible to determine the thermal equilibrium value of $\kappa(B)$ just by waiting. One possibility to achieve thermal equilibrium within the Kagomé-ice phase would be to cool the system applying a constant magnetic field (field cooled), *cf.* the discussion about out-of-equilibrium processes on page 60. As every time-resolved $\kappa(t)$ data show the tendency to increase monotonically with time, it is most probable that in the thermodynamic limit, all curves tend to relax towards the largest observed κ values or even higher.

Magnetostriction

Analogously to the field direction parallel to [001] (Sec. 4.4), $\kappa(B)$ of $Dy_2Ti_2O_7$ also shows a field dependence for $\vec{B} \,||\, [111]$ above the saturation field of the magnetization (Figs. 4.47(e) and 4.48(e) on page 96 and 97, respectively). Magnetostriction measurements of $Dy_2Ti_2O_7$ were performed and give rise to the same interpretation of the high-field dependence of $\kappa_{\mathrm{ph}}(B)$ originating from lattice distortions induced by the external magnetic field. Different from the measurements performed for $\vec{B} \,||\, [001]$, here, the length change was measured along all three crystal directions keeping the field parallel to [111].[29]

Here again, the focus lies on the high-field region above 2 T where the magne-

[29] The sample used here is a thin, bar shaped (3.5 mm long) crystal. Hence, demagnetization effects are rather small.

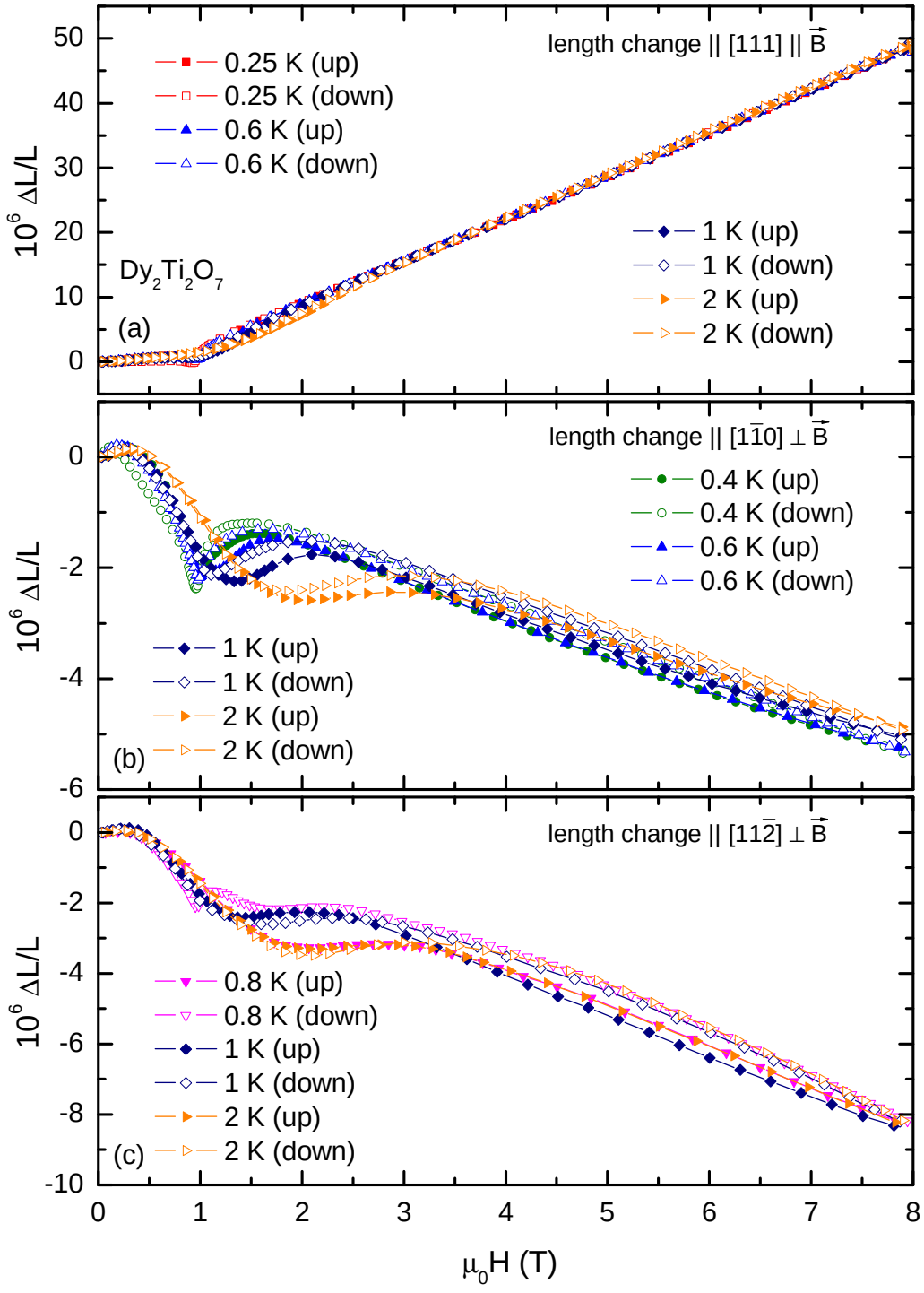

Figure 4.52: Field-induced length change of $Dy_2Ti_2O_7$ for $\vec{B} \,||\, [111]$ at various constant temperatures between 0.25 K and 2 K. The length change is measured (a) parallel and (b)&(c) perpendicular to $\vec{B}$.

tization is saturated (at least for low-enough temperatures). In Fig. 4.52, one can clearly see that the crystal elongates parallel to $\vec{B}$ and contracts in both perpendicular directions. The elongation parallel to $\vec{B}$ is one order of magnitude larger than the contraction along the perpendicular directions. The field dependence of the length change again is temperature independent for magnetic fields above 2 T.

The magnetostriction data clearly show that the crystal is stretched along the space diagonal of the cubic unity cell parallel to $\vec{B}$. Analogously to the [001] field direction, this stretching results in a suppressed phononic thermal conductivity and, hence, in a magnetic-field dependence of the phononic background $\kappa_{\mathrm{ph}}(B)$ of $Dy_2Ti_2O_7$.

4.5.2 $(Dy_{0.5}Y_{0.5})_2Ti_2O_7$

Fig. 4.53 shows the field dependence of the thermal conductivity $\kappa(B)$ of $(Dy_{0.5}Y_{0.5})_2Ti_2O_7$ (green triangles) together with the thermal conductivity of the mother compound $Dy_2Ti_2O_7$ (blue circles). Note, that the data are absolute values and, in particular, not scaled to match each other.

One can clearly see that the thermal conductivity of $(Dy_{0.5}Y_{0.5})_2Ti_2O_7$ is very similar to the thermal conductivity of $Dy_2Ti_2O_7$ above the kink at 1.5 T, whereas the spin-ice features observed below 1.5 T are almost completely suppressed in $(Dy_{0.5}Y_{0.5})_2Ti_2O_7$. Moreover, the thermal conductivity of $(Dy_{0.5}Y_{0.5})_2Ti_2O_7$ is not hysteretic with respect to the field sweep direction (not shown). Analogous to the field direction parallel to [001] (discussed in the previous chapter), one can conclude that the thermal conductivity of $(Dy_{0.5}Y_{0.5})_2Ti_2O_7$ essentially represents the phononic background κ_{ph} of $Dy_2Ti_2O_7$.

For $\vec{B}\,||\,[111]$, the field-induced ground-state degeneracy is lifted above the transition at 1 T. At lower fields (within the Kagomé-ice phase), the ground state is 3-fold degenerate and, hence, one expects κ_{mag} to be present up to a rather large field of 1 T. For $\vec{B}\,||\,[001]$, the situation is different as κ_{mag} for $\vec{B}\,||\,[001]$ is supposed to vanish already above $\sim 0.3\,\mathrm{T}$ (Fig. 4.42 on page 88). The $\kappa(B)$ data for $\vec{B}\,||\,[001]$ rapidly decrease below 0.5 T and stays almost constant up to $\sim 1.5\,\mathrm{T}$. The decrease in $\kappa(B)$ above 1.5 T is attributed to the field-dependent phononic background κ_{ph}. For $\vec{B}\,||\,[001]$, one can estimate the zero-field phononic contribution κ_{ph} by taking the plateau value around 1 T.

Such an estimation is much more difficult for $\vec{B}\,||\,[111]$ as a field of more than 1 T is needed to completely suppress κ_{mag}. For this fields, the suppression of κ_{mag} and κ_{ph} overlap. One can indeed observe a decrease of $\kappa(B)$ above 1 T. However, as also κ_{ph} exhibits a considerable field dependence above 1 T, the drop of $\kappa(B)$ above 1 T ends in kink upon a non-constant phononic background rather than in a plateau.

By considering only the data for $\vec{B}\,||\,[111]$ (Fig. 4.53) one could interpret the

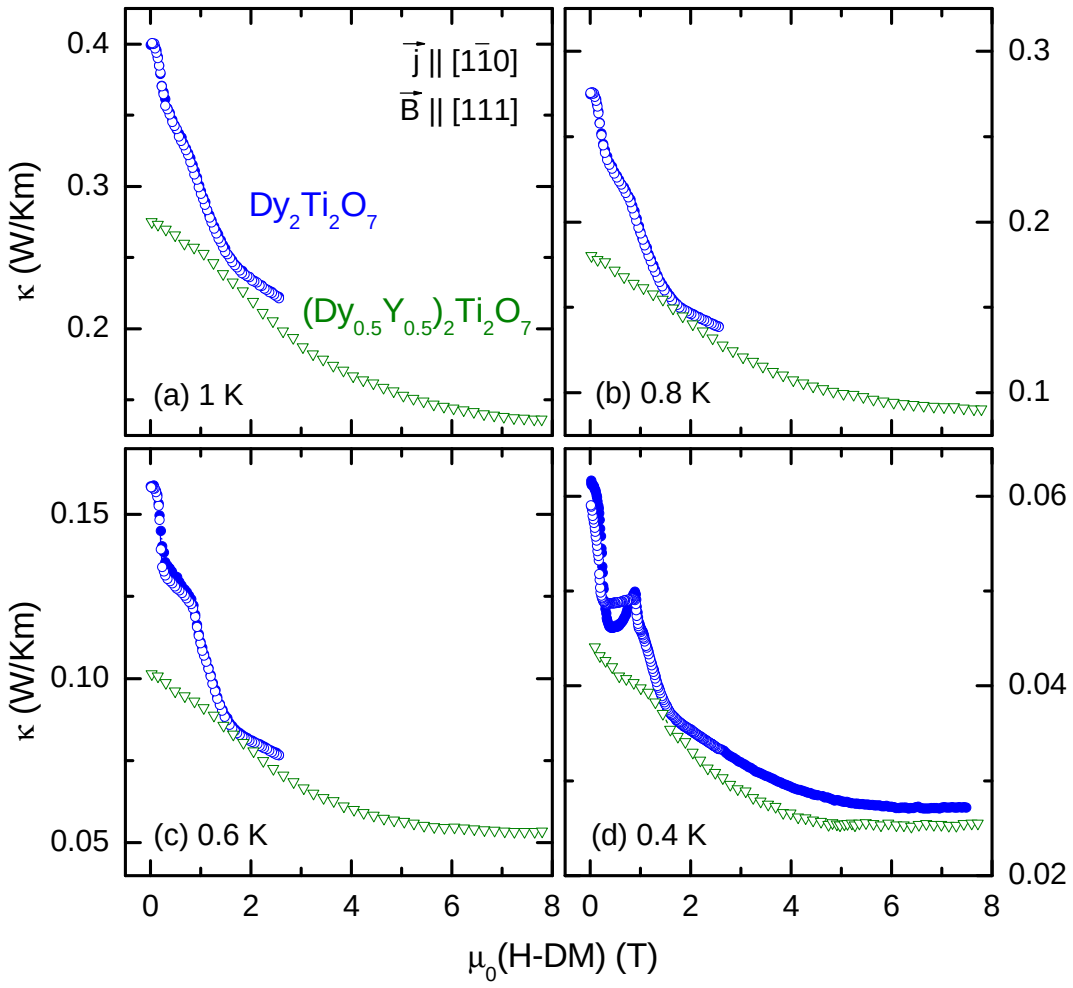

Figure 4.53: Field dependence of $\kappa(B)$ of the mother compound $Dy_2Ti_2O_7$ (blue circles) and of $(Dy_{0.5}Y_{0.5})_2Ti_2O_7$ (green triangles) for $\vec{B} \,||\, [111]$ and $\vec{j} \,||\, [1\bar{1}0]$. Demagnetization effects are taken into account.

whole $(Dy_{0.5}Y_{0.5})_2Ti_2O_7$ data as the phononic background of $Dy_2Ti_2O_7$. Obviously, the zero-field phononic contribution of $Dy_2Ti_2O_7$ cannot depend on the field direction and the zero-field phononic contribution for $\vec{B} \,||\, [111]$ is the same as for $\vec{B} \,||\, [001]$. Hence, it is more convenient to determine $\kappa_{\rm mag}$ and $\kappa_{\rm ph}$ in zero field by means of the data for $\vec{B} \,||\, [001]$. The zero-field contribution $\kappa_{\rm mag}$ obtained for $\vec{B} \,||\, [001]$ is consistent with the kink at $\sim 1.5\,$T, observed in Fig. 4.53.

The enhanced $\kappa(B)$ values of $(Dy_{0.5}Y_{0.5})_2Ti_2O_7$ compared to the phononic background of $Dy_2Ti_2O_7$ below $\sim 1\,$T probably originate from a magnetic contribution of $(Dy_{0.5}Y_{0.5})_2Ti_2O_7$ (*cf.* the discussion for $\vec{B} \,||\, [001]$ in the previous chapter). A detailed discussion comparing the field dependence $\kappa(B)$ for various field directions is presented in chapter 4.7.2.

4.5.3 $Dy_2(Ti_{0.9}Zr_{0.1})_2O_7$

In $Dy_2(Ti_{0.9}Zr_{0.1})_2O_7$, 10% of the non-magnetic Ti ions are replaced by Zr ions. The idea of Zr doping is to enhance the defect scattering and, thus, to reduce the phononic thermal conductivity compared to $Dy_2Ti_2O_7$ while essentially conserving the spin-ice properties. Fig. 4.54(a) shows $\kappa(T)$ of $Dy_2(Ti_{0.9}Zr_{0.1})_2O_7$ in comparison to $Dy_2Ti_2O_7$. The $Dy_2(Ti_{0.9}Zr_{0.1})_2O_7$ data show a glassy behavior, originating from defect scattering due to Zr doping.

Figs. 4.54(b)-(e) illustrate the field dependence of $\kappa(B)$ of $Dy_2(Ti_{0.9}Zr_{0.1})_2O_7$ (red triangles) together with $\kappa(B)$ of $Dy_2Ti_2O_7$ (blue circles). The data are given in absolute values. One can clearly see that in the shown temperature range, $\kappa(B)$ of $Dy_2(Ti_{0.9}Zr_{0.1})_2O_7$ decreases with increasing field and remains almost constant for fields above $\sim 3\,\mathrm{T}$ (dashed red line). This is in contrast to the thermal conductivity of $Dy_2Ti_2O_7$ which exhibits a pronounced field dependence (panel (e)). At lowest temperatures (0.4 K), $\kappa(B)$ for $Dy_2(Ti_{0.9}Zr_{0.1})_2O_7$ exhibits a plateau-like feature below 1 T, consistent with the data for $Dy_2Ti_2O_7$.

In order to compare the magnetic contributions κ_{mag} of $Dy_2Ti_2O_7$ and of $Dy_2(Ti_{0.9}Zr_{0.1})_2O_7$, the $Dy_2(Ti_{0.9}Zr_{0.1})_2O_7$ data are shifted upwards to match the zero-field phononic background κ_{ph} of $Dy_2Ti_2O_7$, illustrated as a blue dashed line which is located at the kink in the $Dy_2Ti_2O_7$ data at $\sim 1.5\,\mathrm{T}$. One can nicely see that both compounds have comparable magnetic contributions. The features in $Dy_2(Ti_{0.9}Zr_{0.1})_2O_7$ are slightly broadened as has also been observed in the magnetization data (Fig. 4.37 on page 80). The decrease of κ_{mag} above 1 T for $Dy_2(Ti_{0.9}Zr_{0.1})_2O_7$ extends over a larger field region compared to $Dy_2Ti_2O_7$, again consistent with magnetization data which saturate at higher fields.

4.5.4 Conclusion

In conclusion, analogous to $\vec{B}\,||\,[001]$, the field-dependent thermal conductivity $\kappa(B)$ of $Dy_2Ti_2O_7$ for $\vec{B}\,||\,[111]$ gives evidence for a considerable magnetic contribution κ_{mag}. Qualitatively, the thermal conductivity can be explained in the same manner as for $\vec{B}\,||\,[001]$. The magnetic contribution κ_{mag} depends on the field-induced ground-state degeneracy. It is maximum at zero field where the ground state is 6-fold degenerate and vanishes above 1 T where the degeneracy is lifted completely. In the Kagomé-ice phase between $\sim 0.3\,\mathrm{T}$ and 1 T, $\kappa(B)$ is strongly hysteretic with respect to the field sweep direction. The differences between the measurements with increasing and decreasing field can be interpreted by magnetic defects within the Kagomé planes which are created by polarizing the triangular planes between the Kagomé planes. When decreasing the field starting from a high field, the measurement starts from a fully polarized, *i.e.* ordered, state. When entering the Kagomé-ice phase below 1 T, the spins within the Kagomé planes can form the 3-fold degenerate ground state without defects as the triangular planes remain polarized.

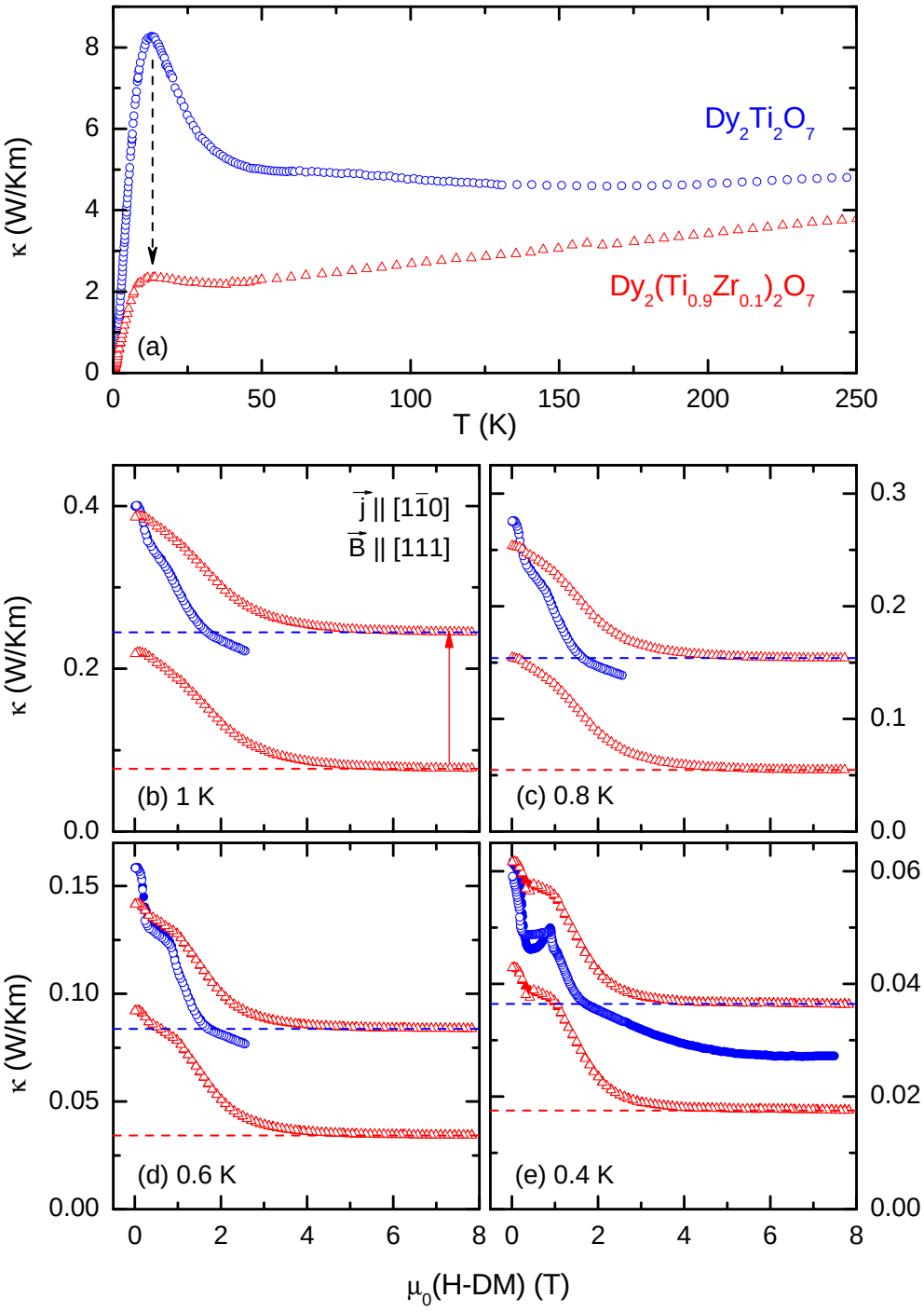

Figure 4.54: Thermal conductivity of $Dy_2(Ti_{0.9}Zr_{0.1})_2O_7$ (red triangles) and of $Dy_2Ti_2O_7$ (blue circles) for $\vec{j} \,||\, [1\bar{1}0]$ and $\vec{B} \,||\, [111]$. The blue and red dashed lines are the estimated zero-field phononic backgrounds of $Dy_2Ti_2O_7$ and of $Dy_2(Ti_{0.9}Zr_{0.1})_2O_7$, respectively. The field-dependent $Dy_2(Ti_{0.9}Zr_{0.1})_2O_7$ curves in panel (b)-(e) are shifted to match the zero-field phononic background of $Dy_2Ti_2O_7$. Demagnetization effects are taken into account.

The field-dependent phononic background κ_{ph} originates from lattice distortions due to torques of the Dy momenta, and can be separated from the magnetic contribution κ_{mag} either by suppressing κ_{mag} or κ_{ph}. The magnetic contribution κ_{mag} can be suppressed by doping with Y, *i.e.* by suppressing the spin-ice features of $Dy_2Ti_2O_7$. This essentially yields the field-dependent phononic background κ_{ph}. By doping with Zr, the phononic background is suppressed essentially leaving κ_{mag} unchanged. Additionally, Zr doping also suppresses the field dependence of the phononic background κ_{ph} as the scattering on the Zr defects turns out to be the dominant scattering process. The analysis of both doped compounds provide a consistent interpretation of the magnetic contribution κ_{mag} in the spin ice $Dy_2Ti_2O_7$.

In addition, the magnetostriction of $Dy_2Ti_2O_7$ nicely illustrates the deformation of the crystal and, hence, the deformation of the cubic unit cell. As a consequence, the phononic thermal conductivity is suppressed leading to a field-dependent phononic background κ_{ph}.

4.6 Thermal Transport for $\vec{B}\,||\,[110]$

4.6.1 $Dy_2Ti_2O_7$

Heat Transport along α and β Chains

For $\vec{B}$ parallel to [110], the Dy ions form α chains (parallel to $\vec{B}$) and β chains (perpendicular to $\vec{B}$) (Fig. 4.11 on page 50). The κ data presented in this chapter were measured on two similar samples of type II, *i.e.* with the long edge parallel to $[1\bar{1}0]$ (Fig. 4.27 on page 71). Thus, the heat-current direction is fixed to $\vec{j}\,||\,[1\bar{1}0]$. In the following, the thermal conductivity of $Dy_2Ti_2O_7$ and of $(Dy_{0.5}Y_{0.5})_2Ti_2O_7$ is investigated along the α and β chains. Both heat-current directions can be realized by the sample type used here. When the magnetic field is applied parallel to [110], the heat current $\vec{j}$ is parallel to the β chains. Applying the magnetic field parallel to the heat current results in $\vec{j}$ parallel to α chains.

Low-Field Thermal Conductivity

Fig. 4.55 shows the comparison of $\kappa(B)/\kappa(0\,\mathrm{T})$ for the heat current $\vec{j}$ directed along α and β chains for various constant temperatures and magnetic fields up to 0.5 T. The extension towards higher fields up to 7 T is shown in Fig. 4.56.

The data for $\vec{B}\,||\,[110]$ have similarities to those obtained for $\vec{B}\,||\,[001]$. However, the field-induced decrease of $\kappa(B)$ is less pronounced for $\vec{B}\,||\,[110]$ compared to $\vec{B}\,||\,[001]$. At 1.5 K, the thermal conductivity along the α and β chains is almost identical. At lower temperatures and magnetic fields around 0.5 T, the thermal conductivity along the β chains is slightly larger than along the α chains. At 0.4 K, this difference is most pronounced (Fig. 4.55(f)).

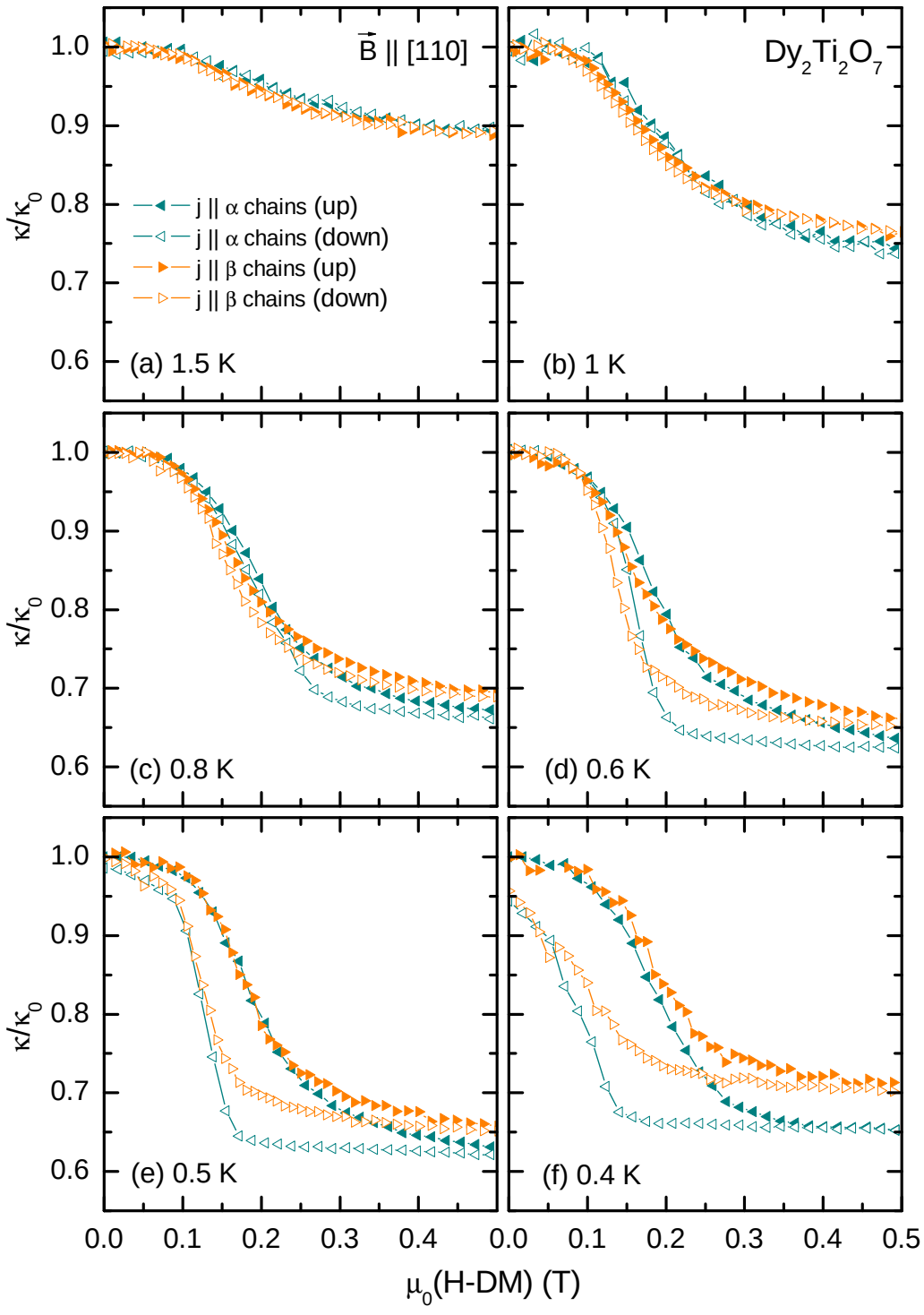

Figure 4.55: Relative change $\kappa(B)/\kappa(0\,\mathrm{T})$ of $Dy_2Ti_2O_7$ along the α and the β chains for $\vec{B}\,||\,[110]$ and magnetic fields up to 0.5 T. Demagnetization effects are taken into account.

For $\vec{B}\,||\,[001]$, κ_{mag} is supposed to be completely suppressed above $\sim 0.5\,\mathrm{T}$ as the field-induced ground-state degeneracy is lifted. For $\vec{B}\,||\,[110]$, however, the field-induced ground state remains 2-fold degenerate as two spins per tetrahedron are perpendicular to the magnetic field and are, thus, not affected. This explains the larger $\kappa(B)$ values for $\vec{B}\,||\,[110]$ above $\sim 0.5\,\mathrm{T}$ compared to the $\kappa(B)$ values for $\vec{B}\,||\,[001]$. It is remarkable that at 0.4 K, the thermal conductivity of $Dy_2Ti_2O_7$ along the β chains is larger then along the α chains. This shows that the monopoles which contribute to the heat transport can, indeed, easier propagate along the β chains which are not affected by the external field compared to the α chains which are polarized due to a magnetic field parallel to [110].

At 0.5 T, the $\kappa(B)$ values along the α chains are larger than the phononic background κ_{ph} estimated from the data for $\vec{B}\,||\,[001]$. Hence, for $\vec{B}\,||\,[110]$, a considerable magnetic contribution κ_{mag} can be observed although the α chains are polarized (*cf.* the magnetization data in Fig. 4.32 on page 75). This shows that the monopoles carrying heat can propagate not only via single spin flips, but can also hop to neighboring β chains, which are not directly linked with each other. A detailed study of κ_{mag} including all measured field directions is presented in chapter 4.7.2.

High-Field Thermal Conductivity

Fig. 4.56 shows the field-dependent thermal conductivity of $Dy_2Ti_2O_7$ along the α and β chains in the high-field region up to 7 T. The high-field data were measured on a different sample as the low-field data (Fig. 4.55).

As also observed for low fields, the thermal-conductivity data along the α and β chains are very similar. Between 1 K and 2 K, $\kappa(B)$ exhibits two kinks at 1 T and 2 T, which are less pronounced at lower temperatures. Above 1.5 K, $\kappa(B)$ for magnetic fields above 2 T essentially decreases linearly with increasing field. Below 1 K, an additional feature around 6 T upon the linear decrease is observed which appears in both measurements, *i.e.* for $\vec{j}$ along the α and the β chains. Below 0.6 K, $\kappa(B)$ is slightly larger along the β chains compared to the α chains. This difference is observable in the whole measured field range up to 7 T.

Below 0.6 K, a hysteresis with respect to the field-sweep direction is observed. A hysteresis has also been observed for $\vec{B}\,||\,[001]$ and $\vec{B}\,||\,[111]$. Compared to these field directions, however, the hysteresis width for $\vec{B}\,||\,[110]$ is much larger. At 0.4 K, the hysteresis in $\kappa(B)$ extends up to 2 T.

Magnetostriction

We also tried to measure the field-induced length change of $Dy_2Ti_2O_7$ for $\vec{B}\,||\,[110]$ in order to obtain information about crystal deformation as observed in the previous chapters. Unfortunately, for $\vec{B}\,||\,[110]$ it was not possible to measure the magetostriction with our setup as the sample starts to tilt in a magnetic field.

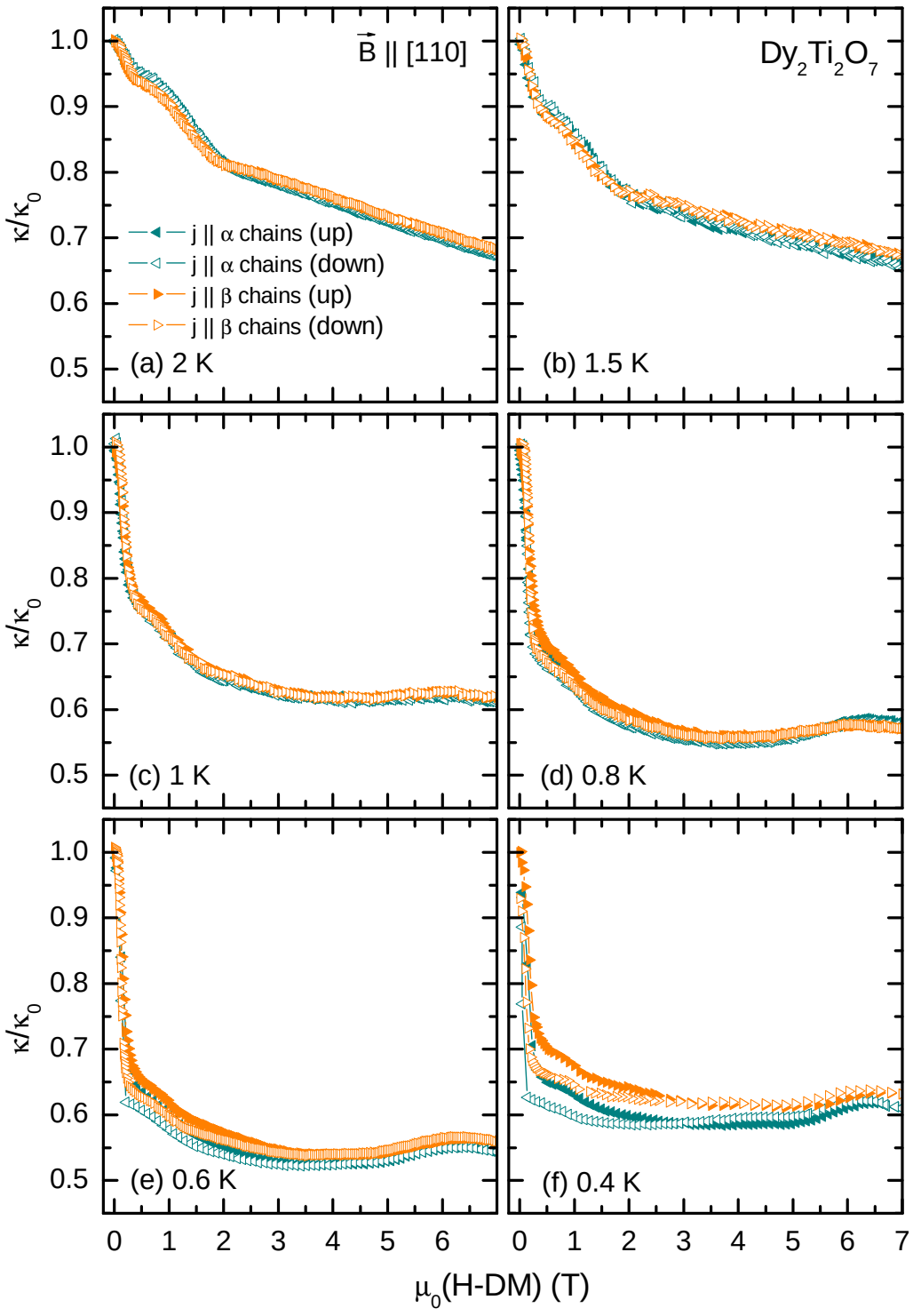

Figure 4.56: Relative change $\kappa(B)/\kappa(0\,\mathrm{T})$ of $Dy_2Ti_2O_7$ ($\vec{B} \,||\, [110]$) along the α and the β chains for magnetic fields up to 7 T. Demagnetization effects are taken into account.

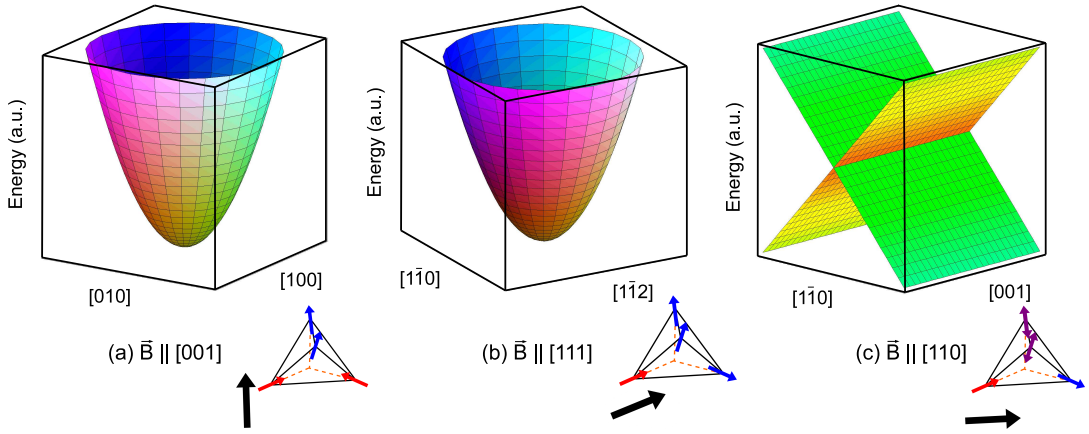

Figure 4.57: Potential energy of a single tetrahedron in an external magnetic field slightly tilted from (a) $\vec{B} \,||\, [001]$, (b) $\vec{B} \,||\, [111]$, and (c) $\vec{B} \,||\, [110]$. The energies are calculated for the field-induced ground states. For $\vec{B} \,||\, [110]$, the field-induced ground state is 2-fold degenerate (green and orange planes). The tetrahedron images are taken from Ref. [121].

This tilting purports an elongation of the crystal. The torque originates from the tendency of the sample to minimize its potential energy. For simplicity, the energy is calculated for a single tetrahedron in an external magnetic field (Sec. 4.2.1).

First, we study the dependence of the energy for the field directions parallel to [001] and [111]. For these field directions, the field-induced ground state (for large-enough fields) is non degenerate (Fig. 4.12 on page 51). The considerations made here restrict to small deviations from the untilted field which obviously do not change the field-induced ground state. Figs. 4.57(a) and (b) show the potential energy (in arbitrary units) of a single tetrahedron for small deviations from $\vec{B} \,||\, [001]$ and $\vec{B} \,||\, [111]$, respectively, calculated for a single tetrahedron. For $\vec{B} \,||\, [001]$ and $\vec{B} \,||\, [111]$, the potential energy has a (rotation symmetric) minimum for an untilted field. Therefore, the orientation of the sample with respect to the external field is stabilized when increasing the magnetic field.

The situation is different for $\vec{B} \,||\, [110]$. First of all, the field-induced ground state is 2-fold degenerate as for the untilted field two spins per tetrahedron are perpendicular to the magnetic field. This degeneracy is lifted for a tilted magnetic field.[30] The potential energies for these two tetrahedron configurations (orange and green plane) are illustrated in Fig. 4.57(c) as a function of a small tilting perpendicular to [110]. For a given tetrahedron configuration, the single tetrahedron (and hence the whole crystal) can lower its energy by tilting with respect to the external field. In thermal equilibrium, both tetrahedron configurations are equally distributed for an exactly aligned field. For the theoretical case of a

[30] Except for two discrete directions [001] and [00$\bar{1}$].

perfect orientation of the crystal combined with an exact population of 50% of the ground-state configurations, all torques cancel each other. However, this is a meta stable situation as an infinitesimally small deviation would prefer one of these configurations. For a more realistic case of a slight deviation of the crystal, one configuration is preferred. Hence, the crystal as a whole can lower its energy by tilting with respect to the external field. Once the crystal starts to tilt, this becomes a self-reinforcing process. Due to the tilting, the lower-lying energy level is even more populated what further enhances the torque. This effect makes it impossible to measure the magnetostriction with our setup.

4.6.2 $(Dy_{0.5}Y_{0.5})_2Ti_2O_7$

The thermal conductivity of $Dy_2Ti_2O_7$ and of $(Dy_{0.5}Y_{0.5})_2Ti_2O_7$ along the α and β chains[31] is shown in Fig. 4.58. Analogously to the other presented field directions ([001] and [111]), the field dependence of $\kappa(B)$ for $(Dy_{0.5}Y_{0.5})_2Ti_2O_7$ essentially resembles the high-field dependence of $\kappa(B)$ for $Dy_2Ti_2O_7$ and can, thus, be interpreted as the field-dependent phononic background κ_{ph} of $Dy_2Ti_2O_7$. At 2 K and 1.5 K (Figs. 4.58(a) and (b)), one can nicely see that the kinks at 1 T and 2 T are also found in the $(Dy_{0.5}Y_{0.5})_2Ti_2O_7$ data.

The enhanced thermal conductivity of $Dy_2Ti_2O_7$ around 6 T cannot be attributed to κ_{ph} as it is only observed for $Dy_2Ti_2O_7$ and not for $(Dy_{0.5}Y_{0.5})_2Ti_2O_7$. However, as the ground-state degeneracy is (at least theoretically) not lifted for an arbitrary large field, it is not straightforward to interpret the high-field data of $Dy_2Ti_2O_7$. In particular, it is unclear why the thermal conductivity $\kappa(B)$ is enhanced around the anomaly at 6 T. As the reference data of $(Dy_{0.5}Y_{0.5})_2Ti_2O_7$ only show a linear decrease for high fields even at lowest temperatures, one can speculate whether the anomaly observed in $Dy_2Ti_2O_7$ can be interpreted as an additional magnetic contribution appearing below 1 K. However, as mentioned above this is only a conjecture.

4.6.3 Conclusion

In conclusion, analogous to the field directions [001] and [111], discussed in the previous chapters, also the data for $\vec{B} \,||\, [110]$ give rise to the existence of a considerable magnetic contribution κ_{mag} of $Dy_2Ti_2O_7$ which correlates with the magnetization data.

A putative field-induced lattice distortion of $Dy_2Ti_2O_7$ for $\vec{B} \,||\, [110]$ cannot be analyzed by means of magnetostriction measurements as the sample tends to tilt due to an external magnetic field. This tilting originates from the tendency of the sample to minimize its potential energy.

[31] The α and β chains no longer are contiguous chains as every second Dy ions is replaced by an Y ion. α chains denote the direction parallel to $\vec{B}$ and β chains the direction perpendicular to $\vec{B}$.

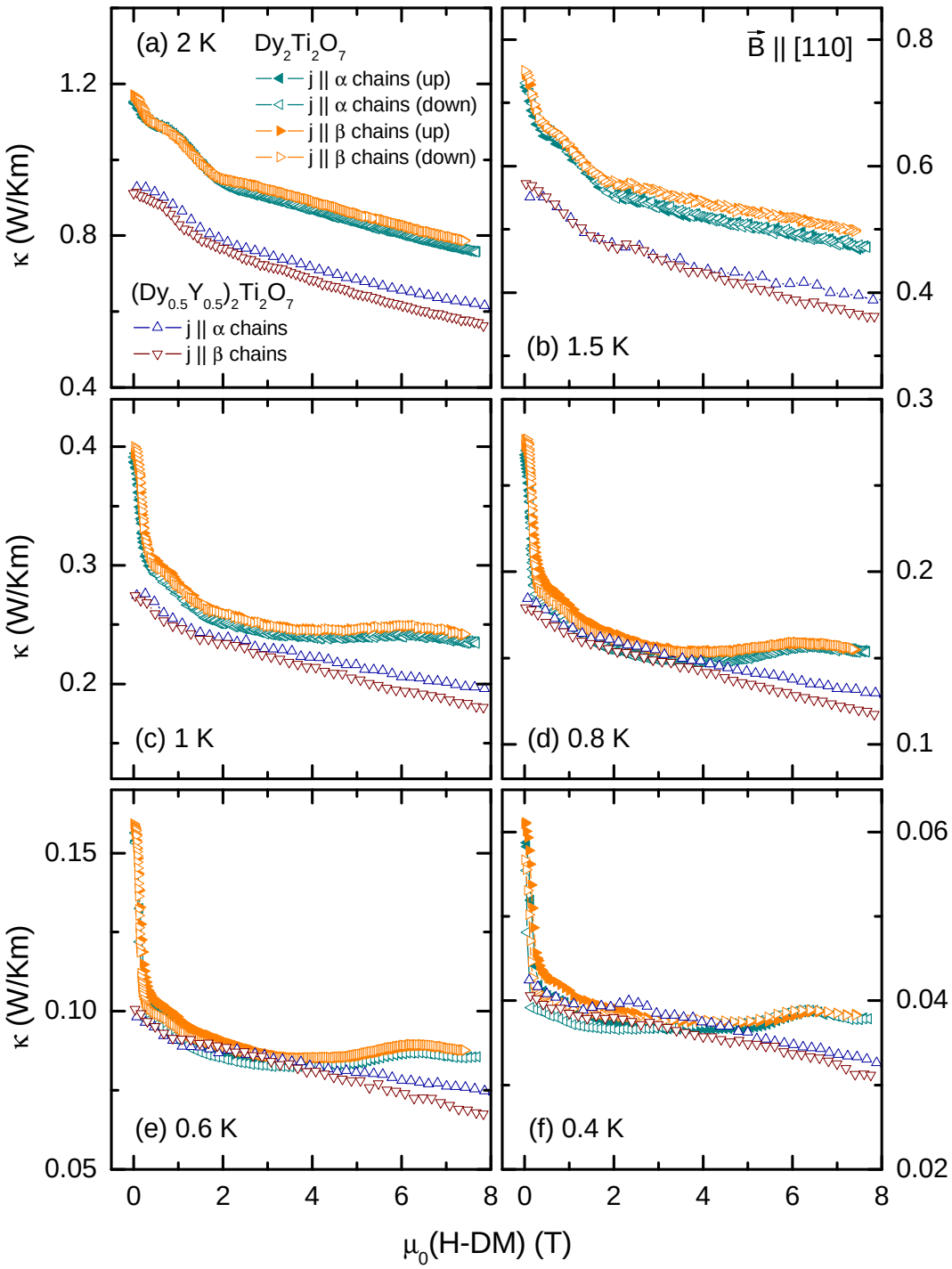

Figure 4.58: Field dependence of $\kappa(B)$ of $Dy_2Ti_2O_7$ and of $(Dy_{0.5}Y_{0.5})_2Ti_2O_7$ for $\vec{B}\,||\,[110]$ and for the heat current $\vec{j}$ directed along α and β chains, respectively. Demagnetization effects are taken into account.

However, by means of the study of the field dependent $\kappa(B)$ of the dilute spin ice $(Dy_{0.5}Y_{0.5})_2Ti_2O_7$, the high-field dependence of $\kappa(B)$ of $Dy_2Ti_2O_7$ can be identified as the field dependence of the phononic background κ_{ph} which is less pronounced compared to the other field directions (discussed in the previous chapters). Below 1 K, the $\kappa(B)$ data of $Dy_2Ti_2O_7$ for $\vec{B} \,||\, [110]$ show an anomaly around 6 T which is not observed in the data of the reference compound $(Dy_{0.5}Y_{0.5})_2Ti_2O_7$. The origin of this anomaly remains unclear.

An important peculiarity of the field direction parallel to [110] is the difference of $\kappa(B)$ for the heat current $\vec{j}$ directed along the α or the β chains. It turns out that below 0.6 K, in the presence of an external field, κ_{mag} is slightly larger for $\vec{j}$ directed along the β chains (*i.e.* $\vec{j} \perp \vec{B}$) compared to $\vec{j}$ parallel to the α chains (*i.e.* $\vec{j} \,||\, \vec{B}$).

A detailed analysis of κ_{mag} including all presented field directions is presented in chapter 4.7.2.

4.7 Discussion

4.7.1 Magnetic Heat Transport

In this chapter, the mechanisms of energy transport, *i.e.* heat transport, in $Dy_2Ti_2O_7$ will be discussed. Parts of this chapter have been published in Ref. [150]. As $Dy_2Ti_2O_7$ and the related doped compounds $Y_2Ti_2O_7$, $(Dy_{0.5}Y_{0.5})_2Ti_2O_7$, and $Dy_2(Ti_{0.9}Zr_{0.1})_2O_7$ are insulators (transparent single crystals), the heat can only be transported by phonons and magnetic excitations, *i.e.*

$$\kappa = \kappa_{ph} + \kappa_{mag} \,. \tag{4.28}$$

In Ref. [6], thermal-conductivity measurements of $Dy_2Ti_2O_7$ in zero field and in a magnetic field along the crystallographic [110] direction were analyzed by assuming that the thermal conductivity was purely phononic, and the field dependence of κ was attributed to phonon scattering on magnetic excitations. This interpretation, however, is not supported by our data presented in the previous chapters.

In this chapter, the presence of a zero-field magnetic contribution κ_{mag} is motivated by a microscopic model making use of the correlation of the magnetic-field dependence of $\kappa(B)$ and of the magnetization $M(B)$. The magnetic contribution κ_{mag} is suppressed by a magnetic field, where the suppression is strongly anisotropic with respect to the applied field direction. The observed suppression of κ_{mag} is attributed to the lifting of the ground-state degeneracy.

The phononic background κ_{ph} also exhibits a magnetic-field dependence, in particular, for magnetic fields above 1 T where, at least for low temperatures, the magnetization is fully saturated. The field dependence of κ_{ph} most likely originates from lattice distortions due to torques of the magnetic moments induced by the external magnetic field.

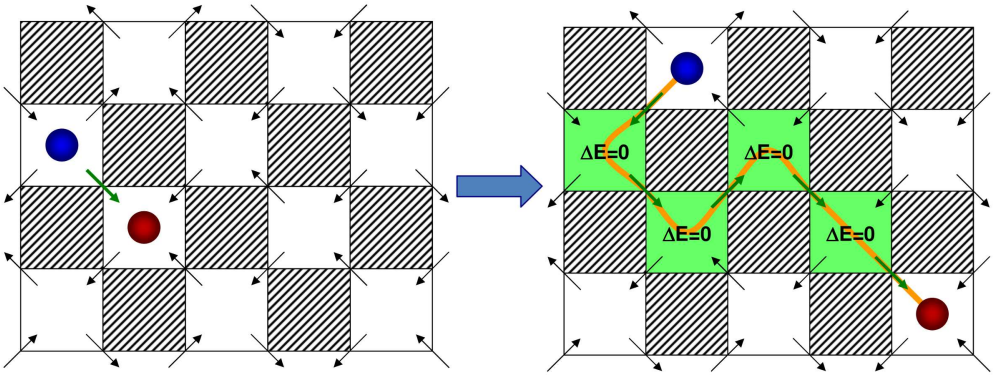

Figure 4.59: Simple 2D mapping of a 3D pyrochlore lattice. The corner-sharing white squares represent corner-sharing tetrahedra of the 3D lattice. The spins at the corners of the squares can either point into or out of the squares. (a) Creation of a monopole/anti-monopole pair by flipping the spin between two neighboring tetrahedra (green bold arrow) upon a ground state consisting of 2in-2out tetrahedra. (b) Separated monopole pair connected via a Dirac string (orange line).

As shown in Fig. 4.38 on page 83, the temperature dependence of the thermal conductivity $\kappa(T)$ of $Dy_2Ti_2O_7$ for a magnetic field of 0.5 T applied along the [001] direction exhibits similarities to the thermal conductivity of the isostructural non-magnetic reference compound $Y_2Ti_2O_7$. Both curves show a power-law behavior up to $\sim 3\,\mathrm{K}$ with a similar exponent. By contrast, the zero-field data of $\kappa(T)$ show a clear shoulder around 1 K. This qualitative differences give rise to the assumption that the field data of $Dy_2Ti_2O_7$ essentially represents the phononic background of the thermal conductivity and the zero-field data comprise an additional magnetic contribution upon the phononic background.

This conclusion is supported by measurements of the field dependence of the thermal conductivity $\kappa(B)$ for various constant temperatures and magnetic fields parallel to [001] (Fig. 4.39 on page 85). One can clearly see that the increase of magnetization $M(B)$ directly correlates with the decrease of thermal conductivity $\kappa(B)$. Even the hysteresis below 0.6 K is observable in both quantities, $M(B)$ and $\kappa(B)$.

A qualitative interpretation of the magnetic-field dependence of $\kappa(B)$ is obtained by means of a microscopic model. Fig. 4.59 shows a simplified two-dimensional mapping of the 3D pyrochlore lattice.[32] The tetrahedra of the 3D lattice are represented by (white) corner-sharing squares. The spins at each corner can point either into or out of the squares.

[32] A 2D lattice of corner-sharing squares does not really represent the correct 3D pyrochlore lattice. However, it is a suitable tool to illustrate spin-flip dynamics on a qualitative level.

Fig. 4.59(a) illustrates the creation of a monopole/anti-monopole pair (red and blue circle, respectively) on the background of randomly distributed 2in-2out tetrahedra, *i.e.* a spin ice in its ground state with one single (pair of) excitation. The monopole/anti-monopole pair has been created by flipping the spin connecting the excited tetrahedra (green bold arrow). This results in two adjacent excited tetrahedra with spin configurations 1in-3out (blue circle) and 3in-1out (red circle), respectively.

Monopoles (and anti-monopoles) can propagate independently via single spin flips (chapter 4.1.3). Fig. 4.59(b) shows the separated monopole/anti-monopole pair, which is connected via a Dirac string (orange line). The arrows which had to be flipped to move the monopoles are marked as green bold arrows. The connection of all these spins together form the Dirac string from monopole to anti-monopole. All tetrahedra through which a monopole had passed (marked as light-green squares) have a 2in-2out configuration differing from the initial state (Fig. 4.59(a)).

First, the case of zero magnetic field is discussed. In the absence of an external field, the ground state is highly degenerate, *i.e.* all 2in-2out configurations are energetically equivalent.[33] Thus, the tetrahedra in Fig. 4.59(b) which changed its 2in-2out configurations as a monopole excitation passed through it have the same energy as the initial configurations (Fig. 4.59(a)). As a consequence, one single monopole can propagate without energy loss. Thus, the monopole/anti-monopole pairs are not confined, and the single monopoles can propagate independently.

Note, that this argument holds strictly only for the single-tetrahedron approximation, *i.e.* for a model including only nearest-neighbor interaction. Numerical simulations, however, show that the long-range dipolar interaction has to be taken into account in order to obtain a correct description of the spin ice on a quantitative level (chapter 4.2.2). Moreover, Monte Carlo studies [129, 171] give rise to a Coulomb-like attraction between a monopole and an anti-monopole.[34] Taking such an interaction into account, the monopoles cannot be regarded as independently propagating excitations but as (weakly) confined charges. Within the Debye-Hückel theory (Sec. 4.2.3), also the possibility of monopole-charge screening is discussed.

In Fig. 4.60, the situation is illustrated schematically for an external magnetic field $\vec{B} \,||\, [001]$. This particular field direction leads to a non-degenerate field-

[33] This qualitative discussion is restricted to the single-tetrahedron approximation (chapter 4.2.1) and, thus, to the corresponding energy levels for the different spin configurations as introduced in Fig. 4.9 on page 48.

[34] The interaction has been obtained by numerical simulations of a dipolar spin ice with one monopole/anti-monopole pair. For this simulated system, the total energy is calculated as a function of the monopole/anti-monopole distance. To my knowledge, up to now, it is unclear whether the monopole excitations also interact with an external magnetic field. In Ref. [3], a monopole current effected by a small external field has been reported. However, this is currently under strong debate [5].

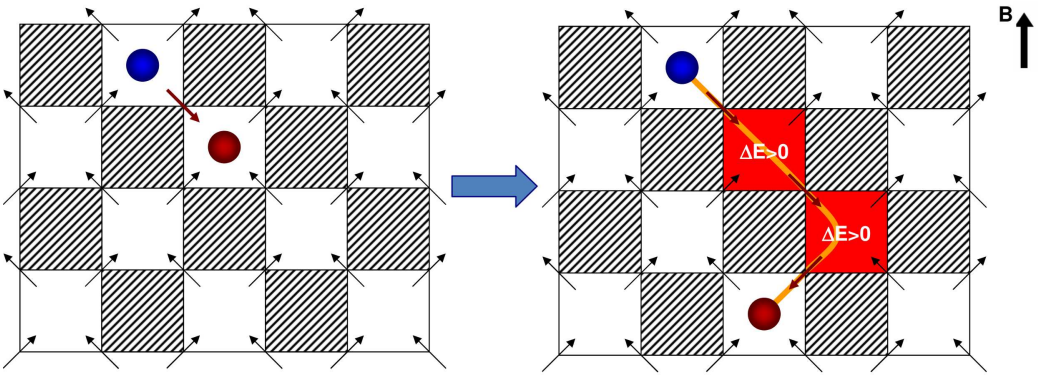

Figure 4.60: Simple 2D mapping of a 3D pyrochlore lattice with a magnetic field $\vec{B} \,||\, [001]$. (a) Creation of a monopole/anti-monopole pair by flipping the spin between two neighboring tetrahedra (red bold arrow) upon a field-induced non-degenerate ground state consisting of one single type of 2in-2out tetrahedra. (b) Separated monopole pair connected by a Dirac string (orange line).

induced ground state which consists of only one single type of 2in-2out tetrahedra (where all spins have a positive component in field direction). First of all, the energy gap increases with increasing field parallel to [001] as can be seen in Fig. 4.12(a) on page 51 (field-dependent splitting of the energy levels). Thus, the energy cost of a single tetrahedron is larger than in zero field. In Fig. 4.60(a), this is indicated by a bold red arrow connecting two adjacent excited tetrahedra. The monopole propagation via single spin flips is strongly suppressed due to the external field. Upon the background of the non-degenerate field-induced ground state, a propagating monopole leaves tetrahedra with an energetically unfavorable spin configuration behind (red squares). As every propagation step costs an additional amount of energy, the total energy cost increases with the distance of the separated monopole/anti-monopole pair. As a consequence, monopoles and corresponding anti-monopoles are strongly confined and, thus, the mobility of the monopole excitations is suppressed.

Summarizing, the mobility of the (anti-) monopole excitations in the spin ice strongly depends on the ground-state degeneracy. The mobility is maximum in zero magnetic field where the ground-state degeneracy is maximum (6-fold). As soon as the degeneracy is lifted (due to an external magnetic field), the monopoles are confined and the mobility decreases. A detailed study of the dependence of $\kappa(B)$ on the ground-state degeneracy is presented in chapter 4.7.2.

In the following, the zero-field contribution κ_{mag} is extracted quantitatively. As a magnetic field applied along the [001] direction lifts the ground-state degeneracy already for rather small magnetic fields, κ_{mag} is supposed to vanish entirely

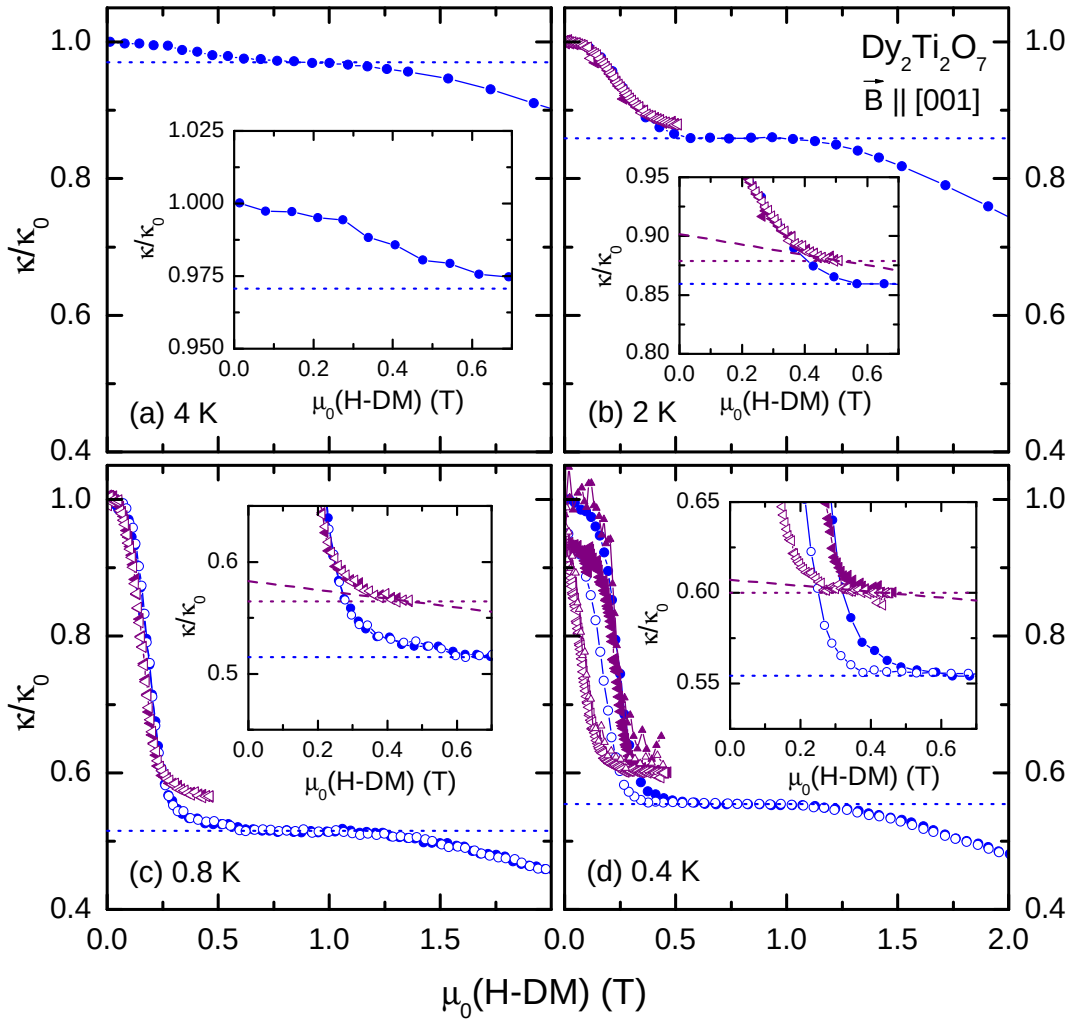

Figure 4.61: Comparison of the magnetic-field dependence of $\kappa(B)/\kappa(0\,\mathrm{T})$ of $Dy_2Ti_2O_7$ for $\vec{B} \,||\, [001]$ and $\vec{j} \,||\, [1\bar{1}0]$ obtained from two different measurements on two different samples (blue and purple symbols). The magnetic-field axes have been corrected from demagnetization effects.

for rather small fields. Therefore, this particular field direction is best suitable to extract the zero-field contribution κ_{mag}. The field dependence of $\kappa(B)$ for $\vec{j} \,||\, [1\bar{1}0]$ and $\vec{B} \,||\, [001]$ has been measured in two different runs on two different samples. In the first run, only the low-field region up to 0.5 T has been investigated. The high-field data, measured in the second run, show a clear plateau around 1 T where the magnetization is almost saturated at low-enough temperatures. The low-field data end before reaching this plateau and, thus, decrease at least above $\sim 0.8\,\mathrm{K}$. Furthermore, the two measurement runs provide slightly different field dependencies (Fig. 4.61). The $\kappa(B)$ data of the first measurement run (purple triangles) are slightly less suppressed compared to the $\kappa(B)$ data obtained from the second measurement run (blue circles).

As both $\kappa(B)$ datasets show a slightly different behavior, one cannot apply the same criteria to extract κ_{mag}. First, we consider the low-field data (purple triangles). The low-field $\kappa(B)$ data are not constant above the steplike decrease. Therefore, one can obtain the phononic background κ_{ph} by either taking the κ value at the highest measured field (purple dotted line) or by extrapolating the (linear) decrease backwards to zero field (purple dashed line). Obviously, the extrapolation provides larger values of κ_{ph}. The magnetic contribution κ_{mag} is obtained by subtracting the κ_{ph} value from the zero-field value $\kappa(0\,\mathrm{T})$. The high-field data (blue circles) show a pronounced plateau around 1 T. Here, one can identify κ_{ph} as the plateau value in $\kappa(B)$ (dotted blue line). As $\kappa(B)$ very weakly decreases within the plateau (not shown), one can extrapolate this decrease back to zero field. This results in slightly larger κ_{ph} values. Analogous to the low-field data, κ_{mag} is obtained by subtracting κ_{ph} from the zero-field data.

The resulting κ_{mag} is shown in Fig. 4.62(a) and (b) for the low- and the high-field data, respectively. The open blue circles are obtained by subtracting the temperature-dependent zero-field data from data measured at a constant suitable magnetic field[35]. The red squares are obtained from field-dependent measurements (Fig. 4.61) as explained in the previous paragraph. For the low-field data, the open red squares represent the κ_{mag} data obtained by identifying κ_{ph} as the κ value at the highest measured field (0.5 T). In case of the closed squares, κ_{ph} is extracted by extrapolating back to 0 T. For the high-field data, the open squares are obtained by identifying the plateau value as κ_{ph}. The open squares additionally take a slight decrease within the plateau into account.

Beside this, the κ_{mag} data obtained from the different approaches and for the different samples are all very similar and show the same behavior. The temperature dependent zero-field contribution κ_{mag} exhibits a maximum around 1.5 K, very close to that of c_{mag} (Fig. 4.7 on page 45) and practically vanishes above 4 K. The similarity of the magnetic specific heat c_{mag} and the extracted magnetic zero-field contribution κ_{mag} supports the interpretation of a magnetic heat transport as discussed above.

[35] 0.5 T for the low-field data (Fig. 4.62(a)) and 1 T for the high-field data (Fig. 4.62(b)).

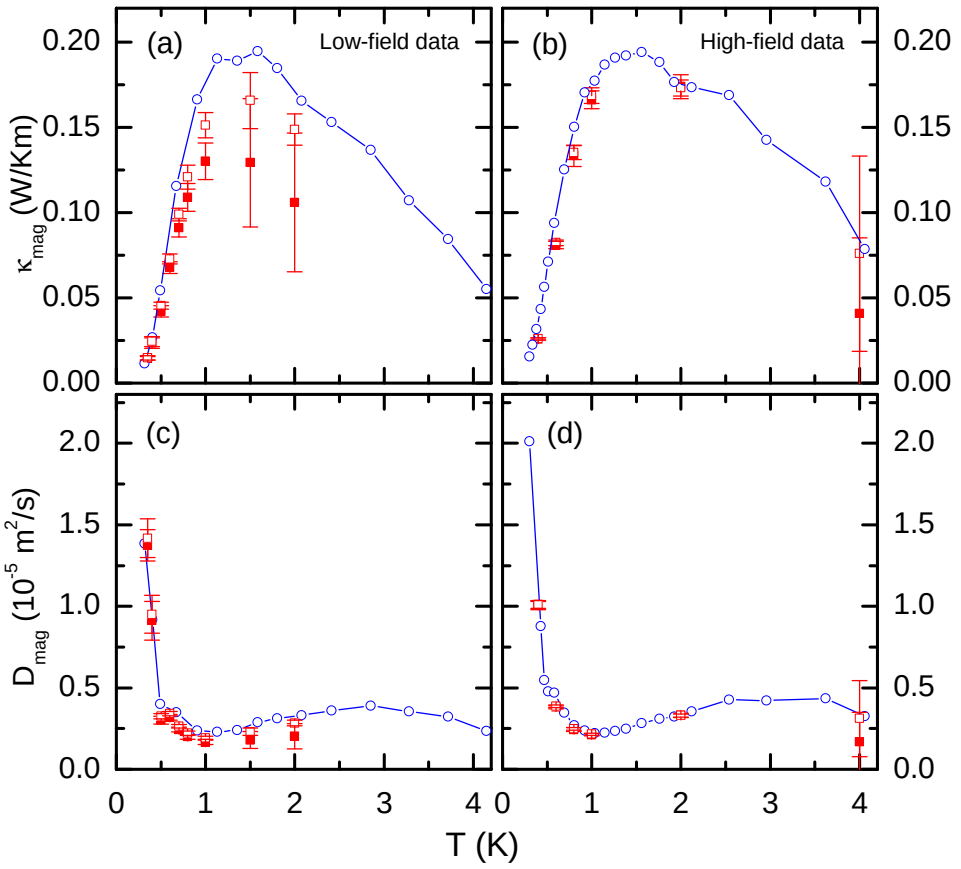

Figure 4.62: (a) and (b): Temperature dependence of the zero-field magnetic contribution κ_{mag} of $Dy_2Ti_2O_7$ obtained from the low-field and the high-field measurement, respectively. (c) and (d): Magnetic diffusion coefficient obtained as the ratio of the corresponding κ_{mag} ((a) and (b)) and c_{mag} [151] (Fig. 4.7 on page 45).

By means of κ_{mag} and the magnetic specific heat c_{mag}, one can calculate the magnetic diffusion coefficient

$$D_{\mathrm{mag}} = \frac{\kappa_{\mathrm{mag}}}{c_{\mathrm{mag}}}\,, \tag{4.29}$$

which is shown in Fig. 4.62(c) and (d) (obtained from the corresponding κ_{mag} data (a) and (b)). Above 1 K, the diffusion coefficient D_{mag} is only weakly temperature dependent, but is strongly increased towards lower temperatures. This fits to the qualitative expectation of a high monopole mobility by single spin flips on the degenerate ground state. At low temperatures, the monopole excitations are highly dilute, what can be demonstrated by numerical simulations (Figs. 4.21 and 4.24 on pages 64 and 68, respectively). This results in a large mean free path and, hence, in a large diffusion coefficient. With increasing temperature,

the number of monopoles increases and, thus, the diffusion coefficient is expected to decrease. In the simplified model of single spin flips, this follows from the fact that a monopole can pass an already excited tetrahedron (*i.e.* another (anti-) monopole) only via simultaneous spin flips.

Within the kinetic gas theory, the diffusion coefficient is related via $D = v\ell/3$ with the mean velocity v and the mean free path ℓ of the particles. However, this relation cannot be directly applied to the actual monopole gas in $Dy_2Ti_2O_7$ for various reasons. First of all, the number of monopoles is not conserved and, moreover, neither the (average) velocity of monopoles nor their interaction with each other or with the phonon excitations is well understood up to now. Quite recently, an expression for the monopole mobility in a (magnetic or electric) field has been derived [134], but it is unclear whether this result can be related to the experimental D_{mag} arising from a finite-temperature gradient in zero field. Despite these uncertainties, a rough estimation of a mean free path is given by assuming the monopole velocity to be $v = t_{\mathrm{eff}}/(\hbar\pi/a_{\mathrm{d}}) \sim 20\,\mathrm{m/s}$, which results from the distance of neighboring tetrahedra $a_{\mathrm{d}} = 4.34\,\text{Å}$ and assuming an effective bandwidth for monopole hopping t_{eff} to be of the order of 1 K. The mean free path $\ell = 3D_{\mathrm{mag}}/v$ linearly scales with $D_{\mathrm{mag}}(T)$ and reaches the μm range, *i.e.* ~ 1000 unit cells for $T < 0.7\,\mathrm{K}$, which may be understood from the low monopole density. Moreover, we can estimate the scattering time $\tau = \ell/v$ to be in the μs range, in agreement with relaxation times observed by muon spin rotation [3, 146, 147]. However, even around 2 K, ℓ is still of the order of ~ 100 unit cells although the mean monopole distance is of the order of a_{d}. This suggests that at least towards higher temperatures, more complex hopping models have to be involved to describe $\kappa_{\mathrm{mag}}(T)$.

Up to this point, only the zero-field contribution κ_{mag} has been discussed (Fig. 4.62). In addition, one can extract the temperature dependence of κ_{mag} for a constant magnetic field by subtracting the temperature dependence of κ_{ph} from the measured $\kappa(T)$ data for a constant magnetic field. The 0.5 T data ($\vec{B} \,||\, [001]$) is determined as κ_{ph}.[36] Fig. 4.63 shows the temperature dependence of κ_{mag} for various constant magnetic fields parallel to [001] between 0 T and 0.29 T. The magnetic fields are corrected with respect to demagnetization effects. The magnetic contribution $\kappa_{\mathrm{mag}}(T)$ is suppressed with increasing $\vec{B} \,||\, [001]$, while the curve shapes basically do not change. All curves have a maximum around $\sim 1.5\,\mathrm{T}$ which is suppressed with increasing field.

Analogously, one obtains the field dependence of $\kappa_{\mathrm{mag}}(B)$ at constant temperatures by subtracting the phononic contribution κ_{ph} obtained from the plateau value of the $\kappa(B)$ data for $\vec{B} \,||\, [001]$. The results are shown in Fig. 4.64 for dif-

[36] The temperature-dependent $\kappa(T)$ measurements at constant magnetic fields have been performed during the first measurement run including only the low-field region below 0.5 T. Although the $\kappa(B)$ data did not reach the plateau value at 0.5 T (purple triangles in Fig. 4.61), the 0.5 T curve of the same measurement run is chosen as the phononic reference for reasons of consistency.

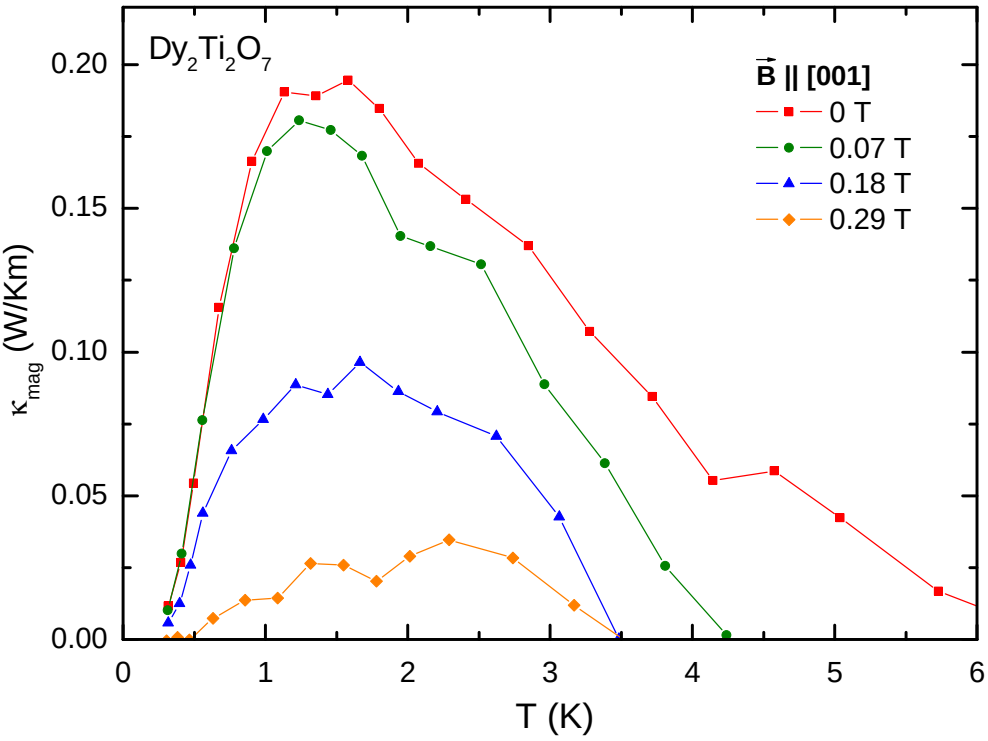

Figure 4.63: Temperature dependence of $\kappa_{\mathrm{mag}}(T)$ of $Dy_2Ti_2O_7$ for various constant magnetic fields between 0 T and 0.29 T applied along [001].

ferent field directions. The shown data have been measured with decreasing field starting from high fields. As discussed in the previous chapters, these data are supposed to be closer to equilibrium than the data measured with increasing field. In the following, $\kappa_{\mathrm{mag}}(B)$ is discussed for the different field directions with reference to the respective field-induced ground-state degeneracy.

4.7.2 Dependency on the Ground-State Degeneracy

In the previous chapter, the lifting of the ground-state degeneracy for a magnetic field parallel to [001] was utilized to completely suppress the magnetic contribution κ_{mag} and, hence, to separate the magnetic from the phononic contribution of the thermal conductivity. For $\vec{B} \,||\, [111]$, the field-induced ground-state degeneracy is lifted not below 1 T. Within the Kagomé-ice phase below 1 T, the ground state is 3-fold degenerate. For $\vec{B} \,||\, [110]$, the ground-state degeneracy is not lifted (at least theoretically) up to arbitrary large fields. The ground state remains 2-fold degenerate. In this chapter, the correlation between κ_{mag} on the degree of the ground-state degeneracy is studied.

Fig. 4.64 compares the field-dependencies of κ_{mag} of $Dy_2Ti_2O_7$ for different magnetic-field directions. Aside the data for $\vec{j} \,||\, \vec{B} \,||\, [111]$ (brown squares), all

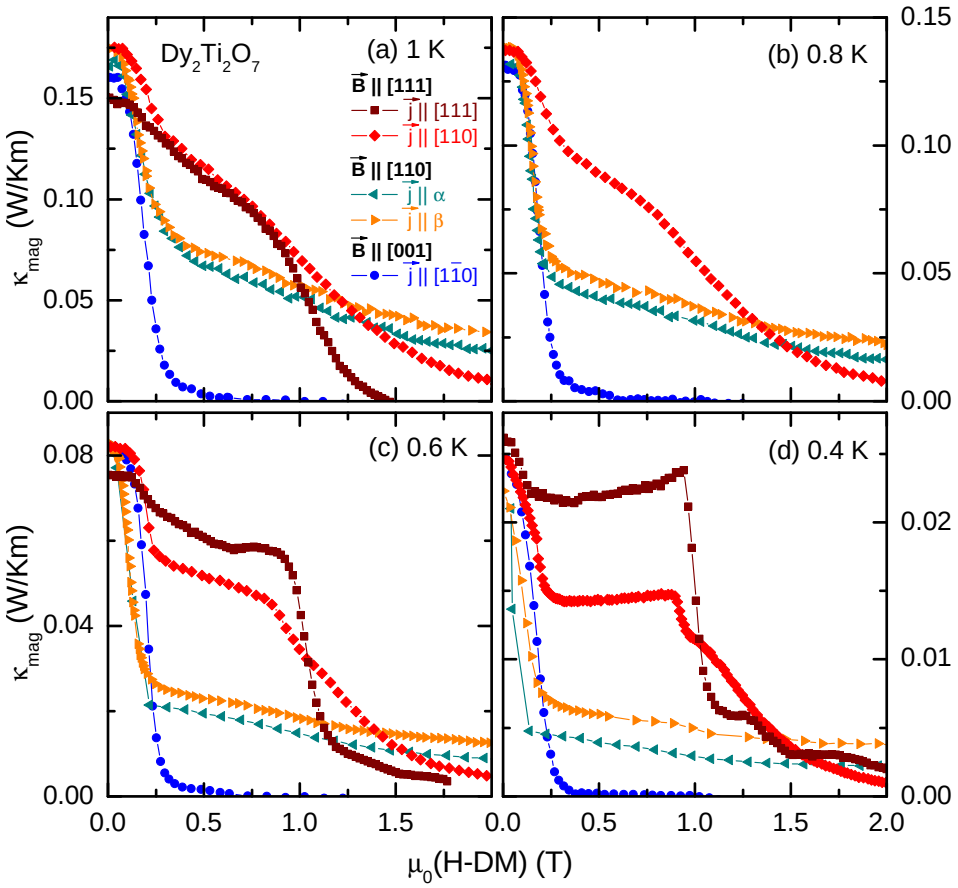

Figure 4.64: Magnetic-field dependence of $\kappa_{\mathrm{mag}}(B)$ at various constant temperatures between 0.4 K and 1 K. The $\kappa(B)$ values for $\vec{j} \,||\, \vec{B} \,||\, [111]$ are scaled by 30% to match the zero-field data for $\vec{j} \,||\, [1\bar{1}0]$. All data are measured with decreasing field starting from high fields. Demagnetization effects have been taken into account to rescale the magnetic-field axis.

datasets have been measured directing the heat current along the $[1\bar{1}0]$ direction. The differences between the $\vec{B} \,||\, [111]$ datasets (red diamonds and brown squares) most likely originate from an inhomogeneous or misaligned magnetic field in the data measured with $\vec{j} \,||\, [1\bar{1}0]$.

Here, the discussion is restricted to magnetic fields below 2 T. In this low-field region, the field dependence of the phononic background κ_{ph} is less pronounced compared to the field dependence of κ_{mag}. Therefore, the reduction of $\kappa(B)$ is supposed to essentially originate from a reduction of κ_{mag} (Fig. 4.61 on page 120). In Fig. 4.64, a clear dependence of $\kappa_{\mathrm{mag}}(B)$ on the ground-state degeneracy is observed. In zero field, κ_{mag} is maximum as the ground-state degeneracy is maximum (6-fold). For $\vec{B} \,||\, [001]$, $\kappa_{\mathrm{mag}}(B)$ vanishes above $\sim 0.5\,\mathrm{T}$ (dependent on temperature) as the ground-state degeneracy is lifted. This is not surprising as

κ_{ph} is determined from the $\vec{B}\,||\,[001]$ data.

For $\vec{B}\,||\,[110]$ (2-fold-degenerate ground state), $\kappa_{\mathrm{mag}}(B)$ remains finite up to 2 T. Above the sharp decline below $\sim 0.5\,\mathrm{T}$, $\kappa_{\mathrm{mag}}(B)$ decreases linearly with increasing field. The slope of this decrease becomes smaller when lowering the temperature. At 0.4 K, $\kappa_{\mathrm{mag}}(B)$ almost stays constant above 0.5 T. Below 0.6 K, a difference is observed with respect to whether the heat current $\vec{j}$ is directed along the α or the β chains. At 0.4 K, this difference is most pronounced. Here, one can clearly see that the heat can be better transported parallel to the β chains compared to the α chains. The heat transport parallel to the α chains will be discussed in Sec. 4.7.4.

For $\vec{B}\,||\,[111]$, the field-induced ground-state degeneracy can be tuned by the magnetic-field strength. The 6-fold-degenerate zero-field ground state changes to a 3-fold-degenerate ground state for magnetic fields between $\sim 0.2\,\mathrm{T}$ and 1 T (Kagomé-ice phase). Above 1 T, the spin ice is fully polarized resulting in a non-degenerate ground state consisting of alternating 3in-1out and 1in-3out tetrahedra. Here, a 3in-1out tetrahedron is surrounded by four 1in-3out tetrahedra and vice versa. Hence, above 1 T, the spin ice is full of (anti-) monopoles. However, these monopoles are not free like it is the case for a sparse monopole gas as every monopole is adjacent to an anti-monopole and vice versa, *i.e.* all monopoles are localized. Within the Kagomé-ice phase (below 1 T, 3-fold degenerate ground state), $\kappa_{\mathrm{mag}}(B)$ is even larger compared to the data for $\vec{B}\,||\,[110]$. This observation holds for both heat-current directions ($\vec{j}\,||\,[1\bar{1}0]$ and $\vec{j}\,||\,[111]$). For the lowest measured temperature of 0.4 K, the plateau-like feature is most pronounced, *i.e.* $\kappa_{\mathrm{mag}}(B)$ and the magnetization $M(B)$ almost remains constant within the Kagomé-ice phase. At higher temperatures, the plateau features in $\kappa_{\mathrm{mag}}(B)$ and $M(B)$ are less pronounced and the step at 1 T starts to broaden. The values of κ_{mag} for $\vec{B}\,||\,[111]$ are well above the data obtained from the other field directions. Above 1 T, $\kappa_{\mathrm{mag}}(B)$ rapidly decreases towards zero (depending on temperature). Above this phase transition, the ground-state degeneracy is lifted. Here again, this feature is best observable at lowest temperatures (0.4 K), where also the step-like increase of the magnetization data $M(B)$ is most pronounced.

In sum, a correlation between κ_{mag} and the ground-state degeneracy is observed for various magnetic-field directions. The data in Fig. 4.64 clearly shows that κ_{mag} is larger the higher the field-induced ground-state degeneracy is.

4.7.3 Influence of Doping on the phononic Thermal Conductivity

In the previous chapters, the temperature range well below 5 K was investigated. The thermal-conductivity data below 5 K give rise to the existence of a magnetic contribution κ_{mag}. At higher temperatures (up to room temperature), the thermal conductivity of $Dy_2Ti_2O_7$ and the related compounds $Y_2Ti_2O_7$, $(Dy_{0.5}Y_{0.5})_2Ti_2O_7$, and $Dy_2(Ti_{0.9}Zr_{0.1})_2O_7$ are supposed to be purely phononic.

Fig. 4.65 shows the thermal conductivity of the mother compound $Dy_2Ti_2O_7$ together with the data for the non-magnetic reference system $Y_2Ti_2O_7$ and the Zr doped compound $Dy_2(Ti_{0.9}Zr_{0.1})_2O_7$. All datasets exhibit a maximum around 15 K, which is characteristic for Umklapp scattering. In $Dy_2(Ti_{0.9}Zr_{0.1})_2O_7$, $\kappa(T)$ resembles a glassy behavior as it is strongly suppressed compared to the data for $Dy_2Ti_2O_7$. Most likely, this originates from additional defect scattering on the Zr ions which are much larger than the Ti ions. Around the maximum at 15 K, the thermal conductivity of the non-magnetic $Y_2Ti_2O_7$ is much larger compared to $Dy_2Ti_2O_7$.

The thermal conductivity of $Y_2Ti_2O_7$ obviously is purely phononic. Below $\sim 1\,\mathrm{K}$, $Y_2Ti_2O_7$ and $Dy_2Ti_2O_7$ provide comparable κ values, and $Y_2Ti_2O_7$ shows the same power-law behavior as the zero-field phononic background of $Dy_2Ti_2O_7$ (Fig. 4.38 on page 83). One possible explanation for the differences between $Dy_2Ti_2O_7$ and $Y_2Ti_2O_7$ at higher temperatures is an additional resonant phonon scattering on the crystal-field excitations of the Dy ions in $Dy_2Ti_2O_7$ (Eq. 2.11 on page 13).

In the following, the thermal conductivity data for $Dy_2Ti_2O_7$, $Y_2Ti_2O_7$ and $Dy_2(Ti_{0.9}Zr_{0.1})_2O_7$ are analyzed above $\sim 5\,\mathrm{K}$ by means of the Debye model (Sec. 2.1.1). We start the analysis by performing a Deybe fit (Eq. 2.5 on page 11) of the thermal conductivity for $Y_2Ti_2O_7$. The best fit is obtained for parameters shown in Tab. 4.1. The parameters L and ℓ_{min} are determined manually and are kept fix during the fit routine. The result is shown in Fig. 4.65 as a solid line.

In order to describe the thermal conductivity of $Dy_2Ti_2O_7$, we account for resonant phonon scattering on crystal-field excitations via the corresponding scattering rate (Eq. 2.11 on page 13). The parameters obtained for $Y_2Ti_2O_7$ (Tab. 4.1) are kept fix and we introduce two additional parameters R and the crystal-field splitting $\Delta = 280\,\mathrm{K}$ [136]. The $Dy_2Ti_2O_7$ data is best described by $R = 0.022 \cdot 10^{-40}\,\mathrm{s}^3$. Around the maximum at 15 K, the fit (solid line in Fig. 4.65) well describes the experimental data for $Dy_2Ti_2O_7$. At higher temperatures, however, the Debye fit provides too small κ values. Note that above $\sim 100\,\mathrm{K}$, $Dy_2Ti_2O_7$ has a larger thermal conductivity than $Y_2Ti_2O_7$. Because it is not possible to enhance $\kappa(T)$ by adding further scattering parameters, a proper description of the $Dy_2Ti_2O_7$ data above 100 K is prevented. One has to keep in mind that there is only one single parameter R to describe the data for $Dy_2Ti_2O_7$ as all other parameters are determined from the previous fit for

$v\,[10^3\,\mathrm{m/s}]$	$L\,[10^{-3}\,\mathrm{m}]$	$P\,[10^{-43}\,\mathrm{s}^3]$	$U\,[10^{-18}\,\mathrm{s}]$	u	$\Theta\,[K]$	$\ell_{\mathrm{min}}\,[10^{-10}\,\mathrm{m}]$
4.07	0.1	15.8	15.7	8.73	490	10

Table 4.1: Fit parameters of the Debye model (Eq. 2.5 on page 11) for $Y_2Ti_2O_7$ (Fig. 4.65).

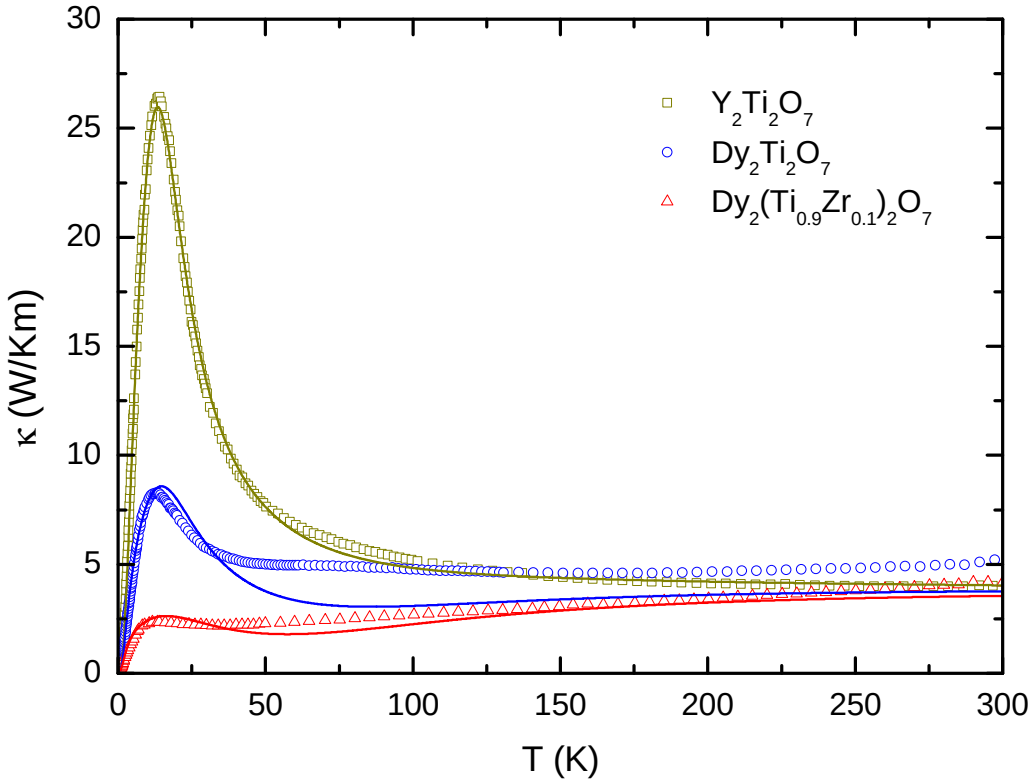

Figure 4.65: Thermal conductivity of $Y_2Ti_2O_7$, $Dy_2Ti_2O_7$, and $Dy_2(Ti_{0.9}Zr_{0.1})_2O_7$ for $\vec{j} \,||\, [1\bar{1}0]$. The solid lines are fits of the phononic thermal conductivity using the Debye model.

$Y_2Ti_2O_7$. Despite the discrepancies above $\sim 50\,\mathrm{K}$, the fits of the experimental $\kappa(T)$ data of $Dy_2Ti_2O_7$ yield at least qualitatively a well description by the Debye model including resonant phonon scattering.

In a second step, we want to describe the data for $Dy_2(Ti_{0.9}Zr_{0.1})_2O_7$. As mentioned above, the Zr ions lead to additional defect scattering. Within the Debye model, the parameter P accounts for defect scattering. Analogously to the previous paragraph, all parameters are kept fix and only the P parameter is adjusted. The best coincidence with experimental data is achieved with $P = 550 \cdot 10^{-43}\,\mathrm{s}^3$ (solid line in Fig. 4.65). Here also, beside slight deviations above $\sim 50\,\mathrm{T}$, the experimental data is in principle well described by the Debye model.

In summary, we obtain a consistent picture of the different phononic conductivities of $Dy_2Ti_2O_7$, $Y_2Ti_2O_7$, and $Dy_2(Ti_{0.9}Zr_{0.1})_2O_7$. Starting from the nonmagnetic $Y_2Ti_2O_7$, the thermal conductivities of $Dy_2Ti_2O_7$ and $Dy_2(Ti_{0.9}Zr_{0.1})_2O_7$ can be described by additional phonon scattering on crystal-field excitations and enhanced defect scattering.

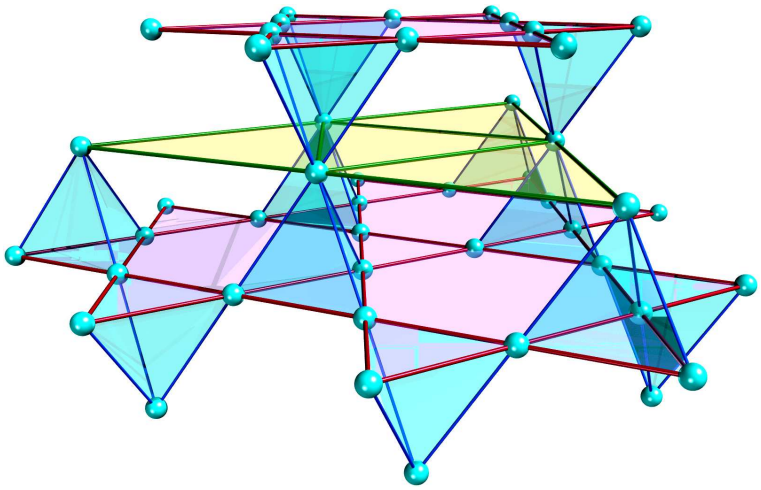

Figure 4.66: Pyrochlore lattice, consisting of alternating triangular (green) and Kagomé (red) layers perpendicular to [111].

4.7.4 Open Questions

In the previous chapters, a variety of arguments for the existence of an additional magnetic contribution κ_{mag} of the thermal conductivity upon the phononic background κ_{ph} were introduced. However, at this moment, some issues are not well understood and give rise to open questions.

The main problem is the lack of a microscopic model which is able to consistently explain the field-dependent thermal-conductivity data including different magnetic-field directions as well as different heat-current directions. In Sec. 4.7.1, the reduction of κ_{mag} due to an external magnetic field parallel to [001] is described by means of a microscopic model including monopole propagation via single spin flips. For this particular field direction, all spins are affected equally and, thus, no crystallographic direction is specified. Hence, one does not expect to observe an anisotropy with respect to the heat-current direction. However, the situation is different for a magnetic field parallel to [111] or [110]. These field directions affect the spins unequally and, thus, break the cubic crystal symmetry.

First, the [111] field direction is discussed here. For $\vec{B} \,||\, [111]$, the spins within the triangular planes, which separate the Kagomé planes (Fig. 4.66), are supposed to be easily polarized parallel to $\vec{B}$ as their local easy axes are parallel to the applied field. Fig. 4.12(b) on page 51 shows the field-dependent energy splitting of the different spin configurations for a single tetrahedron. In zero field, the ground state consists of 6 equivalent 2in-2out configurations. Below 1 T, an applied field $\vec{B} \,||\, [111]$ partly lifts the degeneracy and results in a 3-fold degenerate ground state. These 3 configurations have in common that the spin parallel to the external field is polarized. The remaining three spins, which are affected equally, form the Kagomé planes, and the polarized spins at the tips form the triangular planes

(Fig. 4.66). One has to keep in mind that the energy levels shown in Fig. 4.12 on page 51 only reflect the situation in thermal equilibrium and do not make any assertion about the change from one energy level to the other. The high degeneracy of the ground state within the Kagomé-ice phase below 1 T can, indeed, explains a high monopole mobility and fluctuations. However, restricting to single spin flips (Sec. 4.7.1), one cannot explain how an excitation can propagate along the [111] direction as it has to pass through a fully polarized triangular plane to reach a neighboring Kagomé plane. Thus, regarding propagation only via single spin flips, one would expect the thermal conductivity along the [111] direction to be strongly suppressed within the Kagomé-ice phase resulting in κ values comparable to the values for $\vec{B} \,||\, [001]$. However, the experimental data for $\vec{j} \,||\, \vec{B} \,||\, [111]$ (Fig. 4.64) show the opposite behavior as $\kappa(B)$ is enhanced within the Kagomé-ice phase compared to other field directions and exhibits a sharp drop to a value comparable to $\vec{B} \,||\, [001]$ when leaving the Kagomé-ice phase above 1 T. The fact that for $\vec{B} \,||\, [111]$ the thermal conductivity along the $[1\bar{1}0]$ direction (*i.e.* within the Kagomé planes) is smaller than along the [111] direction (perpendicular to the Kagomé planes) cannot be explained by such a microscopic model. However, as discussed in Sec. 4.5.1, the lower κ values for $\vec{j} \,||\, [1\bar{1}0]$ most likely originate either from a misaligned external field or from an inhomogeneous demagnetization field.

The field direction parallel to [110] has a congeneric problem. This particular field direction splits the pyrochlore lattice into two disjunct subsystems, the α chains (parallel to $\vec{B}$) and the β chains (perpendicular to $\vec{B}$). Again, regarding only single spin flips one would expect the magnetic contribution κ_{mag} to be completely suppressed along the α chains, whereas along the β chains, κ_{mag} is supposed to be less affected or even completely unaffected. Here again, this considerations do not match with the experimental results (Fig. 4.64). Above 0.8 K, the $\kappa(B)$ data along the α and β chains almost perfectly match each other. For lower temperatures, one can observe the tendency that the thermal conductivity along the β chains is slightly larger compared to the α chains. However, even at lowest temperatures (0.4 K), the $\kappa(B)$ values along the α chains are significantly larger than the values obtained for $\vec{B} \,||\, [001]$ which are assumed to reflect the phononic background κ_{ph}.

The discrepancy between the microscopic model including only single spin flips and experimental data show that this model is far too simple. First of all, the restriction to single spin flips is not physically justified and one can certainly extend the model by allowing simultaneous spin flips. The more crucial point is that the microscopic model of propagating excitations via (single or simultaneous) spin flips only accounts for nearest-neighbor interaction. However, numerical simulations of the dipolar spin ice (introduced in Sec. 4.2.2) very clearly show that the restriction to nearest-neighbor interaction provides only a very rough approximation. Fig. 4.17 on page 58 nicely illustrates that the interaction of

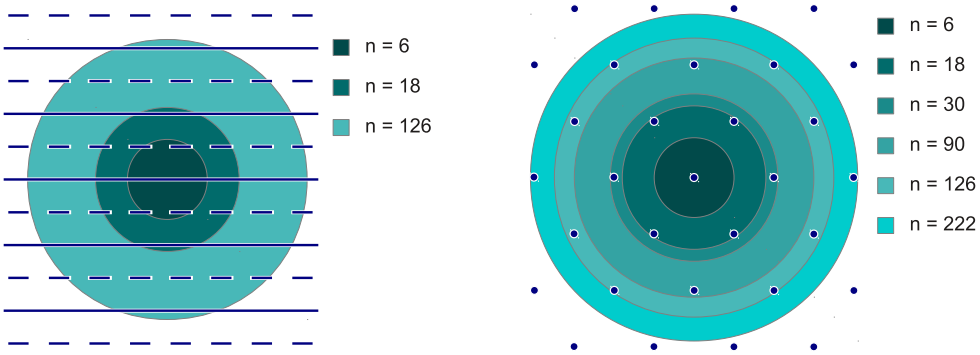

(a) (b)

Figure 4.67: (a) Alternating Kagomé and triangular planes perpendicular to $\vec{B} \,||\, [111]$. Panel (b) shows the plane perpendicular to [110]. The black circles illustrate the α or β chains, depending on the actual field direction. The blue circles illustrate spheres (surrounding a center Dy ion) with a determined number of neighboring Dy ions.

each Dy ion with more than 100 next located surrounding Dy ions needs to be involved for a reasonable quantitative description of the magnetic spin-ice system. This corresponds to a sphere with a radius three times larger than the nearest-neighbor distance r_{nn} of two Dy ions.

Fig. 4.67(a) schematically shows the alternating Kagomé and triangular planes for a field direction parallel to [111]. Two neighboring Kagomé planes have a distance of $\sim 1.64\, r_{\mathrm{nn}}$. The different blue circles depict spheres (surrounding a Dy ion) containing a certain number of neighboring Dy ions. This illustrates the influence of the long-range dipolar interaction depending on the number of considered neighbors (Sec. 4.2.2). For nearest-neighbor interaction only ($n = 6$), two neighboring Kagomé planes do not affect each other. However, taking the next 18 spins into account, the spins of one Kagomé plane interact with the neighboring Kagomé plane. And, if one takes even the next 126 spins into account, each Kagomé plane interacts not only with the neighboring two but altogether with 4 other Kagomé planes.

For $\vec{B} \,||\, [110]$, the situation is very similar. Fig. 4.67(b) shows the α or β chains depending on the field direction. In the case of nearest-neighbor interaction ($n = 6$), two neighboring chains do not affect each other. However, one can clearly see that taking more spins into account, several neighboring chains are affected due to the long-range interaction. For $n = 222$, altogether 18 chains cross the corresponding sphere and, thus, have to be taken into account.

The correlations of different Kagomé planes and different β chains show that it is in principle possible that a magnetic excitation can propagate from a Kagomé plane to the other and from a β chain to the other. However, a consistent theory

which is able to describe such dynamics is still missing.

A fundamentally alternative approach to interpret the experimental data is to analyze the field dependence $\kappa(B)$ by means of phonon scattering on magnetic excitations (monopoles). Such an approach has been proposed by B. Klemke [6, 121], who studied the thermal conductivity along the [110] direction parallel to the external magnetic field with field strengths up to 1.5 T, *i.e.* the heat current is directed along the α chains.

The data presented here do not support such an interpretation for several reasons. For example, the field dependence for $\vec{B} \,||\, [001]$ is not explainable by means of phonon scattering on magnetic excitations. For this particular field direction, the magnetic excitations are completely suppressed by the external field. Thus, one would expect the phononic thermal conductivity to increase with increasing field. This is contrary to the $\kappa(B)$ data for $\vec{B} \,||\, [001]$ presented here which rapidly decrease below 0.5 T. Furthermore, the tendency of the thermal conductivity to be larger the higher the ground-state degeneracy is (Sec. 4.7.2) cannot be explained by phonon scattering. In particular, the enhanced thermal conductivity for $\vec{B} \,||\, [111]$ around the transition at 1 T, where the monopole density is strongly increased, is in contradiction to phonon scattering on monopoles as one would expect the thermal conductivity to be suppressed rather than enhanced. Moreover, the field dependence of $\kappa(B)$ of $Dy_2(Ti_{0.9}Zr_{0.1})_2O_7$ is not explainable by phonon scattering on magnetic excitations. As the zero-field κ data of $Dy_2(Ti_{0.9}Zr_{0.1})_2O_7$ are well below the data for $Dy_2Ti_2O_7$, the additional defect scattering is certainly the dominant scattering process. Hence, one cannot explain why $\kappa(B)$ further decreases when increasing the magnetic field.

Summarizing, the κ data presented in this thesis give rise to a magnetic contribution κ_{mag} rather than to phonon scattering on magnetic excitations as proposed by B. Klemke.

4.7.5 Conclusion

In conclusion, the thermal-conductivity data of $Dy_2Ti_2O_7$ give evidence for a magnetic contribution κ_{mag} on top of a phononic background κ_{ph}. The temperature dependence of κ_{mag} in zero field qualitatively resembles the magnetic specific heat c_{mag} with a maximum around 1.5 K. The additional contribution κ_{mag} strongly depends on the magnitude and direction of the external magnetic field. A qualitative interpretation of the thermal-conductivity data is given by a microscopic model including magnetic excitations (magnetic monopoles) which can propagate via single spin flips. The ability to propagate strongly depends on the degeneracy of the (field-induced) ground state. In zero field, the degeneracy is maximum (6-fold, within the single-tetrahedron approximation) and, hence, the thermal conductivity is maximum in the absence of an external magnetic field. Within this chapter, three different field directions were investigated leading to three different field-induced ground states with different degrees of degeneracy.

For $\vec{B} \,||\, [001]$, the field-induced ground state is non degenerate and, thus, κ_{mag} is completely suppressed. Hence, this field direction is best suitable for a quantitative extraction of κ_{mag} assuming the total thermal conductivity to be composed of magnetic and phononic contribution. The decrease of $\kappa(B)$ directly correlates with the increase of the magnetization $M(B)$ parallel to [001], which (for not too small fields) correlates with the population of the field-induced ground state.

The field direction parallel to [111] exhibits the peculiarity that one can tune the degree of degeneracy by means of the magnetic-field strength. The 6-fold degenerate zero-field ground state changes into a 3-fold degenerate field-induced ground state for magnetic fields below 1 T (Kagomé-ice state). Above the transition at 1 T, the ground-state degeneracy is lifted.

For the [110] field direction, the ground-state degeneracy cannot be entirely lifted by the magnetic field. It remains 2-fold degenerate even for a large magnetic field. This field direction divides the spins into α and β chains (parallel and perpendicular to $\vec{B}$, respectively). The spins of the β chains are perpendicular to $\vec{B}$ and are, thus, not affected by the magnetic field. For very low temperatures, the thermal conductivity parallel to the β chains is larger than parallel to the α chains. For all introduced field directions, one can clearly observe a correlation of field-induced ground-state degeneracy and magnetic thermal conductivity κ_{mag}.

In the high-field region up to 7 T, the phononic background κ_{ph} also shows a field dependence which is anisotropic with respect to the field direction. For $\vec{B} \,||\, [001]$ and $\vec{B} \,||\, [111]$, the field-induced length change (magnetostriction) indicates a lattice distortion due to torques of the Dy ions originating from the external magnetic field. These field-induced lattice distortions are a possible explanation for the emerge of a field dependence of the phononic background κ_{ph}. For $\vec{B} \,||\, [110]$, unfortunately, magnetostriction measurements cannot be performed with our setup due to a tilting of the entire sample.

Furthermore, by means of the doped compounds $(Dy_{0.5}Y_{0.5})_2Ti_2O_7$, as well as $Dy_2(Ti_{0.9}Zr_{0.1})_2O_7$, it is possible to suppress either the magnetic or the phononic contribution of κ, respectively. In $(Dy_{0.5}Y_{0.5})_2Ti_2O_7$, every second Dy ion is replaced by a non-magnetic Y ion resulting in strongly suppressed spin-ice features (Sec. 4.2.2). The $(Dy_{0.5}Y_{0.5})_2Ti_2O_7$ data clearly resembles the high-field data of $Dy_2Ti_2O_7$ for all considered field directions and, thus, supports the interpretation that the high-field data of $Dy_2Ti_2O_7$ essentially reflects the phononic background κ_{ph}. In $Dy_2(Ti_{0.9}Zr_{0.1})_2O_7$, 10% of the Ti ions are replaced by much larger Zr ions. This substitution results in a strongly enhanced defect scattering of phonons and, thus, suppresses the phononic thermal conductivity by essentially conserving the magnetic properties, in particular, the magnetic contribution κ_{mag}. The absolute reduction of κ as a function of the magnetic field is comparable to the reduction for $Dy_2Ti_2O_7$ whereas the phononic background of $Dy_2(Ti_{0.9}Zr_{0.1})_2O_7$ at high fields is almost field independent above saturation of magnetization and is, in

particular, much smaller than for $Dy_2Ti_2O_7$. This is an additional strong support for the presence of a magnetic contribution κ_{mag} as discussed above.

5 Thermal Conductivity in low-dimensional Spin Systems

In this chapter, the thermal-transport properties of spin-chain compounds of the $AM_2V_2O_8$ type are studied, where A is an alkaline-earth metal and M is a transition metal. Here, $BaCo_2V_2O_8$ and two doped compounds $(Ba_{0.9}Sr_{0.1})Co_2V_2O_8$ and $Ba(Co_{0.95}Mg_{0.05})_2V_2O_8$, as well as $BaMn_2V_2O_8$ are discussed. These isostructural compounds realize two different spin-chain types. $BaCo_2V_2O_8$ is an Ising-like effective spin-1/2 chain with strongly anisotropic magnetic properties. $BaMn_2V_2O_8$ is a realization of an isotropic Heisenberg spin-5/2 chain.

Different low-dimensional spin systems (chains, ladders, and 2D square lattices) realize different ground states (*cf.* Sec. 2.1.5). In the context of low-dimensional spin systems, the question arises whether the magnetic elementary excitations contribute to the heat transport or if the thermal conductivity is of purely phononic origin. This issue will be discussed in the following.

5.1 Ising-Type Cobalt Spin Chains

In the first part, the heat transport mechanisms are studied by measurements of the thermal conductivity of $BaCo_2V_2O_8$ parallel ($\kappa_{||}$) and perpendicular ($\kappa_{\perp}$) to the chains. To analyze different contributions of κ, the thermal-conductivity measurements of two doped compounds, $(Ba_{0.9}Sr_{0.1})Co_2V_2O_8$ and $Ba(Co_{0.95}Mg_{0.05})_2V_2O_8$ are discussed.

Replacing 10% of the Ba ions by much smaller Sr ions allows to manipulate the non-magnetic subsystem of the mother compound $BaCo_2V_2O_8$. The Sr ions act as lattice defects, which are supposed to affect the phononic properties. The additional defect sites increase phonon scattering and, thus, reduce the phononic thermal conductivity. It turned out that the magnetic system is hardly affected by 10% Sr doping [172, 173].

In the case of $Ba(Co_{0.95}Mg_{0.05})_2V_2O_8$, 5% of the magnetic Co ions are replaced by non-magnetic Mg ions. By means of this doping, one can manipulate the magnetic system by creating defect sites inside the chains, *i.e.* the spin chains are cut into finite chain segments. The idea here is to mainly influence the magnetic properties. In Refs. [172, 173], it has been shown that doping with 5% Mg, indeed, influences the magnetic properties. For example, the Néel temperature is suppressed and shows a different field dependence compared to $BaCo_2V_2O_8$.

In the second part, the influence of an external magnetic field on the thermal conductivity of $BaCo_2V_2O_8$ is discussed for the low-temperature regime below

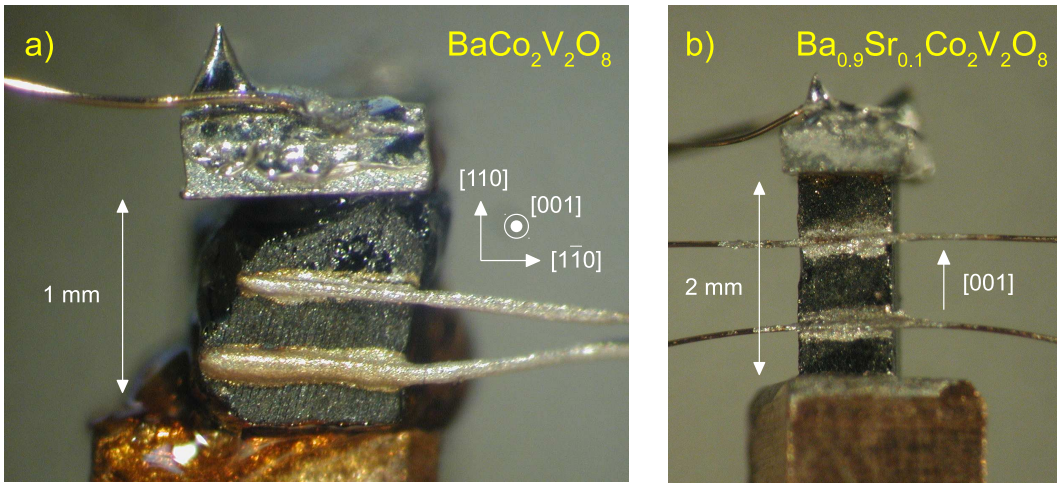

Figure 5.1: Single crystals of (a) $BaCo_2V_2O_8$ and (b) $(Ba_{0.9}Sr_{0.1})Co_2V_2O_8$ with sample heaters on top and contacted wires for thermal-conductivity measurements along [110] and [001], respectively.

$\sim 6\,\mathrm{K}$ and for different magnetic-field directions.

5.1.1 Samples

Single crystals of $BaCo_2V_2O_8$ and the related compounds $(Ba_{0.9}Sr_{0.1})Co_2V_2O_8$ and $Ba(Co_{0.95}Mg_{0.05})_2V_2O_8$ were grown by S. Niesen during her diploma- and PhD theses [172, 174].[37] All compounds are dark-green single crystals. The thermal-conductivity measurements of $BaCo_2V_2O_8$, $(Ba_{0.9}Sr_{0.1})Co_2V_2O_8$, and $Ba(Co_{0.95}Mg_{0.05})_2V_2O_8$ parallel ($\kappa_{||}$) and perpendicular ($\kappa_\perp$) to the spin chains were performed on bar-shaped single crystals (for details see Tab. 5.1). Figs. 5.1(a) and (b) show photographs of a $BaCo_2V_2O_8$ and a $(Ba_{0.9}Sr_{0.1})Co_2V_2O_8$ single crystal, respectively, with wiring for thermal-transport measurements.

For $(Ba_{0.9}Sr_{0.1})Co_2V_2O_8$ and $Ba(Co_{0.95}Mg_{0.05})_2V_2O_8$, $\kappa_{||}$ and $\kappa_\perp$ have been measured on different samples with the long edge parallel the the heat-current direction. However, only one single crystal of $BaCo_2V_2O_8$ was available. Hence, both measurements ($\kappa_{||}$ and $\kappa_\perp$) were performed on the same single crystal (Tab. 5.1). The measurement of $\kappa_\perp$ on this particular sample geometry exhibits several difficulties. Firstly, the sample is thicker than long. Hence, to ensure a homogeneous temperature gradient, all contacts have to be attached exactly parallel to each other and to the sample edges. Secondly, the sample is rather short in heat-current direction. Hence, the attached cables and the sample heater are short of space (Fig. 5.1(a)).

[37] Details of the growth behavior of $BaCo_2V_2O_8$ can also be found in [175, 176].

compound	measurements	sample shape	sample size
$BaCo_2V_2O_8$	$\kappa_{\|\|}$ and $\kappa_\perp$	rectangular	$1 \times 1 \times 2.1\,\mathrm{mm}^3$ (long edge $\|\|\, c$)
$(Ba_{0.9}Sr_{0.1})Co_2V_2O_8$	$\kappa_{\|\|}$	rectangular	$1 \times 1 \times 3\,\mathrm{mm}^3$ (long edge $\|\|\, c$)
$(Ba_{0.9}Sr_{0.1})Co_2V_2O_8$	$\kappa_\perp$	rectangular	$1 \times 1 \times 3\,\mathrm{mm}^3$ (long edge $\|\|\, a$)
$Ba(Co_{0.95}Mg_{0.05})_2V_2O_8$	$\kappa_{\|\|}$	rectangular	$1 \times 1 \times 2\,\mathrm{mm}^3$ (long edge $\|\|\, c$)
$Ba(Co_{0.95}Mg_{0.05})_2V_2O_8$	$\kappa_\perp$	rectangular	$1 \times 2 \times 5\,\mathrm{mm}^3$ (long edge $\|\|\, a$)

Table 5.1: Samples used for thermal-conductivity measurements of $BaCo_2V_2O_8$ and the doped compounds.

5.1.2 $BaCo_2V_2O_8$

Crystal Structure and Characterization

Here, a brief introduction in the crystal structure and the magnetic properties of $BaCo_2V_2O_8$ is given. A more detailed introduction can be found in Refs. [172–174].

$BaCo_2V_2O_8$ crystallizes in a tetragonal structure with the lattice constants $a = 12.444\,\text{Å}$ and $c = 8.415\,\text{Å}$ [177].[38] The rather large unit cell contains 8 formula units. The magnetic Co^{2+} ions are octahedrally surrounded by six O^{2-} ions. The CoO_6 octahedra are edge shared and form Co screw chains (Fig. 5.2). One unit cell contains two spin chains with different helicity which are separated by Ba^{2+} ions and VO_4 tetrahedra. The superexchange between the Co ions leads to an antiferromagnetic coupling. Due to inter-chain couplings, the magnetic system enters a 3D order below the Néel temperature $T_\mathrm{N} \sim 5.5\,\mathrm{K}$ [176, 179]. For $\vec{B} \,||\, c$, an incommensurate ordering is realized above 4 T at very low temperatures [180, 181]. The CoO_6 octahedra are compressed along the [001] direction. This results in a magnetic anisotropy with an easy axis of the Co spins parallel to [001]. Hence, $BaCo_2V_2O_8$ is a realization of an Ising-type effective spin-1/2 chain.[39]

The magnetic system in $BaCo_2V_2O_8$ can be described by the nearest-neighbor

[38] Slightly different lattice constants were published in Ref. [178].

[39] Co^{2+} has a spin of $s = 3/2$ and an effective orbital moment of $\tilde{l} = 1$. The ground state is formed by the $\tilde{j} = s - \tilde{l} = 1/2$ doublet. A detailed introduction into the different spin states of Co can be found in Ref. [182].

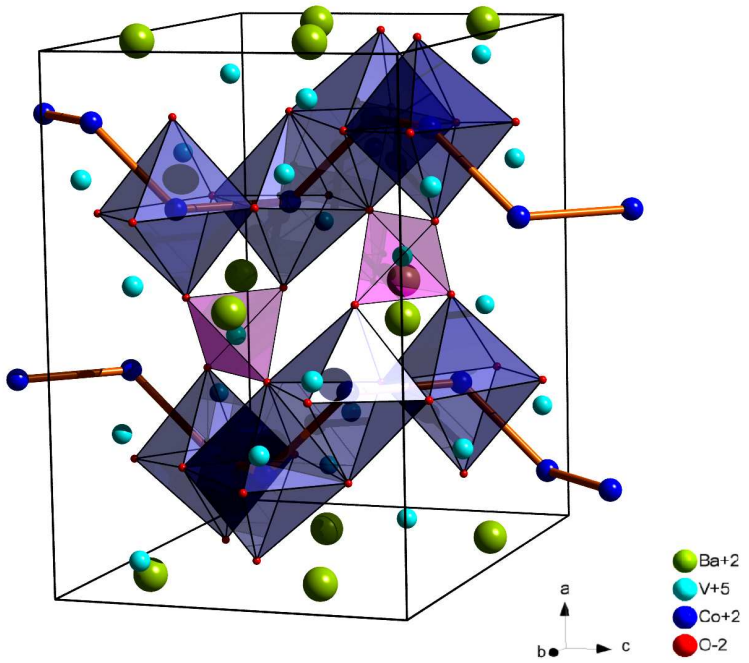

Figure 5.2: Crystal structure of $BaCo_2V_2O_8$ (from Ref. [172]).

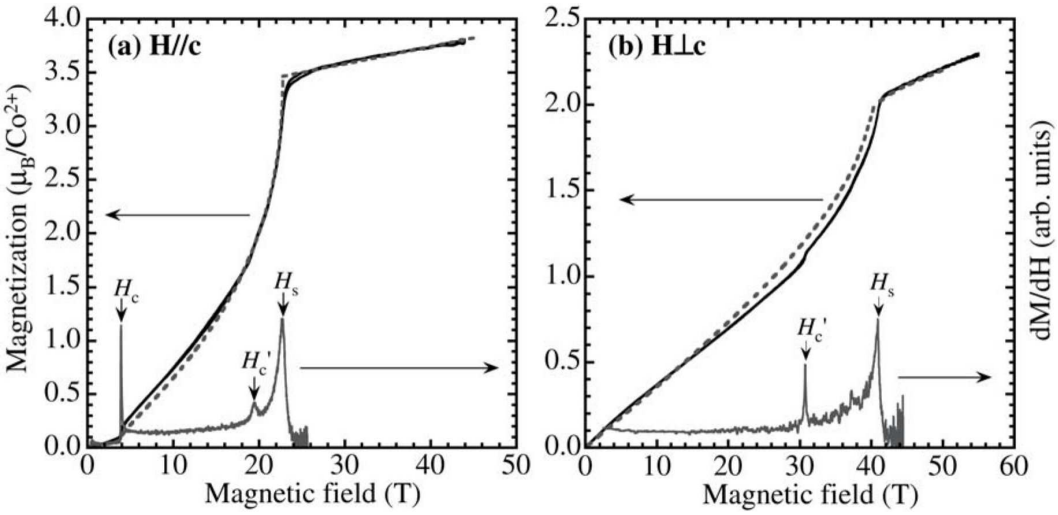

Figure 5.3: Magnetization of $BaCo_2V_2O_8$ for (a) $\vec{B} \,||\, [001]$ and (b) $\vec{B} \perp [001]$ (taken from [7]).

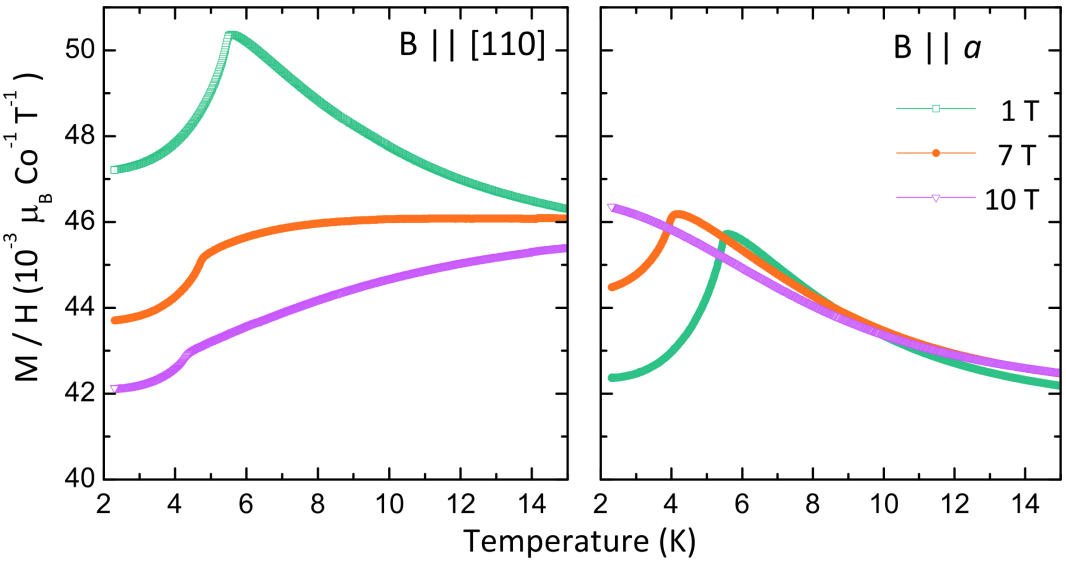

Figure 5.4: Anisotropic magnetic susceptibility of $BaCo_2V_2O_8$ within the *ab* plane [172].

$S = 1/2$ 1D XXZ model [7, 183]

$$\mathcal{H} = J \sum_i [S_{i,z}S_{i+1,z} + \epsilon(S_{i,x}S_{i+1,x} + S_{i,y}S_{i+1,y})] + g\mu_B H \sum_i S_i \qquad (5.1)$$

with exchange coupling $J = 65\,\mathrm{K}$ and anisotropy parameter $\epsilon = 0.46$. These parameters result from applying the XXZ-model (Eq. 5.1) on the low-temperature magnetization data (Fig. 5.3), which show a clear anisotropy with respect to the magnetic-field direction. The saturation fields are $\sim 23\,\mathrm{T}$ and $\sim 41\,\mathrm{T}$ for $\vec{B} \,||\, [001]$ and $\vec{B} \perp [001]$, respectively. This anisotropy has also been reported in [179, 184].

An additional anisotropy within the *ab* plane has been observed in Ref. [174] and is analyzed in detail in Refs. [172–174]. Fig. 5.4 shows the susceptibility of $BaCo_2V_2O_8$ for $\vec{B} \,||\, [110]$ and $\vec{B} \,||\, [100]$. The data show a sharp anomaly at the ordering temperature T_N, which shifts towards lower temperatures with increasing field. The field dependence of T_N is strongly anisotropic with respect to the considered field direction perpendicular to [001]. For $\vec{B} \,||\, [100]$, T_N can be completely suppressed by a field of 10 T, whereas for $\vec{B} \,||\, [110]$, T_N is only slightly reduced for 10 T. The anisotropy within the *ab* plane can be explained by an orthorhombic distortion which originates from a frustration of the magnetic structure [185–187]. In Fig. 5.3(b), the actual field direction perpendicular to [001] is not specified. The critical fields obtained from Fig. 5.3(b) suggest that the magnetic field was applied parallel to the [110] direction.

The anisotropy with respect to the field direction perpendicular to [001] is also observed in the thermal-conductivity data presented in the following section.

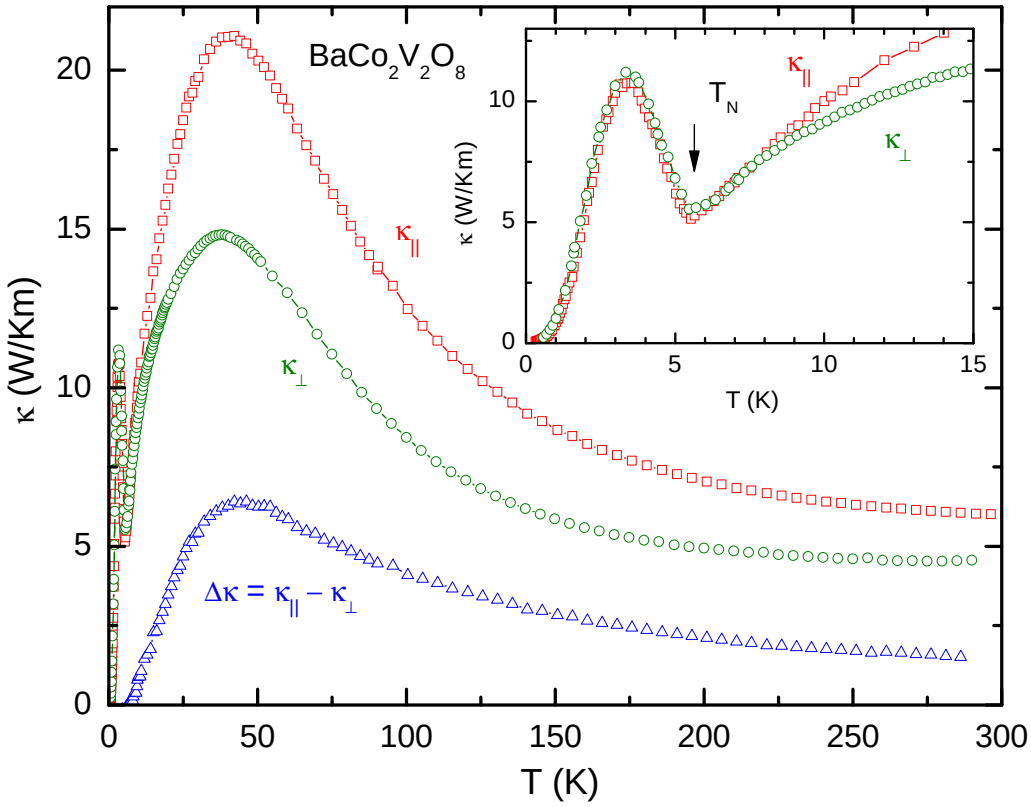

Figure 5.5: High-temperature anisotropy of $\kappa_{||}(T)$ (red squares) and $\kappa_{\perp}(T)$ (green circles) for $BaCo_2V_2O_8$. Below T_N, $\kappa(T)$ is isotropic, *i.e.* $\kappa_{||}(T) = \kappa_{\perp}(T)$ (inset). For temperatures above T_N, $\kappa_{||}(T)$ is significantly larger than $\kappa_{\perp}(T)$. The blue triangles depict the difference $\Delta\kappa = \kappa_{||} - \kappa_{\perp}$.

5.2 Thermal Conductivity of $BaCo_2V_2O_8$

Very recently, thermal-conductivity data of $BaCo_2V_2O_8$ have been published [188]. The data presented in this thesis are very similar and essentially show the same features. The authors of Ref. [188] interpret the thermal conductivity of $BaCo_2V_2O_8$ to be of phononic origin rather than containing a magnetic contribution.

5.2.1 Zero-Field Thermal Conductivity

The zero-field thermal conductivity of $BaCo_2V_2O_8$ parallel ($\kappa_{||}$) and perpendicular ($\kappa_{\perp}$) to the spin chains is illustrated in Fig. 5.5 up to room temperature. As illustrated in the inset of Fig. 5.5, and in more detail in the following section, the thermal conductivity is isotropic with respect to the heat current direction (*i.e.* $\kappa_{||} = \kappa_{\perp}$) within the Néel phase. Above T_N, however, $\kappa_{||}$ is significantly larger than $\kappa_{\perp}$. Both datasets exhibit a pronounced maximum around $\sim 40\,K$

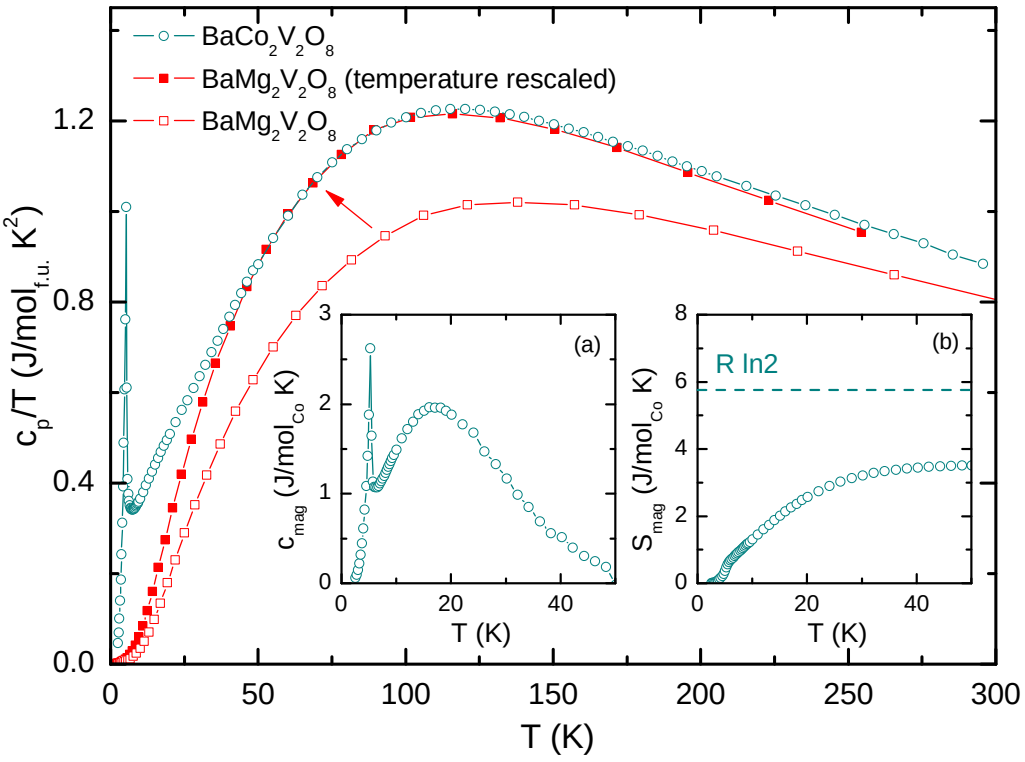

Figure 5.6: Specific heat of $BaCo_2V_2O_8$ together with the non-magnetic reference $BaMg_2V_2O_8$ (from [174]). The red closed squares depict the c/T data of $BaMg_2V_2O_8$ with a rescaled temperature. The inset (a) shows the magnetic specific heat c_{mag} of $BaCo_2V_2O_8$, and (b) shows the magnetic entropy S_{mag} obtained from c_{mag}.

and decrease at higher temperatures. The origin of the isotropy of κ within the ordered phase is unclear as the crystal structure and the magnetic properties are both anisotropic.

The question arises whether the thermal conductivity of $BaCo_2V_2O_8$ contains a magnetic contribution or if it is of purely phononic origin. This cannot be answered conclusively by means of the measured data. Therefore, both scenarios are discussed in the following.

A putative magnetic contribution κ_{mag} would be expected to be anisotropic with respect to the heat current direction, *i.e.* $\kappa_{||}$ would be expected to be larger than $\kappa_{\perp}$. As illustrated in Fig. 5.5, this is, indeed, the case for temperatures above T_{N}. The blue triangles depict the difference $\Delta\kappa = \kappa_{||} - \kappa_{\perp}$. This candidate for κ_{mag} has a broad maximum around 45 K, close to the maxima of $\kappa_{||}(T)$ and $\kappa_{\perp}(T)$.

For the further discussion of κ, first, we consider the magnetic specific heat c_{mag} of $BaCo_2V_2O_8$. The measured specific heat c/T of $BaCo_2V_2O_8$ together with

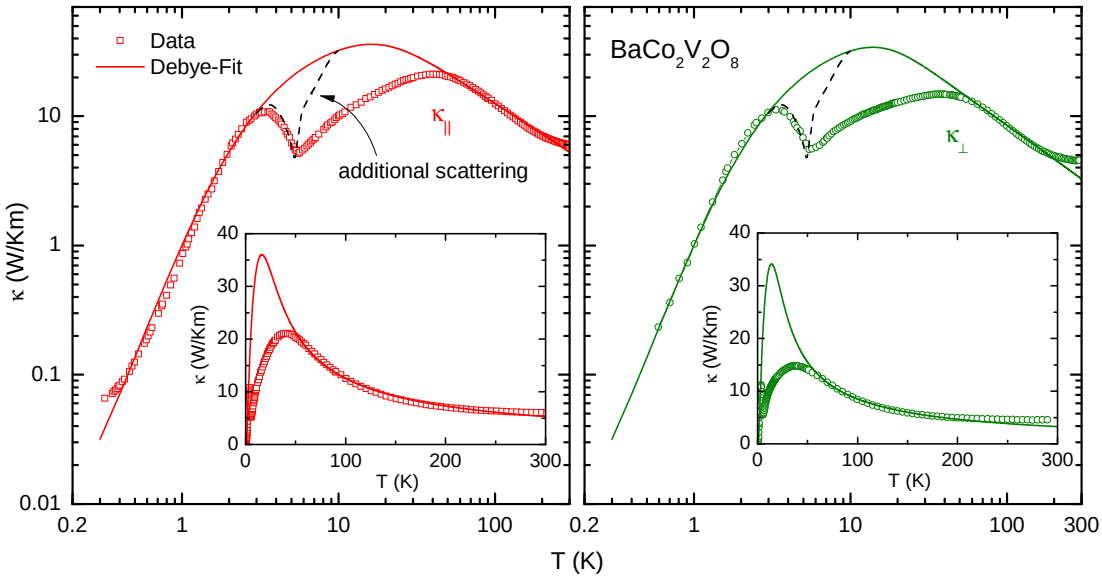

Figure 5.7: Fits of the phononic thermal conductivity of $BaCo_2V_2O_8$ by means of the Debye model (Eq. 2.5 on page 11). The solid lines are obtained by restricting the fits to the low- and the high-temperature region (see text). The dashed lines account for phonon scattering on magnetic excitations around the ordering temperature T_N.

the specific heat of the non-magnetic reference compound $BaMg_2V_2O_8$ is shown in Fig. 5.6.[40] The open circles and squares depict the c/T data of $BaCo_2V_2O_8$ and $BaMg_2V_2O_8$, respectively. The closed red squares show the c/T data of $BaMg_2V_2O_8$ where the temperature axis is scaled by a factor of 0.84 to match the high-temperature data of $BaCo_2V_2O_8$. The specific heat of $BaCo_2V_2O_8$ shows a sharp maximum at the ordering transition T_N, which is absent in the $BaMg_2V_2O_8$ data. The magnetic specific heat is obtained by subtracting the phononic data of the non-magnetic reference compound $BaMg_2V_2O_8$ from the $BaCo_2V_2O_8$ data. The inset (a) shows the resulting c_{mag} per Co ion. Beside the sharp ordering peak, c_{mag} exhibits a broad maximum around 18 K. The corresponding magnetic entropy S_{mag}, shown in the inset (b), saturates above $\sim 40\,K$. The saturation value is smaller compared to the theoretical value of $R \ln 2$ for a spin-1/2 system. However, one has to keep in mind that the phononic reference has been measured on a polycrystalline sample and the temperature axis had to be rescaled. One can increase the magnetic entropy by choosing a larger scaling factor for the rescaling of the temperature axis. As a consequence, however, the entropy would further increase above room temperature. In the following, the extracted magnetic specific heat is used for qualitative discussions.

Compared the the putative magnetic contribution $\Delta\kappa$, the magnetic specific

[40]The specific-heat data for $BaMg_2V_2O_8$ have been measured on a polycrystalline sample.

$v\,[10^3\,\mathrm{m/s}]$	$L\,[10^{-3}\,\mathrm{m}]$	$P\,[10^{-43}\,\mathrm{s}^3]$	$U\,[10^{-18}\,\mathrm{s}]$
6.095	1	17.77	0.9975 / 1.9
u	$\Theta\,[K]$	$\ell_{\mathrm{min}}\,[10^{-10}\,\mathrm{m}]$	$M\,[10^{-41}\,\mathrm{m}^3\mathrm{s}^3/\mathrm{KJ}]$
3.206	145.7	10	(0.021)

Table 5.2: Fit parameters of the Debye model for $BaCo_2V_2O_8$ (Fig. 5.7). All parameters are equal for $\kappa_{||}(T)$ and $\kappa_{\perp}(T)$, except U, where the first value corresponds to $\kappa_{||}$, and the second to $\kappa_{\perp}$.

heat c_{mag} has a maximum at a far lower temperature. However, one would assume κ_{mag} to have a maximum at a comparable temperature as c_{mag}. This is no recommendation for a magnetic heat transport in $BaCo_2V_2O_8$.

An alternative analysis of $\kappa(T)$ makes use of phonon scattering on magnetic excitations around the ordering temperature T_{N} [24]. The anisotropic thermal conductivity of $BaCo_2V_2O_8$ is supposed to be purely phononic. Within the Debye model (Eq. 2.5 on page 11), scattering of phonons on magnetic excitations can be included by a scattering term which is proportional to the magnetic specific heat (Eq. 2.12 on page 13).

At the first step, the phononic thermal conductivity calculated via Eq. (2.5) on page 11 is fitted to the measured data of $\kappa_{||}(T)$ and $\kappa_{\perp}(T)$. These fits are obtained by only considering the low-temperature region below $\sim 3\,\mathrm{K}$ and the high-temperature region above $\sim 50\,\mathrm{K}$, leaving out the region around T_{N}. The obtained fit parameters are summarized in Tab. 5.2.[41] The results of the phonon fits without scattering on magnetic excitations are shown in Fig. 5.7 as solid lines for $\kappa_{||}$ and $\kappa_{\perp}$.

To account for magnetic scattering, the corresponding scattering term (Eq. 2.12 on page 13) is included into the calculations of the phononic thermal conductivity. This temperature-dependent scattering term is proportional to $c_{\mathrm{mag}}(T)$. Here, we restrict the additional scattering term to the temperature region around T_{N} as the dip in the $\kappa(T)$ data at T_{N} is assumed to originate from the sharp peak in $c_{\mathrm{mag}}(T)$. For the calculations of the phononic thermal conductivity, the peak in $c_{\mathrm{mag}}(T)$ is extracted by subtracting an underlying linear background (not shown).

For the phonon fits accounting for additional magnetic scattering the previously obtained parameters are all preserved (Tab. 5.2). The new parameter in Eq. (2.12) on page 13 has been fitted to $R = 0.021$ (*cf.* Tab. 5.2). The resulting phonon fits including magnetic scattering are depicted as dashed black

[41] Some parameters have been determined manually and are, thus, kept fix during the fit, namely $L = 1$ and $\ell = 10$. For the fit of $\kappa_{\perp}(T)$, also $U = 1.9$ is manually set. For the fit without magnetic scattering, the corresponding parameter M is set to zero.

lines around T_N in Fig. 5.7 for $\kappa_{||}$ and $\kappa_\perp$. Around T_N, the data for $\kappa_{||}(T)$ and $\kappa_\perp(T)$ can be qualitatively described by the Debye model including scattering on magnetic excitations around the transition temperature T_N. The peak in $c_{mag}(T)$ results in a sharp dip in the calculated phononic thermal-conductivity data, comparable to the dip observed in the experimental data. Above T_N, it is not possible to describe the experimental data by means of this scattering rate as the T^2 dependence of the scattering term would cause a very strong suppression of κ_{ph} for $T > T_N$.

5.2.2 Field-dependent Thermal Conductivity

The thermal conductivity of $BaCo_2V_2O_8$ has been measured parallel and perpendicular to the spin chains ($\kappa_{||}$ and $\kappa_\perp$) for the field directions [001], [100], and [110].

Fig. 5.8 displays $\kappa_{||}(T)$ and $\kappa_\perp(T)$ of $BaCo_2V_2O_8$ for a magnetic field along the [001] direction (parallel to the spin chains). Below 3.8 T, the $\kappa_{||}(T)$ data (Fig. 5.8(a)) show a very similar behavior as $\kappa_\perp(T)$ (Fig. 5.8(d)) at low temperatures. The direct comparison on Fig. 5.8(g) very clearly illustrates that the thermal conductivity is isotropic within the ordered phase below T_N. In both cases, $\kappa(T)$ exhibits a sharp dip at the Néel temperature and is enhanced below T_N. The ordering temperature T_N decreases with increasing magnetic field. In addition, the maximum below T_N is strongly suppressed by the magnetic field. Above 3.8 T, $\kappa(T)$ shows no anomaly down to lowest temperatures.

The isotropy of κ within the Néel phase can also be observed in magnetic-field-dependent measurements at constant temperatures (Figs. 5.9(d)-(f)). Figs. 5.9(a)-(c) show $\kappa_{||}(B)$ at temperatures between 0.4 K and 8.14 K. A sharp anomaly is observed at the field-induced ordering transition. Figs. 5.9(d)-(f) illustrate the comparison between $\kappa_{||}(B)$ and $\kappa_\perp(B)$ at 0.6 K, 1.3 K, and 3.3 K, respectively. One can clearly see that $\kappa(B)$ is isotropic below a critical field which decreases with increasing temperature. In addition, one can observe that the transition changes from a sharp step at 0.6 K to a kink above 1.3 K. This correlates with observations made in Ref. [172, 185] that the phase transition below 1.3 K is a first-order transition, whereas for higher temperatures, the transition becomes of second order.

The observed phase transitions are illustrated in the phase diagram presented in Fig. 5.10. Similar phase diagrams have been published in [180, 181, 189–191]. The phase boundaries in Fig. 5.10 are obtained from magnetization-, magnetostriction-, and thermal-expansion measurements [172–174]. The anomalies observed in thermal conductivity very well match the phase boundary defining the Néel phase. The other phase boundary in Fig. 5.10, however, is not observed neither in $\kappa_{||}$ nor in $\kappa_\perp$.

As shown in Fig. 5.4 on page 139, $BaCo_2V_2O_8$ exhibits a magnetic anisotropy within the *ab* plane. The thermal-conductivity data for $\vec{B} \,||\, [100]$ are presented

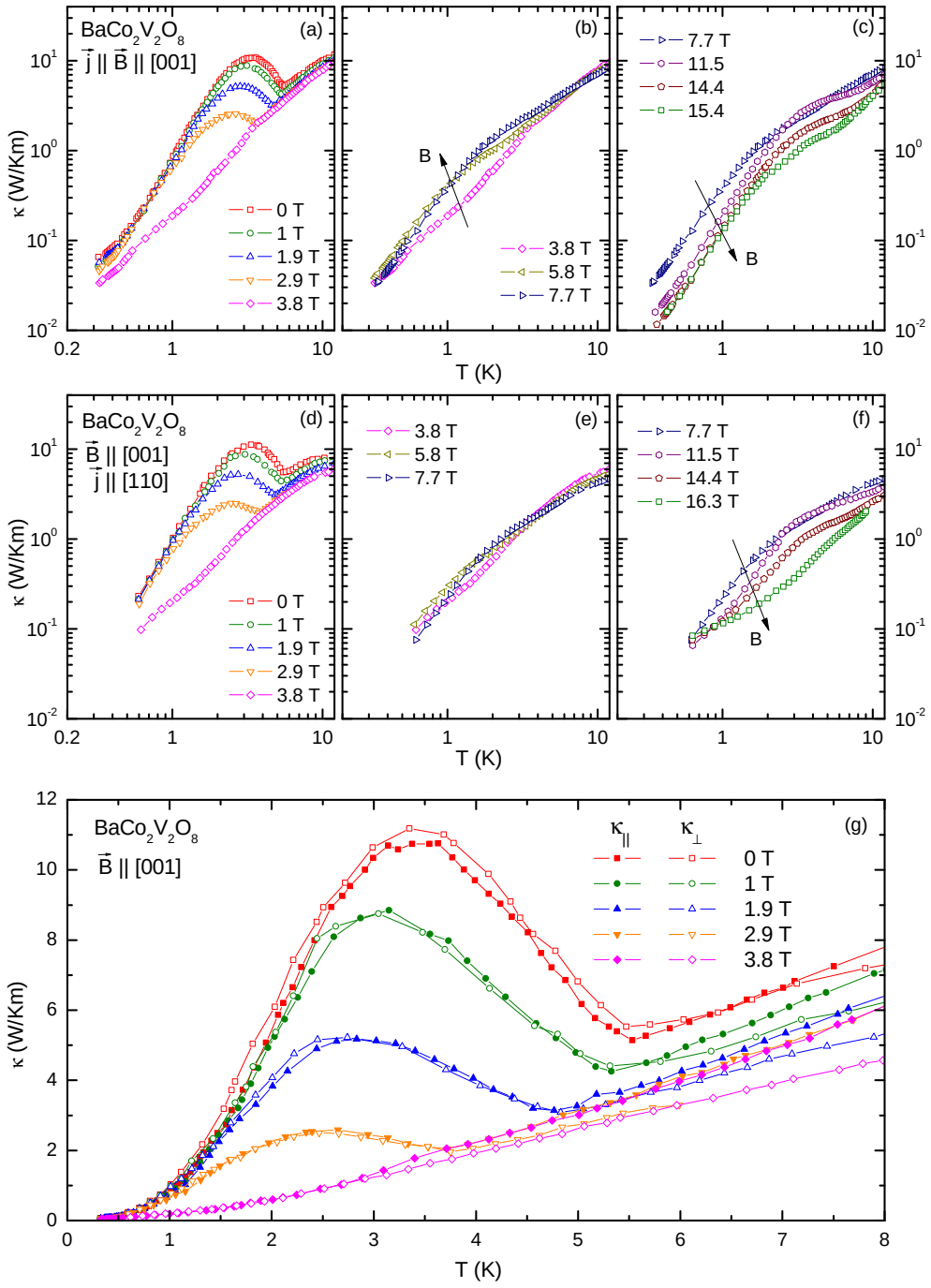

Figure 5.8: Temperature dependence of the thermal conductivity of $BaCo_2V_2O_8$ (a)-(c) parallel ($\kappa_{||}$) and (d)-(f) perpendicular ($\kappa_\perp$) to the spin chains for $\vec{B}\,||\,[001]$. Panel (g) shows the direct comparison between $\kappa_{||}(T)$ and $\kappa_\perp(T)$ below 8 K on a linear scale.

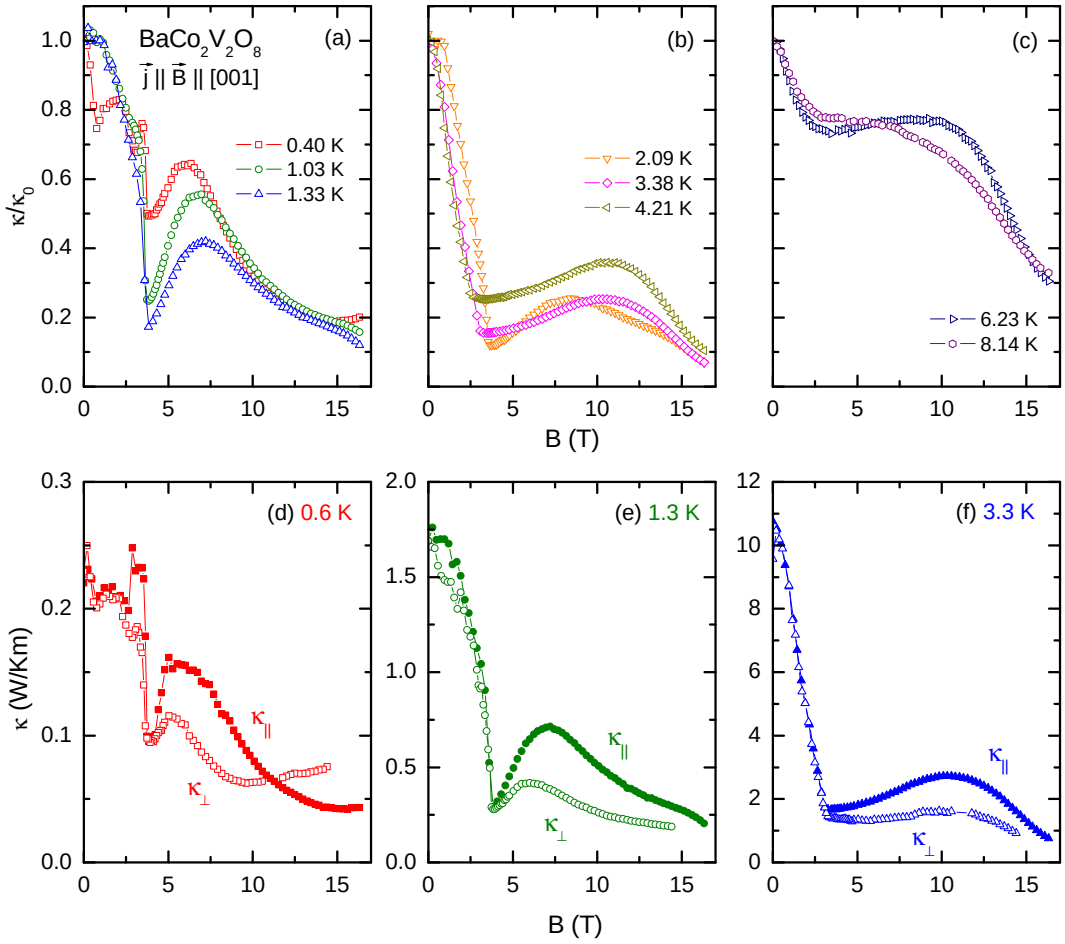

Figure 5.9: (a)-(c): Magnetic-field dependence of the normalized thermal conductivity $\kappa_{||}(B)$ of $BaCo_2V_2O_8$ parallel to the spin chains for $\vec{B}\,||\,[001]$ at various constant temperatures between 0.4 K and 8.14 K. (d)-(f): Direct comparison of $\kappa_{||}(B)$ and $\kappa_{\perp}(B)$ at 0.6 K, 1.3 K, and 3.3 K, respectively.

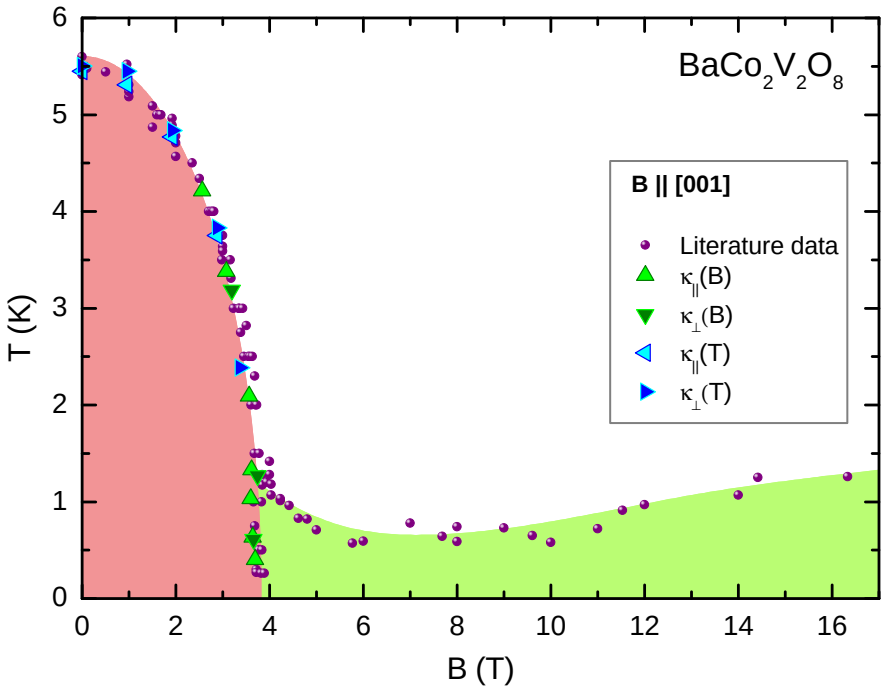

Figure 5.10: Phase diagrams of $BaCo_2V_2O_8$ for $\vec{B} \,||\, [001]$. The circles are obtained from literature data obtained from magnetostriction-, thermal-expansion-, and magnetization data (from [172–174]).

in Fig. 5.11. The data for a field direction parallel to [110] will be presented afterwards. Analogous to the situation for $\vec{B} \,||\, [001]$, the thermal conductivity parallel and perpendicular to the spin chains are very similar[42] (Fig. 5.11(e)). Below the anomaly at T_N, which is observed for both heat-current directions, $\kappa_{||}(T)$ and $\kappa_{\perp}(T)$ very well match each other. The anomaly at T_N shifts to lower temperatures with increasing field and vanishes above $\sim 10\,\mathrm{T}$. In addition, the maximum in $\kappa(T)$ below the anomaly is strongly suppressed for an increasing field up to 10 T. Above 10 T, the thermal conductivity in the region below 10 K again increases and forms a new maximum. The field-induced anomaly for $\vec{B} \,||\, [100]$ can be clearly observed in the field-dependence of $\kappa(B)$. Fig. 5.12 shows the relative reduction of $\kappa_{||}(B)$ at temperatures between 0.3 K and 4 K. $\kappa(B)$ strongly decreases with increasing field up to a critical field. Above this critical field, $\kappa(B)$ again increases. The minimum of $\kappa(B)$ around the anomaly is rather broad at 4 K and sharpens at lower temperatures. At 0.3 K, $\kappa(B)$ has a very sharp dip around the critical field of $\sim 10\,\mathrm{T}$, encompassed by two maxima. Fig. 5.12(d) illustrates the isotropy of $\kappa(B)$. At 0.6 K, $\kappa_{||}(B)$ and $\kappa_{\perp}(B)$ are very

[42] The $\kappa_{||}(T)$ and $\kappa_{\perp}(T)$ data have been scaled by 3.2% and −3.3%, respectively, to adjust the zero-field data to the corresponding zero-field data obtained for $\vec{B} \,||\, [001]$.

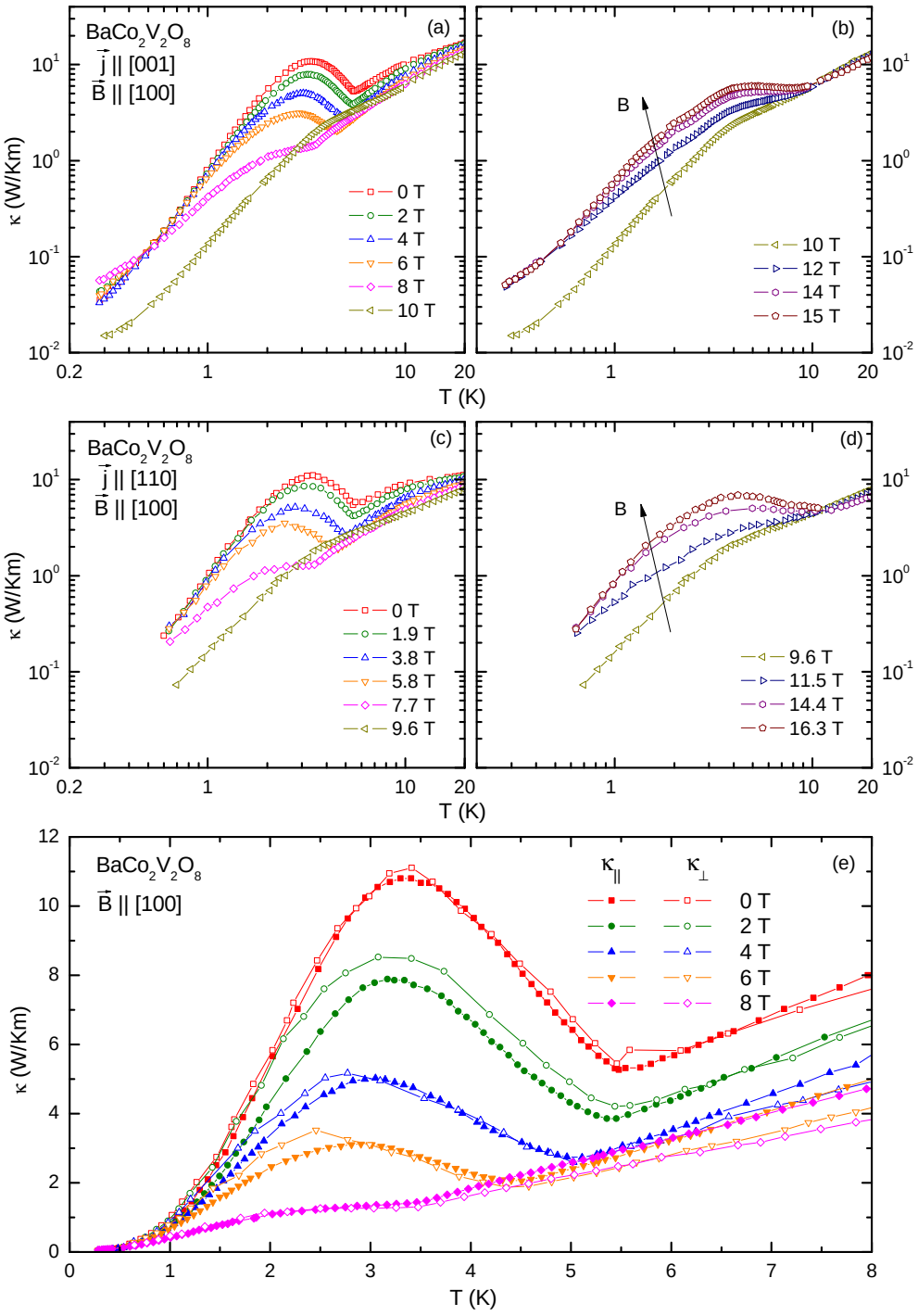

Figure 5.11: Temperature dependence of the thermal conductivity of $BaCo_2V_2O_8$ (a)-(b) parallel ($\kappa_{||}$) and (c)-(d) perpendicular ($\kappa_\perp$) to the spin chains for $\vec{B}\,||\,[100]$. Panel (e) shows the direct comparison between $\kappa_{||}(T)$ and $\kappa_\perp(T)$ below 8 K on a linear scale. The $\kappa_\perp(T)$ data are measured at 3% smaller magnetic fields than the $\kappa_{||}(T)$ data.

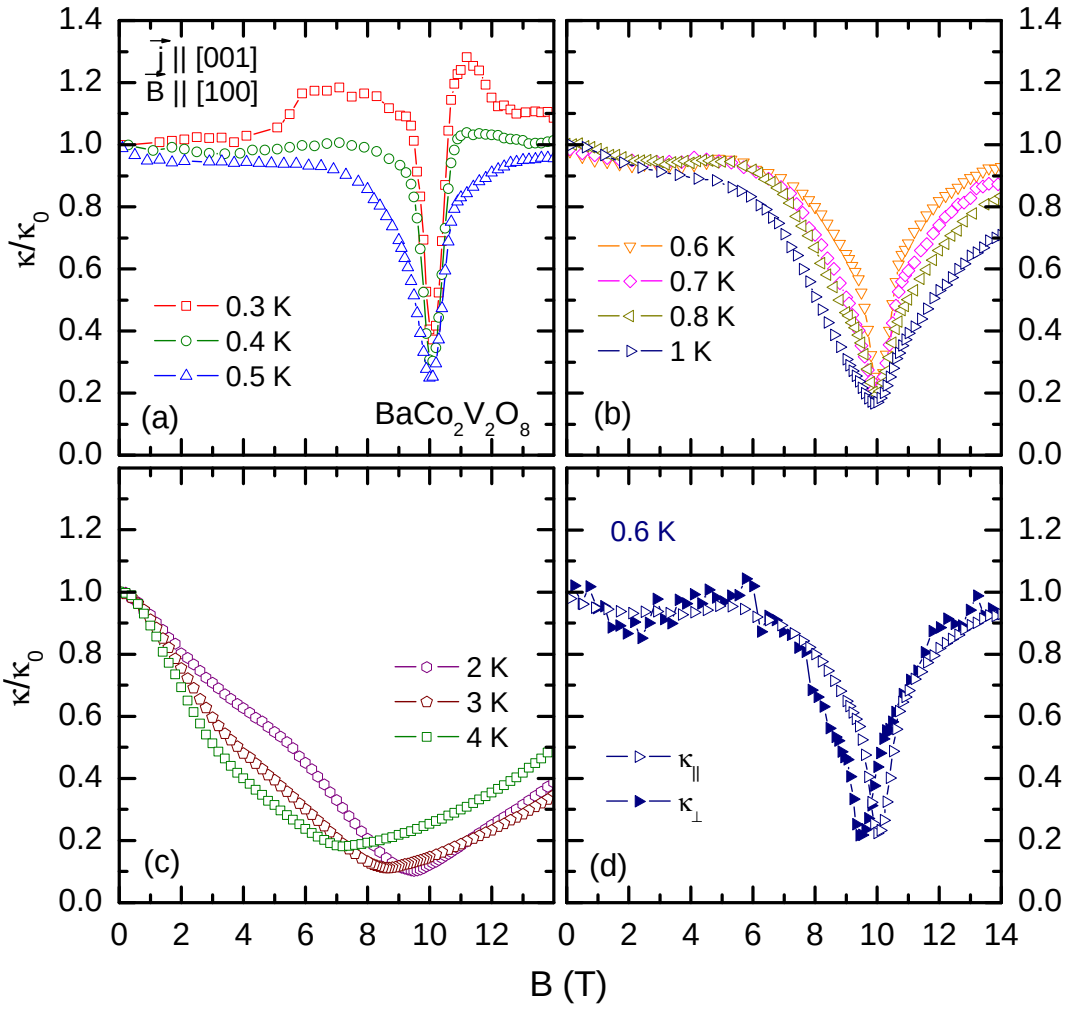

Figure 5.12: Field dependence of the thermal conductivity of $BaCo_2V_2O_8$ parallel ($\kappa_{||}$) to the spin chains for $\vec{B}\,||\,[100]$. Panel (d) shows the relative reduction $\kappa_{||}(B)$ and $\kappa_{\perp}(B)$ of $BaCo_2V_2O_8$ at 0.6 K.

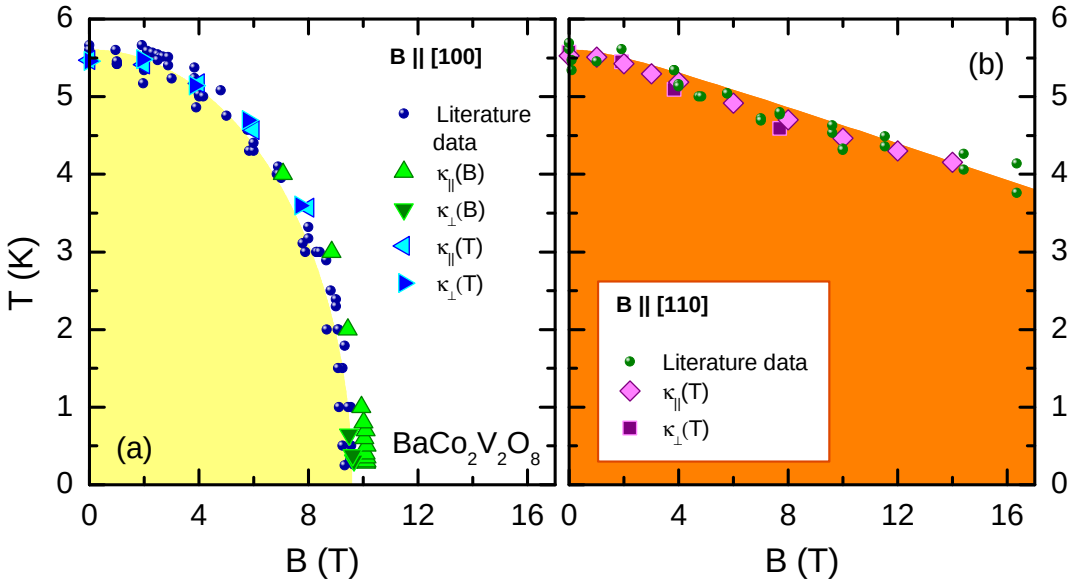

Figure 5.13: Phase diagram of $BaCo_2V_2O_8$ for $\vec{B} \perp [001]$. The circles are obtained from literature data obtained from magnetostriction-, thermal-expansion-, and magnetization data (from [172–174]).

similar. Both data show a sharp minimum around 10 T, where the minimum of the $\kappa_\perp$ data appears at a slightly lower field compared to the $\kappa_{||}$ data.

The anomalies observed in $\kappa(T)$ and $\kappa(B)$ coincide with anomalies observed in magnetostriction-, thermal-expansion-, and magnetization data [172–174] (Fig. 5.13(a)). The $\kappa_{||}(B)$ data exhibit slightly larger critical fields than $\kappa_\perp(B)$. This probably originates from a slight misalignment of the external magnetic field.

As illustrated in the phase diagram for $\vec{B} \,||\, [110]$ (Fig. 5.13 (b)), $\kappa_{||}$ and $\kappa_\perp$ exhibit anomalies at the same critical temperatures and fields as magnetization-, magnetostriction-, and thermal-expansion measurements presented in [172–174]. Fig. 5.14 shows $\kappa_{||}(T)$ and $\kappa_\perp(T)$ of $BaCo_2V_2O_8$ for $\vec{B} \,||\, [110]$. Below 4 T, $\kappa_{||}(T)$ and $\kappa_\perp(T)$ match each other within the ordered phase.[43] Above 4 T, however, the curves for the different heat-current directions deviate. At 14 T, $\kappa_{||}(T)$ shows a clear kink at $\sim 4\,\mathrm{K}$, whereas $\kappa_\perp(T)$ has no prominent feature and is strongly suppressed below 4 K compared to $\kappa_{||}(T)$. Despite this, one can clearly observe that the anomaly at the Néel temperature shifts towards lower temperatures and the maximum below T_N is suppressed when increasing the magnetic field. This behavior is very similar to the other field directions but less pronounced.

[43] Analogously to $\vec{B} \,||\, [100]$, the $\kappa_{||}(T)$ and $\kappa_\perp(T)$ data have been scaled by 3.7% and −6.9%, respectively, to adjust the zero-field data to the zero-field data obtained for $\vec{B} \,||\, [001]$.

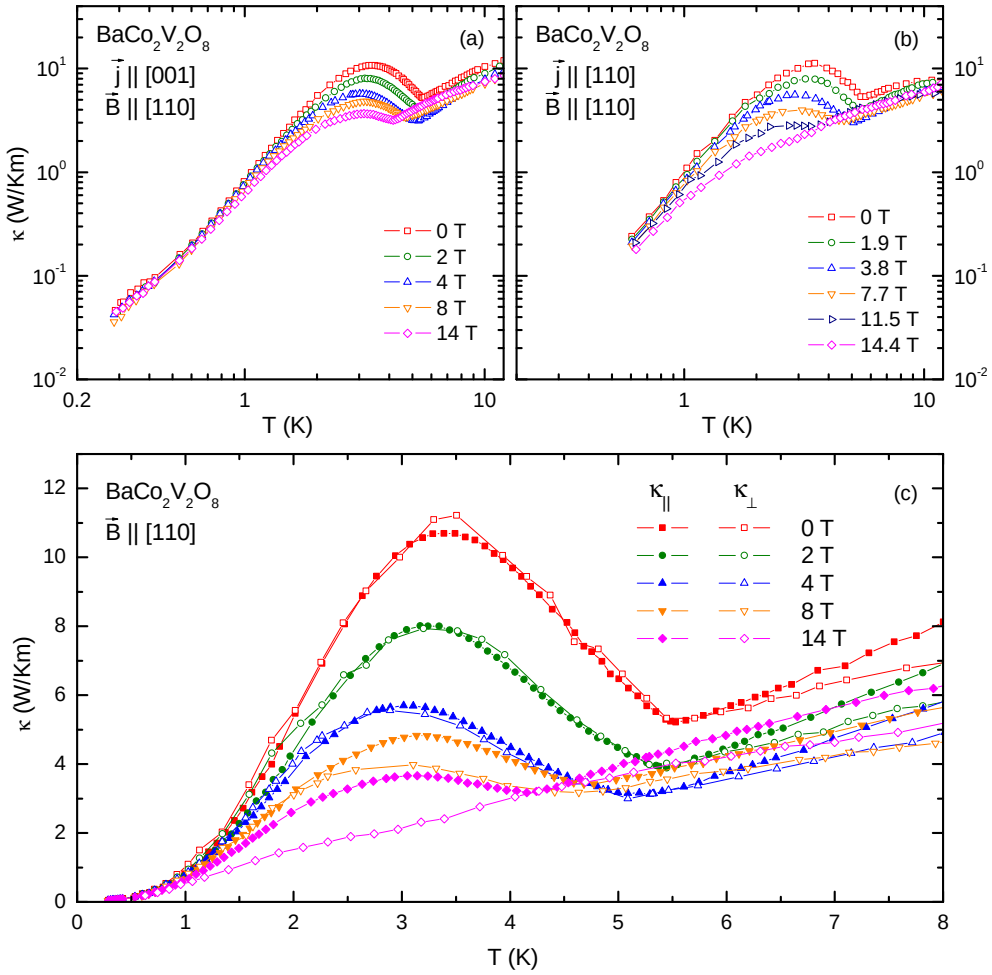

Figure 5.14: Temperature dependence of the thermal conductivity of $BaCo_2V_2O_8$ (a) parallel ($\kappa_{||}$) and (b) perpendicular ($\kappa_\perp$) to the spin chains for $\vec{B}\,||\,[110]$. Panel (c) shows the direct comparison between $\kappa_{||}(T)$ and $\kappa_\perp(T)$ on a linear scale. The $\kappa_\perp(T)$ data are measured at 3% smaller magnetic fields than the $\kappa_{||}(T)$ data, beside the 14 T curve, which has been measured in 14.4 T.

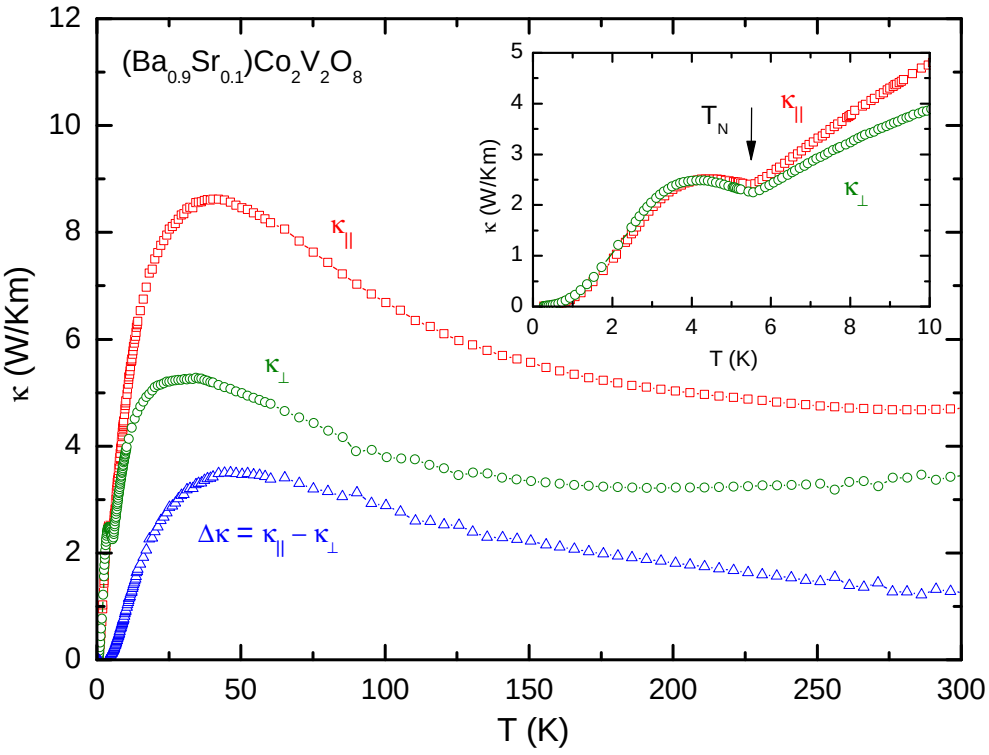

Figure 5.15: Temperature dependence of the thermal conductivity of $(Ba_{0.9}Sr_{0.1})Co_2V_2O_8$ parallel ($\kappa_{||}$) and perpendicular ($\kappa_\perp$) to the spin chains. The inset shows an enlargement of the low-temperature region around T_N.

5.3 Thermal Conductivity of $(Ba_{0.9}Sr_{0.1})Co_2V_2O_8$

In $(Ba_{0.9}Sr_{0.1})Co_2V_2O_8$, 10% of the Ba ions are replaced by smaller Sr ions. In Refs. [172, 173], it has been shown that the ordering temperature is practically unaffected in zero field. This indicates that the magnetic properties are essentially preserved.[44] Due to additional phonon scattering on the Sr ions, one expects the phononic thermal conductivity to be suppressed in comparison to the undoped mother compound $BaCo_2V_2O_8$. Fig. 5.15 shows $\kappa_{||}(T)$ and $\kappa_\perp(T)$ of $(Ba_{0.9}Sr_{0.1})Co_2V_2O_8$ for zero-field up to room temperature. Both, $\kappa_{||}$ and $\kappa_\perp$ are suppressed in the whole temperature range up to room temperature compared to $BaCo_2V_2O_8$ (Fig. 5.5 on page 140). For both heat current directions, the κ data exhibit a broad maximum around $\sim 40\,\mathrm{K}$.

The inset of Fig. 5.15 shows the low-temperature region. At the Néel temperature $T_N = 5.5\ K$, a sharp anomaly is observed. As mentioned above, the ordering temperature has not been affected compared to $BaCo_2V_2O_8$.

Analogous to the κ data of $BaCo_2V_2O_8$, the thermal conductivity of the doped

[44] The undoped compounds $BaCo_2V_2O_8$ and $SrCo_2V_2O_8$ have similar magnetic properties with comparable Néel temperatures [192–195].

compound $(Ba_{0.9}Sr_{0.1})Co_2V_2O_8$ is isotropic within the ordered phase below T_N. Compared to $BaCo_2V_2O_8$, however, the absolute values below T_N are suppressed by a factor of ~ 4. Above T_N, κ is anisotropic, *i.e.* $\kappa_{||} > \kappa_\perp$. The difference $\Delta\kappa = \kappa_{||} - \kappa_\perp$ (blue triangles in Fig. 5.15) has a shape similar to $\Delta\kappa$ obtained for $BaCo_2V_2O_8$. The absolute values, however, are reduced by a factor of ~ 2. Hence, compared to $BaCo_2V_2O_8$ the difference $\Delta\kappa$ scales in a similar way as $\kappa_{||}$ and $\kappa_\perp$ do. The reduction of $\Delta\kappa$ for $(Ba_{0.9}Sr_{0.1})Co_2V_2O_8$ is an argument against the presence of a magnetic contribution κ_{mag}. As the magnetic system in $(Ba_{0.9}Sr_{0.1})Co_2V_2O_8$ is hardly changed compared to $BaCo_2V_2O_8$, one would expect a putative magnetic contribution κ_{mag} to be essentially conserved despite the Sr doping.

5.4 Thermal Conductivity of $Ba(Co_{0.95}Mg_{0.05})_2V_2O_8$

In $Ba(Co_{0.95}Mg_{0.05})_2V_2O_8$, 5% of the magnetic Co ions are replaced by non-magnetic Mg ions. This substitution causes non-magnetic defects within the Co chains and, hence, splits the Co chains into finite chain segments. This substitution is expected to have a significant influence on the magnetic system. The ordering temperature is slightly shifted down to 3.9 K, compared to $BaCo_2V_2O_8$ (Fig. 5.5 on page 140) and to $(Ba_{0.9}Sr_{0.1})Co_2V_2O_8$ (Fig. 5.15).

5.4.1 Zero-Field Thermal Conductivity

Fig. 5.16 shows $\kappa_{||}(T)$ and $\kappa_\perp(T)$ of $Ba(Co_{0.95}Mg_{0.05})_2V_2O_8$ for zero-field up to room temperature. Above T_N, $\kappa_{||}(T)$ and $\kappa_\perp(T)$ are similar to the data obtained for the mother compound $BaCo_2V_2O_8$ and show the same anisotropy. Below T_N, however, $Ba(Co_{0.95}Mg_{0.05})_2V_2O_8$ exhibits another behavior compared to $BaCo_2V_2O_8$ and $(Ba_{0.9}Sr_{0.1})Co_2V_2O_8$. $\kappa_{||}$ and $\kappa_\perp$ are strongly suppressed and, in particular, are not isotropic ($\kappa_{||}$ is larger than $\kappa_\perp$).

The differences between $BaCo_2V_2O_8$ and $Ba(Co_{0.95}Mg_{0.05})_2V_2O_8$ are illustrated in Fig. 5.17. Panel (a) shows the high-temperature region above T_N, where $\kappa_{||}$ and $\kappa_\perp$ are essentially equal for $BaCo_2V_2O_8$ and $Ba(Co_{0.95}Mg_{0.05})_2V_2O_8$. Below T_N, however, the peak observed in the $BaCo_2V_2O_8$ data is strongly suppressed for $Ba(Co_{0.95}Mg_{0.05})_2V_2O_8$. The comparison in Fig. 5.17 shows that Mg doping influences the thermal conductivity asymmetrically with respect to T_N. This behavior is contrary to the case of Sr doping, where the thermal conductivity is suppressed within the entire temperature region.

Here also, no unambiguous interpretation of the thermal-conductivity data is possible by means of the experimental data presented here. It is unclear why κ is mainly suppressed below T_N, whereas above T_N, κ is essentially unaffected by Mg doping. Moreover, it is unclear why the thermal conductivity is no longer isotropic below T_N.

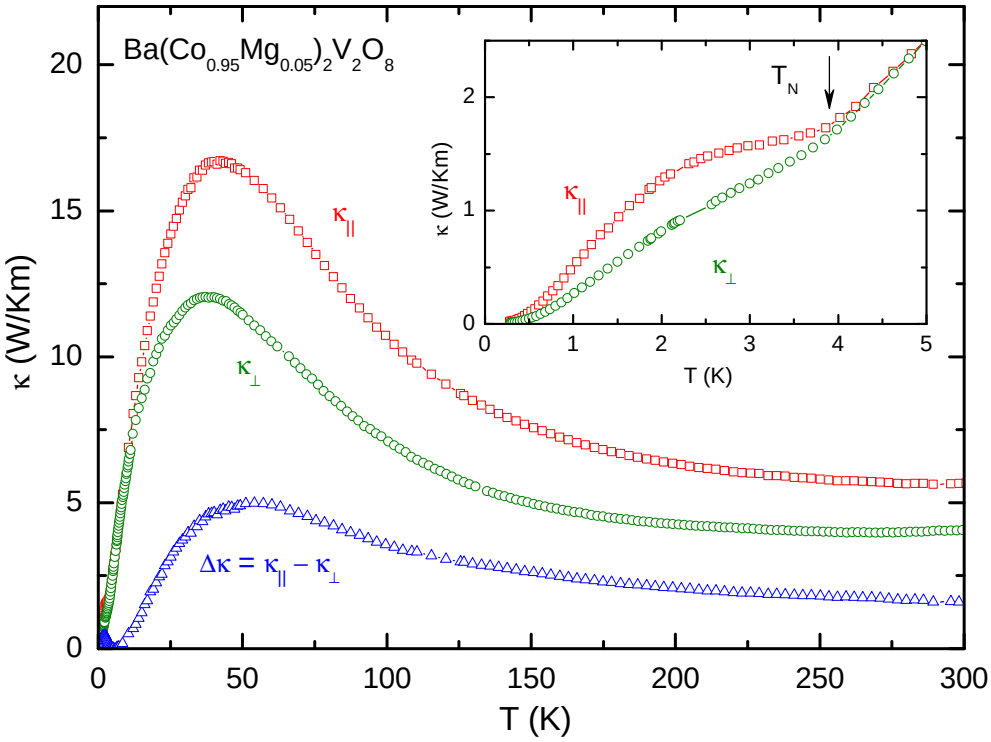

Figure 5.16: Temperature dependence of the thermal conductivity of $Ba(Co_{0.95}Mg_{0.05})_2V_2O_8$ parallel ($\kappa_{||}$) and perpendicular ($\kappa_\perp$) to the spin chains. The inset shows an enlargement of the low-temperature region around T_N.

5.4.2 Field-dependent Thermal Conductivity

Fig. 5.18 shows $\kappa_{||}(T)$ and $\kappa_\perp(T)$ for a magnetic field parallel to [001]. The zero-field Néel temperature $T_N \sim 3.9\,K$ decreases with increasing field and vanishes above 2 T. This is also observed in magnetostriction and thermal-expansion data [173]. In the $\kappa_{||}(T)$ data of $Ba(Co_{0.95}Mg_{0.05})_2V_2O_8$, a shoulder is observed below T_N. In the $\kappa_\perp(T)$ data, however, this feature is hardly observable. When increasing the magnetic field, the shoulder vanishes rapidly for both heat current directions. Above 2 T, neither $\kappa_{||}$ nor $\kappa_\perp$ show an anomaly.

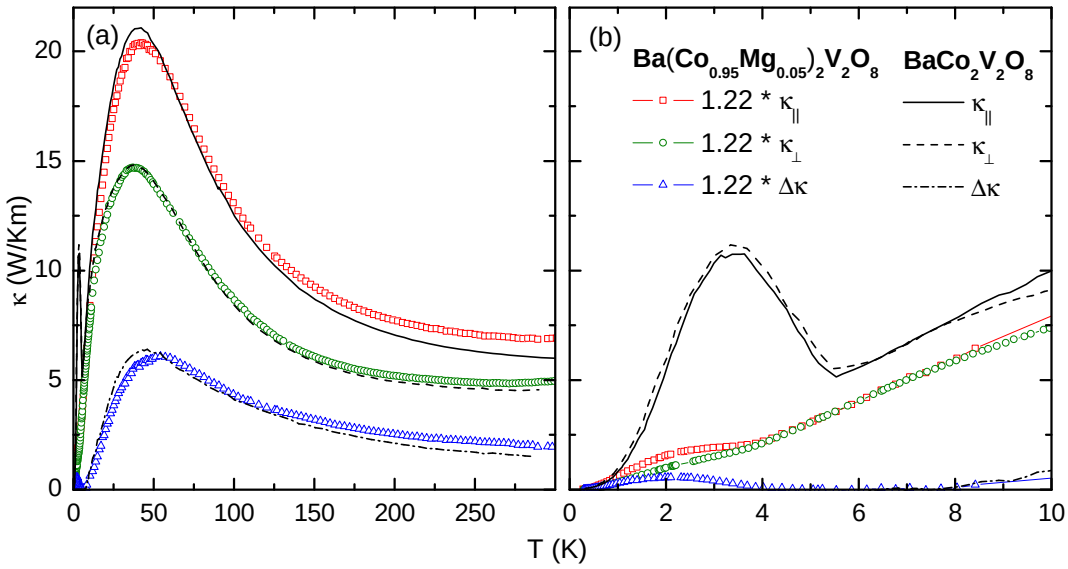

Figure 5.17: Direct comparison between the thermal conductivity of $BaCo_2V_2O_8$ and of $Ba(Co_{0.95}Mg_{0.05})_2V_2O_8$ (a) above T_N and (b) below T_N. For comparison, the $Ba(Co_{0.95}Mg_{0.05})_2V_2O_8$ data are scaled by a factor of 1.22.

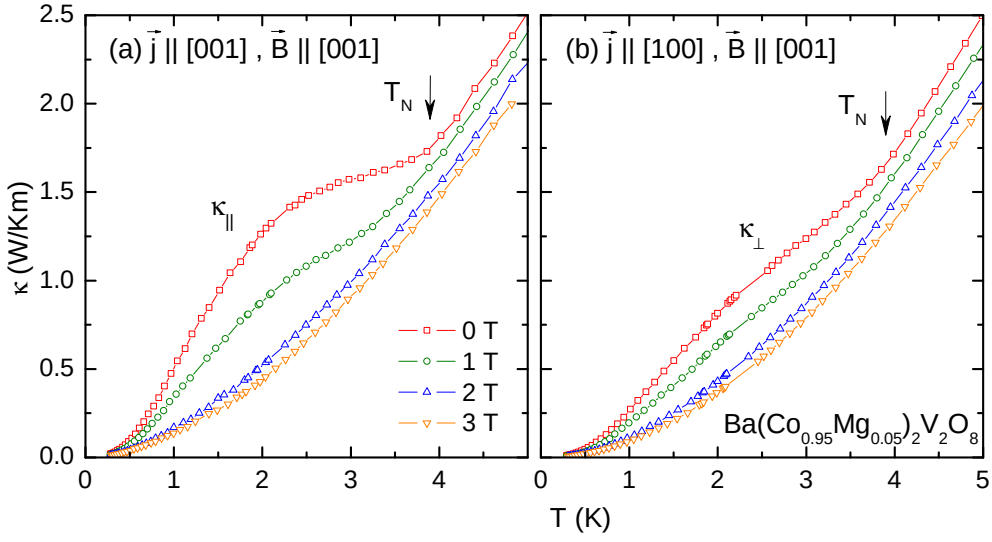

Figure 5.18: $\kappa_{||}$ and $\kappa_{\perp}$ of $Ba(Co_{0.95}Mg_{0.05})_2V_2O_8$ for $\vec{B} \,||\, [001]$ at various constant magnetic fields up to 3 T.

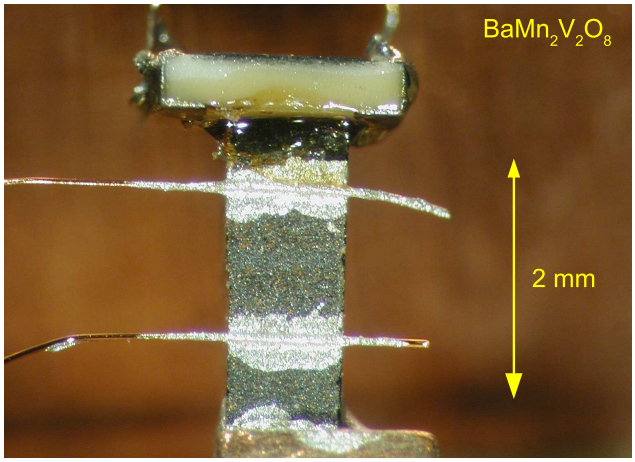

Figure 5.19: $BaMn_2V_2O_8$ single crystal with wiring for thermal-conductivity measurements.

5.5 Heisenberg Spin Chain $BaMn_2V_2O_8$

$BaMn_2V_2O_8$ is a realization of an isotropic Heisenberg spin-5/2 chain. It is a canted antiferromagnet with a Néel temperature of $T_N = 37\,K$ [174, 196]. $BaMn_2V_2O_8$ is iso-structural to $BaCo_2V_2O_8$ but with different magnetic properties. In this chapter, the thermal-transport properties of $BaMn_2V_2O_8$ are discussed and compared to the thermal conductivity of $BaCo_2V_2O_8$, discussed in the previous sections.

5.5.1 Samples

Large single crystals of $BaMn_2V_2O_8$ were grown by the floating zone technique [174]. The samples used here were grown, oriented, and cut by S. Niesen during her diploma thesis [174]. The $BaMn_2V_2O_8$ single crystals are of dark-orange color. The heat-transport measurements were performed on bar-shaped single

compound	measurements	sample shape	sample size
$BaMn_2V_2O_8$	$\kappa_{\|\|}$	rectangular	$1 \times 1 \times 2\,mm^3$ (long edge $\|\|\, c$)
$BaMn_2V_2O_8$	$\kappa_{\perp}$	rectangular	$1 \times 1 \times 3\,mm^3$ (long edge $\|\|\, a$)

Table 5.3: Samples used for thermal-conductivity measurements of $BaMn_2V_2O_8$.

crystals (for details see Tab. 5.3). The thermal conductivity for each heat-current direction has been measured on a sample of suitable shape, *i.e.* with the heat current directed along the long edge of the sample.

5.5.2 Crystal Structure and Characterization

$BaMn_2V_2O_8$ is isostructural to $BaCo_2V_2O_8$. It has a tetragonal structure with lattice constants $a = 12.6229$ Å and $c = 8.6740$ Å [174], comparable to the lattice constants of $BaCo_2V_2O_8$ (Sec. 5.1.2).[45] The spin chains in $BaMn_2V_2O_8$ are aligned parallel to the crystallographic [001] direction.

In Ref. [174], it has been shown that the magnetization is isotropic with respect to the magnetic-field direction and, thus, $BaMn_2V_2O_8$ is a realization of a Heisenberg spin system. $BaMn_2V_2O_8$ has a Néel temperature of $T_N = 36.9\,K$, which is larger than the ordering temperature of $BaCo_2V_2O_8$. The Néel temperature is hardly magnetic-field dependent. It increases to 38.4 K for a magnetic field of 14 T [174]. This behavior differs from the situation for $BaCo_2V_2O_8$ (Sec. 5.1), where the ordering temperature is shifted towards lower temperatures and even vanishes for certain field directions.

Fig. 5.20 shows the specific heat c/T of $BaMn_2V_2O_8$ [174].[46] At the ordering transition at T_N, c_p shows a sharp peak. Analogous to the specific heat of $BaCo_2V_2O_8$ (Fig. 5.6 on page 141), the magnetic specific heat of $BaMn_2V_2O_8$ is estimated via comparison with the non-magnetic reference compound $BaMg_2V_2O_8$. The specific heat of $BaMg_2V_2O_8$ has been measured on a polycrystalline sample and the temperature axis is scaled by a factor of 0.84.[47] The inset (a) of Fig. 5.20 illustrates the magnetic specific heat obtained by subtracting the phononic background from the measured data. Beside the peak at T_N, $c_{mag}(T)$ shows a broad maximum around 70 K. The magnetic entropy S_{mag} obtained by integrating c_{mag}/T (inset (b)) saturates above 200 K. The saturation value of S_{mag}, however, is smaller than the theoretical value $R \ln 6$ for a spin-5/2 system. This was also observed for $BaCo_2V_2O_8$, where the magnetic entropy did not reach the expected value. As discussed for $BaCo_2V_2O_8$, the entropy can be increased by choosing a larger scaling factor for the rescaled temperature axis. However, for reasons of consistency with $BaCo_2V_2O_8$ and as the magnetic specific heat is only discussed qualitatively, the same scaling factor is used here.

[45] In literature, slightly different lattice constants can be found. Ref. [196] report $a = 12.267$ Å and $c = 8.424$ Å, whereas Ref. [197] report $a = 12.5563$ Å and $c = 8.5942$ Å.
[46] Similar data were published in Ref. [196].
[47] This is the same factor used for the extraction of c_{mag} for $BaCo_2V_2O_8$ (Fig. 5.6 on page 141).

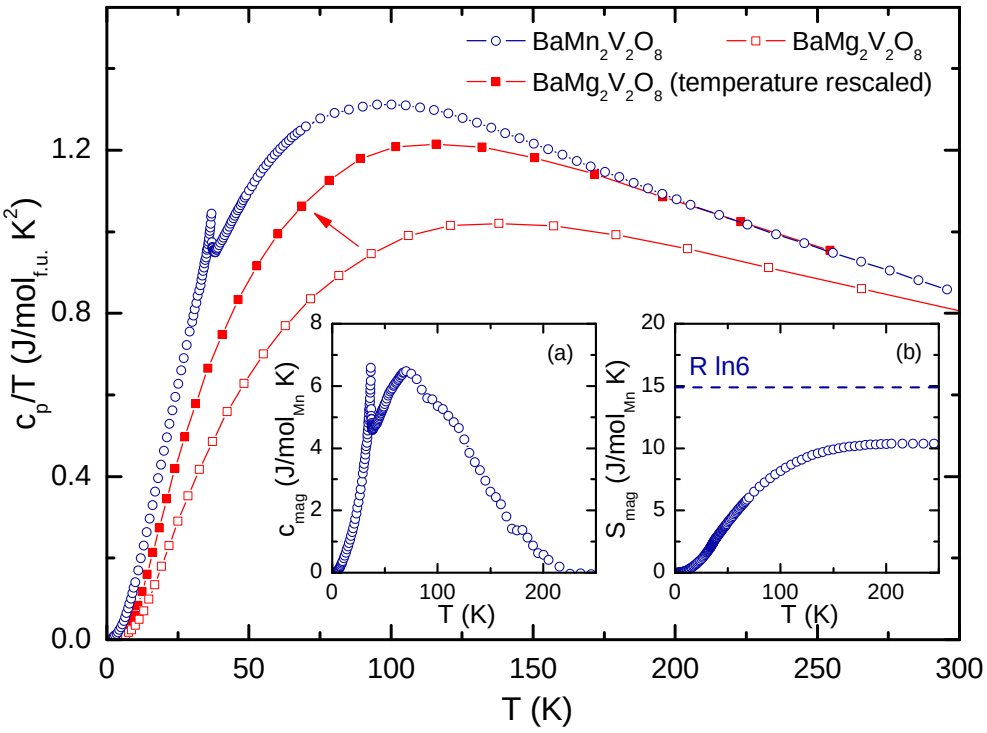

Figure 5.20: Specific heat of $BaMn_2V_2O_8$ together with the non-magnetic reference $BaMg_2V_2O_8$ (from [174]). The red closed squares depict the c/T data of $BaMg_2V_2O_8$ with a rescaled temperature. The inset (a) shows the magnetic specific heat c_{mag} of $BaMn_2V_2O_8$, and (b) shows the magnetic entropy S_{mag} obtained from c_{mag}.

5.6 Thermal Conductivity of $BaMn_2V_2O_8$

The thermal conductivity of $BaMn_2V_2O_8$ has been measured parallel ($\kappa_{||}$) and perpendicular ($\kappa_{\perp}$) to the spin chains (parallel to [001]). The zero-field $\kappa_{||}(T)$ and $\kappa_{\perp}(T)$ data are shown in Fig. 5.21. $\kappa_{||}(T)$ and $\kappa_{\perp}(T)$ exhibit a large maximum around 10.5 K and 11.5 K, respectively. At the transition temperature $T_{\mathrm{N}} = 36.9\,\mathrm{K}$ (depicted as a dashed line), neither $\kappa_{||}(T)$ nor $\kappa_{\perp}(T)$ shows an anomaly in the linear scale (main panel of Fig. 5.21). On the logarithmic scale (inset), a small kink can be observed in the $\kappa_{\perp}(T)$ data. The $\kappa_{||}(T)$ data, however, show no anomalies even on the logarithmic scale. This is different from the $BaCo_2V_2O_8$ data which show a sharp anomaly at T_{N} for both heat-current directions.

As another difference from the $BaCo_2V_2O_8$ data, the thermal conductivity of $BaMn_2V_2O_8$ remains anisotropic below T_{N}. In the whole measured temperature region, $\kappa_{||}$ is significantly larger than $\kappa_{\perp}$. Analogous to the discussions for $BaCo_2V_2O_8$, here also the question arises whether there is an additional magnetic contribution to κ. Both curves, $\kappa_{||}(T)$ and $\kappa_{\perp}(T)$, have a large maximum around

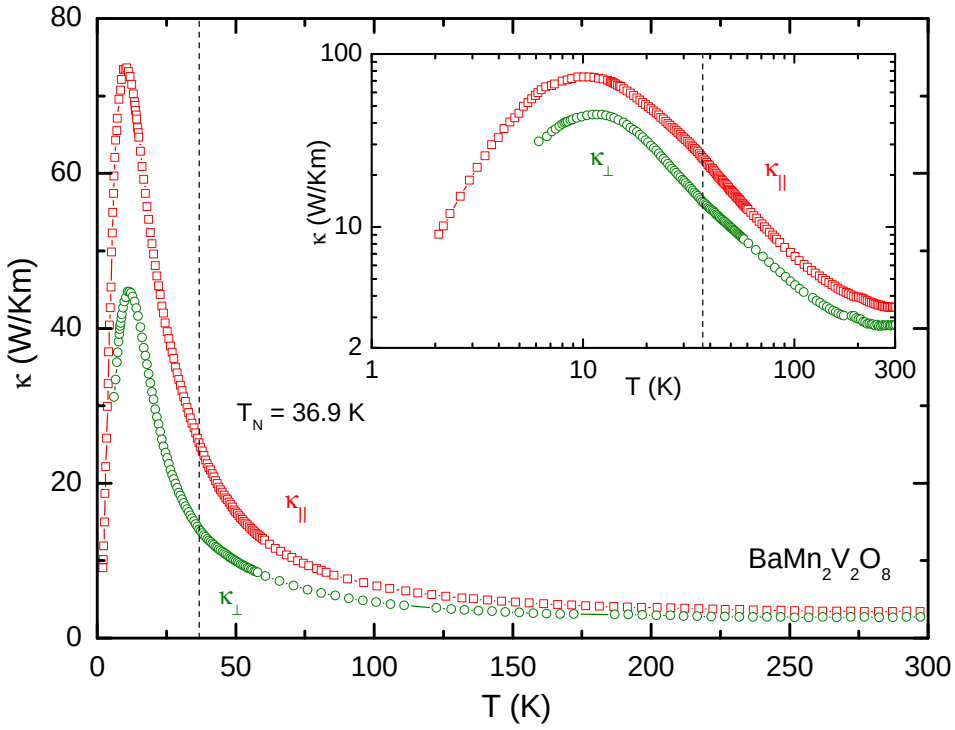

Figure 5.21: $\kappa_{||}$ and $\kappa_\perp$ of $BaMn_2V_2O_8$. The dashed line depict the Néel temperature $T_N = 36.9\,K$ [174]. The inset shows the same data on a logarithmic scale.

$\sim 10\,K$, well below the ordering temperature T_N. As shown in Fig. 5.20, the magnetic specific heat of $BaMn_2V_2O_8$ has a maximum around 70 K. Analogous to the case of $BaCo_2V_2O_8$, there are no indications of magnetic heat transport in $BaMn_2V_2O_8$.

Following the analysis for $BaCo_2V_2O_8$, including phonon scattering on magnetic excitations, one can assume $\kappa_{||}$ and $\kappa_\perp$ to be essentially phononic. As no anomaly is observed at T_N for $BaMn_2V_2O_8$[48], one can assume that the phononic thermal conductivity of $BaMn_2V_2O_8$ is essentially unaffected by scattering on magnetic excitations.

Following the argumentation of the preceding paragraph, the thermal conductivity of $BaMn_2V_2O_8$ can be regarded as an anisotropic phononic reference system to $BaCo_2V_2O_8$ on a qualitatively level. Fig. 5.22 shows $\kappa_{||}(T)$ and $\kappa_\perp(T)$ of $BaMn_2V_2O_8$ and of $BaCo_2V_2O_8$. At temperatures above $\sim 50\,K$, the thermal conductivity of $BaMn_2V_2O_8$ is larger by a factor of ~ 2 compared to the $BaCo_2V_2O_8$ data. Beside this, however, the thermal conductivity of $BaMn_2V_2O_8$ resembles the phonon fits (Fig. 5.7 on page 142) obtained from the Debye formula (Eq. 2.5 on page 11).

[48] Beside a very small kink in the $\kappa_\perp(T)$ data.

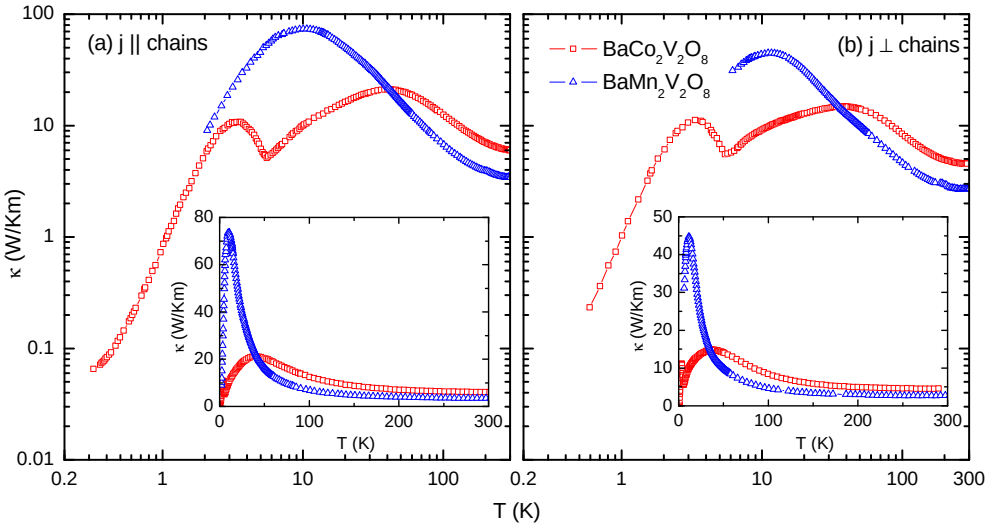

Figure 5.22: Thermal conductivity of $BaMn_2V_2O_8$ together with $BaCo_2V_2O_8$. The $BaMn_2V_2O_8$ data can be regarded as an anisotropic phononic reference system to $BaCo_2V_2O_8$ on a qualitative level (see discussion in the text).

5.7 Conclusion

In this chapter, the thermal transport properties of two iso-structural spin chains, $BaCo_2V_2O_8$ and $BaMn_2V_2O_8$, has been studied. $BaCo_2V_2O_8$ is an Ising-like effective spin-1/2 chain with a strong magnetic anisotropy. $BaMn_2V_2O_8$ is a Heisenberg spin-5/2 chain with isotropic magnetic properties. The thermal conductivity has been measured parallel ($\kappa_{||}$) and perpendicular to the spin chains ($\kappa_{\perp}$). Both compounds show an anisotropic thermal conductivity with respect to the heat-current direction, *i.e.* $\kappa_{||} > \kappa_{\perp}$. In addition, the thermal conductivity of $BaCo_2V_2O_8$ is strongly field dependent and shows a large anisotropy with respect to the magnetic-field direction.

The temperature dependence of $\kappa(T)$ of $BaCo_2V_2O_8$ exhibits a sharp dip at the Néel temperature T_N. Within the ordered phase below T_N, κ is isotropic, *i.e.* $\kappa_{||} = \kappa_{\perp}$. The ordering temperature T_N decreases with increasing magnetic field with different rates depending on the direction of the applied magnetic field. An additional anisotropy within the *ab* plane is observed in the thermal-conductivity data. The critical temperatures and fields obtained from field- and temperature-dependent thermal conductivity data, respectively, very well match phase boundaries in phase diagrams for different field directions obtained from measurements of a variety of physical quantities, *e.g.* thermal expansion and specific heat.

The anomalies in the κ data at the Néel temperature most likely originate from phonon scattering on magnetic excitations around the ordering transition.

The temperature dependence of $\kappa_{||}(T)$ and $\kappa_{\perp}(T)$ are discussed with respect to the phononic Debye model including a scattering rate accounting for scattering on magnetic excitations.

In addition to $BaCo_2V_2O_8$, two doped compounds have been studied. In $(Ba_{0.9}Sr_{0.1})Co_2V_2O_8$, 10% of the Ba ions are replaced by smaller Sr ions. The idea of this substitution is to suppress the phononic thermal conductivity by essentially conserving the magnetic properties. The κ data show that the Néel temperature is indeed not (or hardly) affected. In $Ba(Co_{0.95}Mg_{0.05})_2V_2O_8$, 5% of the magnetic Co ions are replaced by non-magnetic Mg ions. This substitution creates non-magnetic defects within the chains and is, thus, supposed to influence the magnetic system. This can be confirmed by measurements of κ which show that the Néel temperature is suppressed. T_N decreases with increasing field with a larger rate compared to $BaCo_2V_2O_8$.

The thermal conductivity of $BaMn_2V_2O_8$ shows no field dependence and no anomaly around the Néel temperature. This gives rise to the assumption that the thermal conductivity of $BaMn_2V_2O_8$ is essentially of phononic origin and can be used as a phononic reference system to $BaCo_2V_2O_8$ on a qualitative level.

To study the phononic properties of $BaCo_2V_2O_8$ and $BaMn_2V_2O_8$ on a more quantitative level, measurements on a $BaMg_2V_2O_8$ single crystal would be helpful.

In sum, the experimental data presented in this chapter show no indication of a magnetic contribution κ_{mag}. The thermal conductivity of $BaCo_2V_2O_8$ and of the reference compounds presented here most likely are of purely phononic origin. The anomalies at T_N observed for $BaCo_2V_2O_8$ can be attributed to phonon scattering on magnetic excitations at T_N.

6 Summary

In this thesis, the thermal-transport properties of the spin-ice compound $Dy_2Ti_2O_7$ and the spin-chain system $BaCo_2V_2O_8$ have been investigated. For both compounds, the main issue was to answer the question whether the respective magnetic excitations contribute to the heat transport or if the thermal conductivity is of purely phononic origin.

In the rare-earth titanate $Dy_2Ti_2O_7$, a magnetic dipole excitation can fractionalize into two individual monopole excitations, a monopole and an anti-monopole. Restricting to nearest-neighbor interaction, these excitations can propagate without confinement potential. To investigate whether these monopoles have the ability to carry heat, thermal-conductivity measurements were performed on the mother compound $Dy_2Ti_2O_7$, on the non-magnetic reference compound $Y_2Ti_2O_7$, and on two doped compounds $(Dy_{0.5}Y_{0.5})_2Ti_2O_7$ and $Dy_2(Ti_{0.9}Zr_{0.1})_2O_7$. The field dependence of the thermal conductivity κ of $Dy_2Ti_2O_7$ strongly depends on the magnetic-field direction which determines the field-induced ground state of the spin ice. It has been shown that the thermal conductivity of $Dy_2Ti_2O_7$ correlates with the degree of the ground-state degeneracy, which is maximum in zero field (6-fold) and strongly depends on the magnetic field strength and, in particular, on the field direction. This is illustrated by the correlation of thermal conductivity $\kappa(B)$ and magnetization $M(B)$. The field dependence of κ is interpreted as a field-dependent magnetic contribution κ_{mag} which is maximum in zero field and is suppressed due to the external field. A magnetic field parallel to [001] lifts the ground-state degeneracy, resulting in a non-degenerate 2in-2out ground state, *i.e.* κ_{mag} can be completely suppressed. The field-dependent κ measurements for $\vec{B} \,||\, [001]$ are, therefore, best suited to determine the zero-field contribution $\kappa_{\mathrm{mag}}(T)$ and, hence, a zero-field phononic contribution $\kappa_{\mathrm{ph}}(T)$. The magnetic contribution $\kappa_{\mathrm{mag}}(T)$ has a maximum around 1.5 K, similar to the zero-field specific-heat $c_{\mathrm{mag}}(T)$. For $\vec{B} \,||\, [111]$ and magnetic fields below 1 T, the spin ice is in the Kagomé-ice phase. This ground state is 3-fold degenerate and is characterized by a plateau in the magnetization data $M(B)$. Within the Kagomé-ice phase, the thermal conductivity data also form a plateau with enhanced κ values compared to the κ data for $\vec{B} \,||\, [001]$, *i.e.* κ_{mag} is essentially constant and, in particular, non-vanishing within the Kagomé-ice state. Above 1 T, the spin ice changes into a non-degenerate 3in-1out (or 1in-3out) ground state. This is accompanied by a sharp drop of the thermal conductivity to values comparable to the κ data for $\vec{B} \,||\, [001]$, *i.e.* to κ_{ph}. Within the Kagomé-ice phase, $\kappa(B)$ is strongly hysteretic with respect to the magnetic-field direction. This is inter-

preted as a dependence of $\kappa(B)$ on magnetic defects and, hence, disorder within the Kagomé planes when approaching the Kagomé-ice phase from lower fields, *i.e.* from a disordered ground state. Approaching from an ordered (polarized) state above 1 T, the Kagomé-ice state can be realized without (or with less) magnetic defects. Consequently, a large κ_{mag} is observed when the Kagomé-ice phase is entered from high fields, while a reduced κ_{mag} is observed when entered from low fields. The field direction parallel to [110] has several peculiarities. It divides the pyrochlore lattice into two disjunct subclasses, the α chains (parallel to $\vec{B}$) and the β chains (perpendicular to $\vec{B}$). The spins of the β chains are not affected by the magnetic field. Hence, the field-induced ground state is 2-fold degenerate, even for higher fields. Here also, $\kappa(B)$ is less suppressed than the data for $\vec{B} \,||\, [001]$, but the reduction is stronger than for $\vec{B} \,||\, [111]$, *i.e.* κ_{mag} is non-vanishing with values lower than the values within the Kagomé-ice phase for $\vec{B} \,||\, [111]$. For $\vec{B} \,||\, [110]$ at lowest temperatures, κ_{mag} (B) shows an additional anisotropy with respect to whether the heat current is directed along the α or the β chains. The magnetic contribution κ_{mag} is larger parallel to the β chains than parallel to the α chains. The magnetic heat transport via (anti-) monopoles can be explained qualitatively by means of a microscopic model including nearest-neighbor interaction. In zero magnetic field, the monopoles are not confined and can easily propagate without energy loss upon the 6-fold degenerate 2in-2out ground state. Hence, the magnetic contribution κ_{mag} is maximum in zero field. Applying the magnetic field in [001] direction has two effects. First, the energy cost of a monopole/anti-monopole creation increases. The more important effect on κ_{mag}, however, is the lifting of the ground-state degeneracy for $\vec{B} \,||\, [001]$. This results in a strongly suppressed monopole mobility and, hence, in a strongly suppressed κ_{mag}. This model, however, is a strong simplification as it only takes nearest-neighbor interaction into account. For example, within this model, a monopole excitation cannot directly propagate from one β chain to a neighboring one, as the α chains connecting them are polarized by the external magnetic field. However, numerical simulations of the dipolar spin ice taking the long-range dipolar interaction into account clearly show that the interaction with more than 100 next-located Dy ions have to be considered to obtain a reasonable description of the spin ice on a quantitative level. This shows that different β chains, indeed, interact with each other. Analogous considerations for $\vec{B} \,||\, [111]$ show that different Kagomé planes also interact with each other. As a consequence, a monopole excitation should, in principle, be able to hop through polarized α chains or polarized triangular planes in case of $\vec{B} \,||\, [110]$ or $\vec{B} \,||\, [111]$, respectively.

The magnetic-field-dependent thermal-conductivity measurements $\kappa(B)$ of $Dy_2Ti_2O_7$ have been extended towards higher field, well above the saturation field of the magnetization $M(B)$. Even for high magnetic fields, $\kappa(B)$ exhibits a considerable field dependence, although the Dy spins are fully polarized and,

hence, all magnetic excitations are supposed to vanish. This additional field dependence of κ has been analyzed by measurements of the field-induced length change of $Dy_2Ti_2O_7$. For $\vec{B} \,||\, [001]$ and $\vec{B} \,||\, [111]$ above $\sim 1\,\mathrm{T}$, it has been shown that the $Dy_2Ti_2O_7$ crystal elongates almost linearly with increasing field. This is interpreted as a distortion of the lattice which results from torques on the Dy ions effected by the external magnetic field. This lattice distortion is supposed to influence the phononic properties of $Dy_2Ti_2O_7$, leading to a reduced phononic thermal conductivity and, hence, to a field dependence of the phononic background κ_{ph}. The zero-field phononic contribution κ_{ph} has been investigated by thermal-conductivity measurements of the non-magnetic reference compound $Y_2Ti_2O_7$. To study the influence of the magnetic field on κ_{ph}, thermal-conductivity measurements of $(Dy_{0.5}Y_{0.5})_2Ti_2O_7$ have been performed. In $(Dy_{0.5}Y_{0.5})_2Ti_2O_7$, the spin-ice features are supposed to be strongly suppressed, whereas the phononic properties are essentially conserved. The thermal conductivity of $(Dy_{0.5}Y_{0.5})_2Ti_2O_7$ has been measured with the magnetic field parallel to [001], [111], and [110], analogously to the measurements of $Dy_2Ti_2O_7$. The field-dependent $\kappa(B)$ data of $(Dy_{0.5}Y_{0.5})_2Ti_2O_7$ very clearly show the same field dependence of κ of $Dy_2Ti_2O_7$ for magnetic fields above saturation of the magnetization $M(B)$. The magnetic contribution observed for $Dy_2Ti_2O_7$ is absent in the κ data of $(Dy_{0.5}Y_{0.5})_2Ti_2O_7$. In addition, thermal-conductivity measurements of $Dy_2(Ti_{0.9}Zr_{0.1})_2O_7$ have been performed. In $Dy_2(Ti_{0.9}Zr_{0.1})_2O_7$, the spin-ice system is assumed to be hardly affected, whereas the phononic thermal conductivity is supposed to be strongly suppressed due to phonon scattering on the additional Zr defects. The thermal-conductivity measurements of $Dy_2(Ti_{0.9}Zr_{0.1})_2O_7$ clearly show that κ_{mag} is basically conserved, whereas the phononic background κ_{ph} is strongly suppressed. Furthermore, the phononic background κ_{ph} is almost field independent. This can be explained by the mean free path of the phonons to be limited by defect scattering only. In summary, the experimental thermal-conductivity data give clear evidence for a considerable magnetic heat transport by magnetic monopoles in the spin-ice compound $Dy_2Ti_2O_7$. This magnetic heat transport can be qualitatively explained by a microscopic model including single spin flips. However, some questions remain open and need to be resolved. For example, fundamental theoretical models about the monopole dynamics are required.

The second part of this thesis focuses on the thermal conductivity of the Ising spin-chain system $BaCo_2V_2O_8$. The temperature dependence of κ of $BaCo_2V_2O_8$ has a sharp dip at the ordering temperature T_{N}. Above T_{N}, the thermal conductivity $\kappa(T)$ of $BaCo_2V_2O_8$ is larger parallel ($\kappa_{||}$) to the spin chains than perpendicular ($\kappa_{\perp}$) to the spin chains, *i.e.* $\kappa_{||} > \kappa_{\perp}$. Below T_{N}, $\kappa(T)$ is isotropic, *i.e.* $\kappa_{||} = \kappa_{\perp}$. An applied magnetic field decreases the Néel temperature, where the field dependence of T_{N} strongly depends on the applied magnetic field direction. In addition, two doped compounds, $(Ba_{0.9}Sr_{0.1})Co_2V_2O_8$ and $Ba(Co_{0.95}Mg_{0.05})_2V_2O_8$, have been investigated. In $(Ba_{0.9}Sr_{0.1})Co_2V_2O_8$, substitution with 10% Sr increases the defect scattering of phonons and, hence,

suppresses the phononic thermal conductivity. It has been shown that doping with Sr hardly affects the magnetic properties of $BaCo_2V_2O_8$, such that one can reduce a phononic background and distinguish a magnetic contribution κ_{mag}. In $Ba(Co_{0.95}Mg_{0.05})_2V_2O_8$, the spin chains are split into finite chain segments. As a consequence, the magnetic properties are strongly affected. The ordering temperature is reduced compared to $BaCo_2V_2O_8$. Furthermore, the decrease of T_N due to an increasing field is more pronounced compared to $BaCo_2V_2O_8$. Additionally, the thermal conductivity of the iso-structural $BaMn_2V_2O_8$ has been investigated. Within the whole measured temperature range, the thermal conductivity of $BaMn_2V_2O_8$ is anisotropic with respect to the heat-current direction, *i.e.* $\kappa_{||} > \kappa_{\perp}$. Moreover, $\kappa(T)$ has no prominent feature around the ordering temperature T_N.

The thermal-conductivity data of $BaCo_2V_2O_8$ and the reference compounds show no indication of a magnetic heat transport. The temperature dependence of κ can be explained by phonon scattering on magnetic excitations around the phase transition at T_N. The $\kappa(T)$ data of $BaCo_2V_2O_8$ have been described by the phononic Debye model including an additional scattering term which takes scattering on magnetic excitations into account. The thermal conductivity of $BaMn_2V_2O_8$ also is interpreted to be of purely phononic origin, but without scattering on magnetic excitations around T_N.

A Additional Measurements

A.1 Two-Leg $S = 1/2$ Spin Ladder $(C_5H_{12}N)_2CuBr_4$ (HPIP)

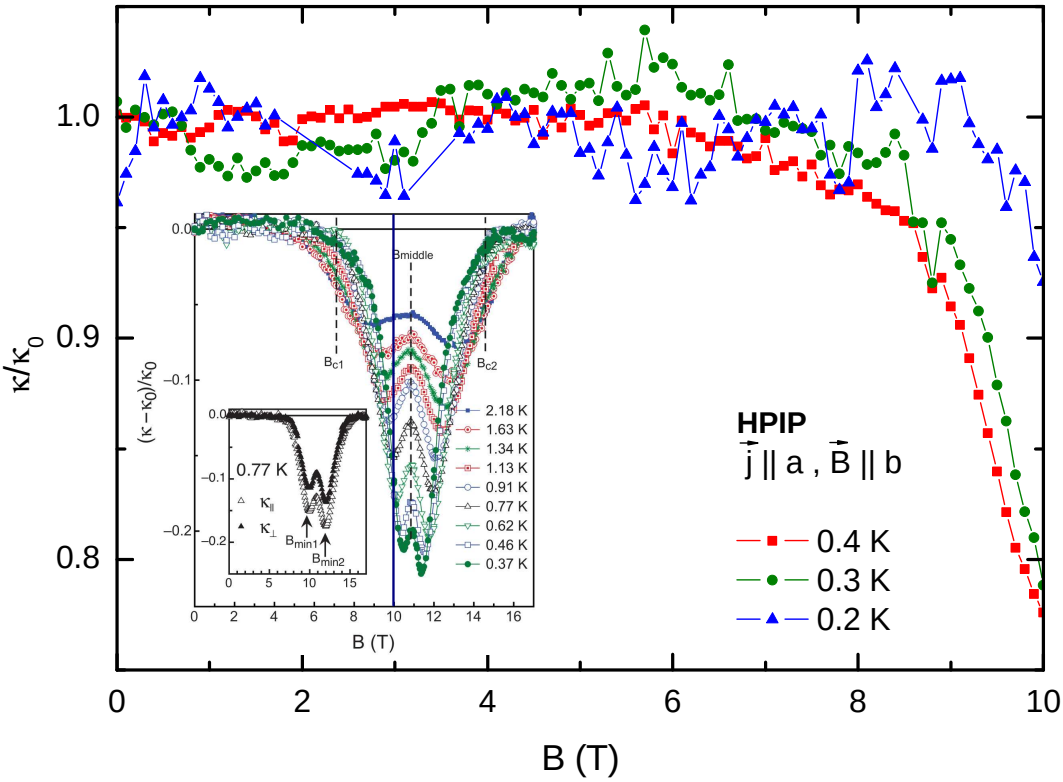

Figure A.1: Thermal conductivity of $(C_5H_{12}N)_2CuBr_4$ (HPIP) along the legs ($\kappa_{||}$) for $\vec{B} \,||\, b$ at 0.2 K, 0.3 K, and 0.4 K and magnetic fields up to 10 T. The inset shows literature data [66] for temperatures down to 0.37 K and magnetic fields up to 17 T. The data shown in the main panel have been measured in a dilution refrigerator and extend the literature data towards lower temperatures. The data was measured up to 10 T and, thus, only shows the first part of the left minimum. The field range of the main panel is denoted as a bold line within the inset. When lowering the temperature, the left part of the minimum shifts towards higher fields. This indicates that the minimum gets sharper for lower temperatures.

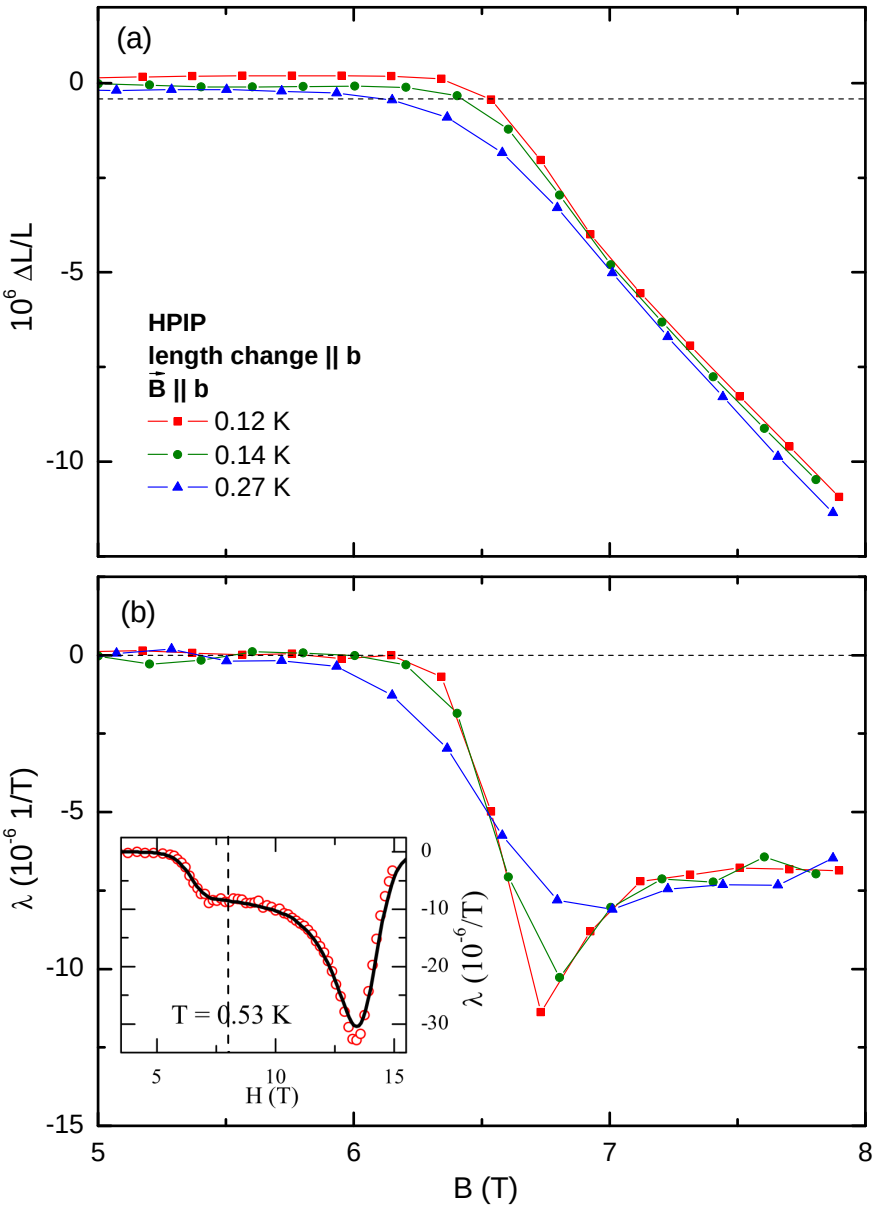

Figure A.2: (a) Field-induced length change of $(C_5H_{12}N)_2CuBr_4$ (HPIP) for $\vec{B} \,||\, b$, measured in a dilution refrigerator. The length change is measured parallel to b. (b) Derivative (magnetostriction). The data is an extension of literature data [73, 75] towards lower temperatures. The data were measured up to 8 T. The corresponding field range is denoted as dashed line within the inset showing the literature data at 0.53 K. When lowering the temperature, the step in λ becomes sharper and an additional sharp minimum appears at the lower critical field (*cf.* Sec. 2.1.5).

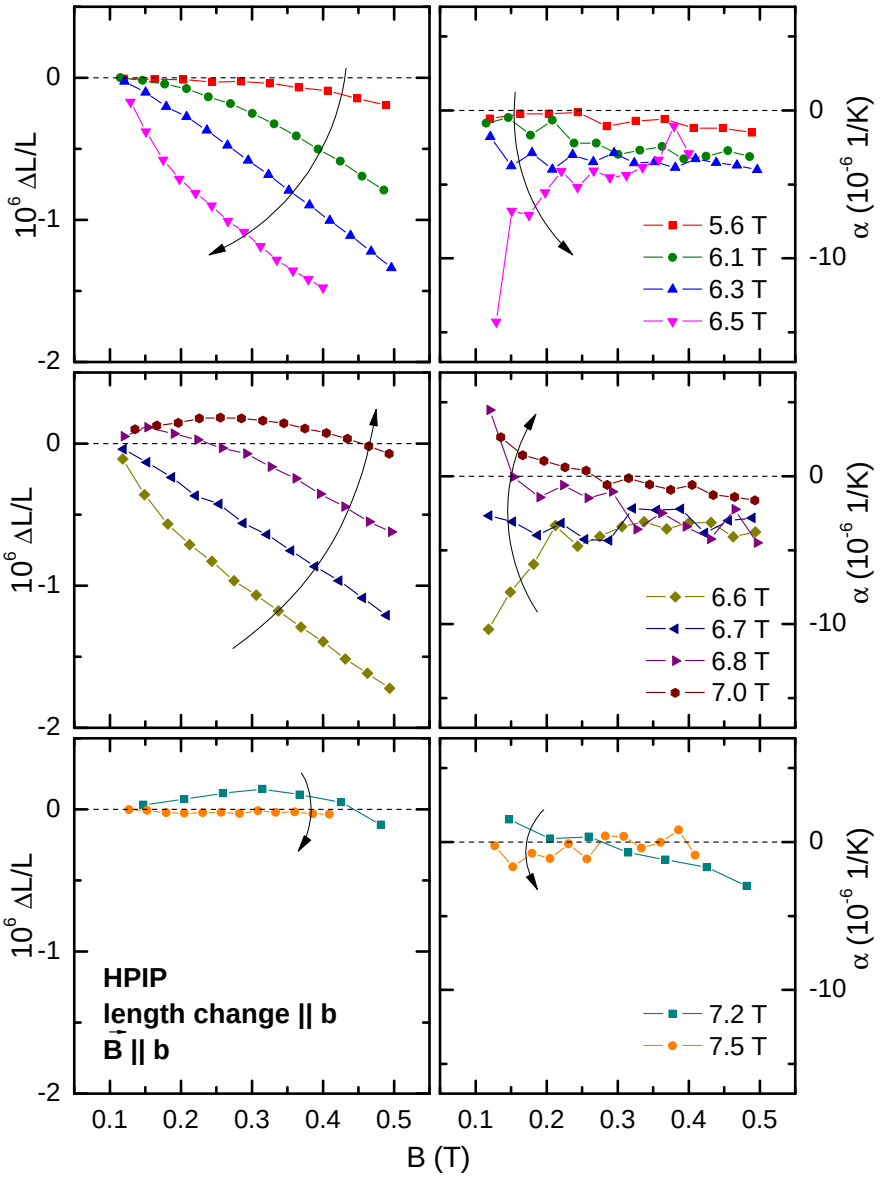

Figure A.3: Thermal expansion of $(C_5H_{12}N)_2CuBr_4$ (HPIP). The length change is measured along the b direction, parallel to the magnetic field $\vec{B} \,||\, b$ in a dilution refrigerator. The idea was to measure the thermal expansion at the ordering temperature $T_N \simeq 110\,\mathrm{mK}$ [74]. This was not possible as the cryostat did not reach sufficiently low temperatures. Nevertheless, the measured data extends literature data [73, 75] towards lower temperatures and nicely show the divergence and the sign change of the thermal-expansion data (*cf.* [73, 75]).

A.2 Two-Leg $S = 1/2$ Spin Ladder $(C_7H_{10}N)_2CuBr_4$ (DIMPY)

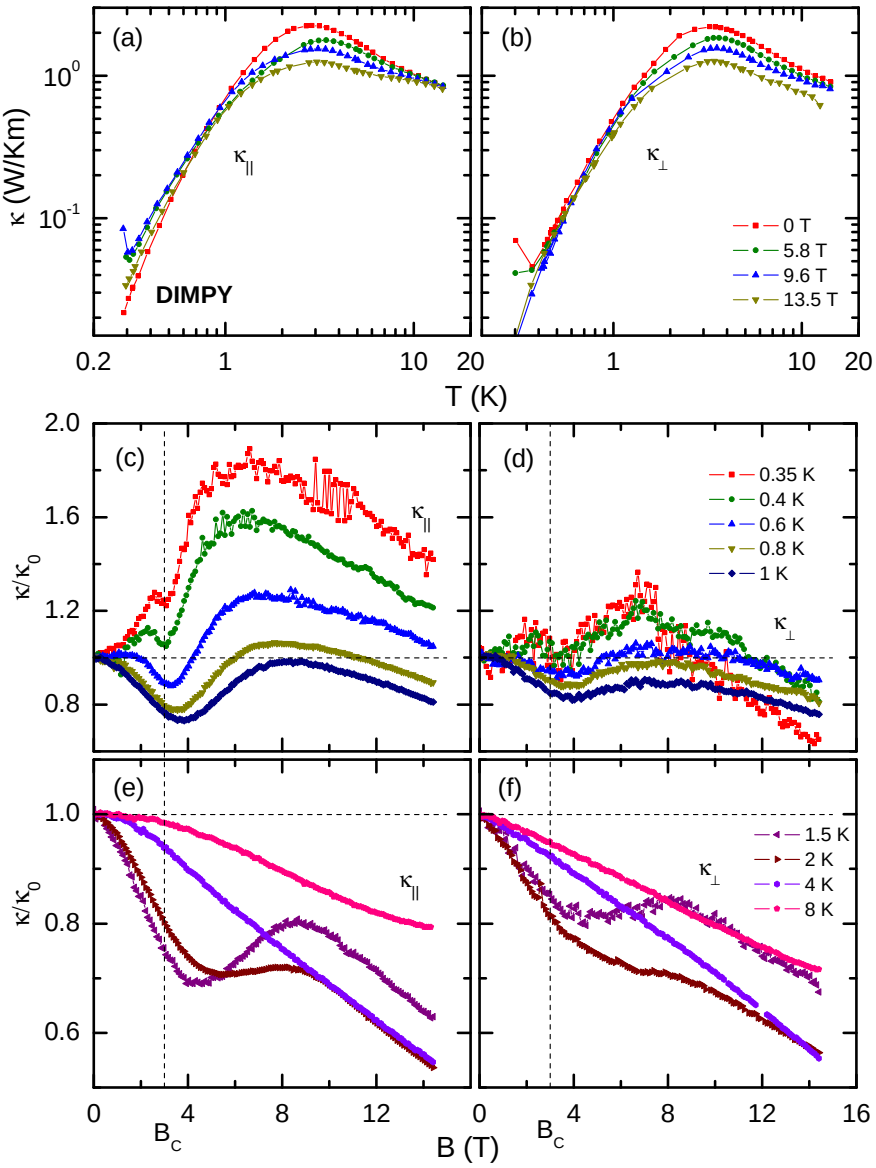

Figure A.4: Thermal conductivity of $(C_7H_{10}N)_2CuBr_4$ (DIMPY) parallel ($\kappa_{||}$) and perpendicular ($\kappa_\perp$) to the legs. Panels (a) and (b) show the temperature dependence $\kappa_{||}(T)$ and $\kappa_\perp(T)$, respectively, for various magnetic fields. Panels (c) - (f) illustrate the magnetic-field dependence at various constant temperatures. To attach the wires and the heater at the sample, a transparent two-component (from Uhu) adhesive has been used. The idea was to measure a possible magnetic heat transport (*cf.* Sec. 2.1.5).

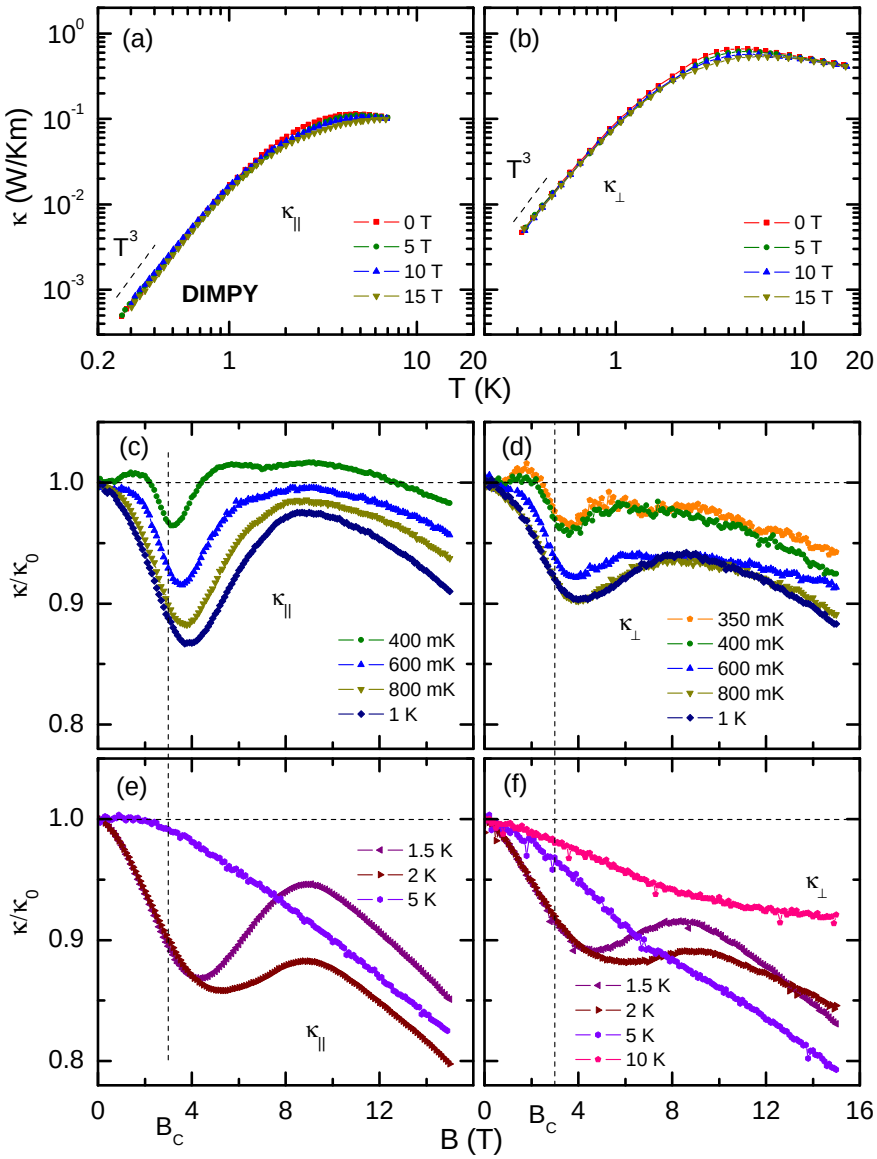

Figure A.5: Thermal conductivity of $(C_7H_{10}N)_2CuBr_4$ (DIMPY) parallel ($\kappa_{||}$) and perpendicular ($\kappa_\perp$) to the legs. Panels (a) and (b) show the temperature dependence $\kappa_{||}(T)$ and $\kappa_\perp(T)$, respectively, for various magnetic fields. Panels (c) - (f) illustrate the magnetic-field dependence at various constant temperatures. To attach the wires and the heater at the sample, the Delta Bond 152 adhesive (Sec. 3.4) has been used. The idea was to measure a possible magnetic heat transport (*cf.* Sec. 2.1.5).

A.3 Cobalt

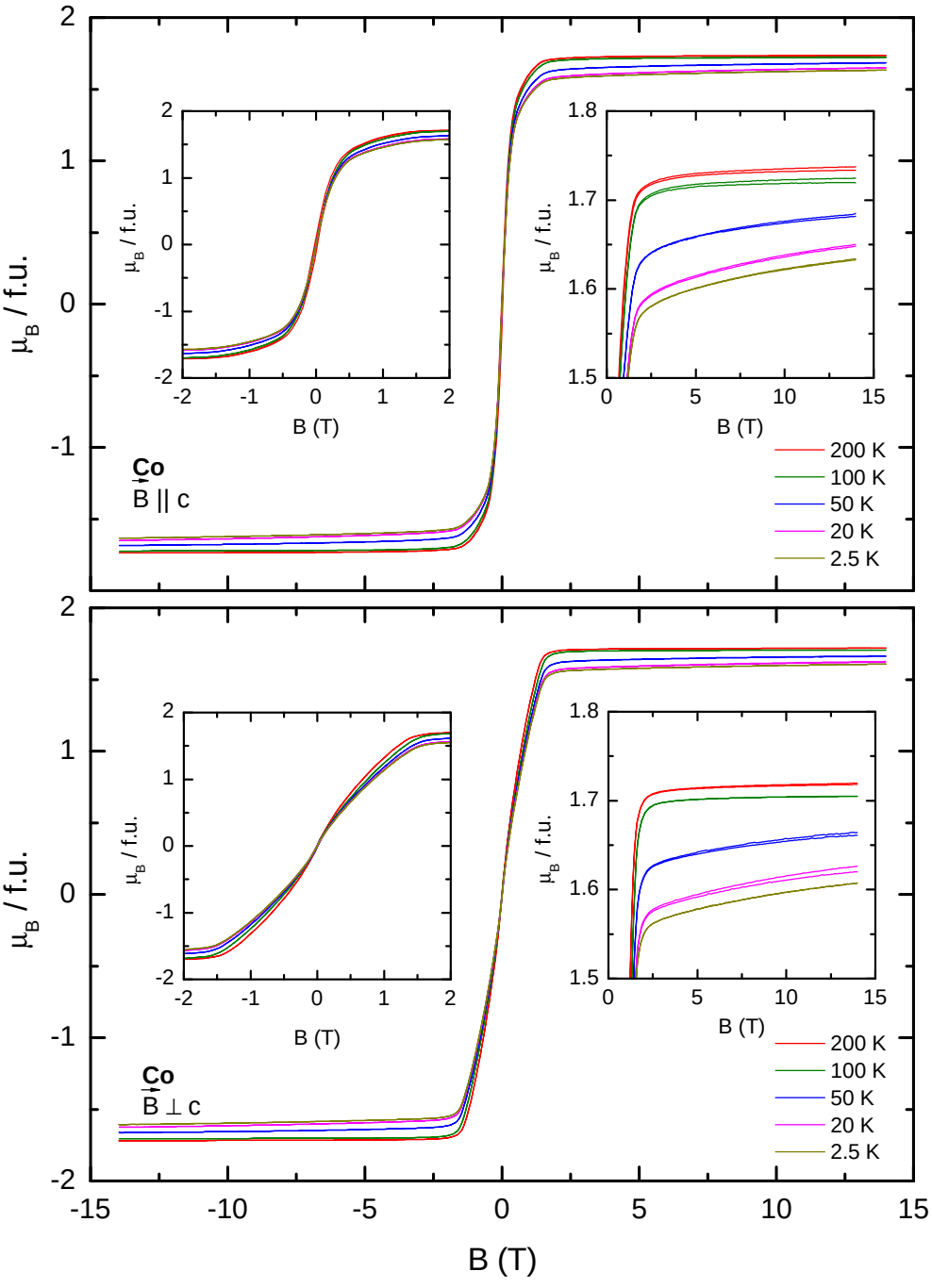

Figure A.6: Magnetization $M(B)$ of metallic Cobalt parallel and perpendicular to c.

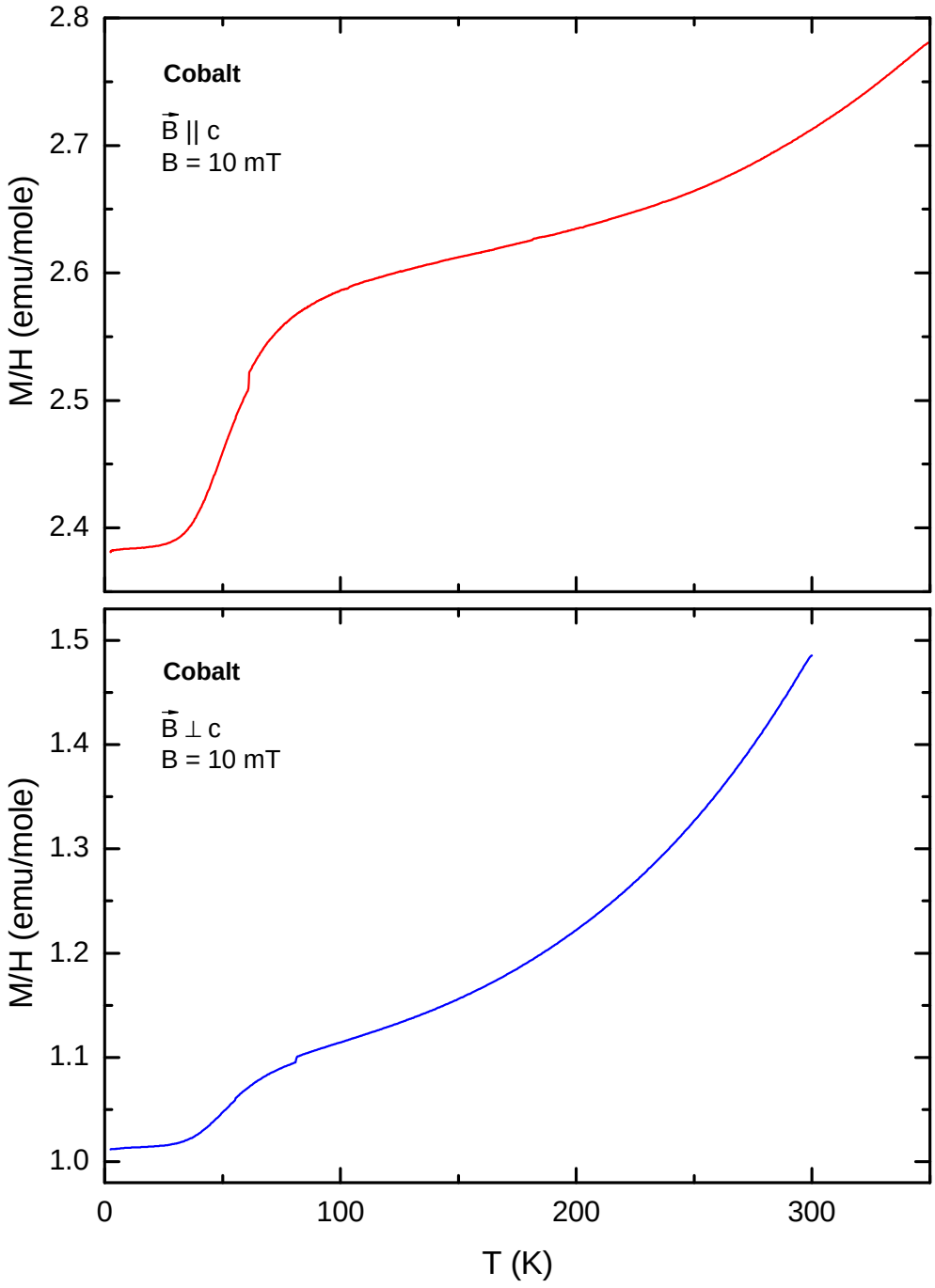

Figure A.7: Magnetic susceptibility M/H of metallic Cobalt parallel and perpendicular to c for a magnetic field of 10 mT.

A.4 Thermopower of Copper (Calibration)

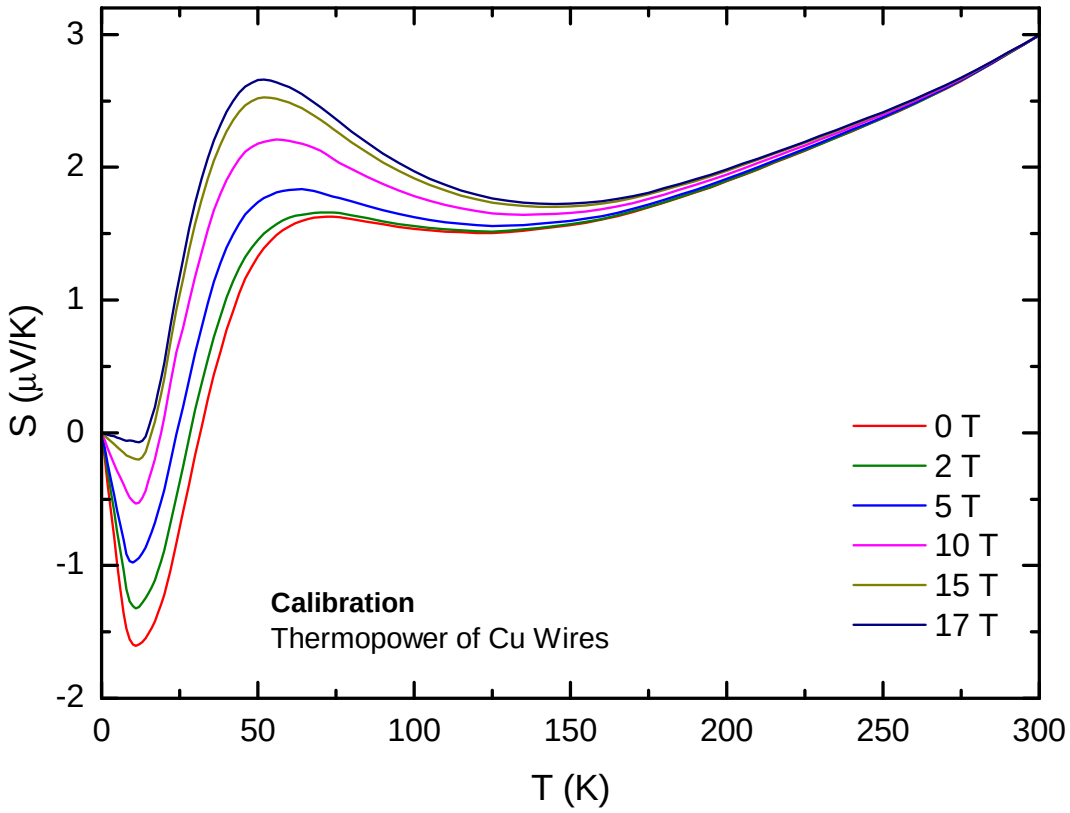

Figure A.8: Calibration of copper wires used for thermopower-measurements. Below 50 K, the thermopower is measured with respect to the high-T_c superconductor YBCO. The calibration up to room temperature has been measured with respect to lead [198]. Due to the small field dependence in the high-temperature region, above 150 K, the thermopower has been measured in zero field and for 15 T. The curves for the intermediate fields are obtained by linear interpolation there. Below 5 K, all curves are extrapolated to zero. The 17T curve is obtained by linearly extrapolating beyond 15 T.

A.5 Thermometer Calibration (Kelvinox Transport Sample Holder)

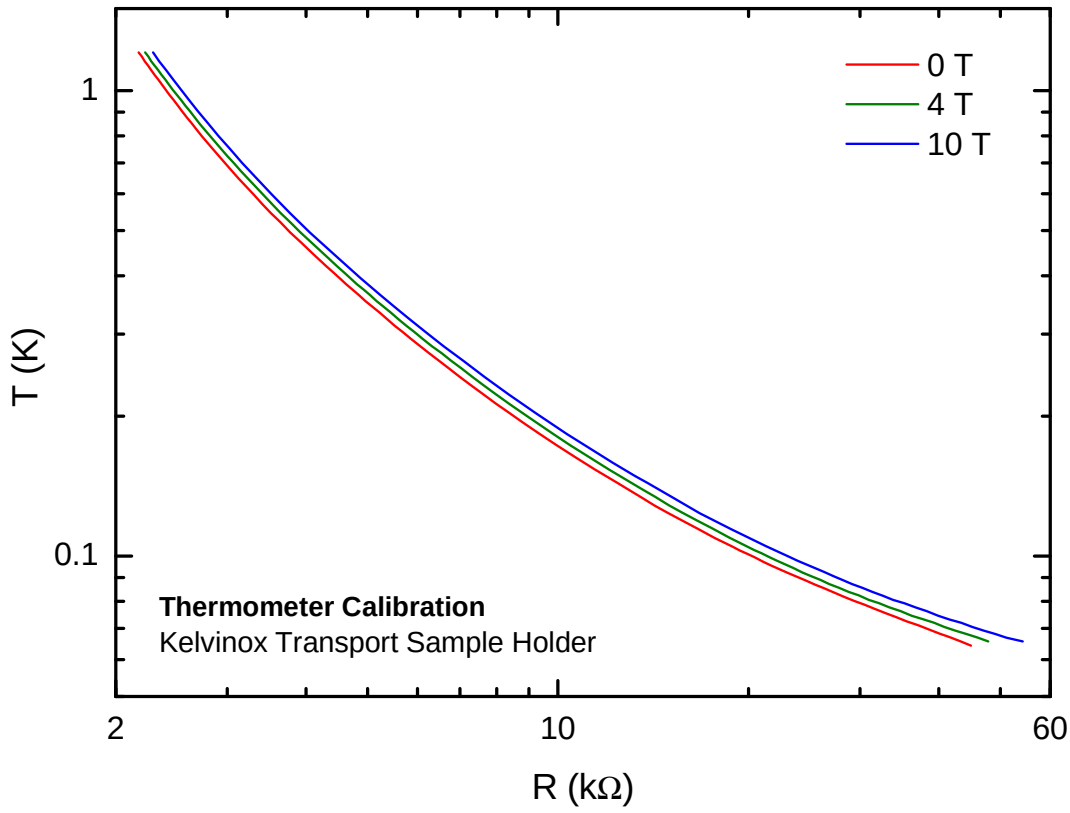

Figure A.9: Resistivity characteristics of the sample-holder thermometer placed at the transport sample holder used in the Kelvinox dilution refrigerator. The figure shows the characteristics for 0 T, 4 T,and for 10 T. The curves measured for 1 T, 2 T, and 8 T are not shown. The thermometer has been calibrated with respect to a calibrated thermometer (serial: U01447+RT).

A.6 LiFeAs

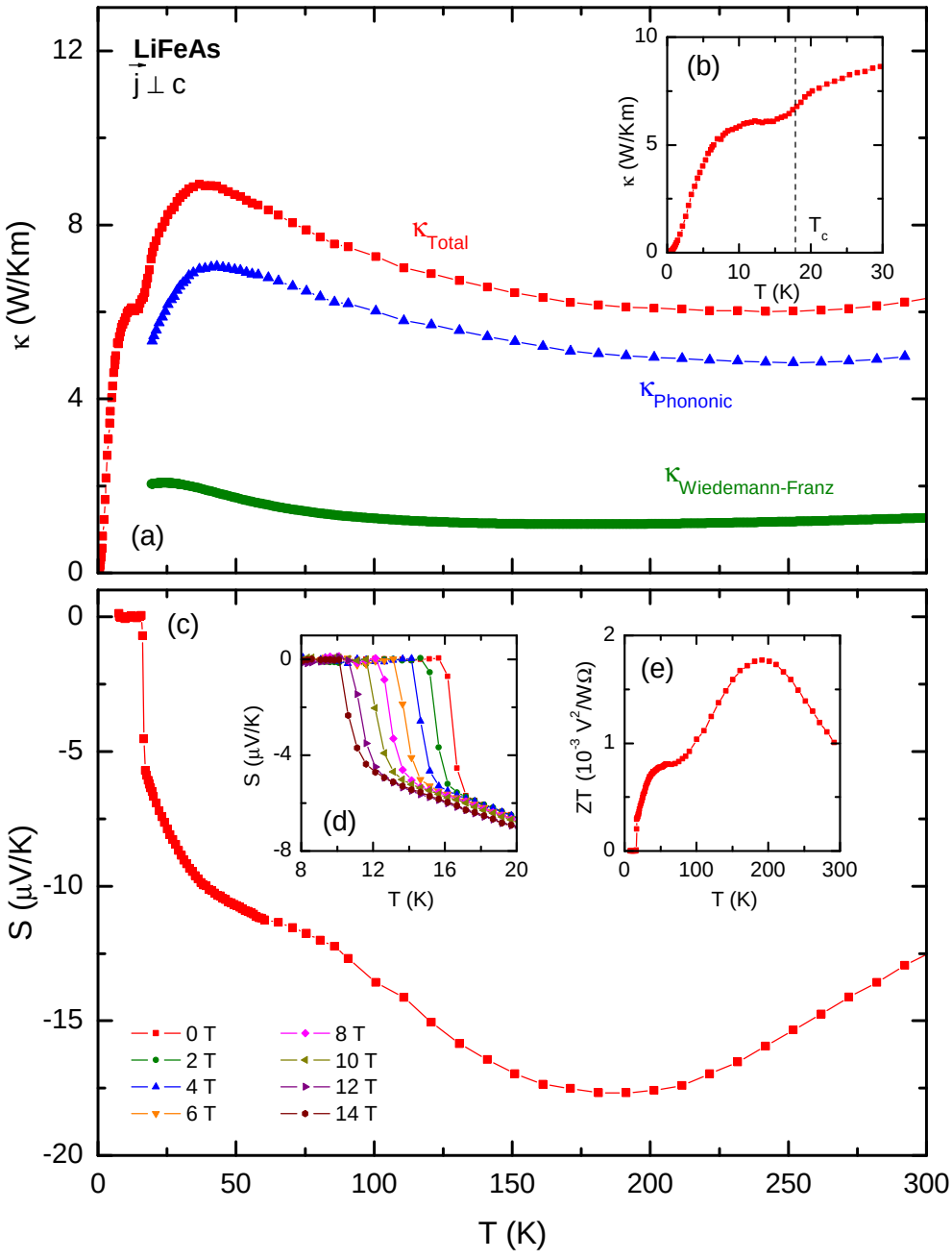

Figure A.10: (a) Thermal conductivity of LiFeAs. The electronic and phononic contributions are estimated via the Wiedemann-Franz law (the resistivity is taken from Refs. [199, 200]). (b) $\kappa(T)$ of LiFeAs around T_c. (c) Zero-field thermopower $S(T)$ of LiFeAs. (d) $S(T)$ of LiFeAs for different magnetic fields. (e) Figure of Merit of LiFeAs.

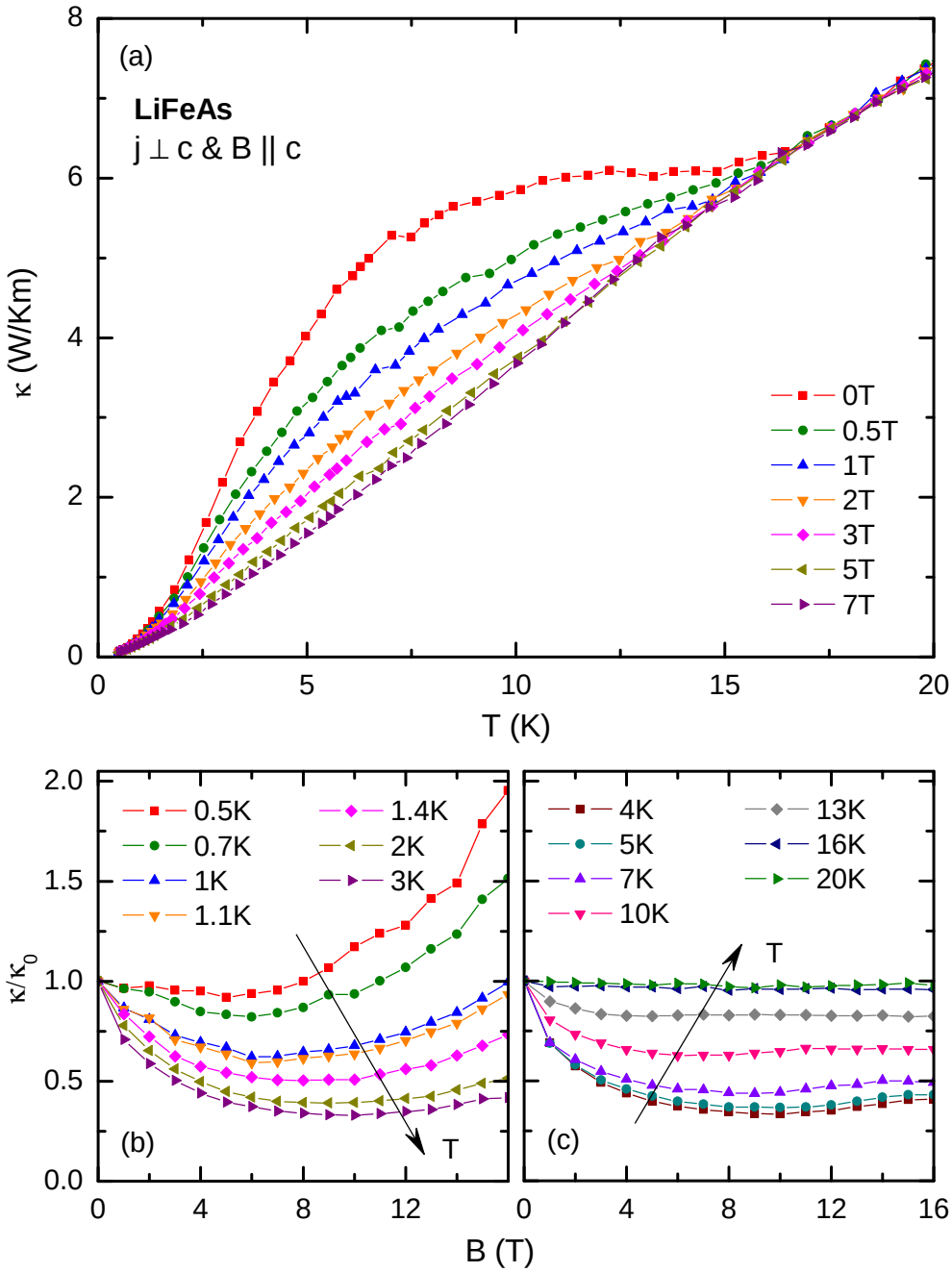

Figure A.11: (a) Low-temperature thermal conductivity of LiFeAs for different magnetic fields. (b) and (c) Magnetic-field dependence of $\kappa(B)$ of LiFeAs at various constant temperatures. The field-dependent data are obtained by resorting field-cooled measurements at respective constant fields.

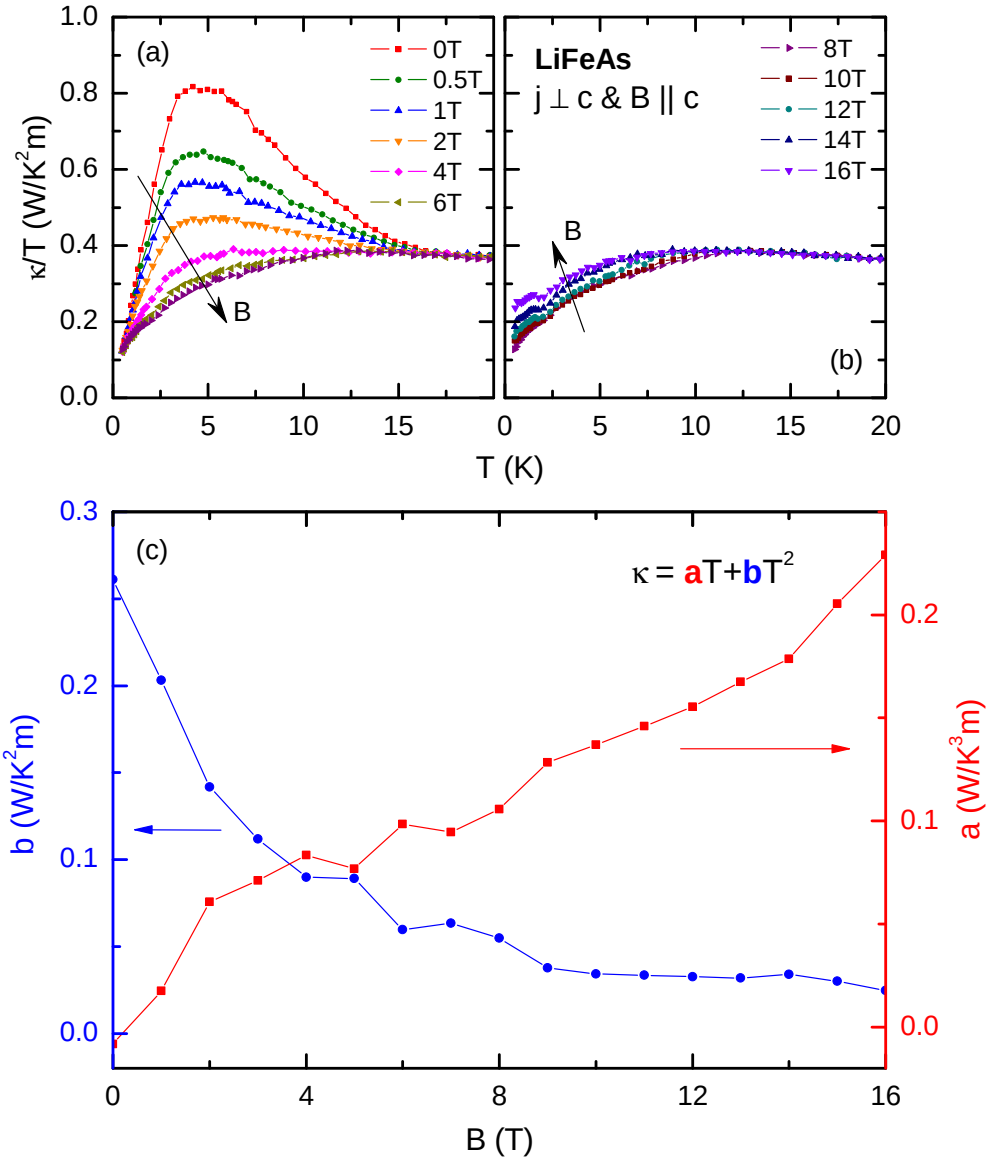

Figure A.12: (a) and (b) κ/T of LiFeAs for different magnetic fields. (c) Linear and quadratic part of $\kappa(T)$ for $T \to 0$ of LiFeAs for various magnetic fields.

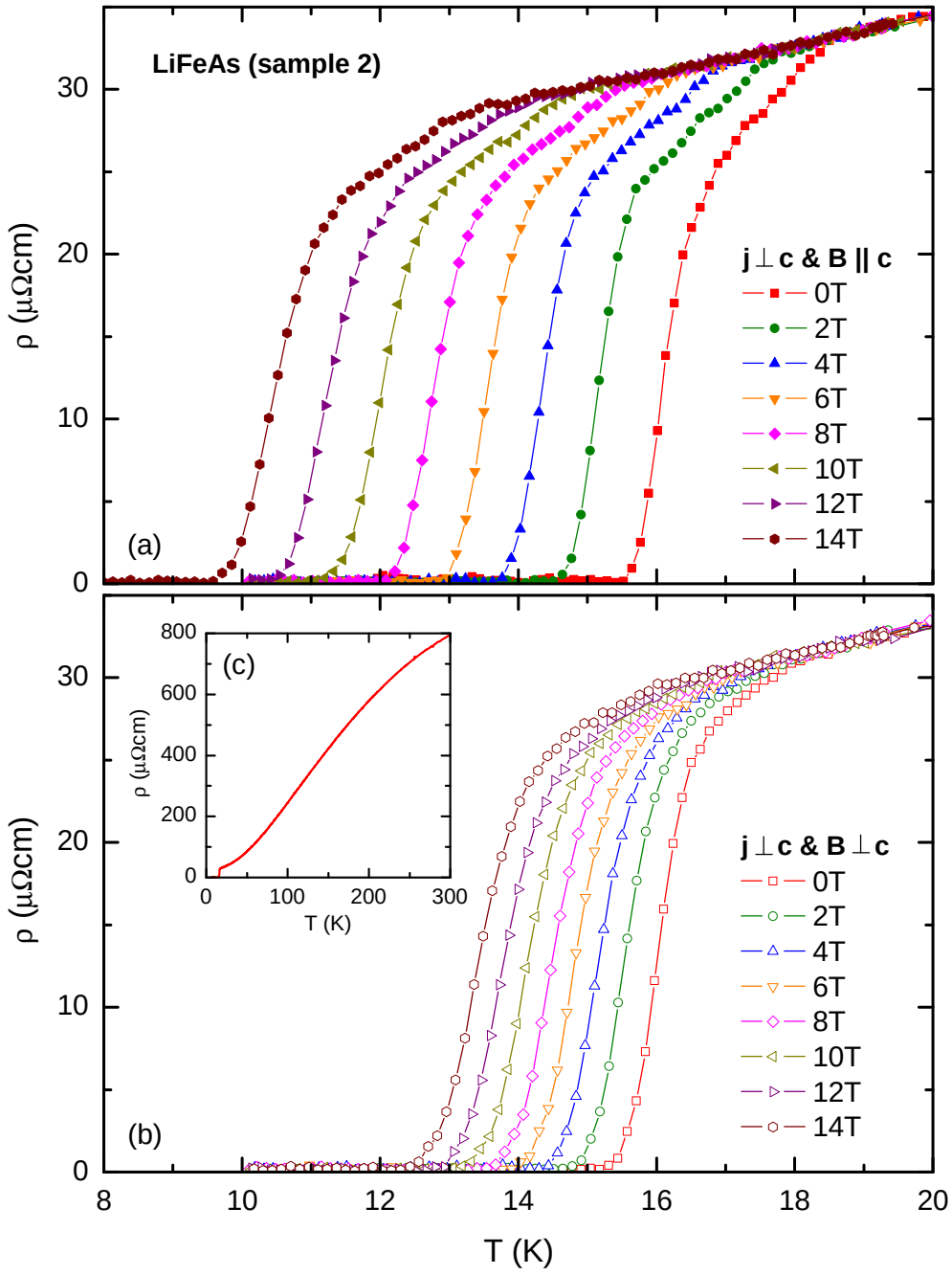

Figure A.13: (a) and (b) Electrical resistivity of LiFeAs measured on another sample as the data of Figs. A.10, A.11, and A.12 for different magnetic-field directions. (c) Zero-field resistivity up to room temperature.

A.7 $(Pr_{1-y}Eu_y)_{0.7}Ca_{0.3}CoO_3$

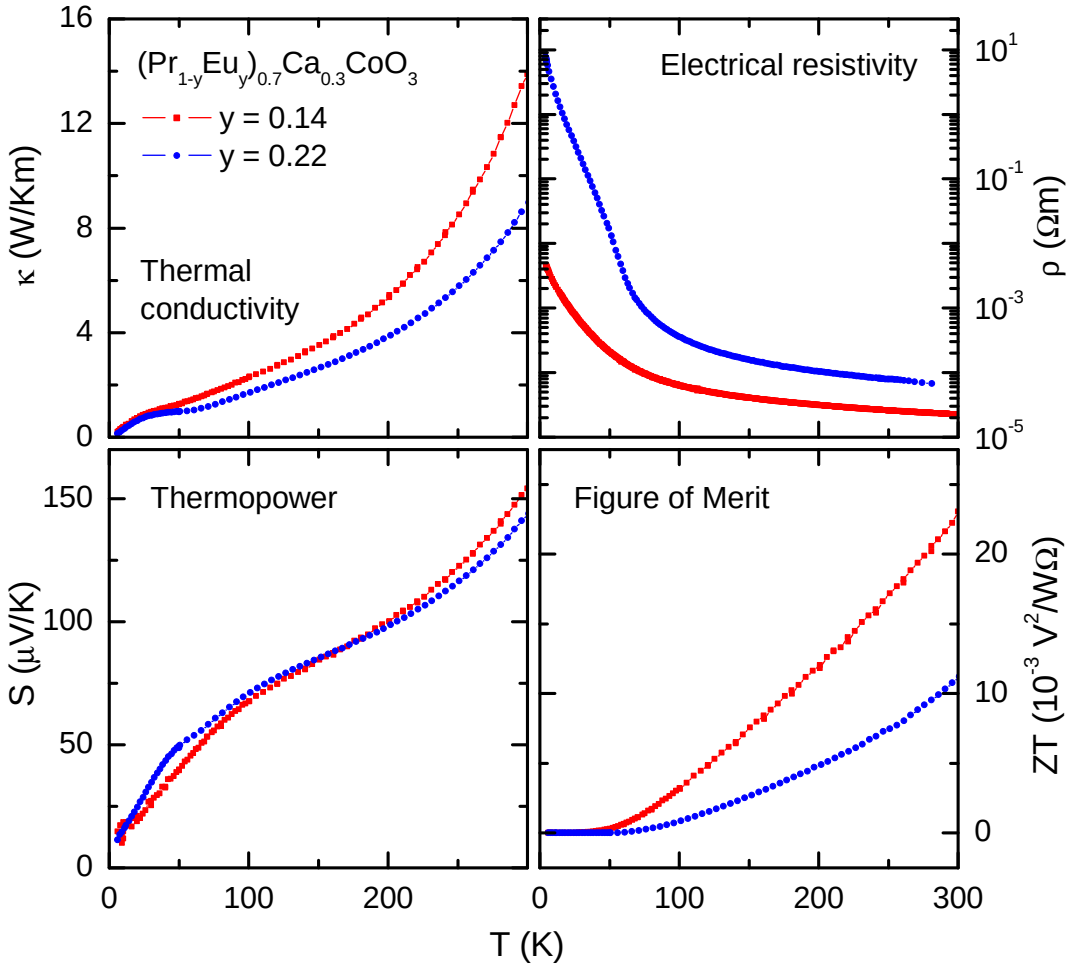

Figure A.14: Thermal conductivity, electrical resistivity, thermopower, and figure of merit of polycrystalline $(Pr_{1-y}Eu_y)_{0.7}Ca_{0.3}CoO_3$ for $y = 0.14$ and $y = 0.22$. The data were measured on samples containing ^{16}O. A phase diagram of $(Pr_{1-y}Eu_y)_{0.7}Ca_{0.3}CoO_3$ is published in [201, 202] where, in addition, the influence of substitution of ^{16}O by ^{18}O is studied.

A.8 $Eu_{0.7}Ca_{0.3}CoO_3$

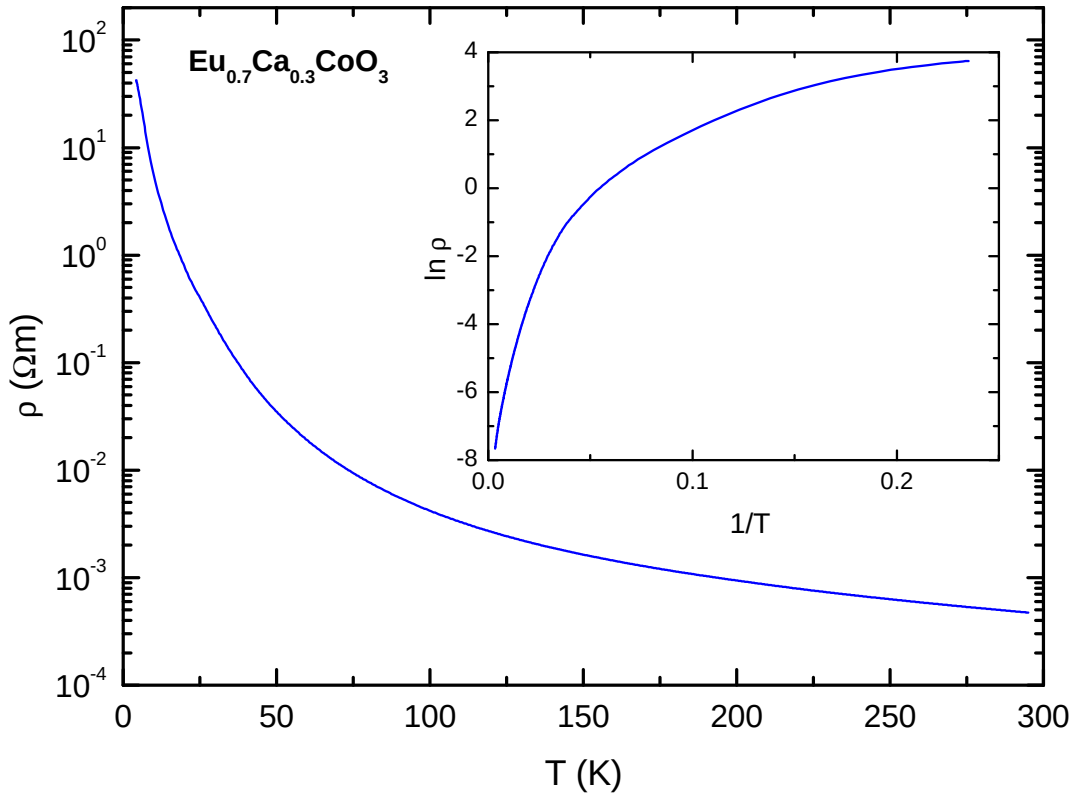

Figure A.15: Resistivity $\rho(T)$ of polycrystalline $Eu_{0.7}Ca_{0.3}CoO_3$ which is a reference system to $(Pr_{1-y}Eu_y)_{0.7}Ca_{0.3}CoO_3$.

Bibliography

[1] L. Pauling, Journal of the American Chemical Society **57**, 2680 (1935).

[2] P. A. M. Dirac, Proceedings of the Royal Society of London. Series A **133**, 60 (1931).

[3] S. Bramwell, S. Giblin, S. Calder, R. Aldus, D. Prabhakaran, and T. Fennell, Nature **461**, 956 (2009).

[4] S. Giblin, S. Bramwell, P. Holdsworth, D. Prabhakaran, and I. Terry, Nature Physics **7**, 252 (2011).

[5] S. Blundell, Physical Review Letters **108**, 147601 (2012).

[6] B. Klemke, M. Meissner, P. Strehlow, K. Kiefer, S. Grigera, and D. Tennant, Journal of Low Temperature Physics **163**, 345 (2011).

[7] S. Kimura, H. Yashiro, M. Hagiwara, K. Okunishi, K. Kindo, Z. He, T. Taniyama, and M. Itoh, Journal of Physics: Conference Series **51**, 99 (2006).

[8] C. Hess, The European Physical Journal Special Topics **151**, 7 (2007).

[9] C. Hess, PhD thesis (Universität zu Köln, 2002).

[10] C. Kittel, *Einführung in die Festkörperphysik* (Oldenburgverlag, München, Wien, 2001).

[11] N. Ashcroft and N. Mermin, *Solid State Physics* (Saunders College Publishing, 1976).

[12] R. Berman, *Thermal Conduction in Solids* (Clarendon Press, Oxford, 1976).

[13] A. Freimuth, *Vorlesung Festkörperphysik I und II* (1999).

[14] J. Ziman, *Principles of the Theory of Solids*, 2nd ed. (Cambridge University Press, 1972).

[15] C. Weissmantel and C. Hamann, *Grundlagen der Festkörperphysik* (Springer, Berlin, 1979).

[16] J. Parrott and A. Stuckes, *Thermal Conductivity of Solids* (Pion Limited, London, 1975).

[17] P. Klemens, *Thermal Conductivity and Lattice Vibrational Modes in Solid State Physics (Vol. 7)* (Academic, New York, 1958).

[18] K. Berggold, PhD thesis (Universität zu Köln, 2006).

[19] K. Kordonis, PhD thesis (Universität zu Köln, 2006).

[20] R. Tye, *Thermal conductivity*, Bd. 1 (Academic P., 1969).

[21] R. Tye, *Thermal conductivity*, Bd. 2 (Academic P., 1969).

[22] http://www.scilab.org.

[23] P. Klemens, Proceedings of the Physical Society. Section A **68**, 1113 (1955).

[24] H. Stern, Journal of Physics and Chemistry of Solids **26**, 153 (1965).

[25] K. Kawasaki, Progress of Theoretical Physics **29**, 801 (1963).

[26] Z. Y. Zhao, X. M. Wang, B. Ni, Q. J. Li, C. Fan, W. P. Ke, W. Tao, L. M. Chen, X. Zhao, and X. F. Sun, Physical Review B **83**, 174518 (2011).

[27] Z. Y. Zhao, X. M. Wang, C. Fan, W. Tao, X. G. Liu, W. P. Ke, F. B. Zhang, X. Zhao, and X. F. Sun, Physical Review B **83**, 014414 (2011).

[28] X. F. Sun and Y. Ando, Physical Review B **79**, 176501 (2009).

[29] L. Taillefer, B. Lussier, R. Gagnon, K. Behnia, and H. Aubin, Physical Review Letters **79**, 483 (1997).

[30] P. D. Thacher, Physical Review **156**, 975 (1967).

[31] M. Hofmann, PhD thesis (Universität zu Köln, 2002).

[32] M. Hofmann, T. Lorenz, G. Uhrig, H. Kierspel, O. Zabara, A. Freimuth, H. Kageyama, and Y. Ueda, Physical Review Letters **87**, 047202 (2001).

[33] J. Graebner, B. Golding, and L. Allen, Physical Review B **34**, 5696 (1986).

[34] D. Cahill, S. Watson, and R. Pohl, Physical Review B **46**, 6131 (1992).

[35] J. M. Ziman, *Electrons and phonons: the theory of transport phenomena in solids* (Clarendon Press, 1960).

[36] C. Gerthsen and H. Vogel, *Gerthsen Physik* (Springer-Verlag GmbH, 1999).

[37] H. Rosenberg, *Low Temperature Solid State Physics* (Clarendon Press, 1963).

[38] A. Sologubenko, T. Lorenz, H. Ott, and A. Freimuth, Journal of Low Temperature Physics **147**, 387 (2007).

[39] B. Lüthi, Journal of Physics and Chemistry of Solids **23**, 35 (1962).

[40] R. L. Douglass, Phys. Rev. **129**, 1132 (1963).

[41] J. E. Rives, G. S. Dixon, and D. Walton, Journal of Applied Physics **40**, 1555 (1969).

[42] D. Walton, J. E. Rives, and Q. Khalid, Physical Review B **8**, 1210 (1973).

[43] F. Gorter, L. Noordermeer, A. Kop, and A. Miedema, Physics Letters A **29**, 331 (1969).

[44] H. N. De Lang, H. van Kempen, and P. Wyder, Physical Review Letters **39**, 467 (1977).

[45] L. Coenen, H. D. Lang, J. Stoelinga, H. V. Kempen, and P. Wyder, Physica B+C **8688, Part 2**, 968 (1977).

[46] A. Klümper, Zeitschrift für Physik B Condensed Matter **91**, 507 (1993).

[47] L. Faddeev and L. Takhtajan, Physics Letters A **85**, 375 (1981).

[48] E. Dagotto, Reports on Progress in Physics **62**, 1525 (1999).

[49] E. Manousakis, Reviews of Modern Physics **63**, 1 (1991).

[50] X. Zotos, F. Naef, and P. Prelovsek, Physical Review B **55**, 11029 (1997).

[51] X. Zotos, Physical Review Letters **82**, 1764 (1999).

[52] J. V. Alvarez and C. Gros, Physical Review Letters **89**, 156603 (2002).

[53] F. Heidrich-Meisner, A. Honecker, D. C. Cabra, and W. Brenig, Physical Review Letters **92**, 069703 (2004).

[54] X. Zotos, Physical Review Letters **92**, 067202 (2004).

[55] E. Boulat, P. Mehta, N. Andrei, E. Shimshoni, and A. Rosch, Physical Review B **76**, 214411 (2007).

[56] A. V. Sologubenko, K. Giannó, H. R. Ott, U. Ammerahl, and A. Revcolevschi, Physical Review Letters **84**, 2714 (2000).

[57] C. Hess, C. Baumann, U. Ammerahl, B. Büchner, F. Heidrich-Meisner, W. Brenig, and A. Revcolevschi, Physical Review B **64**, 184305 (2001).

[58] C. Hess, B. Büchner, U. Ammerahl, L. Colonescu, F. Heidrich-Meisner, W. Brenig, and A. Revcolevschi, Physical Review Letters **90**, 197002 (2003).

[59] C. Hess, H. ElHaes, A. Waske, B. Büchner, C. Sekar, G. Krabbes, F. Heidrich-Meisner, and W. Brenig, Physical Review Letters **98**, 027201 (2007).

[60] A. V. Sologubenko, T. Lorenz, J. A. Mydosh, A. Rosch, K. C. Shortsleeves, and M. M. Turnbull, Physical Review Letters **100**, 137202 (2008).

[61] A. V. Sologubenko, K. Berggold, T. Lorenz, A. Rosch, E. Shimshoni, M. D. Phillips, and M. M. Turnbull, Physical Review Letters **98**, 107201 (2007).

[62] A. Sologubenko, K. Berggold, T. Lorenz, A. Rosch, E. Shimshoni, M. Phillips, and M. Turnbull, Physica B: Condensed Matter **403**, 1445 (2008).

[63] G. Mennenga, L. de Jongh, W. Huiskamp, and J. Reedijk, Journal of Magnetism and Magnetic Materials **44**, 89 (1984).

[64] P. R. Hammar, M. B. Stone, D. H. Reich, C. Broholm, P. J. Gibson, M. M. Turnbull, C. P. Landee, and M. Oshikawa, Physical Review B **59**, 1008 (1999).

[65] T. Lancaster, S. J. Blundell, M. L. Brooks, P. J. Baker, F. L. Pratt, J. L. Manson, C. P. Landee, and C. Baines, Physical Review B **73**, 020410 (2006).

[66] A. V. Sologubenko, T. Lorenz, J. A. Mydosh, B. Thielemann, H. M. Rønnow, C. Rüegg, and K. W. Krämer, Physical Review B **80**, 220411 (2009).

[67] P. Jordan and E. Wigner, Zeitschrift für Physik **47**, 631 (1928).

[68] F. Heidrich-Meisner, A. Honecker, and W. Brenig, Physical Review B **71**, 184415 (2005).

[69] F. Heidrich-Meisner, PhD thesis (TU Braunschweig, 2005).

[70] S. Eggert and I. Affleck, Physical Review B **46**, 10866 (1992).

[71] A. V. Rozhkov and A. L. Chernyshev, Physical Review Letters **94**, 087201 (2005).

[72] B. C. Watson, V. N. Kotov, M. W. Meisel, D. W. Hall, G. E. Granroth, W. T. Montfrooij, S. E. Nagler, D. A. Jensen, R. Backov, M. A. Petruska, G. E. Fanucci, and D. R. Talham, Physical Review Letters **86**, 5168 (2001).

[73] T. Lorenz, O. Heyer, M. Garst, F. Anfuso, A. Rosch, C. Rüegg, and K. Krämer, Physical Review Letters **100**, 067208 (2008).

[74] M. Klanjšek, H. Mayaffre, C. Berthier, M. Horvatić, B. Chiari, O. Piovesana, P. Bouillot, C. Kollath, E. Orignac, R. Citro, and T. Giamarchi, Physical Review Letters **101**, 137207 (2008).

[75] F. Anfuso, M. Garst, A. Rosch, O. Heyer, T. Lorenz, C. Rüegg, and K. Krämer, Physical Review B **77**, 235113 (2008).

[76] C. Rüegg, K. Kiefer, B. Thielemann, D. F. McMorrow, V. Zapf, B. Normand, M. B. Zvonarev, P. Bouillot, C. Kollath, T. Giamarchi, S. Capponi, D. Poilblanc, D. Biner, and K. W. Krämer, Physical Review Letters **101**, 247202 (2008).

[77] B. Thielemann, C. Rüegg, K. Kiefer, H. M. Rønnow, B. Normand, P. Bouillot, C. Kollath, E. Orignac, R. Citro, T. Giamarchi, A. M. Läuchli, D. Biner, K. W. Krämer, F. Wolff-Fabris, V. S. Zapf, M. Jaime, J. Stahn, N. B. Christensen, B. Grenier, D. F. McMorrow, and J. Mesot, Physical Review B **79**, 020408 (2009).

[78] B. Thielemann, C. Rüegg, H. M. Rønnow, A. M. Läuchli, J.-S. Caux, B. Normand, D. Biner, K. W. Krämer, H.-U. Güdel, J. Stahn, K. Habicht, K. Kiefer, M. Boehm, D. F. McMorrow, and J. Mesot, Physical Review Letters **102**, 107204 (2009).

[79] A. Shapiro, C. P. Landee, M. M. Turnbull, J. Jornet, M. Deumal, J. J. Novoa, M. A. Robb, and W. Lewis, Journal of the American Chemical Society **129**, 952 (2007).

[80] D. Schmidiger, S. Mühlbauer, S. N. Gvasaliya, T. Yankova, and A. Zheludev, Physical Review B **84**, 144421 (2011).

[81] J. Osborn, Physical Review **67**, 351 (1945).

[82] http://www.wolfram.com/mathematica.

[83] http://www.esrf.eu/Accelerators/Groups/InsertionDevices/Software/Radia.

[84] M. Hiertz, Diploma thesis (in progress) (Universität zu Köln).

[85] D. Loewen, Diploma thesis (Universität zu Köln, 2011).

[86] S. Scharffe, Diploma thesis (Universität zu Köln, 2012).

[87] O. Heyer, Diploma thesis (Universität zu Köln, 2005).

[88] G. Brndli and R. Griessen, Cryogenics **13**, 299 (1973).

[89] K. Berggold, Diploma thesis (Universität zu Köln, 2003).

[90] http://www.isabellenhuette.de/.

[91] http://www.plano-em.de/.

[92] http://www.epotek.com/.

[93] http://www.lakeshore.com/.

[94] http://www.wakefield.com/.

[95] K. Kordonis, Diploma thesis (Universität zu Köln, 2000).

[96] N. Johannsen, PhD thesis (Universität zu Köln, 2008).

[97] http://www.keithley.com/.

[98] http://www.ni.com/labview/.

[99] C. Zobel, PhD thesis (Universität zu Köln, 2002).

[100] http://www.oxford-instruments.com/.

[101] http://www.picowatt.fi/.

[102] T. Zabel, PhD thesis (Universität zu Köln, 2004).

[103] R. F. Wang, C. Nisoli, R. S. Freitas, J. Li, W. McConville, B. J. Cooley, M. S. Lund, N. Samarth, C. Leighton, V. H. Crespi, and P. Schiffer, Nature **439**, 303 (2006).

[104] S. T. Bramwell, Nature **439**, 273 (2006).

[105] P. Mellado, O. Petrova, Y. Shen, and O. Tchernyshyov, Physical Review Letters **105**, 187206 (2010).

[106] M. Tanaka, E. Saitoh, H. Miyajima, T. Yamaoka, and Y. Iye, Physical Review B **73**, 052411 (2006).

[107] Y. Qi, T. Brintlinger, and J. Cumings, Physical Review B **77**, 094418 (2008).

[108] S. Ladak, D. E. Read, G. K. Perkins, L. F. Cohen, and W. R. Branford, Nature Physics **6**, 359 (2010).

[109] G. Möller and R. Moessner, Physical Review B **80**, 140409 (2009).

[110] L. A. Mol, R. L. Silva, R. C. Silva, A. R. Pereira, W. A. Moura-Melo, and B. V. Costa, Journal of Applied Physics **106**, 063913 (2009).

[111] M. Hayashi, L. Thomas, C. Rettner, R. Moriya, and S. S. P. Parkin, Nature Physics **3**, 21 (2007).

[112] G. Möller and R. Moessner, Physical Review Letters **96**, 237202 (2006).

[113] S. Bramwell, M. Harris, B. den Hertog, M. Gingras, J. Gardner, D. McMorrow, A. Wildes, A. Cornelius, J. Champion, R. Melko, and T. Fennell, Physical Review Letters **87**, 047205 (2001).

[114] H. Molavian and M. Gingras, Journal of Physics: Condensed Matter **21**, 172201 (2009).

[115] D. Cahill and R. Pohl, Annual Review of Physical Chemistry **39**, 93 (1988).

[116] D. G. Cahill, J. R. Olson, H. E. Fischer, S. K. Watson, R. B. Stephens, R. H. Tait, T. Ashworth, and R. O. Pohl, Physical Review B **44**, 12226 (1991).

[117] P. B. Allen and J. L. Feldman, Physical Review B **48**, 12581 (1993).

[118] R. Berman, P. G. Klemens, F. E. Simon, and T. M. Fry, Nature **166**, 864 (1950).

[119] D. G. Cahill and R. Pohl, Solid State Communications **70**, 927 (1989).

[120] R. Higashinaka, H. Fukazawa, K. Deguchi, and Y. Maeno, Journal of the Physics Society Japan **73**, 2845 (2004).

[121] B. Klemke, PhD thesis (Technische Universität Berlin, 2011).

[122] A. Ramirez, A. Hayashi, R. Cava, R. Siddharthan, and B. Shastry, Nature **399**, 333 (1999).

[123] S. Bramwell and M. Gingras, Science (New York, N.Y.) **294**, 1495 (2001).

[124] Z. Hiroi, K. Matsuhira, S. Takagi, T. Tayama, and T. Sakakibara, Journal of the Physics Society Japan **72**, 411 (2003).

[125] T. Sakakibara, T. Tayama, Z. Hiroi, K. Matsuhira, and S. Takagi, Physical Review Letters **90**, 207205 (2003).

[126] J. Nagle, Journal of Mathematical Physics **7**, 1484 (1966).

[127] M. Harris, S. Bramwell, D. Mcmorrow, T. Zeiske, and K. Godfrey, Physical Review Letters **79**, 2554 (1997).

[128] S. Bramwell and M. Harris, Journal of Physics: Condensed Matter **10**, L215 (1998).

[129] C. Castelnovo, R. Moessner, and S. Sondhi, Nature **451**, 42 (2008).

[130] D. Morris, D. Tennant, S. Grigera, B. Klemke, C. Castelnovo, R. Moessner, C. Czternasty, M. Meissner, K. Rule, J. Hoffmann, K. Kiefer, S. Gerischer, D. Slobinsky, and R. Perry, Science (New York, N.Y.) **326**, 411 (2009).

[131] I. Ryzhkin, Journal of Experimental and Theoretical Physics **101**, 481 (2005).

[132] L. D. C. Jaubert and P. C. W. Holdsworth, Nature Physics **5**, 258 (2009).

[133] H. Kadowaki, N. Doi, Y. Aoki, Y. Tabata, T. Sato, J. Lynn, K. Matsuhira, and Z. Hiroi, Journal of the Physical Society of Japan **78**, 103706 (2009).

[134] C. Castelnovo, R. Moessner, and S. Sondhi, Physical Review B **84**, 144435 (2011).

[135] A. Fuentes, K. Boulahya, M. Maczka, J. Hanuza, and U. Amador, Solid State Sciences **7**, 343 (2005).

[136] B. Malkin, T. Lummen, P. van Loosdrecht, G. Dhalenne, and A. Zakirov, Journal of Physics: Condensed Matter **22**, 276003 (2010).

[137] K. Kitagawa, R. Higashinaka, K. Ishida, Y. Maeno, and M. Takigawa, Physical Review B **77**, 1 (2008).

[138] Y. Jana, A. Sengupta, and D. Ghosh, Journal of Magnetism and Magnetic Materials **248**, 7 (2002).

[139] L. Jaubert and P. Holdsworth, Journal of Physics: Condensed Matter **23**, 164222 (2011).

[140] R. Melko and M. Gingras, Journal of Physics: Condensed Matter **16**, R1277 (2004).

[141] B. den Hertog and M. Gingras, Physical Review Letters **84**, 3430 (2000).

[142] J. Snyder, J. Slusky, R. Cava, and P. Schiffer, Nature **413**, 48 (2001).

[143] K. Matsuhira, C. Paulsen, E. Lhotel, C. Sekine, Z. Hiroi, and S. Takagi, Journal of the Physical Society of Japan **80**, 123711 (2011).

[144] L. Yaraskavitch, H. Revell, S. Meng, K. Ross, H. Noad, H. Dabkowska, B. Gaulin, and J. Kycia, Physical Review B **85**, 020410(R) (2012).

[145] J. Snyder, B. Ueland, J. Slusky, H. Karunadasa, R. Cava, and P. Schiffer, Physical Review B **69**, 064414 (2004).

[146] J. Lago, S. Blundell, and C. Baines, Journal of Physics: Condensed Matter **19**, 326210 (2007).

[147] S. Dunsiger, A. Aczel, C. Arguello, H. Dabkowska, A. Dabkowski, M. Du, T. Goko, B. Javanparast, T. Lin, F. Ning, H. Noad, D. Singh, T. Williams, Y. Uemura, M. Gingras, and G. Luke, Physical Review Letters **107**, 207207 (2011).

[148] J. Gardner, G. Ehlers, P. Fouquet, B. Farago, and J. Stewart, Journal of Physics: Condensed Matter **23**, 164220 (2011).

[149] K. Matsuhira, Z. Hiroi, T. Tayama, S. Takagi, and T. Sakakibara, Journal of Physics: Condensed Matter **14**, L559 (2002).

[150] G. Kolland, O. Breunig, M. Valldor, M. Hiertz, J. Frielingsdorf, and T. Lorenz, Physical Review B **86**, 060402 (2012).

[151] O. Breunig, PhD thesis (in progress) (Universität zu Köln).

[152] A. Anderson, B. Holmström, M. Krusius, and G. Pickett, Physical Review **183**, 546 (1969).

[153] Y. Tabata, H. Kadowaki, K. Matsuhira, Z. Hiroi, N. Aso, E. Ressouche, and B. Fak, Physical Review Letters **97**, 257205 (2006).

[154] Y. Tabata, H. Kadowaki, K. Matsuhira, Z. Hiroi, N. Aso, E. Ressouche, and B. Fak, Journal of Magnetism and Magnetic Materials **310**, 1311 (2007).

[155] S. Yoshida, K. Nemoto, and K. Wada, Journal of the Physics Society Japan **73**, 1619 (2004).

[156] http://www.python.org.

[157] P. Ewald, Annalen der Physik (Leipzig) **64**, 253 (1921).

[158] S. De Leeuw, J. Perram, and E. Smith, Annual Review of Physical Chemistry **37**, 245 (1986).

[159] M. Enjalran and M. Gingras, Physical Review B **70**, 174426 (2004).

[160] Z. Hiroi, K. Matsuhira, and M. Ogata, Journal of the Physics Society Japan **72**, 3045 (2003).

[161] P. Debye and E. Hückel, Physikalische Zeitschrift **24**, 185 (1923).

[162] V. Kobelev, A. Kolomeisky, and M. Fisher, The Journal of Chemical Physics **116**, 7589 (2002).

[163] J. Frielingsdorf, Diploma thesis (Universität zu Köln, 2011).

[164] K. Matsuhira, Y. Hinatsu, K. Tenya, and T. Sakakibara, Journal of Physics: Condensed Matter **12**, L649 (2000).

[165] H. Fukazawa, R. Melko, R. Higashinaka, Y. Maeno, and M. Gingras, Physical Review B **65**, 1 (2002).

[166] D. Slobinsky, C. Castelnovo, R. Borzi, A. Gibbs, A. Mackenzie, R. Moessner, and S. Grigera, Physical Review Letters **105**, 267205 (2010).

[167] M. Johnson, D. James, A. Bourque, H. Dabkowska, B. Gaulin, and M. White, Journal of Solid State Chemistry **182**, 725 (2009).

[168] S. Saha, S. Singh, B. Dkhil, S. Dhar, R. Suryanarayanan, G. Dhalenne, A. Revcolevschi, and A. Sood, Physical Review B **78**, 214102 (2008).

[169] N. Kamaraju, S. Kumar, S. Saha, S. Singh, R. Suryanarayanan, A. Revcolevschi, and A. Sood, Physical Review B **83**, 134104 (2011).

[170] R. Moessner and S. Sondhi, Physical Review B **68**, 064411 (2003).

[171] C. Castelnovo, R. Moessner, and S. Sondhi, Physical Review Letters **104**, 107201 (2010).

[172] S. Niesen, PhD thesis (in progress) (Universität zu Köln).

[173] M. Seher, Diploma thesis (Universität zu Köln, 2012).

[174] S. Niesen, Diploma thesis (Universität zu Köln, 2009).

[175] Z. He, T. Taniyama, and M. Itoh, Journal of Crystal Growth **289**, 734 (2006).

[176] Z. He, D. Fu, T. Kymen, T. Taniyama, and M. Itoh, Chemistry of Materials **17**, 2924 (2005).

[177] R. Wichmann and H. Müller-Buschbaum, Zeitschrift für anorganische und allgemeine Chemie **534**, 153 (1986).

[178] S. Kimura, Y. Narumi, N. Terada, Y. Tanaka, M. Iwaki, K. Katsumata, M. Hagiwara, K. Kindo, Z. He, T. Taniyama, M. Itoh, H. Toyokawa, T. Ishikawa, and H. Kitamura, Journal of the Physical Society of Japan **79**, 043706 (2010).

[179] Z. He, T. Taniyama, T. Kyômen, and M. Itoh, Physical Review B **72**, 172403 (2005).

[180] S. Kimura, M. Matsuda, T. Masuda, S. Hondo, K. Kaneko, N. Metoki, M. Hagiwara, T. Takeuchi, K. Okunishi, Z. He, K. Kindo, T. Taniyama, and M. Itoh, Physical Review Letters **101**, 207201 (2008).

[181] S. Kimura, T. Takeuchi, K. Okunishi, M. Hagiwara, Z. He, K. Kindo, T. Taniyama, and M. Itoh, Physical Review Letters **100**, 057202 (2008).

[182] N. Hollmann, Diploma thesis (Universität zu Köln, 2006).

[183] S. Kimura, H. Yashiro, K. Okunishi, M. Hagiwara, Z. He, K. Kindo, T. Taniyama, and M. Itoh, Physical Review Letters **99**, 087602 (2007).

[184] Z. He, T. Taniyama, and M. Itoh, Applied Physics Letters **88**, 132504 (2006).

[185] E. Canévet, B. Grenier, M. Klanjšek, C. Berthier, M. Horvatić, V. Simonet, and P. Lejay, ArXiv e-prints (2012), arXiv:1210.3253 .

[186] M. Klanjsek, M. Horvatic, C. Berthier, H. Mayaffre, E. Canevet, B. Grenier, P. Lejay, and E. Orignac, ArXiv e-prints (2012), arXiv:1202.6374 .

[187] Y. Kawasaki, J. L. Gavilano, L. Keller, J. Schefer, N. B. Christensen, A. Amato, T. Ohno, Y. Kishimoto, Z. He, Y. Ueda, and M. Itoh, Physical Review B **83**, 064421 (2011).

[188] Z. Y. Zhao, X. G. Liu, Z. Z. He, X. M. Wang, C. Fan, W. P. Ke, Q. J. Li, L. M. Chen, X. Zhao, and X. F. Sun, Physical Review B **85**, 134412 (2012).

[189] K. Okunishi and T. Suzuki, Physical Review B **76**, 224411 (2007).

[190] H. Yamaguchi, S. Yasin, S. Zherlitsyn, K. Omura, S. Kimura, S. Yoshii, K. Okunishi, Z. He, T. Taniyama, M. Itoh, and M. Hagiwara, Journal of the Physical Society of Japan **80**, 033701 (2011).

[191] S. Kimura, T. Takeuchi, M. Hagiwara, K. Okunishi, Z. He, T. Taniyama, and M. Itoh, Journal of Physics: Conference Series **150**, 042090 (2009).

[192] P. Lejay, E. Canevet, S. Srivastava, B. Grenier, M. Klanjsek, and C. Berthier, Journal of Crystal Growth **317**, 128 (2011).

[193] Z. He, T. Taniyama, M. Itoh, J.-I. Yamaura, and Y. Ueda, Solid State Communications **141**, 667 (2007).

[194] Z. He, T. Taniyama, and M. Itoh, Journal of Crystal Growth **293**, 458 (2006).

[195] Z. He, T. Taniyama, and M. Itoh, Physical Review B **73**, 212406 (2006).

[196] Z. He, Y. Ueda, and M. Itoh, Solid State Communications **141**, 22 (2007).

[197] M. Von Postel and H. Müller-Buschbaum, Zeitschrift für anorganische und allgemeine Chemie **615**, 97 (1992).

[198] R. B. Roberts, Nature **265**, 226 (1977).

[199] O. Heyer, T. Lorenz, V. B. Zabolotnyy, D. V. Evtushinsky, S. V. Borisenko, I. Morozov, L. Harnagea, S. Wurmehl, C. Hess, and B. Büchner, Physical Review B **84**, 064512 (2011).

[200] O. Heyer, PhD thesis (Universität zu Köln, 2012).

[201] A. V. Kalinov, O. Y. Gorbenko, A. N. Taldenkov, J. Rohrkamp, O. Heyer, S. Jodlauk, N. A. Babushkina, L. M. Fisher, A. R. Kaul, A. A. Kamenev, T. G. Kuzmova, D. I. Khomskii, K. I. Kugel, and T. Lorenz, Physical Review B **81**, 134427 (2010).

[202] N. A. Babushkina, A. N. Taldenkov, A. V. Kalinov, L. M. Fisher, O. Y. Gorbenko, T. Lorenz, D. I. Khomskii, and K. I. Kugel, Journal of Experimental and Theoretical Physics **111**, 189 (2010).

List of Figures

List of Tables

Publikationsliste

Teilpublikationen dieser Arbeit

- **Thermal conductivity and specific heat of the spin-ice compound $Dy_2Ti_2O_7$: Experimental evidence for monopole heat transport**
  G. Kolland, O. Breunig, M. Valldor, M. Hiertz, J. Frielingsdorf, and T. Lorenz
  Physical Review B **86**, 060402 (2012)

- **Tagungsbeiträge**
  - Frühjahrstagungen der Deutschen Physikalischen Gesellschaft (Arbeitskreis Festkörperphysik) in den Jahren 2010 bis 2012
  - SFB 608 Workshops in den Jahren 2009 bis 2011
  - SCES 2011 (Cambridge)
  - Lotherm Summerschool in den Jahren 2010 und 2012

Danksagung

An dieser Stelle möchte ich mich noch bei allen bedanken, die mich in den letzten Jahren begleitet und unterstützt haben.

Der erste und besondere Dank geht an meinen Doktorvater PD Dr. Thomas Lorenz, der zu jeder Zeit ein offenes Ohr hatte und die Zeit und Geduld für unzählige Gespräche und Diskussionen, die diese Arbeit maßgeblich vorangetrieben haben. Bedanken möchte ich mich auch bei den übrigen Mitgliedern der Prüfungskommission, bei Prof. Rosch für die Erstellung des Zweitgutachtens, bei Prof. Bohatý für die Übernahme des Prüfungsvorsitzes und bei Dr. Rückamp für die Anfertigung des Protokolls.

Ich möchte mich hier auch bei allen Kollegen für die unvergessliche Zeit im II. Physikalischen Institut bedanken.

Bei Martin Valldor für viele schöne Proben, die zu noch schöneren Ergebnissen führten, und für den unermüdlichen Eifer, die Grundfesten der Physik zu Fall zu bringen.

Bei Oliver Heyer für die multilaterale musikalische Begleitung beim Kontaktieren.

Bei Jens Rohrkamp, dem unbeirrbaren Kämpfer gegen Homöopathie und andere Skepsis erweckende Lehren.

Bei Sandra Niesen für noch mehr schöne Proben, die zu noch mehr schönen Messungen führten, und für Event-Planungen aller Art.

Bei Martin Hiertz für seinen unermüdlichen Einsatz beim Messen der Magnetisierung der verschiedenen Spin-Eis Dotierungen mithilfe selbsterklärender Messprogramme und bei Daniel Löwen für den Bau des dafür verwendeten Magnetometers.

Bei allen Büro-Mitbewohnern, die im Laufe der Jahre ein- und ausgezogen sind, insbesondere dem längsten Büro-Weggefährten, Oliver Breunig, unerschrockener Vernichter kulinarischer Besonderheiten.

Der Dank geht natürlich auch an alle anderen Mitglieder und ehemalige Mitglieder der Lorenz-Gruppe.

Bedanken möchte ich mich auch bei den Helium-Brauern Harald Kierspel und Rolf Dommel für vier hervorragende Jahrgänge des kalten Elixiers.

Auch bei Ralf Müller für sein Engagement rund um das Kaffeekassensystem, welches auch die Versorgung mit Tütensuppen sicherstellte.

Dank auch an Carmen Handels und Inge Simons für die Hilfe rund um alle weltlichen Belange des Instituts.

Weiterer Dank gilt auch den Werkstätten, denen es immer wieder gelungen ist, aus meinen Zeichnungen “auf Butterbrotpapier” wahre Kunstwerke zu erschaffen.

Unvergessen bleiben auch die Dienstags-Fahrrad-Runden, die so manches mal auf mehr oder weniger improvisierten Alternativrouten endeten.

Der größte Dank geht schließlich an meine Familie. An meine beiden Kinder, Henri und Bruno, die mein Schlafpensum streng limitiert haben und auch sonst dafür sorgten, dass es nie langweilig wurde und an meine Frau Tina, die mir immer den Rücken freigehalten hat, damit ich trotz alledem die Zeit hatte, diese Arbeit zu schreiben.

Zusammenfassung

Diese Arbeit befasst sich mit der Untersuchung des Wärmetransports innerhalb der Spin-Eis Verbindung $Dy_2Ti_2O_7$, sowie innerhalb der Spin-1/2 Ising-Kette $BaCo_2V_2O_8$.

Im Nullfeld zeigt die Wärmeleitfähigkeit von $Dy_2Ti_2O_7$ einen anomalen Wärmetransport. Der zusätzliche Beitrag κ_{mag} zeigt sich als Schulter auf dem phononischen Hintergrund κ_{ph}. Im Nullfeld besitzt die magnetische Wärmeleitfähigkeit κ_{mag} ein Maximum an derselben Stelle wie das Maximum der magnetischen spezifischen Wärme c_{mag}. Dieser Nullfeldbeitrag von κ_{mag} wird im Magnetfeld unterdrückt. Die Feldabhängigkeit von κ_{mag} hängt von der Grundzustandsentartung des magnetischen Systems ab. Im Nullfeld ist die Grundzustandsentartung maximal und daher auch der magnetische Beitrag κ_{mag}. Die vom Magnetfeld realisierte Grundzustandsentartung hängt von der Richtung des angelegten Feldes ab. Das führt zu einer ausgeprägten Anisotropie von κ_{mag} bezüglich der Magnetfeldrichtung.

Darüberhinaus weist auch der phononische Hintergrund κ_{ph} eine Magnetfeldabhängigkeit auf. Diese rührt von Gitterverzerrungen her, welche durch Drehmomente der Dy Ionen im externen Magnetfeld hervorgerufen werden. Um die Feldabhängigkeit von κ_{ph} zu untersuchen, wurden Wärmeleitfähigkeitsmessungen an $(Dy_{0.5}Y_{0.5})_2Ti_2O_7$ vorgenommen, da dort die Spin-Eis-Eigenschaften stark unterdrückt sind. Desweiteren wurde die Verbindung $Dy_2(Ti_{0.9}Zr_{0.1})_2O_7$ untersucht. Durch die zusätzlichen Zr-Störstellen ist die phononische Wärmeleitfähigkeit unterdrückt, was zu einer Reduktion des phononischen Hintergrundes κ_{ph} führt, welcher keine nennenswerte Feldabhängigkeit mehr aufweist. Die magnetischen Eigenschaften werden dadurch kaum beeinflusst, was dazu führt, dass sich κ_{mag} nur wenig verändert.

Im zweiten Teil dieser Arbeit wurden die Transporteigenschaften der effektiven Spin-1/2 Ising-Kette $BaCo_2V_2O_8$ untersucht. Dabei wurde die Wärmeleitfähigkeit parallel und senkrecht zu den Spinketten gemessen. Für beide Wärmestromrichtungen hat die Wärmeleitfähigkeit ein scharfes Minimum an der Ordnungstemperatur T_{N}. Unterhalb von T_{N} ist die Wärmeleitfähigkeit von $BaCo_2V_2O_8$ stark feldabhängig und anisotrop bezüglich der Magnetfeldrichtung.

Um die Transportmechanismen in $BaCo_2V_2O_8$ zu untersuchen, wurden Wärmeleitfähigkeitsmessungen an den dotierten Systemen $(Ba_{0.9}Sr_{0.1})Co_2V_2O_8$ und $Ba(Co_{0.95}Mg_{0.05})_2V_2O_8$, sowie an dem isostrukturellen $BaMn_2V_2O_8$ vorgenommen. Durch die Sr-Dotierung wird die Defektstreuung von Phononen erhöht, wobei das magnetische System nahezu unverändert bleibt. Im Falle der Verbin-

dung $Ba(Co_{0.95}Mg_{0.05})_2V_2O_8$ hat das Dotieren mit unmagnetischem Mg innerhalb der Co-Ketten einen starken Einfluss auf die magnetischen Eigenschaften. Die Heisenberg Spin-5/2-Kette $BaMn_2V_2O_8$ ist eine isostrukturelle Referenz mit isotropen magnetischen Eigenschaften.

Die experimentellen Wärmeleitfähigkeitsdaten von $BaCo_2V_2O_8$ und den Referenzsystemen zeigen keine Anzeichen eines magnetischen Wärmetransports in $BaCo_2V_2O_8$, sondern legen den Schluss nahe, dass der Wärmetransport in $BaCo_2V_2O_8$ rein phononisch ist, wobei das scharfe Minimum bei T_N von Phononstreuung an magnetischen Anregungen herrührt. Diese Interpretation wird gestützt durch die Analyse der Wärmeleitfähigkeitsdaten mithilfe des phononischen Debye-Modells.

Abstract

This thesis concerns the thermal-transport properties of the spin-ice compound $Dy_2Ti_2O_7$ and the spin-1/2 Ising-like spin chain $BaCo_2V_2O_8$.

In zero field, the thermal conductivity of $Dy_2Ti_2O_7$ shows an anomalous magnetic heat transport which appears as an additional shoulder on top of the phononic background κ_{ph}. The zero-field magnetic contribution κ_{mag} has a maximum close to the maximum of the magnetic specific heat c_{mag} and is strongly suppressed by the external magnetic field. The field dependence of κ_{mag} depends on the field-induced ground-state degeneracy of the magnetic spin-ice system. In zero field, the ground-state degeneracy is maximum and, hence, κ_{mag} is maximum. Different field directions result in different field-induced ground states of the spin ice. This leads to a strong anisotropy of $\kappa(B)$ with respect to the field direction.

Moreover, the phononic background κ_{ph} also is magnetic-field dependent. This results from lattice distortions due to torques affecting the Dy momenta in the external magnetic field. The field dependence of κ_{mag} is studied by measurements of the thermal conductivity of the reference compound $(Dy_{0.5}Y_{0.5})_2Ti_2O_7$. Here, the spin-ice features are supposed to be suppressed compared to $Dy_2Ti_2O_7$. In the Zr-doped compound $Dy_2(Ti_{0.9}Zr_{0.1})_2O_7$, the phononic contribution κ_{ph} is suppressed and almost field independent due to additional defect scattering, essentially conserving the spin-ice properties and, hence, the magnetic contribution κ_{mag}.

In the second part of this thesis, the thermal transport properties of the Ising-like effective spin-1/2 chain are studied by measurements of the thermal conductivity parallel and perpendicular to the spin chains. For both heat-current directions, the thermal conductivity exhibits a sharp dip around the ordering temperature T_{N}. Below T_{N}, the thermal conductivity of $BaCo_2V_2O_8$ is strongly field dependent and anisotropic with respect to the field direction. To study the transport mechanisms in $BaCo_2V_2O_8$, additional thermal-conductivity measurements of two doped compounds, $(Ba_{0.9}Sr_{0.1})Co_2V_2O_8$ and $Ba(Co_{0.95}Mg_{0.05})_2V_2O_8$, and of the iso-structural compound $BaMn_2V_2O_8$ were performed. Sr doping increases defect scattering of phonons while the magnetic system is basically unaffected. In case of $Ba(Co_{0.95}Mg_{0.05})_2V_2O_8$, doping into the Co chains strongly influences the magnetic properties. The Heisenberg spin-5/2 chain $BaMn_2V_2O_8$ is an iso-structural reference compound with isotropic magnetic properties.

The experimental κ data of $BaCo_2V_2O_8$ and of the reference compounds show no indication of a magnetic heat transport in $BaCo_2V_2O_8$ and give rise to the

assumption that the thermal conductivity of $BaCo_2V_2O_8$ is of purely phononic origin and that the anomaly around T_N can be attributed to phonon scattering on magnetic excitations. This is supported by analyses of the thermal conductivity of $BaCo_2V_2O_8$ by means of the phononic Debye model.

Offizielle Erklärung

Ich versichere, dass ich die von mir vorgelegte Dissertation selbständig angefertigt, die benutzten Quellen und Hilfsmittel vollständig angegeben und die Stellen der Arbeit – einschließlich Tabellen, Karten und Abbildungen –, die anderen Werken im Wortlaut oder dem Sinn nach entnommen sind, in jedem Einzelfall als Entlehnung kenntlich gemacht habe; dass diese Dissertation noch keiner anderen Fakultät oder Universität zur Prüfung vorgelegen hat; dass sie – abgesehen von unten angegebenen Teilpublikationen – noch nicht veröffentlicht worden ist sowie, dass ich eine solche Veröffentlichung vor Abschluss des Promotionsverfahrens nicht vornehmen werde. Die Bestimmungen der Promotionsordnung sind mir bekannt. Die von mir vorgelegte Dissertation ist von Priv. Doz. Dr. T. Lorenz betreut worden.

Köln, den 19. November 2012

Gerhard Kolland